Experiments on Waves and Currents over a Movable Bed

by

Joshua David Carter

B.S., Ocean Engineering
Texas A&M University, 1999

Submitted to the Department of Civil and Environmental Engineering
in partial fulfillment of the requirements for the degree of

Masters of Science in Civil and Environmental Engineering
at the
MASSACHUSETTS INSTITUTE OF TECHNOLOGY

September 2002

Signature of the Author ______________________________
Department of Civil and Environmental Engineering
August 16, 2002

Certified By______________________________
Ole S. Madsen
Professor of Civil and Environmental Engineering
Thesis Supervisor

Accepted By______________________________
Oral Buyukozturk
Chairman, Departmental Committee on Graduate Studies

Experiments on Waves and Currents over a Movable Bed

by

Joshua D. Carter

Submitted to the Department of Civil and Environmental Engineering
on August 16, 2002 in partial fulfillment of the
requirements for the Degree of Masters of Science in
Civil and Environmental Engineering

ABSTRACT

Several theoretical models have been formulated to characterize the turbulent bottom boundary layer associated with wave and current flows over a rough bed. These models may differ, but they all characterize the interaction between the bottom and the flow by a single roughness length scale, k_n. The use of this single roughness length scale has been verified for co-directional flows over a fixed rippled bed. However, no experimental evidence has been presented which characterizes the bottom roughness for wave, current, and combined wave-current flows over a movable sediment bed covered with naturally formed ripples.

Therefore, an experimental study was performed to characterize the interaction of the movable bed with the flow. The experiments were performed in a 30m long wave flume that can generate co-directional waves and currents over a 10cm thick, 15.2m long bed of sand with a median grain diameter of 0.2mm. The ripple geometry was measured using an acoustic Doppler velocimeter adapted for measuring bedform profiles. The bottom roughness experienced by the current is determined by measuring velocity profiles with an acoustic Doppler velocimeter. The bottom roughness experienced by the waves is determined from friction factors obtained by measuring wave attenuation over the sediment bed.

The roughness values determined from pure wave motion, pure current flow, wave motion in the presence of a current, and a current in the presence of waves are compared. The results show that the roughness is a function of the ripple geometry. For pure wave, pure current, and waves in the presence of a current, a single scaling factor based on the ripple geometry can be used to scale the roughness. For a current in the presence of waves, predictions of the current profiles required that the measurements of the current be adjusted by removing higher order effects for the predictions from the wave-current models to match the measured values. It was found that the roughness scaling factor for the two wave-current models used in this study are model-dependant. For one model, the roughness scaling factor matched that of the other flow types. For the second model, the roughness scaling factor differed by a factor of 3 from the other flow types. To use a single roughness scaling factor to characterize the roughness experienced by pure current, pure wave, and wave-current flows over a movable sediment bed, a specific wave-current model is required. The use of a single scaling factor to characterize the roughness for all flows if other models or modeling techniques are used is not justified based on these conclusions.

Thesis Supervisor: Ole S. Madsen
Title: Professor of Civil and Environmental Engineering

ACKNOWLEDGMENTS

The research presented in this thesis was made possible by the Sea Grant College Program from the Office of Sea Grant of the National Oceanic and Atmospheric Administration, U.S. Department of Commerce, and the Engineering Graduate Fellowship. I would like to express my thanks for their financial support over the past two years.

I was extremely fortunate to have Professor Ole Madsen as my advisor. He was always available to provide me with insight, knowledge, and guidance with research and classwork. His enthusiasm in work and life will follow me throughout my career, for which I am grateful.

Thank you to my friends at MIT. They made life inside and outside the lab more enjoyable and fulfilling in their own unique ways.

Finally, I would like to thank Stephanie for her love, patience, and support throughout this endeavor, and my family, especially my parents Jan and Chip Carter, for all their support, sacrifices, and encouragement. Without them, this accomplishment and all those before and after would not have been possible. Thank you.

TABLE OF CONTENTS

LIST OF FIGURES

LIST OF TABLES

1. INTRODUCTION

Recent US EPA reports state that the sea level is rising, and will rise some 50 to 200 centimeters in the next century or two. They estimate that if no measures are taken, some 36,000 square kilometers (about 14,000 square miles) of US coastal lands, including most of the barrier islands on the Atlantic and Gulf coasts and 1500 square kilometers (about 600 square miles) of densely populated land, may be lost (EPA, 2002; Titus et al., 1991). Further, 100cm of sea level rise would result in a cost on the order of hundreds of billions of dollars, for the most part, from dealing with sediment transport issues such as coastal erosion and maintenance of navigation ways. To better manage these coastal resources under changing conditions, it is necessary to have a thorough understanding of the coastal environment and the processes that directly impact resources in the near-shore region.

At the foundation of the processes that affect the near-shore region are the basic hydrodynamics of the fluid motion in coastal waters. The fluid motion over much of the near-shore water depth can be adequately described by linear potential flow theory due to its inviscid, or frictionless, behavior. Near the bottom of a moving water column, friction (viscosity) plays an increasingly more important role in controlling the flow. Where viscous effects dominate the flow characteristics, called the bottom boundary layer, potential theory is invalid and large interactions take place between the bottom and the fluid. The boundary layer is where the flow transitions from zero velocity to where the viscous effects are no longer significant. It is this boundary layer flow near the bottom that controls the hydrodynamics of almost all coastal processes, especially sediment transport, since it is the interface where the fluid and sediment meet and directly interact. Therefore, to better understand coastal processes, it is necessary to better understand bottom boundary layer flow.

Modeling and predicting coastal processes in turn require the modeling of the velocity field throughout the water column. Waves and currents dominate near-shore waters, and therefore the near-shore velocity field. Waves are generally the result of a wind forcing on the water surface, while currents may be induced by tidal flows, wind forcing, density differences, wave action, or river outflows. In near-shore depths, each of these flows penetrate the water column and create a bottom boundary layer through which both waves and currents transfer forces onto the bottom sediments by shear stresses in the bottom boundary layer. The shear stress of the fluid acting on the sediments is directly related to the velocity gradients, and the velocity gradients depend on how the vertical distance over which flow goes from zero to the free stream velocity. This distance is called the thickness or height of the boundary layer. The height of the boundary layer depends on the intensity and time scale of the flow creating it. The shorter the time scale, the smaller the height of the boundary layer and the more severe the velocity gradients are in the boundary layer. Typically, the time scale of wave action is on the order of seconds, while the time scale of currents is on the order of hours to days. Therefore, the shear stress of the fluid acting on the sediment is directly related to the time scale of the motion of the fluid; consequently, the shear stress from wave action is far greater than that from currents and the waves dominate the shear-stress-dependant processes near the bottom.

It has been observed that the superposition of waves and currents increases the turbulent intensities near the bottom, which increases the motion of the sediment. Sediment motion often leads to formation of bedforms, which interact with the fluid by increasing the turbulence in the water column. This increased turbulence interacts with the waves. In addition, both the wave action and bottom bedforms increase the friction felt by the current. Similarly, the current can affect the bedforms and the waves. Also, increased turbulence near the bottom allows sediments to go into motion and suspension more easily. Thus, waves make sediment available for transport by the current which produces most of the bulk sediment transport.

Theoretical models of turbulent wave-current boundary layer flow use wave, current, and bottom characteristics to predict the bottom shear stress, boundary layer thickness, velocity profile, and energy dissipation. Typically, the waves are specified by their bottom orbital velocity u_{bm} and period T. The current is assumed quasi-steady and characterized by its bottom shear stress τ_c, the current velocity at some specified elevation above the bottom, or the mean current velocity. The bed is often described by the bottom roughness length scale or the Nikuradse equivalent roughness, k_n. The specification of the bottom roughness affects the prediction of all processes associated with the waves, currents, and the resulting sediment transport.

1.1. BACKGROUND

Theoretical analysis of turbulent boundary layer flows requires a turbulence closure method to obtain a solution. Such methods include mixing length models, eddy viscosity models, and advanced turbulence methods, such as the k-ε method, which often results in a complex solution or solution procedure. For this study, an eddy viscosity model is used to model the flow, as it is a compromise between simplicity and accuracy.

1.1.1. EDDY VISCOSITY MODELS

Viscosity relates the stresses between the fluid particles to the fluid kinematics. In laminar flows, the viscosity only depends on the nature of the fluid and its temperature. To model turbulence, Boussinesq developed the eddy viscosity concept. The eddy viscosity is similar in concept to that of kinematic viscosity in laminar flow, but relates the Reynolds stresses to the fluid kinematics, and is a function of the flow intensity in space and time itself, rather than being a constant material property. The Reynolds stresses ($-\overline{u'v'}$) are related to the velocity gradient by

$$-\overline{u'v'} = \nu_t \frac{\partial u}{\partial z} \tag{1.1}$$

where ν_t is the eddy viscosity. Eddy viscosity models of turbulent flow achieve closure by choosing an eddy viscosity which is scaled by some length scale and some velocity scale. Typically, the length scale is taken as the height off the bottom and the velocity scale by some measure of the turbulence or shear stress. Often, the shear velocity u_* is used, where $\rho u_*^2 = \tau$, ρ is the fluid density, and τ is the bottom shear stress.

Various formulations of eddy viscosity models have been proposed. Some of these include Smith (1977), Tanaka and Shuto (1981), Christoffersen and Jonsson (1985), Grant and Madsen (1979 and 1986), Madsen and Wikramanayake (1991), and Madsen and Salles (1998). These models generally differ in how the eddy viscosity is vertically distributed and how it is scaled near the bed. All of these models characterize the interaction between the flow and the bed through a single bottom roughness scale k_n. Typically, the same single roughness scale is chosen to represent pure wave, pure current, and combined wave-current flows. The use of a single roughness scale has been verified experimentally for flows over fixed ripples by Mathisen and

Madsen (1996a, b) (hereafter referred to as MM), with more detail available in Mathisen (1993). It has never been tested or verified for use over a moveable bed with live ripples.

1.1.2. EXPERIMENTS

The interaction between waves, currents, and a movable bed are of fundamental importance to the practice of coastal engineering and to understanding coastal processes. Experimentally, wave-current boundary layer interaction has been studied quite extensively. Some studies include Bakker and van Doorn (1978), Brevik and Aas (1980), Kemp and Simons (1982, 1983), Asano and Iwagaki (1984), Asano et al. (1986), Myrhaug et al. (1987), Simons et al. (1988, 1992, 1994), Sleath (1990), Arnskov et al. (1993), Ranasoma and Sleath (1994), Lodahl et al. (1998).

These studies were done with a rough bottom, not a ripple-covered bottom. A rough bottom is thought to be different in that a ripple bottom is covered with large regular roughness elements that lead to large, regular, organized vortices, rather than the randomly distributed turbulence generated by a plain rough bottom, much like grid-generated turbulence. Much less experimental work on wave or wave-current flows over rippled bottoms has been done: Ranasoma and Sleath (1994), where currents were parallel to the ripple crests, and perpendicular to wave direction, MM, and more recently, Fredsoe et al. (1999). These studies were performed with a *fixed* rippled bottom, not one formed by movable sediment.

Surprisingly little work has been performed on flows over a movable bed that results in live ripples: Carstens et al. (1969), Lofquist (1986), and Rosengaus (1987). Unfortunately, these experiments only considered pure wave flow, not combined wave-current flow.

For combined wave-current flows, the only experiment know to the author which included a movable bed was completed by Gray et. al. (1991). Their study focused on characterizing the bedforms and transport and little information about the bottom boundary layer characteristics or hydrodynamic roughness was reported.

1.2. MOTIVATION

MM verified the use of a single roughness length scale for modeling the interaction between a fixed rippled bottom and pure wave, pure current, and combined wave-current flows. His experiments on waves and currents over a fixed bed helped to explain the role of bedforms in determining the hydrodynamic roughness.

The bottom roughness may differ in two possible ways for the different flow conditions over a movable bed. First, because the flow conditions are fundamentally different in their nature (pure current flow is steady and unidirectional, pure wave flow is unsteady and oscillatory, and combined wave-current flow is some combination of the two), one may expect that the near bottom flow conditions for each separate case may interact in completely different ways with the bedforms and therefore result in a different scale of roughness felt by each separate flow condition. Mathisen (1993) discusses plausible scenarios that may cause the roughness to differ.

The second reason that bottom roughness may differ between flow conditions is that the flow interacts with and changes the bedform geometry. As suggested by Grant and Madsen (1982), the hydrodynamic roughness scales with the bedform geometry. So if one type of flow produces ripples with a larger height, it should experience a larger hydrodynamic roughness. For example, pure wave flows tend to make uniform, symmetric, sharp-crested ripples because of the oscillatory nature of their flow. However, when these pure wave ripples are exposed to a pure current flow, the crest of the ripple may be shaved off and the ripple tends to lean with the direction of flow, making the ripple asymmetric. From a basic knowledge of fluid mechanics, one would expect that flow over the sharp crest of a wave-formed ripple would experience more drag than over a hydrodynamically smoother, asymmetric current modified ripple that has already yielded to the flow, just as the drag around a cube is more than that around a sphere. Then one may logically expect that the bedform geometry will influence the hydrodynamic roughness felt by the flow.

By using a fixed rippled bottom, the effect of the changing ripple geometry can be removed and any differences in roughness must be attributed to the differences in the near-bottom flow characteristics. MM's experiment with fixed ripple geometry determined that the roughness was approximately the same for all flow conditions. While there were some minor variations between the bottom roughness felt by each flow condition, they did not differ significantly because of different near-bottom flow characteristics. This was a vital step in characterizing the bedform – near-bottom flow interaction. The present study takes the next step, and investigates experimentally if the conclusions from fixed ripples of a single roughness scale can be extended to flows over a movable bed.

1.3. OBJECTIVES

This study concentrates on pure wave, pure current, and combined wave-current flows over a movable sand bed. In anticipation of different bedform geometries resulting from the different flow characteristics, we do not propose that the roughness itself will be the same for all flow conditions. However, by formulating the hydrodynamic roughness as

$$k_n = \alpha\eta \tag{1.2}$$

or as

$$k_n = \beta\eta\frac{\eta}{\lambda} \tag{1.3}$$

where η is the bedform height and λ is the bedform length, this study will explore the variation of α and β with the different flow conditions, and aim to verify the assumption that a single hydrodynamic roughness scale can be used to characterize the interaction between the bottom bedform geometry and the turbulent bottom boundary layer flows.

Specifically, we hope to answer the following questions:

1. What is the hydrodynamic roughness k_w experienced by pure wave flows over a movable bed covered with pure wave ripples, and how does k_w compare to the measured physical ripple geometry?
2. What is the hydrodynamic roughness k_c experienced by a pure current flow over a movable bed with current-modified pure wave ripples, and how does k_c compare to the measured physical ripple geometry?
3. What is the hydrodynamic roughness experienced by combined wave-current flows over a movable bed - currents in the presence of waves k_{cw}, and waves in the presence of a current k_{wc} - and how do k_{cw} and k_{wc} compare to the measured physical ripple geometry?
4. Can the hydrodynamic roughness experienced by each flow scenario (k_w, k_c, k_{wc} and k_{cw}) be explained by the same scaling law, e.g., are α and β in equations (1.2) and (1.3) the same for all cases?

1.4. THESIS OUTLINE

In this thesis, pure wave, pure current, and combined wave-current flows over a movable bed are experimentally explored, and the hydrodynamic roughnesses experienced by each flow condition are compared. A theoretical model for wave-current bottom boundary layer flow is required to experimentally characterize the roughness. Chapter 2 summarizes the two models selected to be used in the analysis.

The experimental equipment and procedures developed to characterize the bottom roughness over a movable bed are presented in Chapter 3, and the theory and operation of the wavemaker system is detailed in Chapter 4.

The hydrodynamic roughness is directly related to the movable bedform geometry. So to experimentally relate the bedform geometry to the hydrodynamic roughness, Chapter 5 presents the measured bedform geometries for the different flow conditions.

Chapters 6, 7, 8, and 9 discuss the experiments and results for wave attenuation, pure wave flow, pure current flow, and combined wave-current flow, respectively. Each chapter explains how the bottom roughness is determined for that specific flow condition and analyzes the data to determine the hydrodynamic roughness for each.

Chapter 10 summarizes the results and compares the hydrodynamic roughness values for each flow condition. The conclusions of the thesis are also presented in Chapter 10.

2. TURBULENT WAVE-CURRENT BOUNDARY LAYER FLOW MODELS

The main goal of these experiments is to verify the use of a single hydrodynamic roughness value to characterize the roughness of a movable bed felt by pure wave, pure current, and combined wave-current boundary layer flows. To determine the roughness experimentally, a model of the wave and current boundary layers must be adopted. In this study, the eddy viscosity model of Grant and Madsen (1979 and 1986) (GM) was chosen. Specifically, two models which are modifications of the original GM model are selected to be used for comparison. They are the Madsen and Salles (1998) modifications of the original GM model, hereafter GMm (modified GM model) and the linear-constant model of Barreto-Acobe (2001), hereafter LC.

This chapter briefly discusses other eddy viscosity models and the reasons for selecting the GM models for use in analysis in this study. Also, the basic GM model is explained in some detail, and the modifications of GMm and LC are summarized.

2.1. BACKGROUND

Many different types of theoretical models have been developed for wave and wave-current boundary layers. These include mixing length models, eddy viscosity models, and some advanced turbulence models such as k-ε numerical models. Eddy viscosity models are most commonly used to model wave and current boundary layers, since their treatment of the turbulence is simple and still yields results that match data reasonably well. The underlying approach of most eddy viscosity models is to scale the eddy viscosity near the bottom with a velocity scale that is scaled by a time-invariant shear velocity and a length scale that is scaled by the distance above the bottom. This approach was first applied to the wave-current problem by Lundgren (1972). Since then, a number of eddy viscosity models have been proposed. These include Smith (1977), Tanaka and Shuto (1981), Christoffersen and Jonsson (1985), Grant and Madsen (1979 and 1986), Madsen and Wikramanayake (1991), Sleath (1991), Madsen (1994), Madsen and Salles (1998), and Barreto-Acobe (2001). Generally, the differences in these models involve the vertical distribution of the eddy viscosity and the way in which the time-invariant shear velocity scales the eddy viscosity near the bed. All of these models define the bottom boundary condition using a single bottom roughness length scale. The roughness length scale basically characterizes the interaction between the near-bottom fluid motion and the bottom. Madsen and Wikramanayake (1991) reviewed a number of these models. Their comparison found that the eddy viscosity model by Grant and Madsen (1986) proved the simplest to apply and still resulted in an adequate fit to experimental data. Therefore, the Grant-Madsen model, along with some modified versions of the original GM model, will be used in this study.

2.2. ORIGINAL GRANT-MADSEN MODEL

In the original Grant-Madsen turbulent bottom boundary layer eddy viscosity flow model, the flow in the wave-current boundary layer is characterized by a linearized horizontal momentum equation given as

$$\frac{\partial \vec{u}}{\partial t} = -\frac{1}{\rho}\nabla p + \frac{\partial}{\partial z}\left[\nu_t \frac{\partial \vec{u}}{\partial z}\right] \qquad (2.1)$$

where $\vec{u}$ is the horizontal velocity vector $\{u, v\}$, ρ is the fluid density, ∇ is the gradient operator, p is the pressure, and ν_t is a turbulent eddy viscosity. This equation is analogous to the Navier-Stokes equation for laminar flows, but does not assume a constant viscosity. If ν_t is taken as time-invariant, and by separating the horizontal velocity vector into a wave component u_w and a steady current component u_c,

$$\vec{u} = \vec{u}_w + \vec{u}_c \tag{2.2}$$

equation (2.1) can be considered the sum of an oscillatory component and a time-invariant component where the oscillatory component is related to the waves and the time-invariant (steady) component is related to the current, then equation (2.1) becomes

$$\frac{\partial \vec{u}_w}{\partial t} = -\frac{1}{\rho}\nabla p_c - \frac{1}{\rho}\nabla p_w + \frac{\partial}{\partial z}\left[\nu_t \frac{\partial \vec{u}_c}{\partial z}\right] + \frac{\partial}{\partial z}\left[\nu_t \frac{\partial \vec{u}_w}{\partial z}\right] \tag{2.3}$$

By keeping the requirement that ν_t is independent of time, the time-varying components in equation (2.3) are independent of the time-invariant components and can be separated to form two independent equations: the wave equation and the current equation. The governing equation for the wave is

$$\frac{\partial \vec{u}_w}{\partial t} = -\frac{1}{\rho}\nabla p_w + \frac{\partial}{\partial z}\left[\nu_t \frac{\partial \vec{u}_w}{\partial z}\right] \tag{2.4}$$

And the governing equation for the current is

$$0 = -\frac{1}{\rho}\nabla p_c + \frac{\partial}{\partial z}\left[\nu_t \frac{\partial \vec{u}_c}{\partial z}\right] \tag{2.5}$$

2.2.1. THE EDDY VISCOSITY MODEL

The fundamental assumption made in this model is to define the turbulent eddy viscosity as time-invariant. Then GM assumed that the eddy viscosity is scaled by a shear velocity and the distance away from the bed, so ν_t is defined as

$$\nu_t = \begin{cases} \kappa u_{*m} z & z < \delta \\ \kappa u_{*c} z & z > \delta \end{cases} \tag{2.6}$$

where κ is the von-Karman constant, a non-dimensional number that typically has a value of 0.4, u_{*m} is the maximum combined wave-current shear velocity, u_{*c} is the current shear velocity, and δ is the wave boundary layer thickness, defined as

$$\delta = A \frac{\kappa u_{*m}}{\omega} \tag{2.7}$$

This boundary layer thickness has been the source for much debate and is the main factor in the modifications of the original GM model. In its original formulation, Grant and Madsen (1979) took A to be 2. Later, Grant and Madsen (1986) suggested A to be somewhere between 1 and 2. Further modifications have led to a value of A that depends on the relative roughness of the bed. These modifications will be discussed later in Section 2.3.

Outside the wave boundary layer ($z > \delta$), the eddy viscosity is scaled by the current shear velocity u_{*c}, which is related to the current shear stress

$$\tau_c = \rho u_{*c}^2 \tag{2.8}$$

Within the wave boundary layer ($z < \delta$), the turbulence, and thus the turbulent eddy viscosity, is characterized by the wave-current shear velocity, also called the maximum shear velocity u_{*m}. This is scaled by the maximum combined bottom shear stress τ_m so that

$$\tau_m = \rho u_{*m}^2 \tag{2.9}$$

where τ_m is defined

$$\tau_m = \left| \vec{\tau}_c + \vec{\tau}_{wm} \right| \tag{2.10}$$

Here, $\vec{\tau}_c$ is the bottom current shear stress and $\vec{\tau}_{wm}$ is the maximum wave bottom shear stress. Then, to obtain an expression for u_{*m} in terms of u_{*c} and u_{*wm}, we first define

$$\mu = \left(\frac{u_{*c}}{u_{*wm}} \right)^2 \tag{2.11}$$

Then, the shear stress interaction is modeled as

$$C_\mu = \left[1 + 2\mu \left| \cos\phi_{wc} \right| + \mu^2 \right]^{\frac{1}{2}} \tag{2.12}$$

where ϕ_{wc} is the angle between the wave and the current. Then u_{*m} can be written

$$u_{*m} = \sqrt{C_\mu u_{*wm}^2} \tag{2.13}$$

2.2.2. THE WAVE SOLUTION

To solve the time-varying wave problem, the governing equation for waves, equation (2.4), is simplified by choosing the x-direction to be the same as the direction of propagation of the wave so that $\vec{u}_w = (u_w)_x = u_w$. Then equation (2.4) reduces to

$$\frac{\partial u_w}{\partial t} = -\frac{1}{\rho}\frac{\partial p_w}{\partial x} + \frac{\partial}{\partial z}\left[\nu_t \frac{\partial u_w}{\partial z} \right] \tag{2.14}$$

Near the edge of the wave boundary layer, the velocity approaches the free stream velocity predicted by inviscid theory where viscous forces can be neglected. By continuity, the governing equation at this location becomes

$$\frac{\partial u_w}{\partial t} = \frac{\partial}{\partial t}U = -\frac{1}{\rho}\frac{\partial p_w}{\partial x} \quad \text{as} \quad z \to \infty \quad (\sim \delta) \tag{2.15}$$

where U is the free stream velocity predicted by linear potential theory just outside the boundary layer. At this location, we assume that the pressure gradient just inside the boundary layer is independent of depth and is equal to the pressure gradient just outside the boundary layer. Subtracting (2.15) from (2.14) yields

$$\frac{\partial u_w}{\partial t}-\frac{\partial}{\partial t}U=\frac{\partial}{\partial z}\left[\nu_t\frac{\partial u_w}{\partial z}\right] \tag{2.16}$$

As U is independent of the distance from the bottom, $\partial U/\partial z=0$. Taking the quantity $u_w-U=u_d$ where u_d is termed the deficit velocity, equation (2.16) can be rewritten

$$\frac{\partial u_d}{\partial t}=\frac{\partial}{\partial z}\left[\nu_t\frac{\partial u_d}{\partial z}\right] \tag{2.17}$$

To express the distance above the bottom z in non-dimensional terms, take

$$\zeta=\frac{z}{l} \text{ where } l=\frac{\kappa u_{*m}}{\omega} \tag{2.18}$$

Then equation (2.17) is again rewritten

$$\frac{\partial u_d}{\partial t}=\frac{\partial}{\partial \zeta}\left[\zeta\frac{\partial u_d}{\partial \zeta}\right] \tag{2.19}$$

The boundary conditions for this equation are

$$u_d=0 \text{ at } \zeta\rightarrow\infty \tag{2.20}$$

And expecting the solution to be simple harmonic, the other boundary condition is

$$u_d=-U=-u_{bm}e^{i(\omega t-kx)} \text{ at } \zeta=\zeta_0 \tag{2.21}$$

where u_{bm} is the near-bottom maximum horizontal orbital velocity predicted by linear wave theory, ω is the radian frequency of the wave motion ($\omega = 2\pi/T$), k is the wave number ($k = 2\pi/L$), and

$$\zeta_0=\frac{z_0}{l} \tag{2.22}$$

With these boundary conditions, Grant and Madsen found the solution for the periodic wave velocity profile as

$$u_d = \Re e\left\{ \frac{\ker 2\sqrt{\zeta} + i \operatorname{kei} 2\sqrt{\zeta}}{\ker 2\sqrt{\zeta_0} + i \operatorname{kei} 2\sqrt{\zeta_0}} u_{bm} e^{i(\omega t - kx)} \right\} \tag{2.23}$$

where ker and kei are Kelvin functions of the zeroth order. Since ζ_0 is related z_0, the velocity of the wave motion within the wave boundary layer depends on the hydraulic roughness z_0. This hydraulic roughness for a fully rough turbulent flow can be related to the Nikuradse roughness by $k_n = 30z_0$.

2.2.3. THE CURRENT SOLUTION

The equation governing the current will only depend on the distance above the bottom since we have assumed a time-invariant eddy viscosity. Simplifying the governing equation for the current, equation (2.5), by choosing the x-direction to be the same as the direction of the current so that $\vec{u}_c = (u_c)_x = u_c$, the governing equation becomes

$$0 = -\frac{1}{\rho}\frac{\partial p_c}{\partial x} + \frac{\partial}{\partial z}\left[\nu_t \frac{\partial u_c}{\partial z} \right] \tag{2.24}$$

Using the law of the wall argument to neglect the pressure gradient term close to the bottom, this equation can be simplified to

$$0 = \frac{\partial}{\partial z}\left[\nu_t \frac{\partial u_c}{\partial z} \right] \tag{2.25}$$

The first boundary condition is obtained by defining a boundary shear stress

$$\frac{\tau_c}{\rho} = u_{*c}^2 = \nu_t \frac{\partial u_c}{\partial z} \tag{2.26}$$

The remaining boundary conditions are from velocity matching at δ and near the bottom, which introduces the roughness into the problem:

$$u_c = 0 \quad \text{at} \quad z = z_0 \tag{2.27}$$

With these boundary conditions, the current solution can be written as

$$u_c = \begin{cases} \dfrac{u_{*c}}{\kappa}\dfrac{u_{*c}}{u_{*m}}\ln\dfrac{z}{z_0} & z < \delta \\ \dfrac{u_{*c}}{\kappa}\left[\ln\dfrac{z}{\delta} + \dfrac{u_{*c}}{u_{*m}}\ln\dfrac{\delta}{z_0}\right] & z > \delta \end{cases} \tag{2.28}$$

By defining an apparent roughness z_{0a}, the velocity profile for $z > \delta$ can alternatively be written

$$u_c = \frac{u_{*c}}{\kappa}\ln\frac{z}{z_{0a}} \quad \text{for} \quad z > \delta \tag{2.29}$$

where

$$z_{0a} = \frac{k_{na}}{30} = \delta\left(\frac{\delta}{z_0}\right)^{-\frac{u_{*c}}{u_{*m}}} \tag{2.30}$$

where k_{na} is the apparent Nikuradse roughness. As with the wave velocity profile, equation (2.23), the current velocity profile depends on a hydraulic roughness z_0. Thus, we assume a single value for the hydraulic roughness characterizes the profiles for both the waves and the current.

2.2.4. SHEAR STRESS AND WAVE-CURRENT FRICTION FACTOR

The shear stress due to waves acting on the bottom τ_w can be determined from

$$\tau_w = \rho \nu_t \left.\frac{\partial u}{\partial z}\right|_{z_0} \tag{2.31}$$

Then by substituting equation (2.6) for ν_t, equation (2.23) for the velocity in the above equation and evaluating it at $z = z_0$, the wave shear stress can be written

$$\tau_w(t) = \Re e\left\{ -\kappa\rho u_{*m} u_{bm} \sqrt{\zeta_0} \frac{\mathrm{ker}'\left(2\sqrt{\zeta_0}\right) + i\,\mathrm{kei}'\left(2\sqrt{\zeta_0}\right)}{\mathrm{ker}\left(2\sqrt{\zeta_0}\right) + i\,\mathrm{kei}\left(2\sqrt{\zeta_0}\right)} e^{i\omega t} \right\} \tag{2.32}$$

Alternatively, the wave shear stress may be written in real form as

$$\tau_w(t) = \tau_{wm} \cos(\omega t + \phi) \tag{2.33}$$

Where τ_{wm} is the maximum wave shear stress and ϕ is a phase angle between the bottom shear stress and bottom horizontal orbital velocity.

Jonsson (1966) related $\tau_w(t)$ to the near bottom horizontal orbital velocity through a wave-current friction factor f_w by

$$\left|\tau_w(t)\right| = \rho u_{*wm}^2 = \frac{1}{2}\rho f_{wc} u_{bm}^2 \tag{2.34}$$

Equating this equation and equation (2.32), the friction factor may be related to the equivalent hydrodynamic roughness k_n, or in the case of wave-current flows, k_{wc}, by taking the absolute magnitude of equation (2.32) and relating it to the friction factor defined in equation (2.34). Then since ζ_0 can be written in terms of k_n, a relationship exists between f_{wc} and k_{wc}. However, this relationship involves the quantities u_{*m} and u_{*wm}. Therefore, no explicit relationship can be determined between f_{wc} and k_{wc}, although the implicit relationship can be solved with a simple numeric scheme.

Madsen (1994) formulated approximations to this relationship through the explicit formulas

$$f_{wc} = C_\mu \exp\left\{7.02\left(\frac{C_\mu A_{bm}}{k_n}\right)^{-0.078} - 8.82\right\} \qquad \text{for } 0.2 < \frac{C_\mu A_{bm}}{k_n} < 10^2 \tag{2.35}$$

and

$$f_{wc} = C_\mu \exp\left\{5.61\left(\frac{C_\mu A_{bm}}{k_n}\right)^{-0.109} - 7.30\right\} \qquad \text{for } 10^2 < \frac{C_\mu A_{bm}}{k_n} < 10^4 \tag{2.36}$$

where A_{bm} is the bottom orbital excursion amplitude, $A_{bm} = u_{bm}/\omega$. These expressions are accurate to within about 1% for the indicated ranges of relative roughness.

2.2.5. LIMIT OF PURE WAVES AND PURE CURRENTS

In the limiting case of pure waves, u_{*m} becomes u_{*wm}, and all equations of the wave solution are applicable. When relating the wave friction factors to the wave roughness, the factor $C_\mu = 1$, and no other changes are necessary. For a fixed bed with artificial ripples, MM determined that the value of the pure wave roughness is the same as the roughness for waves in the presence of a current. Also, these roughness values were found to be equivalent to those for a pure current over the same bed. This fact is assumed to be true for similar flows over a movable bed, but the assumption has never been verified.

In the limit of pure current flows, the eddy viscosity simplifies to

$$\nu_t = \kappa u_{*c} z \tag{2.37}$$

Then the velocity profile simplifies to the classical logarithmic form of the law of the wall:

$$u_c = \frac{u_{*c}}{\kappa} \ln \frac{z}{z_0} \tag{2.38}$$

where $z_0 = 30\ k_n$.

2.3. MODIFICATIONS TO THE GRANT-MADSEN MODEL

2.3.1. MODIFIED GRANT-MADSEN MODEL

As mentioned in the previous section, many of the modifications to the original GM model focus on the definition of the thickness of the wave or wave-current boundary layer δ. For the GM model, this quantity is the matching level where the wave-current dominated layer ends and the pure current layer begins. In the original formulation, δ was the level required for the wave orbital velocity to approach its free stream value within a certain percentage. This resulted in

$$\delta = A\frac{\kappa u_{*m}}{\omega} \tag{2.39}$$

with A originally taken as 2 due to the limited amount of data available, but later was updated to be somewhere in the range of 1 to 2. Madsen and Salles (1998) discovered that the parameter A is not a constant, but is in fact a function of the relative roughness and should be defined as

$$A = C_\mu \exp\left\{2.96\left(\frac{C_\mu A_{bm}}{k_n}\right)^{-0.071} - 1.45\right\} \tag{2.40}$$

2.3.2. LINEAR-CONSTANT MODEL

A more recent approach to modeling the wave-current boundary layer was performed by Barreto-Acobe (2001). This model is based on all the best aspects of the various modifications of the GM model. It allows for the no-slip boundary condition to be applied at either $z = z_0$ or $z = 0$ as suggested by Madsen and Salles (1998). The eddy viscosity is defined as

$$\nu_t = \begin{cases} \kappa u_{*m}\left(z + z_b\right) & z + z_b \le \alpha l \\ \kappa u_{*m}\alpha l & \alpha l \le z + z_b \le \alpha l/\varepsilon \\ \kappa u_{*c}\left(z + z_b\right) & \alpha l/\varepsilon \le z + z_b \end{cases} \tag{2.41}$$

where z_b is chosen to be either 0 or z_0 and

$$\varepsilon = \frac{u_{*c}}{u_{*m}} \tag{2.42}$$

This eddy viscosity model provides for a continuous transition between the region where the turbulence is dominated by wave motion to the region where turbulence is dominated by the current. The resulting velocity profile is smooth rather than kinked at the transition as are the GM and GMm. This type of viscosity model was first used by Madsen and Wikramanayake (1991). Finally, the LC model provides a transition point between the wave and current dominated regions that is a pre-set fraction of the boundary layer height, pre-determined by boundary layer experiments. This allows the model to be entirely predictive and eliminates its dependence on application-specific fitting parameters. The resulting height of transition depends on the relative roughness and u_{*c}/u_{*m} .

For the complete derivation of the LC model, the reader is referred to the original text (Barreto-Acobe, 2001). The equations necessary for its application are given here.

The wave current friction factor for the LC model is defined as

$$f_{wc} = C_{\mu LC} \exp\left\{ A_1 \left[\frac{C_{\mu LC} A_{bm}}{k_n} \right]^{A_2} - A_3 \right\} \tag{2.43}$$

where $C_{\mu LC}$ and μ_{LC} are defined (different than C_μ and μ in the GM model):

$$C_{\mu LC} = \left(1 + 2\mu_{LC}^2 \left|\cos\phi_{wc}\right| + \mu_{LC}^4\right)^{1/2} \tag{2.44}$$

and

$$\mu_{LC}^2 = \left(\frac{u_{*c}}{u_{*wm}}\right)^2 \tag{2.45}$$

and the parameters A_1, A_2 and A_3 are given in Table 2.1 for the ranges of relative roughness (RR_{LC}), where

$$RR_{LC} = \frac{C_{\mu LC} A_{bm}}{k_n} \tag{2.46}$$

Table 2.1: Parameters for f_{wc} of LC model in equation (2.43).

Range of Applicaion	A_1	A_2	A_3
$10^{-1} < RR_{LC} < 10^2$	7.02	-0.078	8.82
$10^2 < RR_{LC} < 10^6$	5.61	-0.109	7.30

Then using f_{wc}, the shear velocities are redefined

$$u_{*wm} = \sqrt{\frac{1}{2} f_{wc} u_{bm}^2} \tag{2.47}$$

and

$$u_{*m} = \sqrt{C_{\mu LC} u_{*wm}^2} \tag{2.48}$$

With ε defined in equation (2.42),

$$\alpha_r = Y \exp\left\{1.2\left(\frac{C_{\mu LC} A_{bm}}{k_n}\right)^{-0.2} - 2.12\right\} - 0.02\left(\frac{C_{\mu LC} A_{bm}}{k_n}\right)^{-0.3} \tag{2.49}$$

where Y is a factor greater than or equal to 1, and depends on ε as

$$Y = \begin{cases} S\varepsilon + I & S\varepsilon + I > 1 \\ 1 & S\varepsilon + I \le 1 \end{cases} \tag{2.50}$$

where

$$S = -0.026\left[\log_{10}\left(\frac{C_{\mu LC} A_{bm}}{k_n}\right)\right]^2 + 0.284\left[\log_{10}\left(\frac{C_{\mu LC} A_{bm}}{k_n}\right)\right] + 0.942 \qquad (2.51)$$

and

$$I = -0.013\log_{10}\left[\frac{C_{\mu LC} A_{bm}}{k_n}\right] + 0.712 \qquad (2.52)$$

Finally, the current velocity profile is defined by

$$u_c = \begin{cases} \varepsilon \dfrac{u_{*c}}{\kappa} \ln \dfrac{z + z_b}{z_0} & z + z_b < z_m \\ \varepsilon \dfrac{u_{*c}}{\kappa} \left[\dfrac{z + z_b}{z_m + z_b} - 1 + \ln \dfrac{z_m + z_b}{z_0} \right] & z_m < z + z_b < z_l \\ \dfrac{u_{*c}}{\kappa} \ln \dfrac{z + z_b}{z_{0a}} & z + z_b > z_l \end{cases} \qquad (2.53)$$

in which

$$z_m = \alpha_r l \qquad (2.54)$$

with l is defined in equation (2.18), and

$$z_l = \frac{z_m + z_b}{\varepsilon} \qquad (2.55)$$

Just as in the GM model, z_{0a} is the apparent roughness, and therefore the apparent Nikuradse roughness, k_{na}, can be expressed as

$$z_{0a} = \frac{k_{na}}{30} = z_l \exp\left\{ -\frac{\kappa u_c (z = z_l)}{u_{*c}} \right\} \qquad (2.56)$$

3. EXPERIMENTAL DESIGN AND SETUP

The experimental facilities used for this work are located in the Ralph M. Parson's Laboratory for Water Resources and Hydrodynamics at the Massachusetts Institute of Technology. This chapter describes the experimental conditions, the wave flume and its features, the sediment used in the study, and additional experimental equipment such as wave gages and the ADV velocity probe. Much of this information, especially about the experimental facilities, can be found in Mathisen (1993) and Rosengaus (1987), but is included here in some detail for completeness.

3.1. THE WAVE FLUME

The wave flume at the Parson's Laboratory, show in Figure 3.1, consists of 3 main sections: a long, rectangular flume, a large basin behind the wavemaker at one end of the flume, and another large basin at the other end of the flume. The flume section is 28m long, 76.2cm wide, and can accommodate a water depth of up to 91cm. It is lined with ½" thick glass walls on the sides and most of the bottom, except for the first 3m and last 12m of the bottom, which are metal plates. At one end of the flume, the wavemaker (described in Section 3.5) separates the flume from the basin, while at the other end a 1 on 10 sloping permeable wooden beach covered with 2" thick fibrous "horsehair" material separates the basin from that end of the flume. The beach combined with the horsehair act to dissipate wave energy and help to reduce wave reflection in the tank. The beach toe is 19.5m from the wavemaker's mean position and extends completely to the free surface for the maximum depth in the channel. The large basins at either end of the flume have smooth transitions to the dimensions of the flume.

An inlet for the current is provided by a rectangular hole and basin just lee of the wavemaker. The hole can be covered by a solid metal lid if desired (for generation of pure waves without reflection from the current inlet basin), or can be covered by a mesh grid to be used in wave-current cases. The mesh grid was in place for all experiments performed in this study so the physical conditions in the flume were the same for all experiments. The dissipating beach was made porous to allow for recirculation of the current by drilling 3" holes in the beach over approximately half the water depth.

The entire structure is 36.5m long, and is supported by a metal frame of cross-members every 3m, dividing the glass into 10' long plates. The glass plates attach to the metal frame with a strong but flexible silicon sealant, which acts as small irregularities to the flow. Two rails run along the top of the channel to allow for easy positioning and movement of instruments via wheeled carts.

The coordinate system used throughout this thesis will treat the longitudinal axis of the flume as x, with $x = 0$ at the mean position of the wavemaker and positive toward the beach. Using a right-handed coordinate system, the z-axis is positive upwards from the inside bottom of the flume or bedforms (to be defined where appropriate), and the y-axis positive from right to left along the incident direction of propagation of the waves.

The wave flume has been used successfully in many previous studies. Some of these include breaking wave studies by Rapp (1986) and Chan (1986), wave attenuation and wave – movable bed interaction (Rosengaus, 1987), wave-current-fixed bedform interaction (Mathisen, 1993), and current and wave-fixed bedform interaction studies (Barrantes, 1996). Major modifications were made to the flume (Mathisen, 1993) to allow for a current to be generated simultaneously with waves. His thesis contains details of the design of the current generation system.

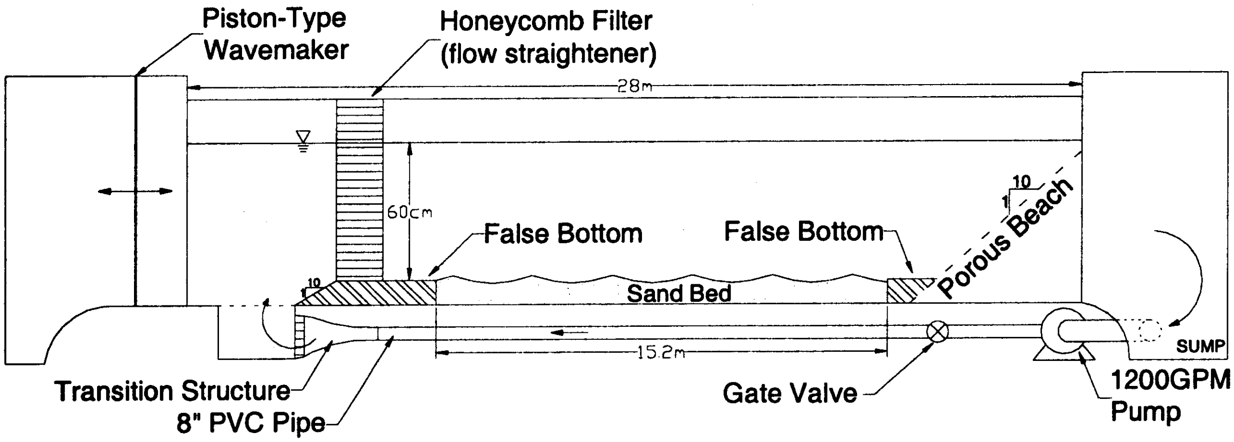

Figure 3.1: Schematic of wave flume and experimental setup.

3.2. SEDIMENT TEST SECTION

The sediment test section is a uniform layer of sediment 10cm deep across the width of the flume extending 15.2m along the flume. A ¼" thick rubber mat was placed over the glass bottom of the flume to protect the glass from scratches by the sediment or tools used to load and unload the sediment. False bottoms were constructed to enclose the sand and provide for a smooth transition from the flume bottom to the level of the sand and from the sand bed to the beach. The false bottom near the wavemaker also protects the sediment bed from jets formed from the honeycomb current filter placed near the current inlet (discussed in Section 3.4.1).

Figure 3.1 shows a schematic of the false bottoms. The false bottom near the wavemaker has a smooth 1m long 1:10 slope transition up to a 1m long flat section that rests at 10cm off the bottom of the flume. The slope starts just after the current inlet basin. The slope at the beach end consists of a 1m long 1:10 slope that, when positioned on top of the first 1m of beach, acts as a level transition from the sand bed to the beach slope at 10cm off the flume bottom. The false bottoms required more than 100lbs of lead weight fixed to their underside in order to remain stationary and not move under the action of the waves.

Both false bottoms were equipped with an optional sediment trap adjacent to the sediment test section as a means to measure sediment transport. This 12" section of the false bottom can be removed or replaced with a fine mesh lid which allows sand to pass through with minimal effect on the flow. This feature was not utilized in these experiments, as measurement of sediment transport is not within the scope of this project.

The gaps between the false bottoms and the flume walls and bottoms proved difficult and important to seal. If not sealed properly, strong turbulent jets formed and often had a severe local impact on the sediment bed. Along the top of the false bottom nearest the wavemaker, silicon sealant was used to seal the gaps between the false bottom and the flume wall (which often were quite large). A thick gauze was stuffed into the gaps larger than 1/8" to keep the silicon from falling through the gap. Unfortunately, the sediment trap was not sealed with silicon in case the solid lid was to be removed. Instead, the trap was sealed with a secure layer of duct tape. The silicon sealant proved quite effective over the 9 months the false bottoms were submerged. The duct tape held quite well for the first 4 months. Shortly after that period, the duct tape failed and could not be re-applied; no amount of drying or cleaning could completely remove the sediment from the surface where the tape was to be applied. The resulting jets rendered the area of the sediment bed within 2m lee of the wavemaker side false bottom unsuitable for measurement.

The false bottom near the beach was not sealed with silicon in order to allow for water to drain out of the test bed if necessary. There were no local effects of jets near this transition.

About 2500kg of sediment was used to fill the sediment test section. In order to move all this sediment, a special transport box was built. The box can carry approximately 100kg of sediment in a load, and can hook up to the overhead motorized crane in the lab which passes almost directly overhead of the flume. The box fits inside the flume and has foam padded contact points to insure that is does not damage the glass. When placing the sand, the flume was filled with about 30 cm of water, and the sand was slowly poured into the flume to insure the sediment was fully saturated. After the sediment was placed, it was raked thoroughly to try to remove air pockets and aid in uniform settling. Several days of raking were required for all large bubbles to be removed. This was important in order to insure that, as much as possible, the sand had uniform properties.

Starting experiments with a smooth, flat bed increases repeatability and insures a uniform starting point for the measurements. To attain a flat bed, a scraper was built. It ran on the rails above the flume, and consisted of two 1.5" angle irons placed back to back with a piece of rubber between the two to increase the effective height of the scraper. The scraper blade ran the width of the flume, and was connected to the cart with two rods fitted inside linear ball bearings, allowing for vertical movement of the blade. This scraper was very effective in achieving a flat bed. However, it is possible it could induce some nonuniformities in the bed through compaction by putting a large stress on the bed when moving large quantities of sediments. Note that there is no vertical compaction of the bed through the scraper since its weight rests on the rails and not the bed. The scraper was originally designed by Rosengaus (1987), and was only slightly modified here.

Rosengaus (1987) found that the final bedform geometry obtained for a particular wave condition was independent of the initial bed shape. That is, if the bed was initially flat, or had a few disturbances on it, it would form uniform bedforms given enough time. However, for a flat bed the shear stress and turbulence at the bed is not enough to initiate motion of the sediment to quickly generate bedforms – the bedforms will eventually form, but the period of time it would take is unsatisfactory. Therefore, to speed up the formation of the ripples, initiator ripples were drawn on the sediment across the flume width spaced at 10ft along the bed. These initiators increased the speed of bedform development significantly.

3.3. SEDIMENT PARAMETERS

This section quantitatively describes the sediment used in the experiments and specifies the sediment parameters under actual laboratory conditions that are pertinent to later analysis.

The sediment used in these experiments is the same sediment used in Rosengaus's (1987) study. It is 0.2mm Ottawa silica F-75 sand purchased from New England Silica, Inc., of South Windsor, Connecticut. The manufacturer's specifications state the sand is nearly pure (99.75%) SiO_2 silica sand. The manufacturer provided a sieve analysis of the sand, which gave the median grain diameter (d_{50}) to be 0.2mm. However, an in-house sieve analysis was performed as a check on the manufacturer's specifications.

Figure 3.2 shows the in-house and manufacturer's sieve analysis. The abscissa is plotted in both grain diameter and in the ϕ format (Shore Protection Manual (SPM), 1984) where ϕ is $-\log_2$ of the grain diameter in millimeters. The ordinate shows the fractional percentage of weight which is coarser than the corresponding grain size. Parameters of the distributions, based on the analysis procedure given in the SPM (1984), are shown in Table 3.1. Here, ϕ_x is the value of ϕ that occurs at the percent x, M_ϕ is an approximation to mean ϕ, σ_ϕ is the standard deviation of the distribution (a measure of uniformity), and α_ϕ is the skewness or a measure of asymmetry. These parameters are given as (SPM, 1984)

$$M_\phi = \frac{\phi_{16} + \phi_{50} + \phi_{84}}{3}, \quad \sigma_\phi = \frac{\phi_{84} - \phi_{16}}{2}, \text{ and } \alpha_\phi = \frac{M_\phi - \phi_{50}}{\sigma_\phi}$$

Table 3.1: Distribution parameters of the sediment from both in-house and manufacturer's analysis.

	ϕ_{50}	ϕ_{84}	ϕ_{16}	M_ϕ	σ_ϕ	α_ϕ	d_{50} [mm]
in-house	2.357	2.840	1.788	2.328	0.526	-0.055	0.195
manufacturer	2.431	3.010	1.925	2.455	0.542	0.045	0.186

The in-house distribution shows that the distribution of sediment has a slightly larger d_{50} than the manufacturer's. This difference could be attributed to the fact that more of the fines in the sediment have been washed away with use, or could simply be that the in-house analysis was performed on only one sample which happened to be slightly larger than the entire sample. Regardless, we will always treat the sand for the experiments to have $d_{50} = 0.2$mm and a density $\rho = 2650$ kg/m^3.

Rosengaus (1987) determined the sand used in this study has a distribution similar to that of natural sands found on a beach with grain sizes in the same range as those used here.

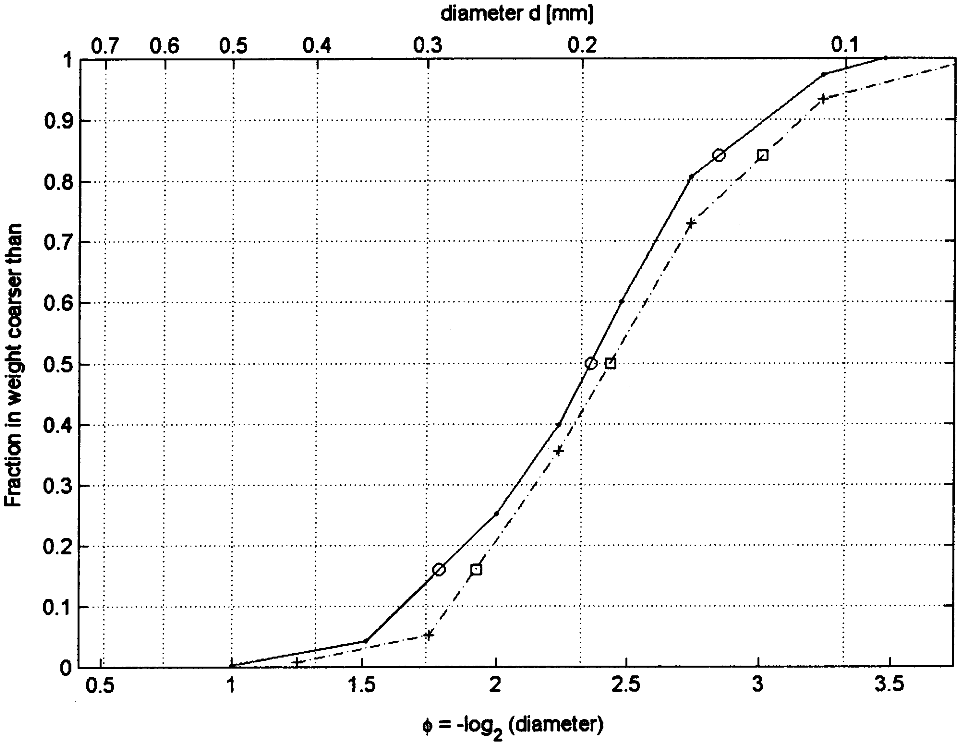

Figure 3.2: Grain size distribution from in-house (solid line with ·) and manufacturer's (dash-dot line with +) sieve analysis; also, ϕ_{16}, ϕ_{50}, ϕ_{84} plotted for in-house (open circles) and manufacturer's (open squares).

3.4. CURRENT GENERATION SYSTEM

In order to study wave and current interaction, a re-circulating pump system was installed in the flume by Mathisen (1993). For full details and capabilities of the current generation system, please refer to that paper; it is summarized below.

The current generation system consists of a 1200gpm pump, a gate valve to control the flow rate, a flow meter on the return pipe, and intake and outflow transition sections. The current is generated by circulating water through the perforated beach and the beach-end basin where an intake leads to the pump. The water is pumped through a pipe running the length of the flume, and introduced into the flume through a transition section just lee of the wavemaker. At the maximum flow rate of 1200gpm it is capable of generating a depth-averaged current of approximately 16cm/s in a depth of 60cm.

3.4.1. CURRENT FILTER (FLOW STRAIGHTENER)

The inflow transition structure for the current was designed to produce a uniform flow entering the flume. However, tests by Barrantes (1996) showed that with no modifications, the flow has a rather large secondary flow that is helicoidal in nature. This has serious implications for boundary layer development. The flow near the bottom will only be near the bottom from the time it starts at the sidewall until it reaches the other wall, or in this case until it reaches the center of the flume (since all measurements were conducted at b/2 or 38.1cm from the sidewalls). Then the distance the flow has to develop is inversely proportional to the lateral velocity, given by

$$x_{develop} = \left(\frac{ub}{2}\right)\frac{1}{v} \tag{3.1}$$

where $x_{develop}$ is the distance the boundary layer has to develop, u is the velocity in the x-direction along the flume, v is the lateral velocity in the y-direction across the flume, and b is the flume width (76.2cm). For the best-case scenario, if u is 16cm/s and v is 1cm/s, the boundary layer only has 6m of development length. That means the effective length of the tank is $x_{develop}$ = 6m, and having such a long tank is of no use. In a more realistic case, the near-bottom velocity u is closer to 10cm/s. Then, with v at 1cm/s, $x_{develop}$ is only 3.8m. Clearly, these are not acceptable conditions to perform measurements on near-bottom flow and boundary layers, as the boundary layer will not have time to fully develop.

To correct this problem, Barrantes employed a honeycomb filter to straighten the flow. The filter was designed to fit the exact width of the flume: it is 76.2cm wide and tall, 35cm long, and is made of thin PVC cylinders with a 2cm diameter stacked together as tightly as possible. To keep the filter from moving under the action of the waves and current, it was braced with strong nylon string from its four corners, and tied to the top of the flume. Also, a metal brace was fit on the top of the filter and fixed to the flume, keeping the filter from tilting. These simple braces proved quite satisfactory; the filter does not move even under the most extreme conditions possible. Section 3.7.5 discusses the performance of the filter for straightening the flow – it was found that the filter is successful at removing the secondary, helicoidal flow from the flume.

The use of the filter is not without cost - two major problems result from use of the filter: 1) turbulent jets are produced near the bottom of the filter which can affect the sediment bed and 2) the filter interacts with wave generation. To accommodate the turbulent jets, the false bottom was extended 65cm past the lee side of the filter, allowing time for the jets to dissipate enough to not disturb the bed.

The filter interacts with the waves by acting as a frequency dependent semi-permeable barrier; some of the wave energy is reflected off the filter and some is transmitted through. Because of this, correction for the free second harmonic (discussed in Section 4.4) is often made impossible since some of the higher harmonics cannot pass through the filter. Reflection from the filter also results in resonance behind the filter if careful consideration is not given to its placement. In these experiments, the lee edge of the filter was placed at x = 3m.

3.5. THE WAVE GENERATION SYSTEM

This section describes the wave generation system in detail, covering the mechanical and control aspects of the wavemaker and the wavemaker control system. The wavemaker calibration transfer function and procedure is also discussed.

3.5.1. THE WAVEMAKER

The wavemaker consists of a servo-controlled hydraulic piston-type wavemaker. The wave paddle itself moves horizontally over the entire depth of the water. This type of motion is best for producing shallow or near shallow water waves, as the paddle motion closely simulates the kinematics of the water column under shallow water waves. The paddle is fitted with rubber seals on both sides of the paddle to reduce leakage through the gaps between the paddle and the walls of the flume. The importance of reducing leakage is described in Madsen (1970).

The piston that drives the wave paddle is inside a double chambered cylinder that responds to changing oil pressure on either side of the moving piston. Since the oil pressure drives the pistons, it is necessary to allow the wavemaker to warm up and thus heat the oil to a constant operating temperature before a constant oil pressure can be reached. About 30 minutes, depending on the ambient temperature, is required to achieve this condition and to ensure repeatable motion of the wavemaker. The motion of the paddle can be controlled by an internal signal generator or an external analog signal (-10V to 10V), and the actual paddle motion is measured by a built-in linear displacement transducer. The basin behind the wavemaker has been fitted with horsehair and other wave dampening devices to reduce wave motion and the possibility of resonance in the basin.

3.5.2. THE WAVEMAKER CONTROLS

The wavemaker is controlled by a basic DOS-based PC and a Keithly DAS-1600 series D/A (Digital to Analog) board. The software developed in house allows the user to specify the exact wave conditions required (period, amplitude, generation time, adjustments for reducing free second harmonic – see Section 4.4, and calibration parameters), then computes the real-time wavemaker position which is transformed by the wavemaker calibration transfer function (discussed in Section 3.5.3) to produce the actual signal for input to the wavemaker. The software was written in the Borland C/C++ programming language using libraries provided for control of the D/A card.

Note that it is extremely important to initialize the D/A board before sending any signal to the wavemaker – the board must be re-initialized each time the wavemaker control computer is turned on. To initialize the board, simply tell it to generate for a short time. The first signal it outputs is a –10V pulse, which if sent to the wavemaker could physically damage the wavemaker or the electronics controlling the wavemaker.

3.5.3. WAVEMAKER CALIBRATION

The ultimate goal of using the wavemaker is to be able to ask for a specific wave condition in the flume (typically wave amplitude and wave period), enter those conditions into the control computer, and obtain a wavemaker motion that produces the desired wave conditions. This process can be broken into two parts. The first is to control the real-time motion of the wavemaker, and the second is to specify a wavemaker motion that will generate the actual waveforms desired in the flume. Generating waves with a wavemaker is accomplished through a wavemaker theory; Chapter 4 deals with the wavemaker theory used in these experiments. The motion typically desired of the wavemaker is some combination of simple harmonic motions. In order to control the movement of the wavemaker, a transfer function must be developed that relates the input from the user to the motion of the wavemaker in both amplitude and phase for each harmonic component. The amplitude of the transfer function relates the magnitudes of the amplitude of the simple harmonic motion of the input to the output, and the phase is the lag of the output leading or following the input. Defining the motion that the user specifies as

$$\zeta_{in}(t) = \mathrm{Re}\left\{|\zeta_{in}| e^{i(\omega t+\beta_{in})}\right\} \tag{3.2}$$

and the actual motion of the wavemaker paddle

$$\zeta_{out}(t) = \mathrm{Re}\left\{|\zeta_{out}| e^{i(\omega t+\beta_{out})}\right\} \tag{3.3}$$

then the transfer function is defined by

$$\mathrm{H}(t) = |\mathrm{H}| e^{i\gamma} = \frac{\zeta_{out}}{\zeta_{in}} \tag{3.4}$$

where H(t) is a complex quantity. The amplitude of the transfer function is

$$|\mathrm{H}| = \left|\frac{\zeta_{out}}{\zeta_{in}}\right| = \frac{|\zeta_{out}|}{|\zeta_{in}|} \tag{3.5}$$

and it's phase is

$$\gamma = \beta_{out} - \beta_{in} \tag{3.6}$$

Then, to obtain the desired motion ζ_{out} at the wavemaker, we modify the input signal by

$$\xi_{in}(t) = \frac{|\zeta_{out}|}{|\mathrm{H}|} e^{i(\omega t + (\beta_{in} - \gamma))} \tag{3.7}$$

and substitute ξ_{in} into equations (3.4) and (3.5) instead of ζ_{in} to actually get an output of ζ_{out}. Typically, the user specifies $\zeta_{out}(t)$ and the generation system computes $\xi_{in}(t)$ which is sent to the wavemaker and results in the desired motion of the paddle $\zeta_{out}(t)$.

Determining the transfer function requires calibration of the wavemaker system. Typically, the transfer function depends on the frequency and amplitude of the wavemaker motion as well as the water depth at the wave paddle. However, Rosengaus (1987) and Mathisen (1989) showed that the transfer functions for this wavemaker are strongly dependent on the frequency of motion of the wave paddle, depend weakly on the amplitude of the motion, and are independent of water depth. Therefore, to specify a transfer function requires only specifying the amplitude and phase for each frequency or harmonic component to be generated.

To calibrate the transfer function for a particular frequency, a priori knowledge is required of the relationship between V_{in} and ζ_{in} (to transform the signal from the displacement ζ_{in} specified to equivalent voltage V_{in} output by the D/A card for input to the wavemaker control electronics), and the calibration between V_{out} and ζ_{out} (to transform the voltage output by the linear transducer V_{out} on the wavemaker to the actual displacement of the wave paddle ζ_{out}). Then a signal is generated using the wavemaker control system V_{in} and input into the wavemaker; the subsequent motion of the wavemaker is recorded by the linear displacement transducer V_{out}. Both V_{in} and V_{out} are sampled using the data acquisition system (see Section 3.6.2). By applying a Fast Fourier Transform (FFT) to each signal, an amplitude and phase for each can be determined, and therefore, the transfer function can be defined by applying equations (3.5) and (3.6). The values obtained for the transfer function here are nearly identical to those obtained by Rosengaus (1987) and Mathisen (1993). Rosengaus (1987) showed that the amplitude of the transfer function increases while the phase lag decreases as the frequency of the wavemaker motion decreases within the range of possible generating frequencies.

It should be noted that during the experiments of Rosengaus (1987) and Mathisen (1989), the approximate maximum possible displacement of the wave paddle is from 8cm at T = 0.5s to 15cm at T = 3s, at an oil pressure of 1000psi.

3.6. THE WAVE MEASUREMENT SYSTEM: WAVE GAGES

To determine the wave conditions present in the flume the variation of the free surface elevation must be measured. This is accomplished through surface piercing wave gages and a data acquisition system. In this experiment, we employed three surface-piercing wave gages mounted on a carriage that travels on the rails on top of the flume. The signal produced by the gages is sampled by an A/D board (analog to digital sampling board) and stored digitally in the data acquisition computer. This section describes all components involved in wave measurement

3.6.1. WAVE GAGES

The wave gages are DHI surface piercing wave gages that consist of two 1/8" rigid wires arranged vertically, parallel to each other and approximately 1cm apart. The gages are positioned in the flume so the two wires lay in a plane norma to the direction of wave propagation to insure that the slope of the wave does not affect the measurement of the water level. The gages are mounted with clamps onto a movable vertical arm with a vernier scale with a 1mm spacing for accurate vertical positioning. The movable arm is then mounted on the carriage for positioning and movement along the flume. The accuracy of the vertical positioning is taken to be half the smallest vertical increment, ± 0.5mm, and the accuracy of the positioning in the *x*-direction is ±1mm.

The gages respond to the changes in water level by detecting a change in conductance across the wires as the surface of the water moves up and down. A signal conditioning module sends a current to the gages and receives the change in current induced by the change in conductance by the water level. The transmission to and from the gages is through a 25m insulated cable which provides insulation from outside noise and also allows access to the entire length of the tank.

Periodically, a thin film builds up on the gages which could affect the temporal stability of their calibration. To reduce this effect, the gages were cleaned weekly with rubbing alcohol. The wave gage calibration and calibration procedures are discussed in Section 3.6.4.

3.6.2. DATA ACQUISITION SYSTEM

The signals from the three wave gages as well as the signal from the wavemaker linear displacement transducer are sampled by a 16 bit A/D (analog to digital) board, and stored on a DOS-based PC. The sampling hardware and basic code were provided with the Sontek Acoustic Doppler Velocimeter (ADV) system (see Section 3.7) and tied to the acquisition system of the ADV, so that the analog input A/D card sampled simultaneously with the velocity measurements, assuring synchronized measurements. The sampling code, based in the Borland C language, was modified at MIT to work as a stand alone system independent of the ADV and the ADV software. The system samples over a range of 10V (either –5V to 5V which is used here, 0V to 10V, or –10V to 0V) and stores the data as integer numbers from 0 to 4096. A simple linear relationship converts integers to volts,

$$Volts = \frac{20 * Integers}{4096} - 10 \tag{3.8}$$

The sampling rate is user-specified and ranges from 0.1Hz to 25Hz. A total of eight channels may be sampled; these experiments generally only required four channels. If there are channels not in use during sampling, these must be independently grounded to reduce the possibility of cross-talk between channels.

3.6.3. WAVE GAGE SAMPLING CONSIDERATIONS

Data acquisition, or sampling, is the collection of data points from an instrument. Several relevant parameters must be established when setting up the sampling procedure. These parameters are the number of data points to collect and the rate at which they are collected. They could also be considered the length of time to sample and the sampling rate, or the number of points to sample and the length of time to sample. No matter how you look at the problem, two parameters are specified. There are two major factors that play a role in choosing the sampling parameters when measuring waves. One is for convenience in using the Fast Fourier Transform (FFT) routine for analyzing the wave time series – FFT computation is most efficient when the number of data points is an integer power of 2. Typically, 2048 points (2^{11}) were collected in these experiments, as it is a trade off between a small sampling record for easier storage and processing and a record that is long enough to ensure stable sampling statistics.

The second factor is that the total sampling time should be chosen to equal an integer number of wave periods. Typically, this was taken as 32 wave periods. This ensures that the wave frequency would fall into one of the discrete frequencies resolved in the FFT, and that the energy determined for the principal frequency would be minimally affected by leakage into adjacent frequency bins.

To assist in choosing the sampling time, sampling frequency, and number of data points, a simple relationship is employed that balances all these requirements, given as

$$N_w T = \frac{N_p}{f} \tag{3.9}$$

where N_w is an integer number of waves, T is the primary wave period in seconds, N_p is the number of points to be sampled, and f is the sampling frequency in Hertz. In these experiments with the primary wave period of $T = 2.63$s, we choose N_p to be 2048 points. Then by varying N_w, a sampling frequency can be found which satisfies equation (3.9). In this case, f was taken as 24.333Hz.

Figure 3.3 (a) and (b) show a typical wave record ($T = 2.63$s) recorded using the above principles. Figure 3.3 (a) is the entire record of 2048 points sampled at 24.333Hz, approximately 84 seconds or 32 waves. Figure 3.3 (b) shows three wave cycles . These waves were recorded at $x = 9.5$m from the wavemaker for the case of pure waves.

Figure 3.4 is a wave energy spectrum – the result of an FFT - of the time series plotted in Figure 3.3. Figure 3.4 (a) is a stem plot plotted on a linear scale. Here it can be seen that the wave energy is concentrated in discrete frequency bins and almost no energy has leaked into the adjacent bins. Figure 3.4 (b) is the same spectrum plotted on a log-log scale, and shows that nearly all the energy is located in the first and second harmonic components of the wave ($T^{(1)} = 2.63$s and $T^{(2)} = 1.315$s), with the second harmonic contributing energy two orders of magnitude less than the first harmonic. Other higher harmonics are also present with energy contributions three or more orders of magnitude less than the first harmonic

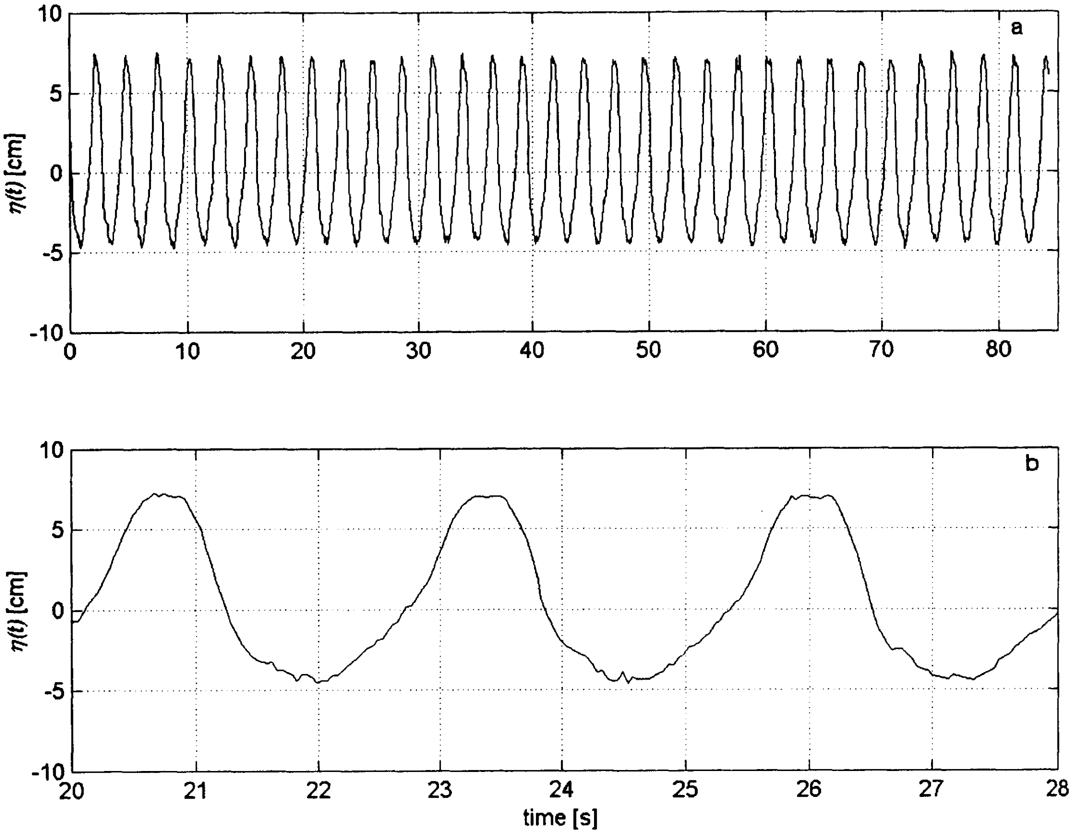

Figure 3.3: Typical wave record recorded by the wave gages: (a) entire record and (b) 3 wave cycles.

3.6.4. WAVE GAGE CALIBRATION

The wave gages are nearly perfect linear instruments – that is, a displacement of δ cm will give a change in voltage of δ_v Volts, no matter on what part of the gage the measurement is made. Therefore, the calibration is a purely linear relationship between physical displacement and a change in voltage.

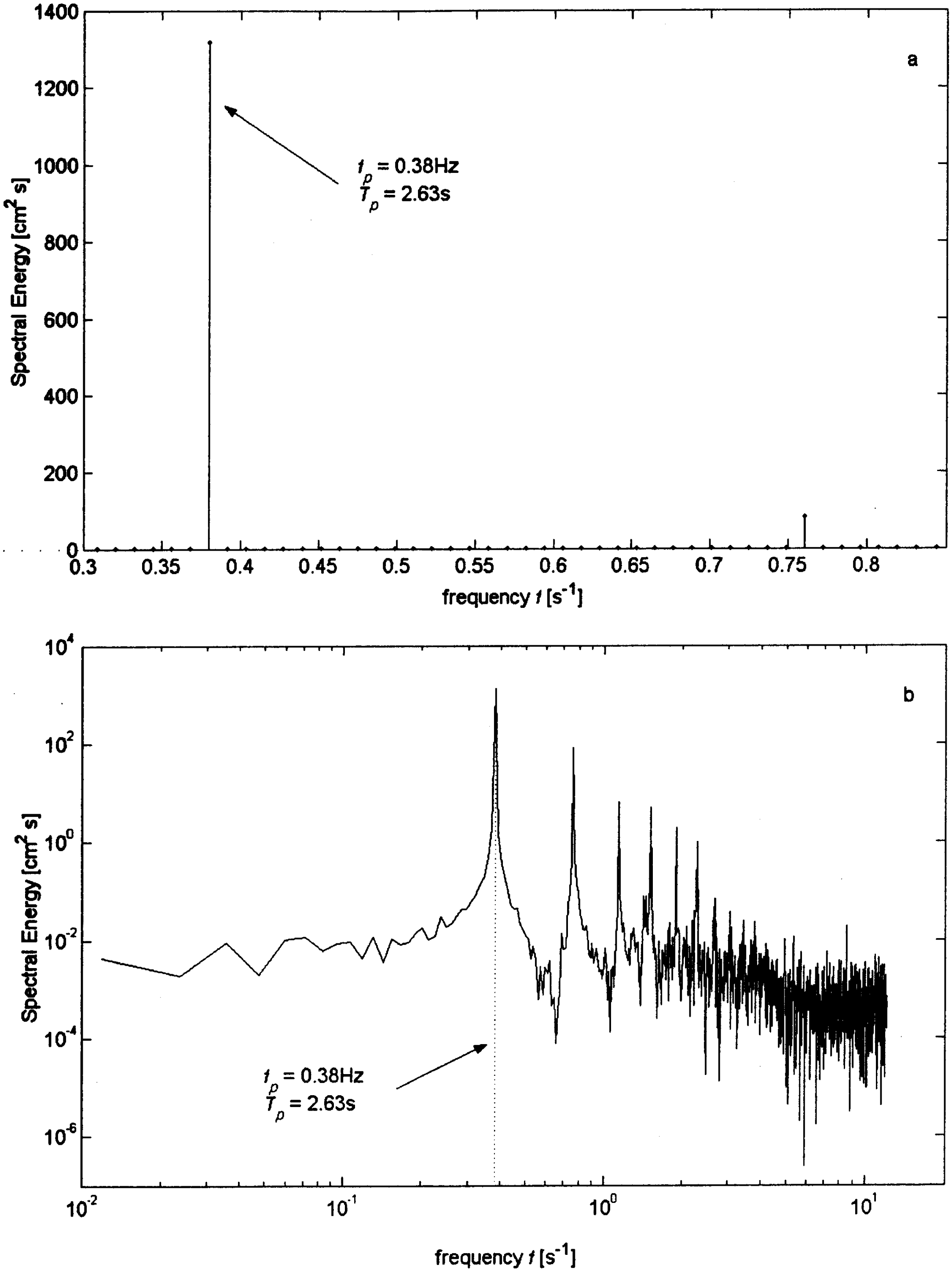

Figure 3.4: Energy spectra of a typical wave record, (a) stem plot on linear scale, (b) log-log scale. Both (a) and (b) are from the same wave record.

The first step in wave gage calibration is to set the voltage range for the gages using the wave gage amplifier/signal conditioner. The calibration should only cover the portion of the gage that will be exposed to wave activity. For example, if the wave amplitude is 5cm, it is only necessary to calibrate over ±5 or 6cm on the gage. Also, the voltage should be near maximum allowed at the maximum displacement of the gage in order the keep the magnitude of the signal much larger than that of the instrument noise. Set the gage at its still water position (zero displacement) in the tank so about half the gage is in the water and half is out. Be sure that the gage is long enough to remain piercing the water at the crest and trough of the wave. Next, use the zero-shift on the amplifier to set this gage position to be approximately zero volts. Then, adjust the gage to the maximum displacement, and adjust the gain (voltage multiplier) on the amplifier so the voltage output by the gage is approximately the maximum allowed for the sampling computer input.

After the voltage is zeroed and the output gain is set on the amplifier, the actual calibration can be performed. Displace the gage to a known amount and sample the voltage at that location. It is best to sample for approximately 30 seconds and take an average of the voltage reading to ensure an accurate sample. Repeat this until sampling has occurred over the entire length of the gage that is exposed to wave activity. Table 3.2 shows typical values obtained during a calibration. Figure 3.5 shows the physical displacement and the corresponding voltage reading.

A linear regression is performed to determine calibration parameters. Figure 3.5 shows the best fit line that results from the linear regression. The calibration equation is

$$\text{Displacement} = \text{slope} * V + \text{offset} \tag{3.10}$$

where the slope (interchangeably used with the word gain) is the slope of the best-fit line to the measured data, the offset (interchangeably used with the word y-intercept) is the *y*–intercept of the best fit line to the measured data, and *V* is the measured Voltage.

Table 3.2: Typical wave gage calibration table for a total excursion of 20cm.

Displacement [cm]	Gage 1 [V]	Gage 2 [V]	Gage 3 [V]
-10	-4.60	-4.57	-4.63
-5	-2.23	-2.20	-2.27
0	0.18	0.22	0.12
5	2.56	2.60	2.54
10	4.93	5.00	5.00
0	0.16	0.22	0.14
slope	2.0960	2.0888	2.0764
y-intercept	-0.3427	-0.4416	-0.3098
r^2	1.0000	1.0000	1.0000

3.6.5. ACCURACY OF WAVE MEASUREMENTS

Inaccuracies in the wave measurements could come from two main sources, noise in the sampling system or inaccuracies in the calibration of the gages due to human measurement error. It is important to resolve these errors, since it is necessary to know how accurately we can measure the free surface level and thus parameters important to the experiments such as second order wave characteristics, which tend to be on the order of 1cm, and wave attenuation, which in these experiments is on the order of millimeters.

To characterize the noise in the free surface measurements resulting from noise in the sampling system, simply measure a perfectly still water surface; any resulting deviations from zero are the noise. For this experimental setup, the noise is gaussian and has a peak to peak voltage of 0.2V (±0.2V). This translates into a noise of ±0.2cm at each step in time when calibrated by the above procedure and with typical calibration values. However, by increasing the number of points sampled and averaging, the error decreases as the square root of the number of samples. So if 400 samples were measured and averaged for the still water level, the accuracy is ±0.01cm. Inaccuracies from the calibration procedure can arise from misreading the vernier scale on the vertical arm of the gages. The smallest increment on the scale is 1mm, so we take the accuracy of the physical displacement reading in the calibration to be ±0.5mm. Then by an error propagation analysis performed by Rosengaus (1987), if the incident wave is assumed to be 6cm high and

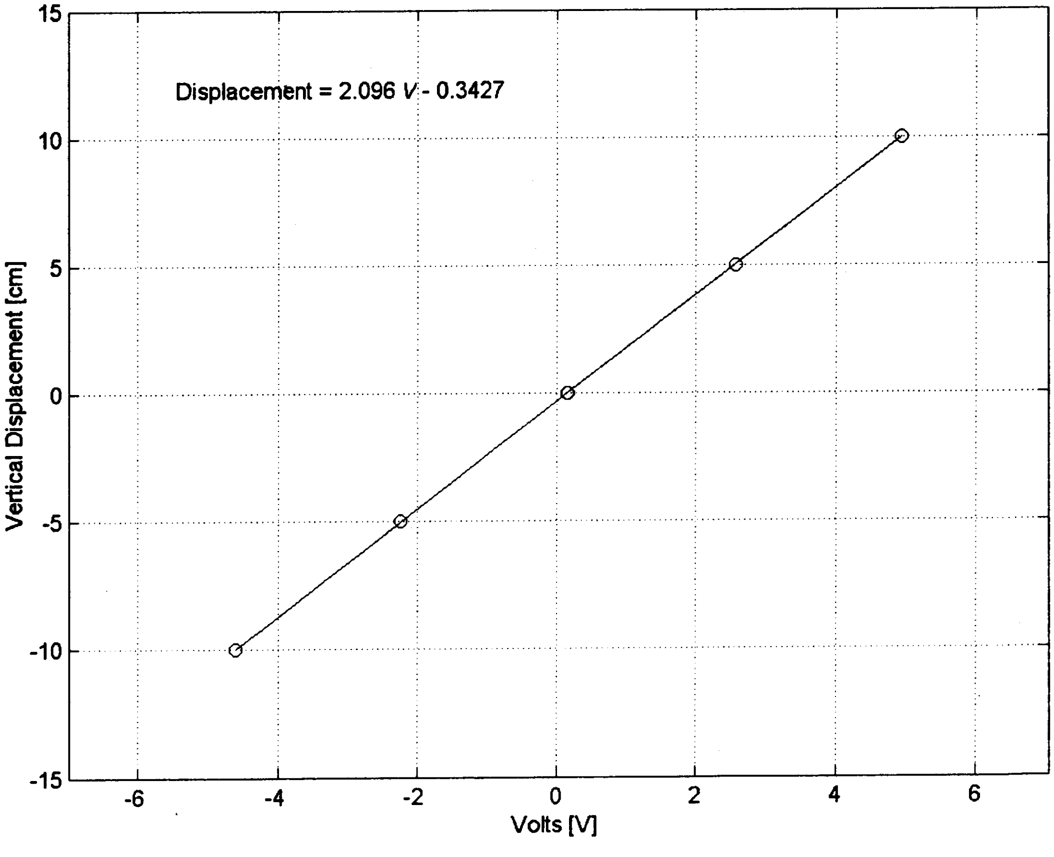

Figure 3.5: Typical wave gage calibration for a total excursion of 20cm (-10cm to 10cm), circles are measured points, line from best fit regression.

about 6m long, the accuracy of the amplitude can be measured to approximately 0.1mm and the phase can be resolved to approximately 0.03 radians. This reduction occurs in part because of the sinusoidal fit to the data resulting from the FFT analysis.

3.7. VELOCITY MEASUREMENTS: ADV PROBE

In this study, velocimetry (measurement of velocity) was performed by a method called acoustic Doppler velocimetry. The instrument used is a probe called the Sontek Acoustic Doppler Velocitmeter (Sontek ADV). This section addresses the ADV, its operating principles, advantages and limitations.

3.7.1. ADV OPERATING PRINCIPLES

The Sontek ADV probe consists of three receivers positioned in a horizontal circle around a 10MHz transmitter, and are slanted at 30° from the axis of the transmitter in order to focus on a cylindrical sampling volume approximately 5cm below the probe. Figure 3.6 shows a detailed schematic of the probe.

When submerged in the water, the probe operates by transmitting periodic, short acoustic pulses from the transmitting transducer in the center of the probe. As the pulses travel through the water, ambient scatterers such as microbubbles, suspended sediments, or seeding material scatter a small fraction of the acoustic energy. These acoustic echoes are detected by the receiving transducers if the echoes originate in the sampling volume, defined by the intersection of the transmitting and receiving beams. When a moving particle scatters the transmitted acoustic

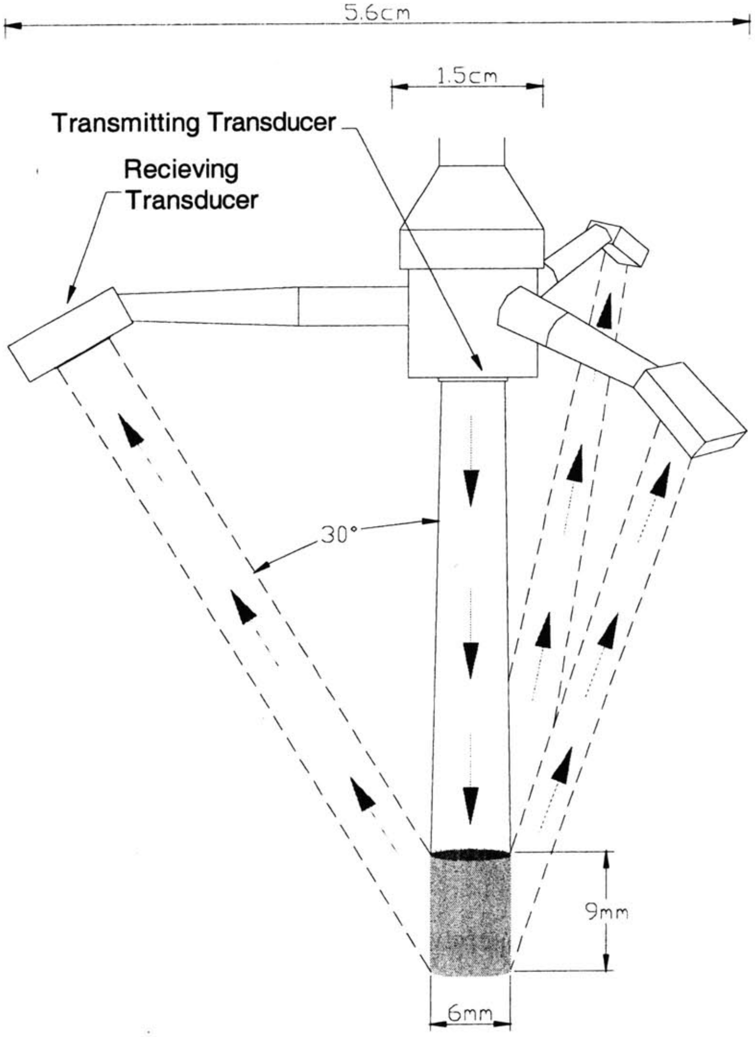

Figure 3.6: Schematic diagram of the Sontek ADV probe.

signal, the frequency of the scattered signal is shifted. This is known as the Doppler Shift. Assuming that the ambient scatteres are traveling at the velocity of the fluid, the frequency shift of the scattered echoes is proportional to the speed of the ambient scatterers and thus the velocity of the fluid. Orthogonal components of the velocity vector can then be computed from knowledge of the geometry of the beams, which is provided by Sontek and is unique for each individual probe (Kraus *et. al.*, 1994).

The ADV probe is connected to a waterproof signal processing module, which calculates the velocities and transforms the measured velocity projections via the provided transformation matrix. The velocity determination from the Doppler shift depends only on the transmitted pulse frequency, the frequency shift, and the speed of sound in the water. Therefore, velocity measurements with the ADV are inherently drift free, and the only calibration required by the user is to determine the temperature and salinity of the water, which affect the speed of sound in water. In these experiments, the salinity is assumed to be zero, and the temperature is measured with a Temprite alcohol thermometer before each test. The flume itself is positioned in the lab near a wall full of windows, which can unevenly heat the water in the flume. To insure that there were no temperature stratification or gradients during the experiments with the ADV, the current was run for approximately 6 minutes (about the time it takes to circulate the flume twice) while mixing the water with a broom near the current intake.

For more detailed information on the operating principles of the Sontek ADV, see Kraus *et. al.* (1994), Lohrmann and Cabrera (1994), Anderson (1994), or the Sontek website (Sontek, 2002).

3.7.2. ACCURACY AND RESOLUTION

The ADV probe is capable of sampling at frequencies of 0.1HZ to 25Hz, and for velocities ranging from 1mm/s to 2.5m/s. To achieve the best accuracy, the velocity range that the probe samples can be limited; the probe's accuracy is specified as 1% of the velocity range. In other words, if the maximum velocity one plans on measuring is 30cm/s (as it is in these experiments), the velocity range should be set at 30cm/s, giving an accuracy of ±0.3cm/s in the measurements.

The velocity range specifications are pre-set by the manufacturer, so the smallest range available for the expected velocities should be selected.

The probe's sampling volume geometry is governed by the probe geometry and factory calibration. The typical sampling volume is cylindrical with a diameter of 6mm and a height of 9mm (see Figure 3.6). However, it is possible to change the height of the sampling volume. This would be a great benefit for near-bottom measurement, as the velocity gradient is increasingly large as one approaches the bottom – the larger the sampling volume, the more the velocity gradient is averaged over the height of the volume and thus giving a less realistic picture of the point measurement of the velocity. Unfortunately, as the sampling volume height is decreased, the variance of the measured velocity increases exponentially, resulting in a much less accurate measurement with an increasingly more unpredictable accuracy (Sontek, 2002). In these experiments, the typical configuration of the sampling volume (6mm diameter and 9mm height) is used.

Barrantes (1996) suggests that the velocity range near the bed (less than 5cm from the bed) should be set at 100cm/s to account for turbulent fluxuations, and because a smaller variance of the signal is achieved. However, tests run prior to these experiments suggested that this is not the case, and the variance is actually higher if the velocity range is set to 100cm/s. These differences may be from the fact that at elevations of less than 5cm from the bed, Barrantes (1996) was using a smaller sampling volume which naturally introduces more variance into the measurement, whereas in the present experiments, the standard sampling volume size is used.

Before data collection, the ADV measures the distance to the nearest boundary by measuring the time taken for a reflection of an acoustic pulse, within an accuracy of about ±1mm. The probe then corrects for this reflection during data collection. Furthermore, Sontek (2002) states that near-boundary measurements can be made by placing the bottom of the sampling volume as close as 0.5mm to the boundary. In experiments with a movable bed, this is not practical or possible, since the bed is constantly moving and hard to define. Because of this, all measurements were made at least 2cm above the local bottom.

The underlying assumption of all forms of Doppler velocimetry is that the velocity of the ambient particles is equal to that of the water. This assumption is generally valid, except for the case of large or rapidly rising bubbles, or of suspended sediment with a relatively large fall velocity. No bubbles were present in the flume during the measurements. However, near the bed suspended sediments were present in the pure wave and wave-current experiments. These sediments can have an unavoidable impact on the velocity measurements if the concentration is much larger than the concentration of the seeding material (discussed later). At an elevation of 2cm above the bed, the concentration of suspended sediment is extremely small for these experimental conditions, and is assumed not to influence the measurements. For velocity measurements in a flume, the water must be seeded with small particles to achieve a sufficiently strong scattering signal. The relative strength of the signal to the electronic noise of the instrument (called the signal to noise ratio or SNR), which is the strength of the backscattered signal minus the instrument noise in units of decibels (dB), is monitored in real time by the probe. Sontek (2002) recommends that the SNR level be more than 15dB at all times. Furthermore, the reliability of the backscattered signal is called the correlation of the signal, and is measured in percent. Sontek recommends that the correlation level be greater than 70%, and points with a correlation lower than this should be discarded. These levels were achieved by periodically adding a slurry of fine titanium dioxide particles provided by Sontek to the water. These particles are approximately neutrally buoyant in fresh water and are three orders of magnitude smaller than the length scales of the ADV sampling volume. This validates the fundamental assumption of the ADV that the particles moving through the sampling volume are traveling at the same velocity as the water that carries them.

The accuracy of the velocity measurements (±0.3cm/s) can have a significant impact on the bulk hydrodynamic properties determined from the measured velocity profiles derived from individual velocity point measurements. Appendix A describes these effects in more detail.

3.7.3. TRAVERSE AND ADV CONTROL

For use in these experiments, the ADV was mounted on a 3-axis remotely controlled traverse which was fitted on a cart that rolled along the top of the flume along its longitudinal axis. The traverse was manufactured by the Dantek Measurement Technology company. The motion of the traverse is controlled by three step motors (one for each axis) which move at 1/800th of a centimeter per step, or 800 steps per centimeter. The total longitudinal (x) excursion allowed by the physical dimensions of the traverse is 475mm, while the vertical excursion (z) is 540mm and the cross-tank excursion (y) is 600mm. This allows for extreme accuracy in moving and positioning the probe over nearly any position in the flume. The maximum speed allowed for movement in x and y directions is 40mm/s or 3200 steps/s, and in the z is 25mm/s or 2000steps/s.

The traverse is controlled by a motor control box, which in turn communicates with its controlling computer through a standard serial communications interface (RS232). The control computer sends instruction to the motor box control via a DOS QBASIC program or any language that allows control of serial communications. This facilitates simple DOS command line control of the traverse movement.

The ADV probe tip is mounted on the end of a stainless steel tube that is connected to the traverse. From the probe tip, a flexible cable carries the signal to the waterproof signal conditioning module fixed to the cart carrying the traverse. Finally, a 10m long cable connects the signal conditioner to a data acquisition and signal processing card fitted into a standard expansion slot inside the sampling computer (discussed in Section 3.6.2). The interface software for the ADV, 'adva.exe', allows easy control of all settings (velocity range, water temperature, sampling rate) and also provides a means to acquire data and view its acquisition in real time.

For measuring velocity profiles, as is the case in these experiments, DOS command line control of the ADV makes the combined use of the ADV and the traverse much more efficient and allows for automation of the profiling procedure. To this end, a C program (the backbone of the 'adva.exe' ADV software) was modified at MIT so that the ADV could be controlled via command line controls. Then, together with the command line control of the traverse, a simple batch file was written that automates the profiling procedure. The batch file (simply a list of command line commands that are executed in sequential order) samples at one vertical position with the ADV, moves to the next vertical position with the traverse, samples at that position with the ADV, moves vertically (or longitudinally or laterally) and so on. This is a powerful procedure that was employed in all the profile measurements presented in this study, as well as in the bottom profiling, discussed in Section 3.8.

3.7.4. SAMPLING CONSIDERATIONS

Just as in Section 3.6.3, two of the factors that determine the sampling parameters for the velocity measurements are convenience of use of the FFT algorithm and that the sampling time should be equivalent to an integer number of wave periods (if waves are present in the sampling). Equation (3.9) is applied to balance these requirements.

Another consideration in determining the sampling requirements is the stability of the sampling statistics. That is, if the system you are measuring is steady, then the average and variance of the measured signal should be repeatable. Therefore, it is necessary to determine the length of time required to sample in order to ensure a statistically stable measurement. At the same time, the sample length should be as short as possible to keep the data storage requirements small and to keep the sampling time to a reasonable length. To determine the length necessary to achieve a statistically stable sample, we first recorded a sample on the order of ten times longer than the expected sampling time (referred to as the benchmark sample). Then we calculated the sampling statistics – average and variance – of the benchmark sample. These benchmark statistics are assumed to be the steady state sampling statistics of the system. Next, we divided the benchmark sample into incrementally smaller sub samples and calculated the average and variance of the smaller sub samples. As the sub samples get smaller, their statistics will begin to diverge from those of the benchmark samples. Then the necessary length of time to sample is the sub sample that gives essentially the same sample statistics as the benchmark samples, or at least the length of time necessary for the variability of the sample to be within the accuracy of the probe.

The wave-current flow is the most variable system measured in these experiments. In order to determine the necessary length of time to sample this system, the benchmark process described above was used. Figure 3.7 shows the variation of the standard deviation of the benchmark sample as a function of sampling time. The variation of the mean is not shown as it is approximately constant and does not change. The benchmark standard deviation (steady state sampling statistic) in this case is $\sigma_{u_{wc}}$ = 0.045cm/s. From this figure, a sampling time of seven minutes is sufficient so that the variability of the signal from the variability of the system is within the accuracy of the ADV. To achieve this time and still satisfy the requirements imposed by equation (3.9), we established a sampling scheme made of five sets of measurements, each consisting of 2048 points at a sampling rate of 24.333Hz for each point. That is equal to 7.01 minutes of data, 10240 data points, or 160 wave periods at each point. Then, simple averaging or Fourier analysis could be performed on the 5 separate samples, which are kept separate to facilitate the application of the FFT algorithm. Note that most modern FFT algorithms, such as those used in the MATLAB r12 data analysis software package, do not require the number of points to be an integer power of 2. However, much of the analysis was performed with a FORTRAN 77 compiler and an FFT algorithm that requires 2^n points. Furthermore, as discussed earlier, by satisfying equation (3.9) and having 2^n points, we minimize the leakage into adjacent frequency bins in the spectral representation of the time series, resulting in more accurate estimates of the values obtained though the spectral analysis.

The variance of the velocity measurements can have a significant impact on the bulk hydrodynamic properties derived from the measured velocity profiles composed of individual velocity point measurements. Appendix A describes these effects in more detail.

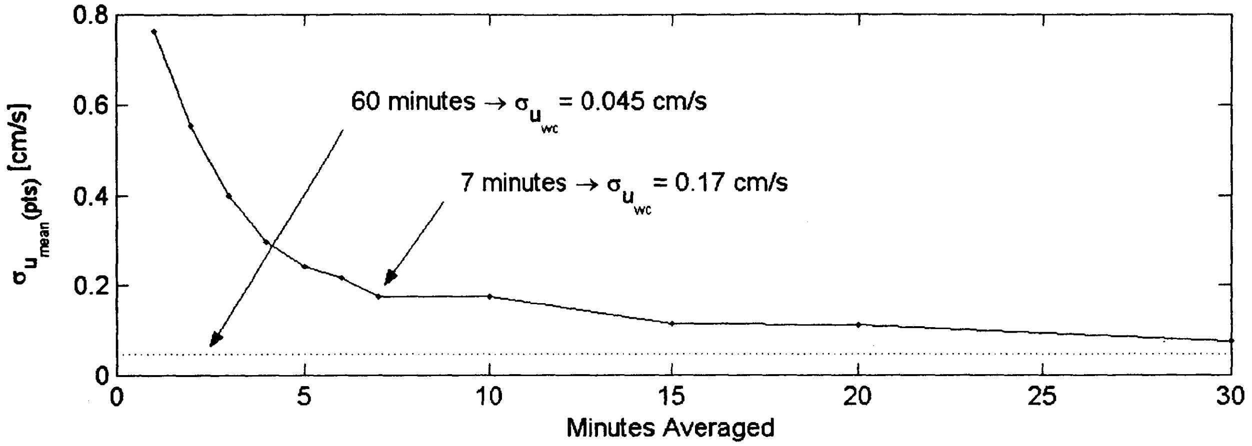

Figure 3.7: Variation of standard deviation of the measured velocity as a function of the sampling time, measured at 2cm above the bottom.

3.7.5. PROBE ALIGNMENT AND UNIDIRECTIONAL FLOW VERIFICATION

The setup of the ADV probe described above is quite versatile and allows for accurate, repeatable measurements. However, one aspect of the setup that is not fixed is the alignment of the probe relative to the direction of the flow. It would be ideal if the probe were somehow automatically able to align itself with the longitudinal axis of the tank. Unfortunately, the positioning and aligning of the probe is completely manual. Therefore, it is necessary to determine if the probe is aligned orthogonally with the tank. Then, as discussed in Section 3.4.1, the flow structure for pure currents must be examined to determine if there is a secondary flow present in the flume that could interact with the boundary layer development, such as the helicoidal flow shown to exist by Barrantes (1996).

The first step in aligning the probe is to minimize any possible rotations around the desired coordinates manually. We can first remove the rotations around the y and x – axes by using the still water surface as a level. We position the probe so the three receiving transducers nearly touch the water surface. Then, slowly step the probe down until the transducers touch the surface. Each transducer tip should touch the water surface at the same time. If not, manual adjustments should be made until they do.

After this leveling is completed, the only possible inaccuracy in the alignment is a rotation around the z-axis. To check this rotation, one can measure three components of a velocity profile over depth; by conservation of mass, the only component that should have a net velocity is along the x-axis, and any net velocity measured in the y or z projection of the velocity vector is from a rotation in the probe. This is true for pure current, pure wave, and wave-current flows (and both the net motion and the harmonic motion) since waves made by the wavemaker are inherently two dimensional, and we can assume correctly that no cross-tank flow exists in the wave-induced flow field. Note that there will be a net vertical w velocity in the pure wave and wave-current harmonic flows since waves induce a two-dimensional (u, w) velocity structure.

To determine the rotation angle around the z-axis, a profile of the mean wave velocity is measured under the waves. Then the net cross-tank velocity is

$$\begin{aligned} &\int_0^h \left(\bar{v}(z) - \bar{u}(z)\sin\alpha\right)dz = 0 \quad \text{for pure currents} \\ &\int_0^h \left(v^{(1)}(z) - u^{(1)}(z)\sin\alpha\right)dz = 0 \quad \text{for pure waves} \end{aligned} \tag{3.11}$$

where $\overline{v}(z)$ is the measured time averaged velocity vector and $v^{(1)}(z)$ is the magnitude of the velocity of the first harmonic motion in the y (cross-tank) direction, $\overline{u}(z)$ is the time averaged velocity and $u^{(1)}(z)$ is the magnitude of the velocity of the first harmonic motion in the x-direction for the particular profile, and α is the rotation angle of the probe about its z-axis. Note in the following description, $v^{(1)}(z)$ and $\overline{v}(z)$ can be used interchangeably, but will be designated for the pure current case. The rotation angle α is found by iterating equation (3.11) about α until the net cross-tank velocity is zero.

If the resulting rotation angle is large, then the probe is manually adjusted, and the procedure is repeated. However, for small angles (less than about 2°, but varies with the magnitude of $\overline{u}$), the error introduced in the $\overline{v}$ component of the measured velocity is less than the accuracy of the probe (±0.3cm/s). Similarly, for rotation angles less than about 10° (again, depending on the magnitude of $\overline{u}$), the error in $\overline{u}$ is less than the accuracy of the probe. This problem also works the other way – because of the accuracy of the probe, the estimate of the rotation angle depends on the magnitude $\overline{u}$. Its estimation is limited by the fact that $\sin\alpha > |\pm 0.3/\overline{u}|$. For pure wave flows, $u^{(1)}_{\max}$ is about 26cm/s, thus allowing a resolution of α to be about 0.6°. For pure current flows where $\overline{u}_{mean}$ is about 16cm/s, α can only be resolved to about 1° - still much better than could be done by eye.

Figure 3.8 shows plots of this procedure for a pure current case. Figure 3.8 (a) is the cross-tank velocity $\overline{v}(z)$ in the $y-z$ plane before alignment and (b) is after alignment. The rotation angle was found to be 0.88° ± 1°. The resulting velocity vectors shown in (b) are quite small – the dotted lines in the figure represent the ADV probe's accuracy of ±0.3cm/s. All but one of these points is below the accuracy of the probe. This adjustment is sufficiently small so that even if the probe was rotated 1° out of alignment, the final bulk results would not be affected by more than the probe's accuracy.

As an example to better explain the random pattern shown in Figure 3.8 (b), we examine the nature of the ADV probe. The noise generated by the ADV is random and gaussian by design. Therefore, the noise can be represented by a normal distribution with zero mean and a standard deviation of 0.15cm/s (since the ±0.3cm/s encompasses the whole range of possible measurement error, it is approximately the 95% confidence interval, or about 2 standard deviations). Then we can generate a 'noise velocity' profile that essentially represents what is shown in Figure 3.8 (b) by generating a random velocity based on the noise distribution. Figure 3.9 (b) shows a possible example of this nose velocity profile. For comparison, Figure 3.9 (a) is the result of the probe alignment shown in Figure 3.8 (b). The profiles are essentially the same, each showing random variations that are of the order of the accuracy of the probe.

With a probe that is properly aligned, we can investigate the flow structure for pure currents and determine if a destructive secondary flow structure exists. To do this, the current was run over a glass bottom, and the ADV was used to sample the cross-tank structure of the velocity at several points along the flume with the sampling scheme described earlier. Figure 3.10 shows the results of these measurements at 11m from the wavemaker. Seven vertical lines were measured with 10 points in each line. The resulting, aligned flow pattern is quite random, as expected. Most of the vectors shown in the figure are less than the accuracy of the probe. The maximum velocity, $\bar{v} =$

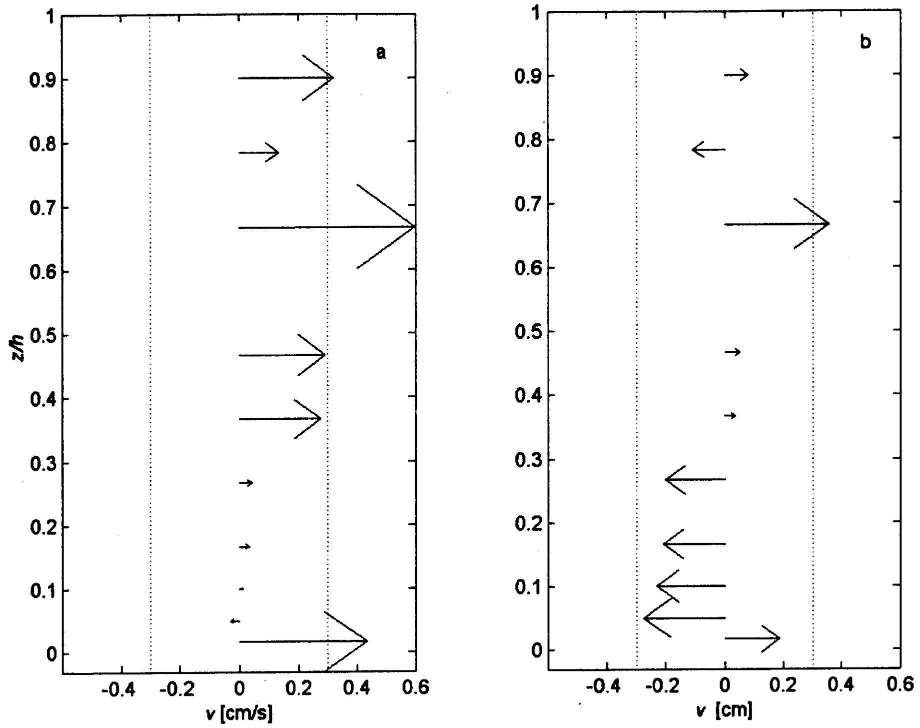

Figure 3.8: Cross-tank $\bar{v}$ velocity vectors in the $y-z$ plane. (a) is before alignment, (b) is after. Dotted lines are ±0.3cm/s accuracy of the probe. Elevation is plotted in dimensionless elevation, *z/h*.

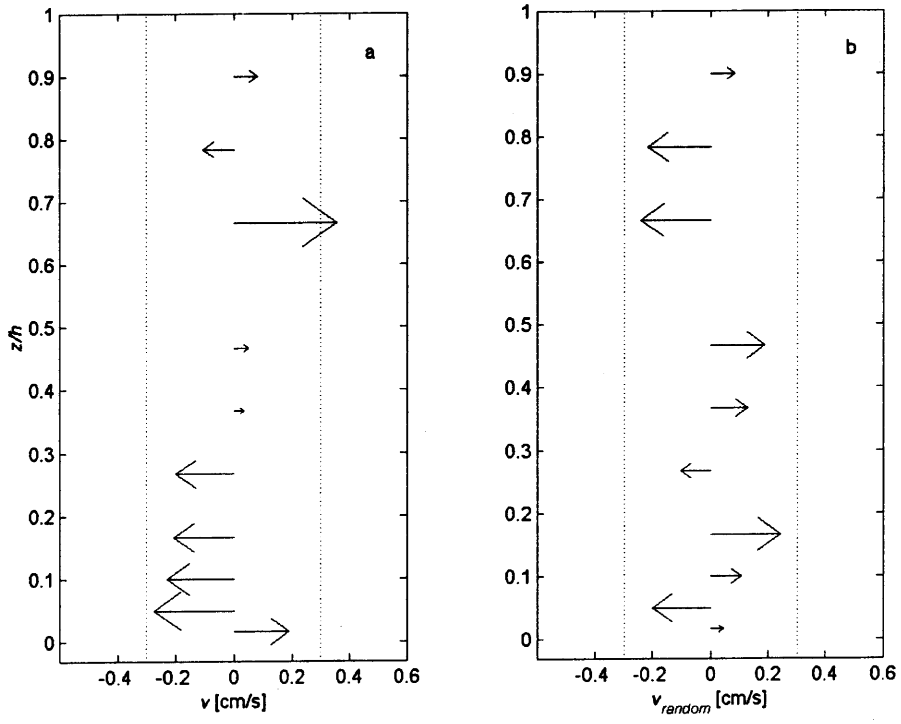

Figure 3.9: (a) Results of the pure current probe alignment, and (b) a random 'noise velocity' profile generated from the noise distribution of the probe. Elevation is plotted in dimensionless elevation, *z/h*.

0.5cm/s (at y/b=0.5, bottom point), is of the order of 4% of the longitudinal velocity component, so the above correction can be assumed quite good. This is evidence that no helicoidal structure is present in the flume, and the filter adequately corrects the flow. However, a secondary pattern is suggested by the flow structure – two counter-rotating cells in the lower half region of the flume, similar to that shown by Barrantes and Madsen (2000) in their Figure 4a. Close to the bottom, flow moves from the sidewalls toward the center of the flume with a maximum velocity of about 0.5cm/s. The small magnitudes of the measurements here do not allow for definite conclusions, but with a depth-averaged $\bar{u}$ =12.9cm/s and assuming a maximum of 0.5cm/s lateral flow, equation (3.1) gives an effective length of the tank of 12.1m. Therefore, the longest development length possible in the flume is 12.1m, and no measurements should be made past x = 15.8m from the wavemaker.

The above calculations show that α is small and any mis-alignment of the probe less than about 10° will not have an affect on the velocity measurements in the x-direction as it is within the accuracy of the probe. Furthermore, a small rotation of the probe or a weak secondary circulation in the tank will only affect the $\bar{v}$ measurements and therefore the estimate of the effective length of the tank; these have been accounted for above.

3.8. BOTTOM PROFILING

This study is concerned with the interaction of the bed with the hydrodynamics – that is how the movable bed affects the hydrodynamic properties of the wave, current, and wave-current flows. Therefore, it is vital to be able to characterize the movable bed in terms of relevant bedform parameters. The combination of the ADV and the traverse was adapted to act as a bottom profiler to measure the small scale bedforms. It proved quite successful at measuring ripple heights and lengths.

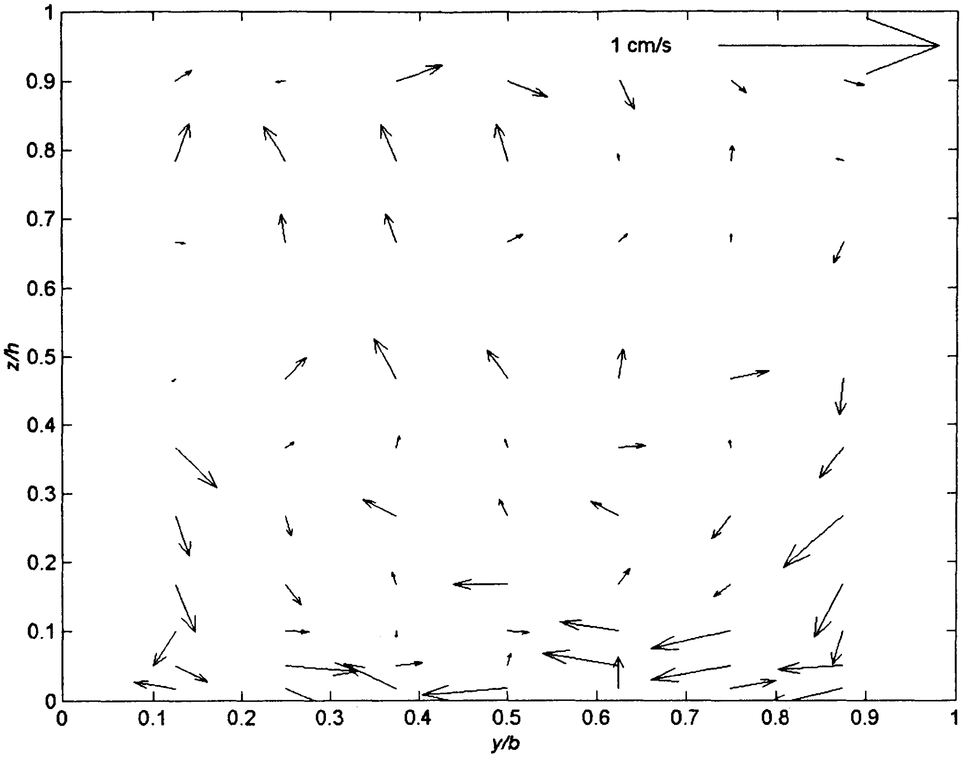

Figure 3.10: Cross-tank velocity structure of the pure current at x = 11m from the wavemaker.

As a result of an unexpected phenomena, the mean elevation of the bed changed, and formed dunes with lengths on the order of half the primary wavelength (3m) and heights of up to 5cm. Because of the limited longitudinal excursion of the traverse, the ADV/traverse bottom profiler was not adequately suited to measure these mean-bed variations. An ad-hoc method was devised to qualitatively describe these variations with limited success. This section describes the use of the ADV/traverse bottom profiler for measuring ripple characteristics, and the procedure employed for measuring the mean-bed variation.

3.8.1. RIPPLE GEOMETRY MEASUREMENT

Before the ADV begins sampling, it measures the distance to the closest boundary to minimize the effects of reflection off the boundary on the signal. The ADV can be adapted for use as a bottom profiler by using this measurement. A C program was developed at MIT to control the bottom profiling of the ADV via a command-line interface. Then, just as the ADV was used in combination with the programmable traverse for measuring velocity profiles (described above), it can be used to measure the small-scale bedform profiles.

By extrapolating the geometry of the sampling volume, the beam is assumed to have a 6mm footprint on the bottom. Longitudinal profiles were measured with spacing between measurements of 2.5mm and 5mm. Since the footprint is assumed to be 6mm, the 5mm spacing proved sufficient in resolving the ripples. Because of the slope of the bedforms, the reflected signal was often reflected away from the probe and could not be recorded. These dropouts occurred at a frequency of approximately 5% of the measurements, and occurred randomly over the length of the ripples – they were not concentrated near the peaks or on the slope of the ripples but distributed randomly over the length of the ripple. Therefore, 8 measurements were taken at each longitudinal point in order to provide redundancy in the measurements. By removing all dropout points and averaging the remaining of the 8 measurements at each point, the dropout points were virtually eliminated, and occurred for less than 1% of the profile. If drop out occurred for all 8 measurements at a point, the missing point was replaced by using linear interpolation between the two adjacent points. Throughout the entirety of the experiments, there was no occurrence of two consecutive longitudinal points dropping out.

Sontek (2002) gives the accuracy of the distance to the boundary measurement to be ±1mm. No information could be provided on the dependence of the accuracy with distance to the boundary, or the geometry of the beam at the boundary. To check this, profiles were measured of the same bed from different heights above the bed. Over the range of the probe (5cm to 30cm from the bed), no effect on the mean statistics of the measurements was found. Therefore, all measurements were made with the probe located 18cm above the starting point of the profile. Note, however, that this distance is not fixed over the length of the profile, and can change by as much as 4cm due to the change in mean bed elevation. The geometry of the footprint of the beam at the boundary is unknown, but assumed to be circular with a diameter of 6mm. Also, Sontek could not provide information on how the measurement is performed on a sloped surface. The steepness (ratio of the ripple height to the ripple length, η / λ, where η is the ripple height and λ is the ripple length) of ripples is of the order of 0.1. Then the tangent of the ripple slope, $\tan(\theta)$, is of the order 0.2. If the footprint is 6mm across, it could be possible that the measure of the height is anywhere in the range of the footprint length d_f times the tangent of the slope $d_f \tan(\theta)$, or on the order of $d_f \tan(\theta) \sim 1.8$mm. This is still in the range of the specified accuracy of the measurement of ±1mm, so any effect of the slope on the accuracy is accounted for.

From the measured bed profiles, we want to determine parameters that describe the bedform – the ripple height η and the ripple length λ. Ideally, a high pass filtering algorithm would be employed to determine these characteristics. Unfortunately, the length of the profiles is often not long enough to accurately use filtering, since for the larger bedforms, we can only measure one or two ripples per profile. Therefore, we used zero-crossing methods, both up and down, to determine these parameter. First, because of the variation of the mean bed elevation, the ripples often occur on a slope which can significantly affect the zero-crossing methods. So all profiles were de-trended by subtracting the best-fit linear trend in the profile. Then, a three-point moving average was applied to the measured points. The moving average was used to specify the zero-crossing points (±0.5cm, the spacing between measurements) as it allowed for smoother, more natural profiles unaffected by the variations in the individual measurements which could occur near the zero-crossing point. Then, the raw measurements were used to determine the ripple heights as the difference between the maximum and minimum points over each individual ripple length. Depending on the phase of the profile, either a zero-up crossing or zero-down crossing method was chosen; the method that captured more ripples was the method used. If the same number of ripples were measured by each method, the zero-up crossing method was used.

Typically, for each x location where a profile was taken, three longitudinal profiles spaced 9cm apart across the tank were measured. The profiles were each 44.5cm long, containing either 89 or 178 points in x, with an x-spacing of 0.5cm or 0.25cm, respectively, and centered on the desired x location. The three lines were taken at $y/b = 0.38, 0.5, 0.62$ and designated Line 1, Line 2 and Line 3, respectively. Each line was analyzed separately, and their parameters averaged to give a more representative value, since the bedforms often varied across the tank. Typical profiles for pure wave formed ripples, ripples resulting from a current run over wave formed ripples, and combined wave-current formed ripples are shown in Figure 3.11. Figure 3.11 (a) and (b) are taken with 178 points and (c) is with 89 points in x. All are the middle (L2) $y/b = 0.5$ profile. Notice the downward trend in (c). This is removed prior to analysis. The values of η and λ shown on the figures are the result of the zero-crossing analysis.

Figure 3.11 illustrates two problems with this method of analysis. One is that the ripple heights are calculated taking the difference between highest high and lowest low of the raw data for each ripple determined by the zero-crossing points. If, therefore, some points are outliers, they can change the actual ripple height. An example of this is shown in Figure 3.11 (b) in the third trough. The low point in this trough is definitely the lowest point, and will be used in the zero-crossing analysis. Its validity is questionable. This could be eliminated by simply using the moving average for the height calculations. However, when the ADV measures the bottom, its footprint is on the order of 6mm and probably already has smoothed out any possible sharp point in the data and biasing the ripples to a smaller height. Therefore, the variations in the raw points is accepted as an increased inaccuracy in the measurement in the hope of removing the bias, and increasing our ability to capture the actual ripple heights. The small variation in height experienced because of this one point is insignificant when it is considered that there are 3 profiles at each measurement location, most of which have between 3-6 ripples in each profile. So one point makes only a small difference in the average. The second problem is also illustrated in Figure 3.11 (b). The second to last crest in (b) is not high enough to cross the zero-level, even after the trend has been removed. This reduces the number of ripples measured from 4 to 3, and effectively doubles the length of the last ripple which causes an over-prediction of the ripple length λ for this particular profile. However, this may not really be an over-prediction - if the ripple is so small, the flow may not feel the ripple, and treat this locally as an elongated ripple. Whether or not the flow feels this ripple is a matter of debate. Either way, the estimates may be slightly biased towards longer ripples lengths λ because the analysis method cannot resolve this type of ripple. The effect of this is small, however, as many measurements are made and averaged. This type of variation adds to the error of our ability to measure λ, and is reflected in the length's large standard deviation.

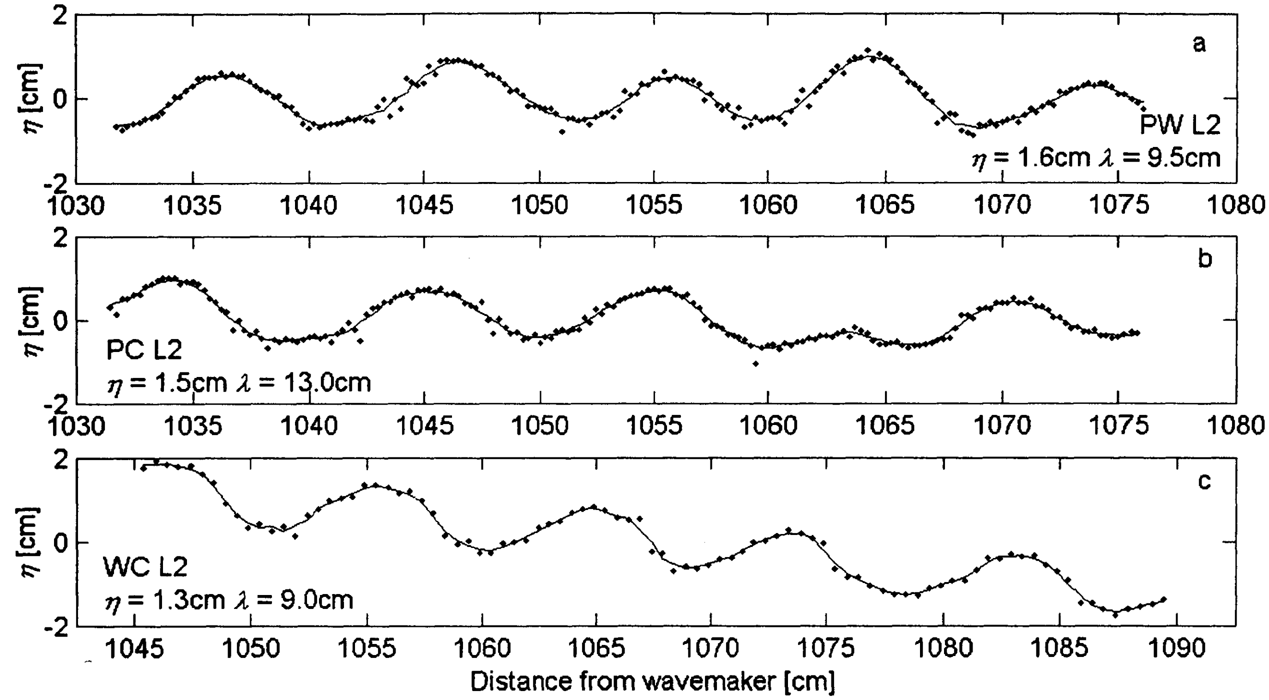

Figure 3.11: Typical ripple measurements. (a) pure wave ripples, (b) pure current run on pure wave ripples, (c) wave-current ripples. Points (·) are the actual measurements and the solid line is a seven point moving average of the measurements in (a) and (b), and a three point moving average of the measurements in (c).

3.8.2. MEAN BED ELEVATION MEASUREMENT

During the initial planning of the experiments, the mean level of the bed was expected to remain constant. However, an unexpected periodic variation of the mean bed elevation with a length of half the incident wave length (typically 3m) was observed to develop over time. For the combined wave-current flows, these variations could be as high as +5cm and as low as –6cm from the mean level.

These variations have a significant impact on the resulting hydrodynamics and need to be characterized. Initially, the severity of the variations was not apparent as they typically take on the order of 10 hours of wave action to become observable. To measure the variations, a simple method was devised. First, when the bed is flat, the mean elevation of the bed is drawn on the glass walls on the side of the tank. This serves as a baseline for all following measurements. Then, the variations were traced by hand on the side of the tank. Since ripples were superimposed on the mean bed, the mean bed level was estimated as the level mid way through the crest and trough of the ripples. Then, the displacement of the mean bed variation trace is measured by hand from the initial flat-bed level at 10cm increments along the flume.

There are limitations to this method. One is that the tracing is done by hand, and subject to a large degree of human error - they were "traced with a thick pen" and at best are a rough quantitative description of the variations that should be subject to great scrutiny. At worst, they are a qualitative description of the phenomenon. The error is assumed to be on the order of half the ripple height, or approximately ±0.8cm but varies depending on the particular location as the ripple height varies in x. Another limitation is the actual location where measurements can be made. Close to the wavemaker the false bottom interferes with the bed, and farther from the wavemaker (about 13m), there is no physical access to the side of the tank, so no traces can be made. That limits the traces to x = 6.9m to 12.8m, or about 2 bedform lengths. Figure 3.12 shows the measured mean bed variations after the pure wave and wave-current experiments were complete. More details of this mean bed variation are discussed in Sections 5.3.3 and 7.2.1.

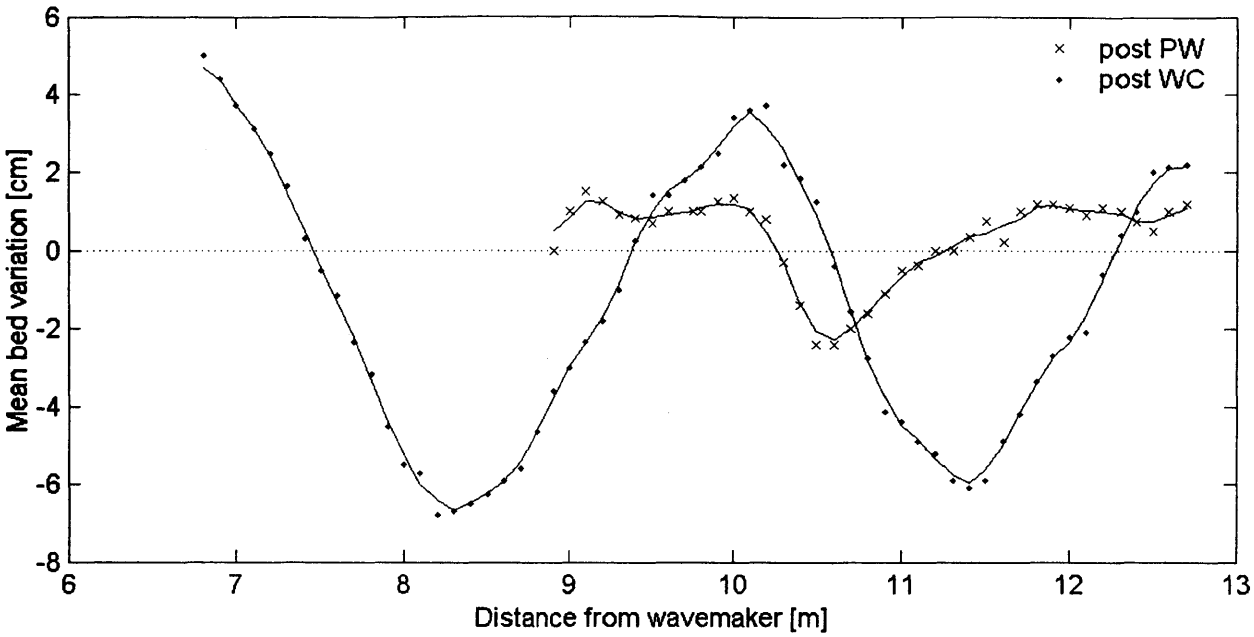

Figure 3.12: Mean bed elevation after Pure Wave (PW) experiments (x) and after wave-current experiments(·). The solid lines are the respective three point moving averages and the dotted line is the initial flat bed level.

3.9. EXPERIMENTAL DESIGN

Experiments with monochromatic waves and currents were used to determine the bottom roughness experienced by pure currents, pure waves, and combined wave-current flows over a movable bed. This section summarizes the parameters for these experiments and the expected resulting parameters to report.

A preliminary set of experiments was performed on a fixed bed consisting of a single layer of 0.64mm diameter spheres on the bottom of the flume. It was not possible to determine if the wave boundary layer for this bottom condition was fully rough turbulent, and therefore the application of the wave current model was limited. The results of these experiments are shown in Appendix B. Another preliminary set of experiments was performed on a movable bed with d_{50} =

0.2mm sand, wave period $T = 1.5$s, and a water depth $h = 40$cm. For this case, the waves could not be adequately generated – the current filter (discussed in Section 3.4.1) would not permit correction for the free second harmonic and the waves generated are not waves of permanent form (see Chapter 4). Some information can be gleaned from these experiments; their results are presented in Appendix C.

Experiments were performed using a combination of waves and currents: pure wave experiments (PW) where only waves are present in the tank, pure current experiments (PC) where only a current is present in the tank, and combined wave-current experiments (WC) where waves are generated in the presence of a current. The parameters that specify the wave conditions are the water depth h, wave period T, and the wave amplitude a. For these experiments, the water depth $h = 60$cm, the wave period $T = 2.63$s, and the wave amplitude $a \cong$ 6cm. The exact wave amplitude varies slightly because of wave reflection, wave attenuation, and wave-current interaction and must be defined at each separate x location along the flume for every experimental case. The current is specified by the water depth h and the depth-averaged current velocity u_c. The typical depth-averaged current velocity $u_c \cong$ 16cm/s, but varies depending on the current-wave interaction and the size of the roughness elements present in the flume.

The main set of experiments were performed with a movable bed of sediment with a $d_{50} =$ 0.2mm (sand). The general outline of the experiments is as follows. Waves were generated to obtain a rippled bottom. Then the roughness felt by pure waves k_w was measured through wave attenuation (see Section 6.3.1). Velocity profiles of the pure wave motion were measured at different locations along the flume. Pure currents were then run over the wave-rippled bed, and velocity profiles were measured at different locations along the flume. The roughness felt by the current k_c is derived from the current profiles (see Section 8.2). Finally, waves are generated in the presence of a current. The roughness felt by the waves in the presence of the current k_{wc} is measured through wave attenuation (Section 6.3.2). Velocity profiles were measured at different locations along the flume, and the roughness of the current in the presence of waves k_{cw} was derived from the velocity profiles and the application of the wave-current interaction models (Chapter 9). For each separate measurement of the bottom roughness and for each location along the flume where velocity profiles were measured, the ripple geometry was measured by the ADV following the method described in Section 3.8.1 in order to estimate the actual roughness present at the specific location.

As discussed in Chapter 4, it is impossible to completely eliminate wave reflection off of the absorber beach in the flume. This reflection creates a partially standing wave in the flume, with the reflected wave's amplitude as high as 20% of the incident wave. This results in a wave velocity that varies 40% between the partially standing wave's node and antinodes. The variation in wave velocity will cause larger ripples to form where the velocity is larger (node) and smaller ripples where the velocity is smaller (antinode). Further, both the variation in wave velocity and variation in ripple size will affect the interaction between the waves and the current. In order to define the variation of all parameters along a partially standing wave length (called a beat or beat length), PW, PC, and WC velocity profile measurements must be made at points along the partially standing wave. Then, with knowledge of the spatial variation of the parameters, a spatial average over an integer number of beat lengths can be obtained to better represent the ideal conditions of no wave reflection. To accomplish this, measurements were performed over the entire beat at spacings of some fraction of the beat length. Table 3.3 shows the location of all measurements and their respective position along the beat. Typically, measurements were performed at four locations along the beat: the node, halfway between the node and antinode (upslope), the antinode, and halfway between the antinode and the node (downslope). For the pure current and wave-current cases, measurements were made at eight locations along the beat: all previous four plus a point between the antinode and the downslope (anti-down), the downslope and the node (down-node), the node and the upslope (node-up), and the upslope and the antinode (up-anti). This allowed for a better picture of the parameter variations along the beat. Also, for the pure current and the wave-current cases, two beat lengths were covered in order to show the repeatability of the measurements.

Table 3.3: Design characteristics of pure wave, pure current, and wave-current experiments.

		Pure Wave		Pure Current		Wave-Current			
Experiment ID	beat location	x [m]	Velocity Profile	x [m]	Velocity Profile	Experiment ID	beat location	x [m]	Velocity Profile
a	node	9.800	yes	9.800	yes	A	antinode	8.416	yes
b	node-up	--	no	10.343	yes	B	anti-down	8.934	yes
c	upslope	10.540	yes	10.540	yes	C	downslope	9.183	yes
d	up-anti	--	no	10.84	yes	D	down-node	9.411	yes
e	antinode	11.290	yes	11.290	yes	E	node	9.930	yes
f	anti-down	--	no	11.813	yes	F	node-up	10.448	yes
g	downslope	12.030	yes	12.030	yes	G	upslope	10.676	yes
h	down-node	--	no	12.331	yes	H	up-anti	10.946	yes
I	node	12.790	yes	12.790	yes	I	antinode	11.423	yes
j	node-up	--	no	13.336	yes	J	anti-down	11.900	yes
k	upslope	--	no	13.579	yes	K	downslope	12.149	yes
l	up-anti	--	no	13.833	yes	L	down-node	12.397	yes
m	antinode	--	no	14.309	yes	M	node	12.916	yes
n	anti-down	--	no	14.838	yes	N	node-up	13.434	yes
o	downslope	--	no	15.103	yes	O	upslope	13.725	yes
p	down-node	--	no	15.346	yes	P	up-anti	13.953	yes
q	node	--	no	15.822	yes	Q	antinode	14.430	yes

4. WAVE GENERATION

This chapter discusses the wave generation concepts and methodologies used in this study. Emphasis is placed on the concepts which affect the ability to measure wave attenuation accurately, since estimates of bottom roughness experienced by waves are obtained from the measurement of wave attenuation. Using wave attenuation to determine roughness requires the generation of pure second order Stokes waves. Because of non-linear components which arise due to the wavemaker forcing, the motion of the wavemaker must be carefully controlled. Also, the wave interactions with the current inlet, the transition in depth between the flume bottom and the sandy bed, and the current filter are explored.

4.1. GENERATION OF STOKES WAVES

Biesel and Suquet (1951) established a linear theory for a piston-type wavemaker which specified the paddle motion to generate monochromatic waves as

$$\zeta(t) = -\zeta_0 \cos\omega t = -\frac{a n_1}{\tanh(kh)} \cos\omega t \tag{4.1}$$

where ζ is the wavemaker displacement from its mean position, k is the wave number, h is the water depth, and n_1 is given as

$$n_1 = \frac{C_g}{C} = \frac{1}{2}\left[1 + \frac{2kh}{\sinh(2kh)}\right] \tag{4.2}$$

where C_g is the group celerity and C is the phase velocity of the primary wave motion. Madsen (1971) showed that when using a sinusoidally moving piston-type wavemaker to generate long waves with an amplitude large enough to be nonlinear, especially those described by Stokes second order theory, the resulting wave motion included two second harmonic waves. One is bound to the first harmonic motion and is

$$a_B^{(2)} = \frac{ka^2}{4}\frac{[2+\cosh(2kh)]\cosh(kh)}{\sinh^3(kh)} \tag{4.3}$$

and the other is free of the first harmonic motion and described as

$$a_F^{(2)} = \frac{a^2}{2}\frac{\coth(kh)}{h}\left[\frac{3}{4\sinh^2(kh)} - \frac{n_1}{2}\right]\frac{\tanh(k_F h)}{n_2} \tag{4.4}$$

and

$$n_2 = \frac{1}{2}\left[1 + \frac{2k_F h}{\sinh(2k_F h)}\right] \tag{4.5}$$

$a_B^{(2)}$ is the bound second harmonic amplitude, $a_F^{(2)}$ is the free second harmonic amplitude, and k_F is the free second harmonic wave number. The more nonlinear the wave is (the higher the Ursell number $U = 2aL^2/h^3$), the more that $a_F^{(2)}/a_B^{(2)}$ approaches one. The second harmonic bound wave of amplitude $a_B^{(2)}$ travels with the main wave and produces the more peaked crest and flatter troughs that characterize the second order Stokes wave. The free second harmonic wave with amplitude $a_F^{(2)}$ travels at a slower speed and results in a non-uniform wave that varies along the length of the flume. This has the effect of producing a large second harmonic amplitude that changes position relative to the first harmonic amplitude with its location along the flume, thus producing a wave with changing form along the flume (Rosengaus 1987).

To correct for this, Madsen (1971) suggested that a progressive second order Stokes wave of permanent form may be generated in a flume of uniform depth by specifying a wavemaker motion of

$$\zeta = -\zeta_0 \cos\omega t - \zeta_0 \frac{a}{2h}\left[\frac{1}{n_1}\frac{3}{4\sinh(kh)} - \frac{n_1}{2}\right]\sin 2\omega t \tag{4.6}$$

where n_1 is given in equation (4.2), and ζ_0 is the amplitude of the wavemaker motion, which can be related to the wave amplitude by

$$\zeta_0 = \frac{an_1}{\tanh(kh)} \tag{4.7}$$

The first term in equation (4.6) reflects the linearized wavemaker theory of equation (4.1), and the second term is the correction for the free second harmonic which results from the wavemaker forcing. Previous experiments by Mathisen (1989 and 1993), and Rosengaus (1987) have verified the removal of the second free harmonic in the facilities used in these studies by operating the wavemaker as prescribed by equation (4.6).

4.2. RESOLUTION OF THE INCIDENT WAVE

Rosengaus (1987) developed a measuring procedure to resolve the various wave components of pure waves (called the Reference Measurement Method (RMM)). Mathisen (1993) modified this method to include wave-current flows. Only the general formulation and results of this method are presented here.

For a combined wave-current flow, the wavemaker forces a first harmonic motion with and absolute radian frequency ω_a. If the frame of reference is shifted so that the wave is observed moving with the current, the incident radian frequency ω_i and the reflected radian frequency ω_r may be defined

$$\begin{aligned} \omega_i &= \omega_a - k_i u_c \quad \text{incident wave} \\ \omega_r &= \omega_a + k_r u_c \quad \text{reflected wave} \end{aligned} \tag{4.8}$$

where k_i is the incident wave number, k_r is the reflected wave number, and u_c is the depth-averaged current. Then these frequency definitions can be used to determine their respective wave numbers as

$$\begin{aligned} \omega_a^2 &= g k_a \tanh(k_a h) \quad \text{absolute wave number} \\ \omega_i^2 &= g k_i \tanh(k_i h) \quad \text{incident wave number} \\ \omega_r^2 &= g k_r \tanh(k_r h) \quad \text{reflected wave number} \end{aligned} \tag{4.9}$$

where g is the acceleration of gravity. These equations show that the incident wave traveling with the current is lengthened while the reflected wave traveling against the current is shortened.

The surface profile along the flume can be characterized from the above definitions of the wave parameters. By linearly combining the incident and reflected waves in the first harmonic, the first harmonic surface $\eta^{(1)}$ can be described by

$$\eta^{(1)} = \eta_i + \eta_r = a_i \cos(k_i x - \omega_a t + \phi_i) + a_r \cos(k_r x + \omega_a t + \phi_r) \tag{4.10}$$

where ϕ_i is the incident wave phase angle and ϕ_r is the reflected wave phase angle. Then, by taking the absolute value and performing some algebraic manipulations detailed in Rosengaus (1987) and Mathisen(1993), and by assuming that $a_r << a_i$, the surface profile can be rewritten as

$$\left|\eta^{(1)}\right| = a_i + a_r \cos[(k_i + k_r)x + (\phi_r - \phi_i)] \tag{4.11}$$

and the beat length (the length of the partially standing wave) is determined from

$$L_b = \frac{2\pi}{k_i + k_r} \tag{4.12}$$

By allowing for a linear decay in the incident wave amplitude along the tank to account for the wave attenuation, the incident wave amplitude is expressed as

$$a_i = a_{i0} - m_t x \tag{4.13}$$

where a_{io} is the incident wave amplitude at the wavemaker ($x = 0$) and m_t is the total wave attenuation slope in cm/cm. Finally, by substituting equation (4.13) into equation (4.11), the resulting approximate absolute free surface variation along the tank is

$$\left|\eta^{(1)}\right| = a_{io} - m_t x + a_r \cos[(k_i + k_r)x + (\phi_r - \phi_i)] \tag{4.14}$$

In the limit of an extremely weak or nonexistent current, k_i approaches k_r and equation (4.14) approaches the results of Rosengaus (1987) for pure waves. For the first harmonic, the current lengthens the incident wave approximately as much as it shortens the reflected wave. Therefore, the resulting beat length for the wave-current case is nearly identical to that of the pure wave case.

For the second harmonic variation of combined wave-current flows, the bound second harmonic travels with the first harmonic at a radian frequency of $2\omega_i$ and with a wave number of $2k_i$. The free second harmonic has a radian frequency ω_{Fi} of

$$\omega_{Fi} = 2\omega_a - k_{Fi} u_c \tag{4.15}$$

and therefore the free second harmonic wave number k_{Fi} is defined as

$$(\omega_{Fi})^2 = g k_{Fi} \tanh(k_{Fi} h) \tag{4.16}$$

Then, following the same methodology as with the first harmonic but neglecting reflection of both the bound and the free second harmonic, the second harmonic surface profile can be described by

$$\eta^{(2)} = \eta_B + \eta_F = a_B \cos(2k_i x - 2\omega_a t + \phi_B) + a_F \cos(k_F x - 2\omega_a t + \phi_F) \qquad (4.17)$$

where ϕ_B is the phase of the bound second harmonic and ϕ_F is the phase of the free second harmonic. Again, following the procedure for the first harmonic described above and assuming that $a_F << a_B$, the absolute second harmonic free surface amplitude is approximated by

$$\left|\eta^{(2)}\right| = a_B + a_F \cos[(k_F - 2k_i)x - (\phi_B - \phi_F)] \qquad (4.18)$$

and the beat length that describes the length scale of the variation of the second harmonic $L_b^{(2)}$ is defined as

$$L_b^{(2)} = \frac{2\pi}{k_F - 2k_i} \qquad (4.19)$$

It is possible to include an attenuation term in equation (4.18) as was done for equation (4.11) with equation (4.13). Generally, this attenuation is small, and can often be neglected, since the second harmonic wave amplitudes are generally small. However, for completeness, the attenuation of the second harmonic is included for completeness in the following investigation, so the free second harmonic profile is

$$\left|\eta^{(2)}\right| = a_{B0} - m_t^{(2)} x + a_F \cos[(k_F - 2k_i)x - (\phi_B - \phi_F)] \qquad (4.20)$$

In the limit of a weak current, this result approaches that obtained by Rosengaus (1987) for pure waves.

By measuring the free surface at locations along the flume, a least squares fit of equations (4.14) and (4.18) can be used to determine the parameters a_i, a_r, m_t, for the first harmonic and a_B, and

a_F, (and $m_t^{(2)}$, if desired) for the second harmonic. Rosengaus (1987) details this procedure and examines its accuracy.

4.3. WAVE – FILTER INTERACTION

The current filter is necessary to straighten the current flow structure and remove any secondary flows in the flume (as described in Section 3.7.5). Unfortunately, the filter interacts with the waves generated by the wavemaker in that it acts as a semi-permeable barrier to the waves - some of the wave energy is transmitted through the filter and some is reflected off of it. The amount of energy transmitted or reflected is a function of the wave period. Therefore, it was necessary to characterize how the filter affects the waves in amplitude and phase for the wave periods of interest so that it is possible to generate a wave described in Sections 4.1 and 4.2; more specifically, it is necessary to be able to remove the free second harmonic with the filter in the flume (see Section 4.4 for more information on the removal of the free second harmonic).

First, the location of the filter placement is important. If it is placed at a harmonic fraction of the wave length from the wavemaker, resonance is possible and violent wave action could result. Also, the filter should be placed as close to the wavemaker and current inlet as possible in order to maximize the length of the test bed. The length of the first harmonic is $L^{(1)} = 6.0$m, the second bound harmonic is $L_B^{(2)} = L^{(1)}/2 = 3.0$m, and the free second harmonic is $L_F^{(2)} = 2.46$m. Therefore, to avoid these lengths, the stoss side (wavemaker side) of the filter was placed at 2.65m from the wavemaker.

To characterize the wave-filter interaction, a simple series of experiments were performed. Monochromatic waves of $T = 2.63$s and $T/2 = 1.315$s were generated and their amplitudes were measured without the filter in the flume at different x locations along the flume. Then, the filter was placed in the flume and the wave amplitudes were measured again. By matching the locations along the flume, K_T was found by taking the ratio of the amplitude with a filter to the amplitude without a filter. By averaging all these values, the mean K_T was found. Using the same approach, K_R can be calculated as 1- K_T. Table 4.1 shows these mean K_T and K_R values for the first and second harmonics. It also shows the standard deviation for all measurements.

The phase change caused by the filter should be determined to obtain a more precise estimate of the wave-filter interaction. Therefore, the phase for each point was measured. Unfortunately, the phase data was unorganized and seemingly random. This is not a major concern since the phase will be dramatically affected by other factors not so easily controlled or predicted such as the interaction with the current inlet basin. The phase is left to be determined though the procedure outlined in Section 4.4.

Table 4.1: Transmission and reflection coefficients for the current filter for the primary periods.

T [s]	K_T	σ_{KT}	K_R	σ_{KR}
2.63	0.76	0.01	0.24	0.01
1.315	0.58	0.01	0.42	0.01

Through some further exploratory tests, it was found that wave periods of less than about one second could not successfully be transmitted through the filter; the resulting wave pattern is random with no consistent harmonic forcing. Therefore, any wave generated with a first harmonic period less than 2 seconds will not be able to have the free second harmonic adequately removed.

As mentioned in Section 3.9, a set of experiments were performed with a water depth $h = 40$cm and wave period $T = 1.5$s. Since the second harmonic period $T/2 = 0.75$s, it is below the threshold of wave generation in which the free second harmonic can be removed (because a wave with a period of less than 1 second cannot be adequately transmitted through the filter). However, it was possible to resolve the wave conditions in the flume, which showed a strong interaction between the first and second harmonics. The method used to resolve these wave conditions is discussed in detail in Appendix C.

4.4. REMOVAL OF FREE SECOND HARMONIC

As discussed earlier, generating progressive second order Stokes waves of permanent form requires the removal of the free second harmonic. For the facilities used in this study, Mathisen (1993) showed that the correction formulated by Madsen (1971) adequately removes the free second harmonic for pure waves when the flume has a completely flat bottom and the current inlet basin is covered. He also showed that when the current inlet basin is uncovered, the first order wave amplitude $a^{(1)}$ decreases and the free second harmonic amplitude $a_F^{(2)}$ increases relative to the bound second harmonic $a_B^{(2)}$. The reason for this is given as reflection and re-reflection off the current inlet basin; $a^{(1)}$ feels the effect more than $a^{(2)}$ because the wavelength of the first harmonic is at least two time larger than the second harmonic. Further, Mathisen argues that while the effects can be theoretically explained, an actual theoretical modification of the free second harmonic correction by Madsen would be extremely complicated due to the complex hydraulics of the transition region. Therefore, Mathisen suggested an organized trial and error methodology for removing the free second harmonic. These arguments apply to both the pure wave case and the wave-current case.

While Mathisen's methodology proved effective, the present experiments presented even more complicated transitional hydraulics due to the introduction of the current filter and the transition between the flume bottom and the sand bed. Therefore, a modified trial and error method based on experimental conditions is presented here which allows for much faster determination of the correction factors.

For this methodology, regardless of the experimental setup, the first step is to generate a second order Stokes wave with no correction at all and measure $\left|\eta^{(1)}\right|$ and $\left|\eta^{(2)}\right|$ over the length of the flume. Next, by applying the least squares fit for the second harmonic variation to $\left|\eta^{(2)}\right|$, an estimate of $a_B^{(2)}$ and $a_F^{(2)}$ can be obtained. Figure 4.1 shows the measured $\left|\eta^{(2)}\right|$ as dots (·) and the fit based on equation (4.21) as the solid line. The dotted line is $a_B^{(2)}$, and $a_F^{(2)}$ is qualitatively shown as the deviation from $a_B^{(2)}$ by the arrow. Now, with knowledge of the actual free second harmonic amplitude that needs to be removed in the test section, we can back-calculate the amplitude of $a_F^{(2)}$ at the wavemaker ($x = 0$) if the effects of the transition region can be adequately represented. Then, with a priori knowledge of $a_F^{(2)}$ at the wave paddle, we can use the same logic as Madsen (1971) and generate a waveform that matches $a_F^{(2)}$ at the wavemaker but with opposite sign, therefore canceling $a_F^{(2)}$ in the test section.

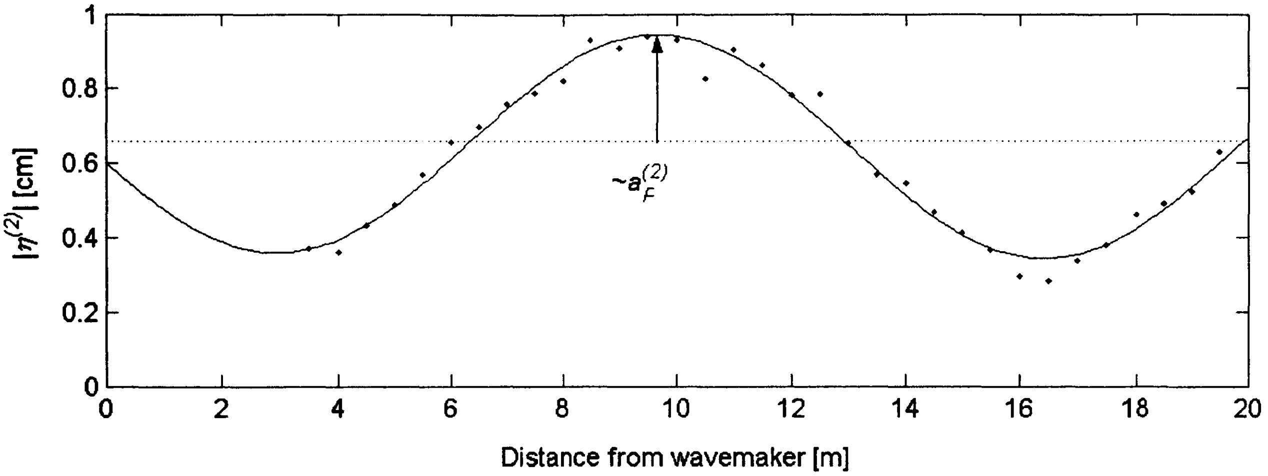

Figure 4.1: Pure wave variation of the second harmonic along the flume. Points (·) are the measured second harmonic variation, the solid line is the best least-squares fit based on equation (4.20), and the dotted line is the estimated bound second harmonic amplitude.

As mentioned above, many factors will change $a_F^{(2)}$ between the test section and the wavemaker; unfortunately only two can be readily accounted for: the current filter transmission coefficient and the change of depth between the sand bed and the flume bottom. While this correction will not exactly determine $a_F^{(2)}$ at the wavemaker, possessing an order of magnitude estimate of the free second harmonic correction to be generated reduces much of the trial and error time of the method of Mathisen (1993).

The filter will allow only approximately $K_T = 58\%$ of the free second harmonic energy generated to pass through it (for the typical $T/2 = 1.315$s of the second harmonic – see Section 4.3). Similarly, for the change of depth between the sand bottom and the flume bottom (Δh = 10cm), the wave amplitude will change (shoal) according to

$$K_s = \frac{a_0}{a} = \sqrt{\frac{C_g}{C_{g0}}} \tag{4.21}$$

where K_s is the shoaling coefficient, a_0 is the amplitude at the depth h_0, a is the amplitude at depth h, C_{g0} is the wave group velocity at depth h_0, and C_g is the group velocity at depth h. C_g is defined

$$C_g = \frac{1}{2}\left[\frac{\omega - ku_c}{k}\right]\left[1 + \frac{2kh}{\sinh(2kh)}\right] \tag{4.22}$$

and C_{g0} is found by replacing k with k_0 and h with h_0 in equation (4.22). In practice for these experiments, the second harmonic wavelength was sufficiently small so that $K_s \cong 1$, and can be neglected. Then with the value of the free second harmonic amplitude in the test section $a_F^{(2)}$ known, the free second harmonic amplitude at the wavemaker $a_{F,wm}^{(2)}$ can be obtained from

$$a_{F,wc}^{(2)} = \frac{a_F^{(2)}}{K_T K_s} \cong \frac{a_F^{(2)}}{K_T} \tag{4.23}$$

Now the amplitude of the free second harmonic correction is approximately known. To further correct for $a_F^{(2)}$, experiments were completed with this amplitude correction and the phase of the free second harmonic was varied, using a different phase until a phase was found that optimized the removal of the free second harmonic. Once the optimal free second harmonic phase was found, the amplitude correction can be fine-tuned until the free second harmonic is adequately removed from the flume.

4.4.1. CORRECTION OF THE FREE SECOND HARMONIC FOR PURE WAVES

To verify the above method, an initial set of experiments were performed with the filter in the flume but the sand bed was not present (no depth transition occurred). Pure waves were generated with no correction for the free second harmonic to estimate the $a_F^{(2)}$ present in the test section. Figure 4.2 shows the results of this experiment. The variation of the second harmonic shown in Figure 4.2 (b) is large, and its interaction with the first harmonic can be seen in Figure 4.2 (a) – where the second harmonic is large, the first harmonic tends to be smaller, and where the second harmonic is small, the first is larger. After correcting for the free second harmonic using the procedure described above and accounting for the filter interaction, a waveform is generated where the free second harmonic is almost completely removed. This is shown in Figure 4.3. The second harmonic is virtually free of any free second harmonic interaction. The variation of the second harmonic in Figure 4.3 (b) about the fit seems to be spatially periodic, with a variation of the order of half the incident wave length (~3m). This is the same as the variation of the first harmonic wave due to reflection. If the variation in the second harmonic was due purely to the reflection of bound second harmonic, the length of the oscillation should be one quarter of that of the incident wave period (~1.5m). However, the variations seen in Figure 4.3 (b) are of the same order as the first harmonic, and are large where the first harmonic is large and small where the first harmonic is small – the variations are therefore likely due to some nonlinear effect in the partially standing wave motion. Nevertheless, this variation is negligible when compared to the bound second harmonic amplitude, and its effects are expected to be insignificant.

4.4.2. CORRECTION OF THE FREE SECOND HARMONIC FOR COMBINED WAVES AND CURRENT

In order to verify that the free second harmonic could be effectively removed in wave-current flow, another set of experiments was performed with the same conditions as in the previous section, but with waves generated with a current. Figure 4.4 shows the first (a) and second (b) harmonics with no correction for the free second harmonic. Notice that in Figure 4.4 (b), the

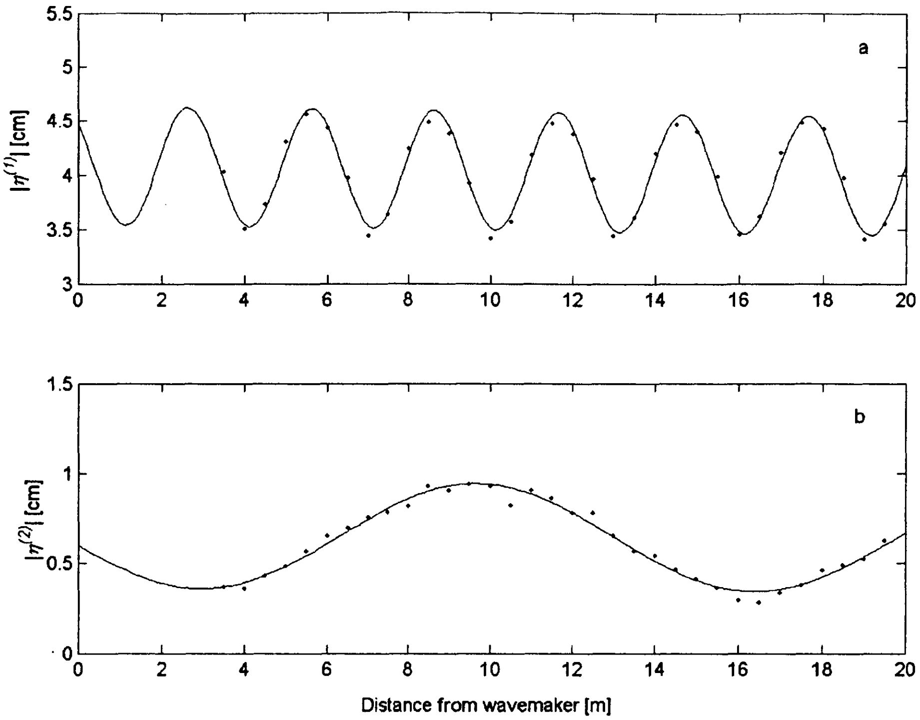

Figure 4.2: Pure wave (a) 1st and (b) 2nd harmonic free surface variations with no free 2nd harmonic correction. Points (·) are the free surface measurements and the solid line is the best-fit of the free surface using equation (4.14) for (a) and equation (4.20) for (b); both beat lengths are determined from the fit.

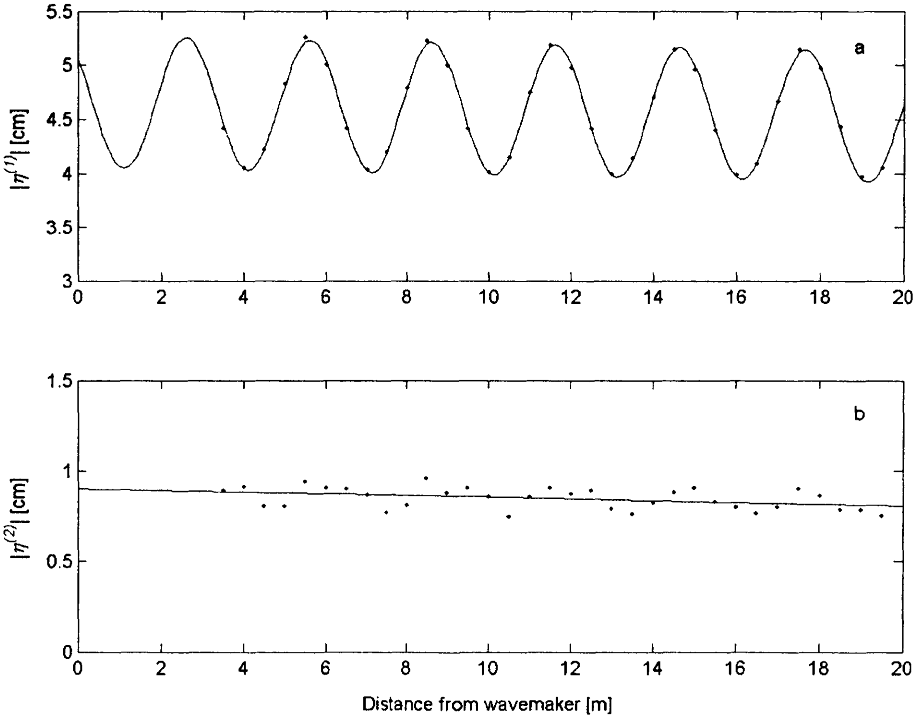

Figure 4.3: Pure wave (a) 1st and (b) 2nd harmonic free surface variations with free 2nd harmonic correction. Points (·) are the free surface measurements and the solid line is the best-fit of the free surface using equation (4.14) for (a) and equation (4.20) for (b); both beat lengths are determined in the fit.

variation of the second harmonic, or $L_B^{(2)}$, is longer than for the case of pure waves in Figure 4.2. This demonstrates how the current lengthens the waves when the waves are propagating with the current, as is predicted by equation (4.19) when the incident wave lengths are adjusted to account for traveling with the current. Figure 4.5 shows the wave-current free surface after the free second harmonic has been effectively removed using the method described in Section 4.4.

Table 4.2 shows the predicted and measured beat lengths for the first and second harmonic free surface elevation, for both the pure wave and wave-current conditions. The measured beat lengths are 'measured' by adjusting their length in the fitting process until a best fit to the measured free surface data is obtained. The pure wave 1st harmonic predicted beat length is $L^{(1)}/2$, and and 2nd harmonic beat length is from equation (4.19). This equation neglects reflection in the 2nd harmonic and only reflects the interaction of the 2nd free and bound harmonics. The wave-current 1st harmonic predicted beat length is calculated from equation (4.12) where the incident wave number is traveling with the current, and the reflected wave number is against the current. The 2nd harmonic predicted beat length is from equation (4.19), neglecting the reflected wave length that travels against the current. Note that k_F and k_i in equation (4.19) are treated as having been modified only by traveling with the current. As the reflected 2nd harmonic is neglected, the effects of traveling against the current are neglected.

Table 4.3 and Table 4.4 show the wave conditions used in these experiments. The results presented are the average of the pre and post measurements of the free surface. Note the reflection coefficient R is given as the ratio of $R = a_r/a_i$ for the 1st harmonic.

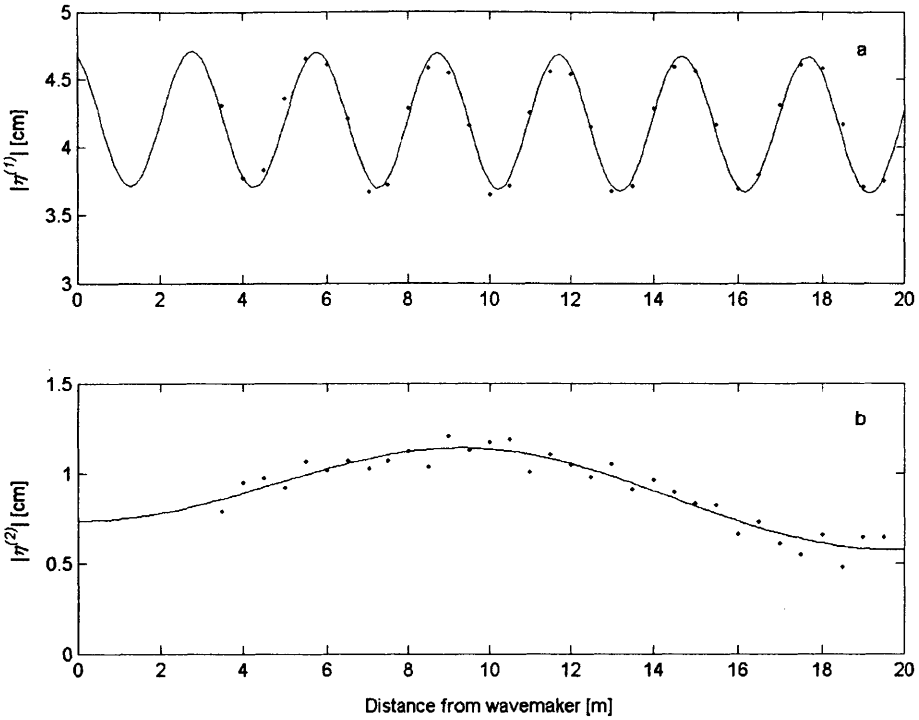

Figure 4.4: Wave-current (a) 1st and (b) 2nd harmonic free surface variations with no free 2nd harmonic correction. Points (·) are the free surface measurements and the solid line is the best-fit of the free surface using equation (4.14) for (a) and equation (4.20) for (b).

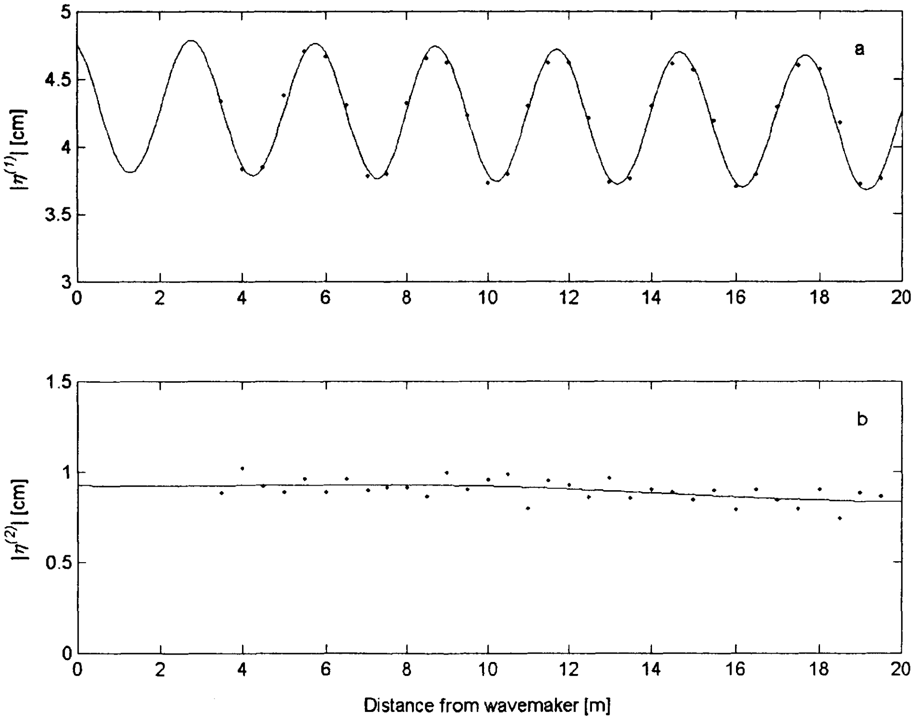

Figure 4.5: Wave-current (a) 1st and (b) 2nd harmonic free surface variations with free 2nd harmonic correction. Points (·) are the free surface measurements and the solid line is the best-fit of the free surface using equation (4.14) for (a) and equation (4.20) for (b).

Table 4.2: Predicted versus measured 1st and 2nd harmonic beat lengths for pure waves and wave-current.

	Pure Wave		Wave-Current	
	Predicted [m]	Measured [m]	Predicted [m]	Measured [m]
1st Harmonic	3.002	3.008	2.981	2.976
2nd Harmonic	13.534	13.550	19.196	19.639

Table 4.3: Wave conditions obtained from the best-fit of the free surface profiles using equation (4.14) for the 1st harmonic.

	L_i [m]	$L_b^{(1)}$ [m]	a_i [cm]	a_r [cm]	R	m_t [cm/cm]
PW 1st	6.004	3.008	5.74	1.15	0.20	-3.13E-04
WC 1st	6.472	2.976	5.91	1.08	0.18	-2.71E-04

Table 4.4: Wave conditions obtained from the best fit of the free surface profiles using equation (4.18) for the 2nd harmonic.

	L_i [m]	$L_b^{(2)}$ [m]	a_B [cm]	a_F [cm]	a_F/a_B	m_t [cm/cm]
PW 2nd	3.002	13.55	1.35	0.02	0.02	-1.22E-04
WC 2nd	3.236	19.639	1.66	0.17	0.10	-1.53E-04

5. BEDFORM GEOMETRY

This section summarizes the results of the measurements of ripple parameters and mean bed variation for the pure wave, pure current, and combined wave-current flows, and also presents some empirical predictions of the bedforms based on the hydrodynamic conditions. Another factor considered is the response of the sediment bed to the wave conditions, especially from an initially flat bed. The developing process of the bed is briefly discussed, and some quantitative aspects of the bedform shapes and formation are presented.

Accurate measurements of the bedform geometry are required to verify the selection of a characteristic hydrodynamic roughness for a movable bed in turbulent boundary layer wave and current flows. These measurements allow for a comparison between the predicted hydrodynamic roughness and the actual physical roughness of the bed. Also, other phenomenon which may affect the hydrodynamics of the system, namely the variation of the mean bed elevation, are characterized to allow for a more complete understanding of the conditions present during the experiments.

For small scale bedforms (i.e. ripples), the ADV-traverse system facilitates the characterization of the bedform parameters, as discussed in Section 3.8. The large scale mean bed variation measurement and characterization was limited and few measurements of the phenomena were made, as its significance was not appreciated during the planning and the initial phases of the experiments. The measurement procedure adopted for the mean bed variation is also discussed in Section 3.8.

5.1. BEDFORM GENERATION AND DEVELOPMENT

It was found that during preliminary experiments with the sediment bed, and as noted by Rosengaus (1987), an initially flat sediment bed becomes rippled at boundary irregularities when exposed to wave or wave-current action because of flow perturbations induced by these irregularities. These initial patches develop into a random and unorganized pattern of bedforms, which, if given enough time, will eventually form regular ripples. In order to obtain a uniform rippled bed in a reasonable amount of time, Rosengaus (1987) suggested making initiator ripples at 10ft intervals along the bed by manually tracing a line across the flume width using a 1.5cm angle iron rod. This resulted in a small depression in the bed with sand forming a small crest on each side of the depression.

Using this method, ripples developed in an organized way. When acted on by waves, the first ripple grows and initiates the formation of another crest on either side. This continues and the patch grows outward from the initiator, in both directions for pure waves and only in the direction of the current for wave-current flows. When the ripple patches merge, the pattern is somewhat disorganized. Depending on the wave conditions, the ripples may rearrange themselves and become organized or a chaotic and highly three-dimensional ripple patter may form.

Rosengaus (1987) performed detailed experiments on the development time and ripple propagation rate for various wave conditions. This is beyond the scope of the present paper; however, it is important to establish the fully developed bed conditions. A fully developed bed is defined as the state were the statistics of the bedform geometry parameters (length λ, height η) do not change with time. The individual bedforms will change in geometry and location, but the bed as a whole should be statistically constant for discrete sections of the bed. This definition is difficult to assess, and in these experiments, it was sometimes incorrectly assumed that the bed was fully developed. This resulted in changing bedform statistics during the hydrodynamic measurements which affects the hydrodynamic results in a way that is difficult, if not impossible to assess. Fortunately, these variations are over a long time scale, while most hydrodynamic measurements are done over a short time scale. Therefore, measures were taken to avoid any effects of changing bedforms. However, they remain a source of uncertainty in the hydrodynamic results, especially when comparing results that have a large interval of time between the individual measurements.

It should be mentioned that the glass walls of the flume have an influence on the bedforms, especially during their development. Rosengaus (1987) explored the wall effects quantitatively. He found that if the bed is fully developed, there is little difference in the statistics of the bed across the flume, although the individual profiles across the flume width may vary.

5.2. BEDFORM PREDICTION

Numerous studies exist where bedform geometry is compared to the steady unidirectional and oscillatory flow conditions. Rosengaus (1987) summarizes and expands on these studies. In unidirectional flow, the Shields parameter is defined as

$$\psi = \frac{\tau_b}{\rho g (s-1) d} \tag{5.1}$$

where s is the sediment density relative to the fluid density, τ_b is the shear stress acting on the sediment, and d is the grain size diameter. The Shields parameter has been successfully used to characterize flow-bottom interactions. ψ can be interpreted as the ratio of the drag force from the fluid to the submerged weight of a sediment particle. When bedforms are present, the total bottom shear stress is due to both skin friction from the roughness of the grains themselves and the form drag from the bedforms. Then for predicting the bedform geometry, only the shear stress due to skin friction and sediment characteristics are required

$$\psi' = \frac{\tau_b'}{\rho g(s-1)d} \tag{5.2}$$

where τ_b' is the bottom shear stress due only to the skin friction.

5.2.1. PURE WAVE BEDFORM PREDICTION

Madsen and Grant (1976) extended this relationship to include oscillatory (pure wave) flow by taking τ_b' as the maximum value during a cycle. Then the Shields parameter becomes

$$\psi' = \frac{\frac{1}{2} f_w' u_{bm}^2}{\rho g(s-1)d} = \frac{u_{*wm}'^2}{g(s-1)d} \tag{5.3}$$

where the prime indicates the parameters are calculated only for skin friction, and the wave friction factor is obtained as detailed in Section 2.2 with $k_n = d_{50}$.

To predict the bedform geometry for pure oscillatory flow (pure waves), Madsen (1993) suggested

$$\frac{\eta}{A_{bm}} = 0.27 - 0.33\psi'^{(0.55)} \tag{5.4}$$

and

$$\frac{\eta}{\lambda} = 0.16 - 0.36\psi'^{(2.3)} \tag{5.5}$$

where A_{bm} is the maximum bottom excursion amplitude of the wave motion.

5.2.2. WAVE-CURRENT BEDFORM PREDICTION

To extend this to wave-current flows, we must reconsider linear wave theory. If we consider the current velocity as the same order as the wave orbital velocity, the velocity potential becomes

$$\Phi = \frac{a(\omega - ku_c)}{k \sinh kh} \cosh k(z+h) \sin(kx - \omega t) \tag{5.6}$$

Then the bottom velocity and excursion amplitude at their maximums are defined as

$$u_{bm} = \left.\frac{\partial \Phi}{\partial x}\right|_{z=-h} = \frac{a(\omega - ku_c)}{\sinh kh} \tag{5.7}$$

and

$$A_{bm} = \frac{u_b}{\omega} = \frac{a(\omega - ku_c)}{\omega \sinh kh} \tag{5.8}$$

where k is from the modified dispersion relation

$$(\omega - ku_c)^2 = gk \tanh kh \tag{5.9}$$

Using these values for u_{bm} and A_{bm}, a wave-current boundary layer model must be used to determine the total shear stress u'_{*m} that is felt on the bottom. Notice that this is the maximum shear stress due only to the skin friction. For information on how to calculate the shear stresses based only on skin friction, refer to Madsen (1993) or the Coastal Engineering Manual (CEM) Part III, Chapter 6 (2001). Then the Shields parameter is modified as

$$\psi' = \frac{u'^2_{*m}}{g(s-1)d} \tag{5.10}$$

where the shear velocity is the maximum shear velocity u'_{*m} based on the total skin friction shear stress.

The parameter that dominates the formation of the ripples is the physical distance that the fluid near the bottom moves over a period of oscillation. For pure oscillatory motion, this is simply A_{bm}, the maximum excursion of the orbital motion. When a current is superimposed on the wave oscillations, the excursion amplitude increases when it is in the direction of the current, and becomes

$$A'_{bm} = A_{bm} + u_c \frac{T}{4} = \frac{u_{bm}}{\omega} + u_c \frac{T}{4} \tag{5.11}$$

Where u_c is at the same z elevation as u_{bm}, i.e. at the edge of the wave boundary layer, where δ is defined in Section 2.3.1. The distance moved over the backward motion of the wave period will be decreased proportionally. However, it is the maximum distance traveled in the forward direction over a wave period that is the most important control on the ripple generation. Therefore, when using equations (5.4) and (5.5) to predict η and λ, equation (5.4) should be modified as

$$\frac{\eta}{A'_{bm}} = \frac{\eta}{\frac{u_{bm}}{\omega} + u_c \frac{T}{4}} = 0.27 - 0.33\psi'^{(0.55)} \tag{5.12}$$

Trowbridge and Madsen (1984a, b) (TM) predicted a mass transport, or wave streaming, that moves in the direction opposite that of the wave propagation for long waves over a rough bottom. MM showed that this wave streaming affects the current profile in the presence of waves by effectively offsetting the profile by the magnitude of the wave streaming velocity. It is unclear how this interacts with the formation of bedforms. However, the effect of the wave streaming would be small, at least for the experiments in this study. Typical values of the negative wave streaming for pure waves is shown to be on the order of 1cm/s in Chapter 7. The current velocity near the bottom is on the order of 5cm/s, and the bottom excursion amplitude based only on the bottom velocity (equation (5.8)) is on the order of 5cm. When modifying the bottom excursion amplitude by equation (5.11), the effect of the current $u_c(T/4)$ is on the order of 5cm; it effectively doubles the excursion amplitude. If the wave streaming of 1cm/s does change the current velocity it would change it at most by 20%. This in turn would result in only a 10% difference in the excursion amplitude which, when considering the significant scatter present in the data used to obtain the empirical equations (5.4) and (5.5), makes an insignificant difference to the overall prediction of the ripple geometry. Therefore, in the present analysis, the wave streaming will be neglected in any ripple geometry calculations.

5.3. BEDFORM MEASUREMENT AND CHARACTERIZATION

This section describes the detailed measurements and results for the ripples and mean bed variation for pure wave, pure current, and wave-current flows. As the measurements were performed in that order (PW, PC, WC), the understanding of the response of the bedforms to the flow conditions progressed throughout the course of the measurements, and the measurement methodologies were slightly adapted to obtain more accurate characterization of the bedforms. Therefore, each sub-section here describes in detail the progression of the experiments in time and how the measurements were completed for each case.

5.3.1. PURE WAVE BEDFORMS

The measurement scheme in these experiments begins with a flat sediment bed with initiator ripples at a spacing of 10ft. Waves are then generated and allowed to interact with the bed until a steady state was reached. It was found through measurements that to achieve steady state ripples for pure waves with $T = 2.63$s, $a_{i0} \cong$ 6cm, and $h = 60$cm, approximately 1.5 hours of wave action is required. Also, it was found by observation that the mean bed variation becomes visible after about 4 hours and reaches a steady state after 6 to 8 hours.

For the pure wave case, the bed was allowed to develop from a flat bed for 1.5 hours. The ripples were measured at each of the measuring stations for pure waves a, c, e, g, and i (as shown in Table 3.3), according to the procedure outlined in Section 3.8, and are shown in Table 5.1, under the heading 'pre', referring to pre-pure wave velocity measurements. Then the pure wave velocity measurements were performed (discussed in Chapter 7). These experiments exposed the bed to a total of 12.8 hours of wave action (including the 1.5 hours of initial development time before the pure wave experiments began). To check the steadiness of the bed (and because the mean bed variation had now become visible and steady), the ripple geometry was measured again and is shown in Table 5.1 under the heading 'post' indicating post-pure wave velocity experiments. Note that each point is the mean of the statistics of 22.5cm of bedforms on either side of the x measurement location and for 3 profiles across the flume at that x. The columns η_{mean} and λ_{mean} are the mean of the pre and post measurements, while σ_η and σ_λ are the standard deviations of the entire set of individual measurements that make up each measurement location, including both pre and post measurements. The row labeled mean is the mean of the parameters in the column above it, and the row labeled cycle mean is the mean over one beat cycle, experiments a, c, e, and g, and excluding i. The variability of η and λ between pre and post measurement times is within the accuracy of their measurements, and therefore the assumption that steady state ripple characteristics are reached after 1.5 hours of initial development time is valid.

Table 5.1: Pure wave measured ripple parameters.

Expt ID	x [m]	η [cm] pre	post	η_{mean} [cm]	σ_η [cm]	λ [cm] pre	post	λ_{mean} [cm]	σ_λ [cm]
a	9.80	1.64	1.84	1.74	0.40	10.35	10.97	10.66	1.93
c	10.54	1.76	1.64	1.70	0.31	10.01	9.26	9.64	1.20
e	11.29	1.31	1.41	1.36	0.25	7.79	8.72	8.25	1.47
g	12.03	1.93	1.66	1.80	0.30	10.50	9.74	10.12	2.05
i	12.79	1.95	2.02	1.99	0.60	12.00	11.65	11.82	2.13
			mean	1.72	0.37			10.10	1.76
			cycle mean	1.65	0.31			9.67	1.66

Figure 5.1 (a) and (b) shows the spatial variability of the ripple parameters η_{mean} and λ_{mean} in x. The open circles are the mean values η_{mean} and λ_{mean} in Table 5.1, and the error bars are ± one standard deviation. The lines are predictions of the ripple parameters based on equations (5.4) and (5.5). The solid line with points (·) is based on the bottom first harmonic wave orbital velocity calculated by using the measured wave amplitude. The dotted line with crosses (x) used the measured first harmonic wave orbital velocity just outside the wave boundary layer (typically about 6cm). The predicted wave parameters are shown in Table 5.2. The bottom velocities used for the predictions, both calculated from the wave amplitude (labeled predicted u_{bm}) and measured at the boundary layer height (labeled measured $z = \delta_w$), are also shown. These velocity measurements are discussed more in Chapter 7. Both methods of predictions work quite well and all predicted points fall within one standard deviation of the measurements.

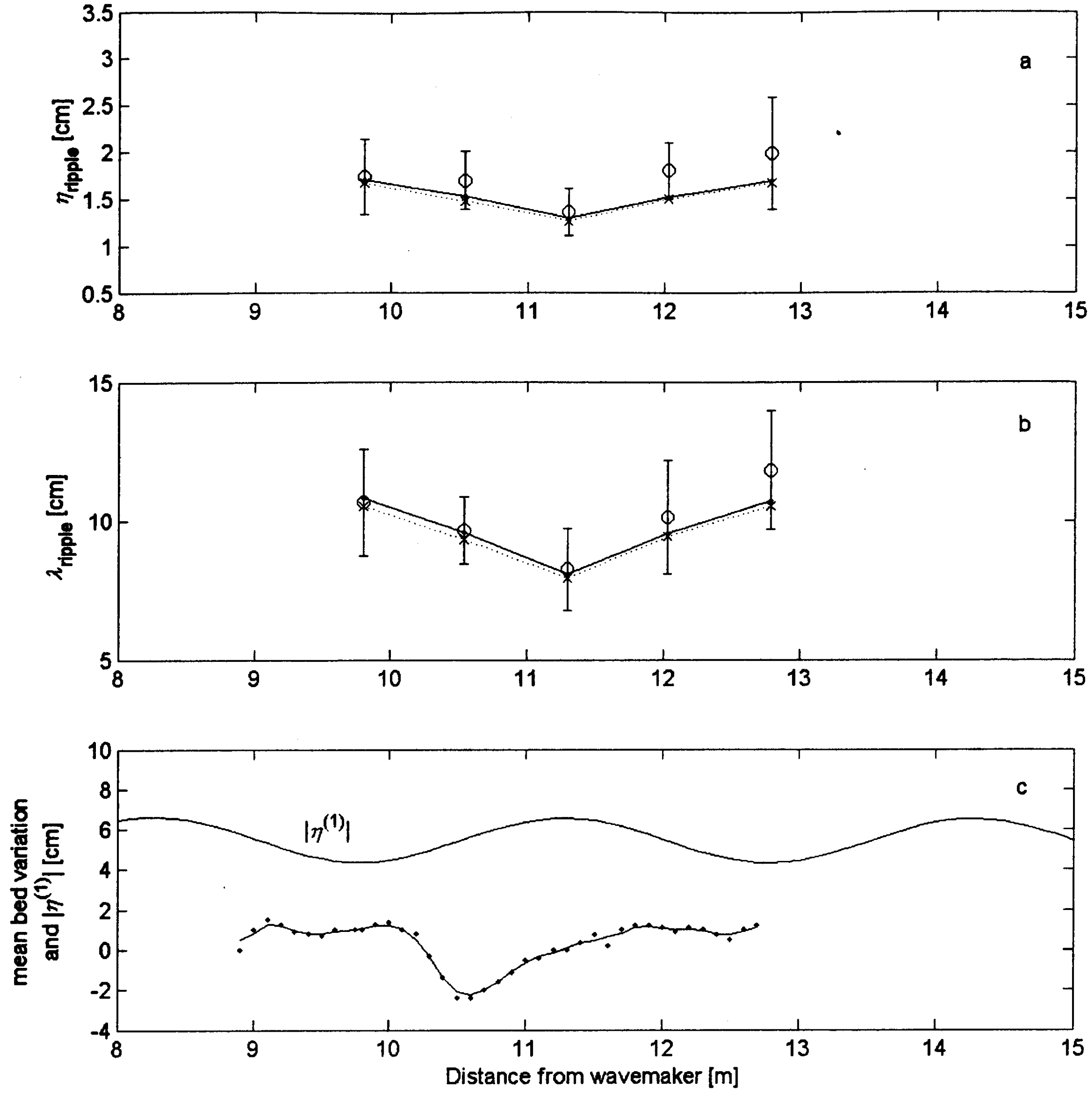

Figure 5.1: Measured and predicted pure wave ripple height (a) and length (b). Open circles are measurements from the ADV, and the error bars represent ± one standard deviation. The solid line with points (·) is a prediction using the measured wave amplitude and the dotted line with crosses (x) is a prediction from measured orbital velocity at $z \cong \delta_w$. (c) shows the first order wave amplitude variation (solid line), and the mean bed elevation (points (·)) after the PW experiments. The solid line through the points is a 3 point moving average of the mean bed elevation.

The measured and predicted ripple parameters in Figure 5.1 (a) and (b) show a trend. Both η and λ decrease, hit a minimum value at $x = 11.29$m, then increase. This trend can be explained with knowledge of the wave conditions. Figure 5.1 (c) shows the absolute first harmonic free surface variation over the test section (solid line labeled $|\eta^{(1)}|$). The pattern is the partially standing wave that is a result of the reflected wave in the tank. At the maximum $\left|\eta^{(1)}\right|$, an antinode, the wave orbital velocities destructively interact and u_{bm} is a minimum. Conversely, at the minimum $\left|\eta^{(1)}\right|$, a node, the wave orbital velocities interact constructively and u_{bm} is a maximum. For the range of velocities present in these experiments, a larger orbital velocity yields a larger ripple (both η and λ). This dependency is clearly demonstrated in the figure – the antinode coincides with the minimum ripple parameters and the nodes with the maximum ripple parameters. This is further supported by the predictions of the ripple parameters which follow this same trend.

Figure 5.1 (c) also shows the mean bed variation. The points (·) are the measurements and the solid line through the points is a three-point moving average of the data. These measurements were made after 12.8 hours of wave interaction with the bed. The pattern of the mean bed suggests some dependency on the partially standing wave, although its dependency is neither clear nor well defined.

Table 5.2: Pure wave predicted and measured ripple parameters.

Expt ID	predicted u_{bm} [cm/s]	measured $(z=\delta_w)$ u_{bm} [cm/s]	from predicted u_{bm} η [cm]	λ [cm]	from measured u_{bm} at $(z=\delta_w)$ η [cm]	λ [cm]	η_{mean} [cm]	λ_{mean} [cm]
a	23.20	22.16	1.71	10.81	1.67	10.53	1.74	10.66
b	19.02	18.19	1.53	9.59	1.48	9.32	1.70	9.64
c	14.83	14.43	1.29	8.08	1.26	7.92	1.36	8.25
d	18.85	18.52	1.52	9.54	1.50	9.43	1.80	10.12
e	22.87	22.17	1.70	10.72	1.67	10.54	1.99	11.82
		mean	1.55	9.75	1.52	9.55	1.72	10.10
		cycle mean	1.51	9.50	1.48	9.30	1.65	9.67

5.3.2. PURE CURRENT BEDFORMS

One of the objectives of this study is to determine if the hydrodynamic roughness experienced by waves is the same as that experienced by a current flowing over the same wave-generated bedforms. So in preparing the bed for the pure current experiments, one should simply run the current over the bedforms developed in the pure wave experiments. However, as explained in the previous section, after the 12.8 hours of pure wave action on the bed the mean bed elevation varies. These variations could cause the current flow to accelerate and decelerate, making the current flow non uniform. So before the pure current tests, the bed was smoothed and subjected to 1.5 hours of pure wave action. This is long enough to form steady state ripples but short enough so that no measurable variation in the mean bed has yet occurred. Then the bed is subjected to a steady current of u_c = 16cm/s.

It is important to note that the 16cm/s current on its own is not enough to initiate motion of the sediment – if the bed is initially flat, it remains flat except for extremely small (millimeter scale) perturbations near the boundary irregularities such as the joints in the glass walls. When the bed is rippled, the current initially shaves a small bit of the sharp crest off the ripple and moves it in the direction of the flow, making the ripples slightly asymmetric. This asymmetry was not measurable by the ADV bottom profiler and therefore, the time to achieve steady state ripples was difficult to judge. As there was no noticeable change in the ripples after about 1.5 hours of exposure to currents, it was assumed that this was sufficient time for current modification of the wave-formed ripples.

The measurement scheme for pure currents was modified part way through the experiments, and deserves some detailed explanation. The original methodology was to follow that of the PW measurements: measure the ripple geometry, perform the experiment, and measure the geometry again with all measurements occurring at the locations listed in Table 3.3, experiment locations a, c, e, g, and i. Because the ripple geometry of the PW experiments is assumed to be steady state, and because the ripple geometry did not change after being exposed to 1.5 hours of current, it was thought that the PW bedforms would be the same as the initial PC bedforms, and therefore no record of the PC ripples was taken before the measurements began.

After this time, the PC bedform measurements made can be divided into 3 sections. 1) The first set of PC velocity measurements were performed, exposing the bedforms to a total of 12 hours of current. These measurements were taken at experiment locations a, c, e, g, and i. After the velocity measurements were taken, the bedform geometry was measured at the same locations. When the velocity profiles were analyzed, it was found that more detail and more points were necessary to better explain the current hydrodynamics. The next set of measurements, section 2), measured velocity profiles over the next beat length at locations k, m, o and q, and exposed the bed to a current for a cumulative total of 38 hours. Bedform geometry measurements were then taken after the current velocity measurements. The measurements from both sections 1) and 2) (12 hours at a, c, e, g, and i , and 38 hours at k, m, o and q) are shown in Table 5.3 under the heading 'pre'. Footnotes distinguish the values experiencing 12 hours from those experiencing 38 hours. Finally, the last section 3) measurements were made of the PC velocity, where measurements were made at all experiment locations a-q. This now exposed the bed to a cumulative total of 80 hours of current. After these final velocity measurements, the bedform geometries were again measured. These measurements are shown in Table 5.3 under the heading 'post'.

Table 5.3: Parameters of pure wave formed ripples modified by pure current flow.

Expt	x	η [cm]		η_{mean}	$\sigma_{\eta}{}^{2}$	λ [cm]		$\lambda_{mean}{}^{1}$	$\sigma_{\lambda}{}^{2}$
ID	[m]	pre	post^{5}	[cm]	[cm]	pre	post^{5}	[cm]	[cm]
a	9.80	2.02^{3}	1.51	1.77^{1}	0.22	12.72^{3}	11.28	12.00	1.37
b	10.34		1.32	1.32	0.36		9.91	9.91	1.83
c	10.54	1.65^{3}	1.32	1.49^{1}	0.28	11.06^{3}	11.07	11.06	2.70
d	10.84		1.04	1.04	0.19		9.88	9.88	2.33
e	11.29	1.12^{3}	0.92	1.02^{1}	0.22	9.39^{3}	9.36	9.37	2.64
f	11.81		1.01	1.01	0.20		9.23	9.23	0.87
g	12.03	1.18^{3}	0.92	1.05^{1}	0.22	9.60^{3}	9.48	9.54	1.80
h	12.33		1.27	1.27	0.33		10.50	10.50	2.11
i	12.79	2.00^{3}	1.71	1.86^{1}	0.48	11.83^{3}	11.97	11.90	1.05
j	13.34		1.26	1.26	0.23		10.28	10.28	0.91
k	13.58	1.14^{4}	1.09	1.12	0.49	9.67^{4}	8.29	8.98	1.07
l	13.83		1.01	1.01	0.23		8.63	8.63	0.96
m	14.31	0.80^{4}	0.84	0.82	0.15	8.08^{4}	8.00	8.04	1.15
n	14.84		0.88	0.88	0.24		9.40	9.40	1.56
o	15.10	0.71^{4}	0.79	0.75	0.23	7.58^{4}	8.80	8.19	2.70
p	15.35		1.10	1.10	0.36		9.39	9.39	3.16
q	15.82	1.33^{4}	1.16	1.24	0.41	10.85^{4}	10.47	10.66	2.27
		mean	1.13	1.07	0.28		9.76	9.82	1.79
		cycle mean	1.13	1.05	0.28		9.72	9.77	1.76

[1] - These values are not correct, as explained later in the section, and are only included here for completeness. Only the post-run measurements are correct here.

[2] – These values represent the standard deviation of only the pure current 'post' measurements.

[3] – these values have been exposed to 12 hours of current

[4] – these values have been exposed to 38 hours of current

[5] – these values have been exposed to 80 hours of current

All these ripple parameter measurements are shown in relation to their location along the flume in Figure 5.2, where (a) shows η_{pre} and η_{post}, and (b) shows λ_{pre} and λ_{post}. The open squares are the 'pre' measurements and the solid triangles are the 'post' measurements. The error bars show ± one standard deviation.

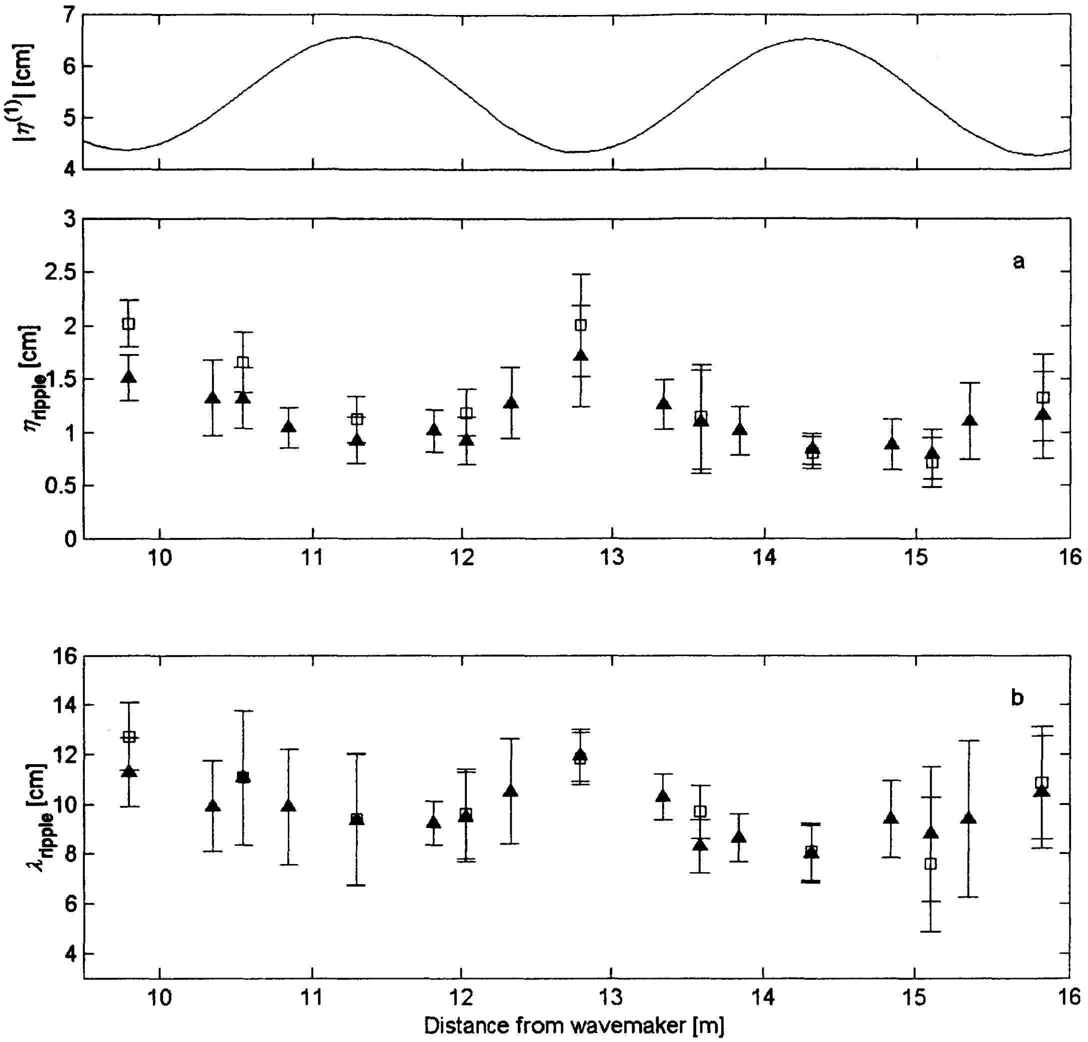

Figure 5.2: Wave formed ripples modified by pure current flow. Open squares are the 'pre' measurements and the solid triangles are the 'post' measurements. The error bars represent ± one standard deviation. The variation of the 1st harmonic free surface is shown above (a) for reference.

From this figure, we are able to gather some understanding of the development and the spatial variation of the ripples. The same basic variation of a large and small ripples relative to the nodes and antinodes of the standing wave are present here. This is due to the fact that the ripples were initially pure wave generated ripples; the action of the current was not able to remove this shape. The shape of the PW partially standing wave is shown above (a) on separate axes. Here, two beat lengths have been measured, as the three maxima and two minima can be seen in the figure.

The progression of the development of the ripples can be explained if the chronology of the measurements is considered. The 'pre' points on the first beat length (x = 9.8 to 12.79m) were measured after 12 hours of exposure to the current. The 'pre' points on the second beat length (x = 13.58 to 15.82m) were measured after 38 hours of current exposure. Finally, the 'post' points over both beat lengths have been exposed to 80 hours of current. Comparing the 'pre' and 'post' points over the first beat, the 'pre' points are larger than the 'post'. But over the second beat where the 'pre' points have had more development time (38 hours); they are nearly identical to the 'post' points. It can be assumed with some confidence that the 'post' points with 80 hours of current exposure are in their steady state. This is further supported by the fact that the 'pre' ripples with 38 hours have the same value. Therefore, the 'pre' points with only 12 hours are not in their steady state, and the steady state must have been reached sometime between 12 and 38 hours of current exposure.

5.3.3. WAVE-CURRENT BEDFORMS

Another objective of this study is to determine if the hydrodynamic roughness experienced by combined wave-current flows can be expressed the same way as that experienced by a current or a wave with similar characteristics as the individual components of the wave-current flow while flowing over the bedforms generated by the wave-current flow. To prepare the bed for the wave-current experiments, the bed was smoothed, initiator ripples drawn, and the wave-current flow was allowed to interact with the bed until an approximate steady state could form. It appeared to be steady after about 7 hours, but was allowed to develop for a total of 13.4 hours.

After the experiences with bedforms changing during the pure current experiments even though they were believed to be in steady state, a different approach to the ripple geometry measurement was taken for the wave-current case. If the bedforms are going to change over the course of the hydrodynamic measurements, it was thought that one could obtain a more accurate estimate of the roughness experienced by the flow at a particular location if the bedform parameters were measured just before and just after the velocity profile was measured at that location. Then the bedform parameters experienced by the flow over the measurement of the velocity profile could be better approximated by taking the average of the measured ripple parameters before and after the velocity profile. Rather than having on the order of 10 hours separating bedform measurements, by using this method only 2 hours would separate the measurements, as that is the time it takes to measure a wave-current velocity profile.

Table 5.4 shows the measured ripple parameters. The column labeled 'pre' are the parameters measured just before each profile, and the column labeled 'post' the parameters measured just after each profile. The columns η_{mean} and λ_{mean} are the mean of the 'pre' and 'post' measurements, while σ_η and σ_λ are the standard deviations of all measurements at each location.

Figure 5.3 (a) and (b) show the measured ripple parameters η_{mean} and λ_{mean}, respectively, as they vary along the flume. The open diamonds are the measurements, and the error bars show ± one standard deviation of the parameters. Ripple geometry predictions are also shown on Figure 5.3. Predicting the ripple geometry for wave-current flows requires special considerations. As no direct method has been formulated, we extend the method presented in Section 5.2 here. Four estimates of the ripple parameters were made, two were by using the measured wave amplitude

Table 5.4: Wave-current ripple parameters.

Expt	x	η [cm]		η_{mean}	σ_{η}	λ [cm]		λ_{mean}	σ_{λ}
ID	[m]	pre	post	[cm]	[cm]	pre	post	[cm]	[cm]
A	8.42	1.56	1.85	1.71	0.41	11.24	12.08	11.66	1.83
B	8.93	1.71	1.84	1.78	0.48	11.06	12.18	11.62	2.27
C	9.18	2.04	1.90	1.97	0.47	12.94	12.86	12.90	2.34
D	9.41	2.45	1.91	2.27	0.65	15.74	12.96	14.19	4.05
E	9.93	2.83	2.52	2.67	0.43	19.33	15.49	17.41	4.04
F	10.45	1.44	1.45	1.45	0.42	11.28	12.88	12.08	3.85
G	10.68	1.29	1.24	1.26	0.26	10.08	10.19	10.14	2.66
H	10.95	1.07	1.34	1.20	0.29	9.01	10.47	9.74	3.02
I	11.42	1.40	1.58	1.49	0.43	9.63	9.96	9.79	2.78
J	11.90	1.41	1.70	1.55	0.32	10.29	11.31	10.80	1.76
K	12.15	1.78	1.92	1.85	0.37	11.64	12.06	11.85	1.51
L	12.40	2.21	2.02	2.11	0.65	15.74	14.57	15.15	3.96
M	12.92	2.24	2.11	2.17	0.73	15.25	15.61	15.43	4.66
N	13.43	2.01	1.66	1.84	0.60	14.59	12.00	13.30	2.76
O	13.73	1.26	1.20	1.23	0.30	10.40	8.44	9.42	3.32
P	13.95	1.01	1.13	1.07	0.26	7.52	9.05	8.28	2.25
Q	14.43	1.07	1.05	1.06	0.27	7.72	7.15	7.44	1.06
mean		1.69	1.67	1.69	0.43	11.97	11.72	11.83	2.83
cycle mean		1.73	1.71	1.73	0.44	12.23	12.01	12.11	2.94

and calculating the bottom velocity from linear wave theory, and the other two were by using the actual measured bottom velocity at the top of the wave-current boundary layer (more information on the wave-current velocity measurements is presented in Chapter 9). Traditional school of thought would suggest that very near the bottom, the wave completely dominates the flow, as the bottom velocity of the wave is on the order of 20cm/s, while the velocity of the current near the bottom is between 5 and 10cm/s. Then the formation of the ripples would only depend on the wave characteristics near the bed. Following this thinking, predictions of the bedforms are made by directly applying equations (5.4) and (5.5). On Figure 5.3 (a) and (b), the dotted lines are the predictions of the bedform geometry neglecting the current. The dotted line with points (·) is based on the calculation of u_{bm} from measured wave amplitude, and the dotted line with crosses (x) is based on the values of u_{bm} measured at the wave-current boundary layer. While these predictions approximately follow the same trend as the ripple geometry, on the average the predictions are low.

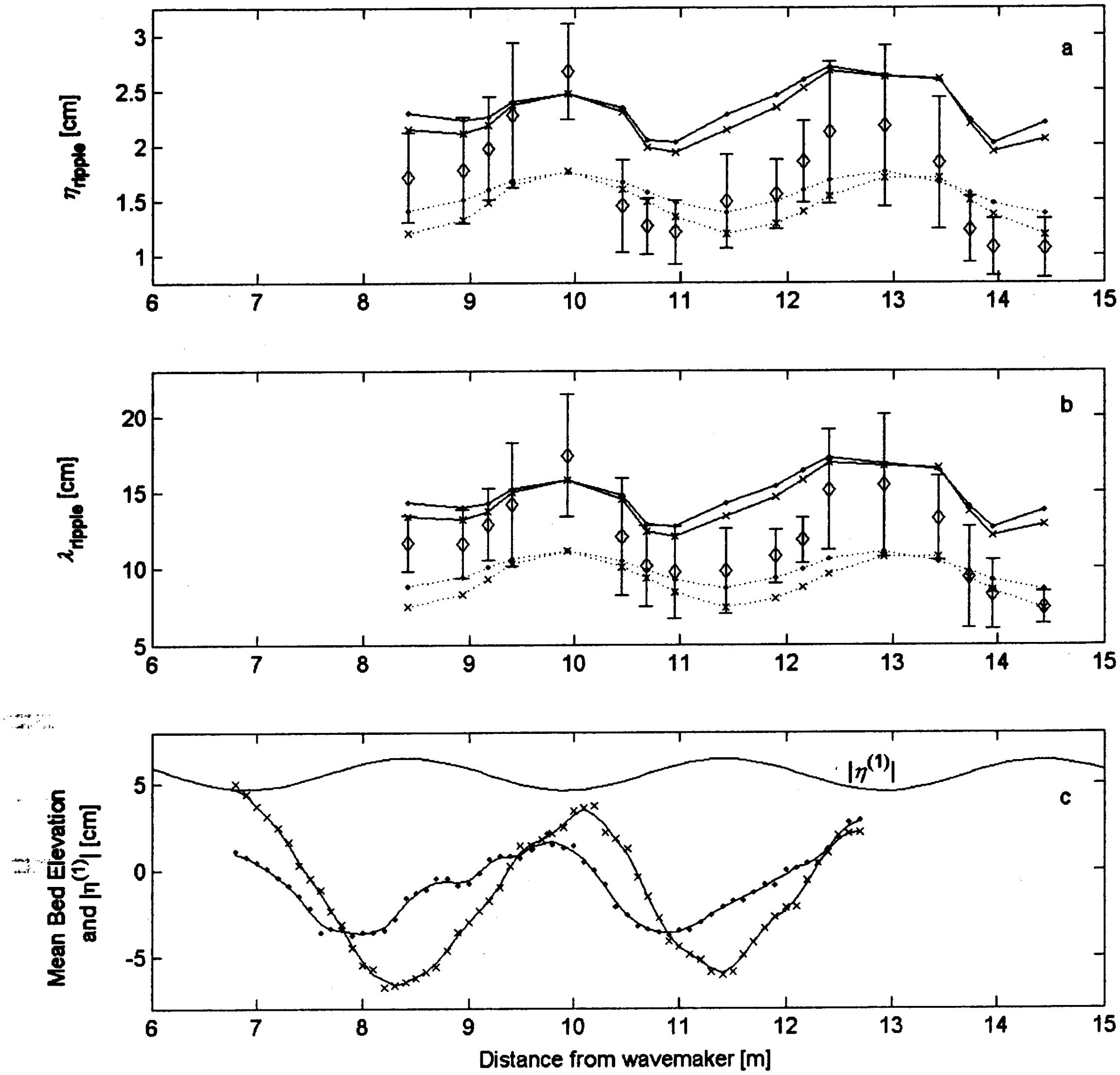

Figure 5.3: Measured and predicted wave-current ripple height (a) and length (b). Open diamonds are measurements and the error bars represent ± one standard deviation. The dotted lines are predictions neglecting the current interaction, and the solid lines are predictions accounting for the current. The lines with points (·) use a prediction of u_{bm} from measured wave amplitude and the lines with crosses (x) use u_{bm} from the measured velocity at $z = \delta_w$. (c) shows the first order wave amplitude variation (solid line), and the mean bed elevation before (points (·)), and after (crosses (x)) the WC experiments. The line through the points and the line through the crosses are 3 point moving averages.

In an attempt to better predict the geometry, the current is accounted for. To account for the current, the Shields parameter is modified as in equation (5.10). u'_{*m} is calculated from the GMm model applied to only account for skin friction. More information on this can be found in

Madsen (1993) or the CEM Part III, Chapter 6 (2001). Then, when applying the empirical equations to predict η and λ, the excursion amplitude is modified by equation (5.11). The current velocity used in this modification should be picked at the height of the wave-current boundary layer. For these measurements, the wave-current boundary layer was located at between 4 and 7cm, but with an average value of 5cm, which also coincides with one of the vertical measuring locations. So the current to be used in (5.11) and (5.12) was selected at this elevation from the measurements. The predictions resulting from accounting for the current are shown on Figure 5.3 (a) and (b) as the two solid lines. The solid line with points (·) is from using u_{bm} predicted from the wave amplitude, and the solid line with crosses (x) is based on the values of u_{bm} measured at the wave-current boundary layer. The predictions with the current accounted for follow the trend of the measured geometry much more closely than that neglecting the current. However, the magnitudes of the geometry are in general over-predicted. At worst, the methods presented here for predicting the ripple geometry for wave current flows give reasonable estimates for the upper and lower bounds of the actual geometry measurements.

Table 5.5 shows the values of the predicted ripple heights and lengths for the four methods discussed, as well as u_{bm} from measured wave amplitude (labeled predicted from $a^{(1)}$), u_{bm} from measured 1st harmonic velocity (labeled measured at $z=\delta_w$), and the current velocity at z=5cm off the bottom used to modify the bottom excursion amplitude. The row labeled mean is the mean of all values in the column, experiment A-Q, and the row labeled cycle mean is the mean of the values across 2 beat lengths, experiments A-P.

In general, both η and λ follow the same trend seen in the pure wave and pure current bedforms. The ripple parameters are maximum at the partially standing wave nodes and minimum at the antinodes. Figure 5.3 (c) shows the $|\eta^{(1)}|$ over the measurement locations as a solid line labeled $|\eta^{(1)}|$. Notice that the variability of the measurements increases as the parameter magnitudes increase. This reflects the observation that the ripples were much more organized and uniform at the antinodes where the velocity is smaller, and more random and three-dimensional at the nodes where the velocity is larger.

Figure 5.3 (c) also shows the mean bed variation before and after the full WC experiments. The profile before (line with points($\cdot$)) has been subjected to 13.4 hours wave wave-current action, while the profile after (line with crosses (x)) has felt 33.5 hours of wave-current action. The measurement of the mean bed variation was physically limited to x = 12.8m from the wavemaker, and could not be measured over the entire second beat length where the WC velocity and bedform measurement were made. It is apparent that the mean bed was not fully developed at 13.4 hours, as it had changed significantly by 33.5 hours. The length of the mean bed variation appears to be related to the length of the partially standing wave, although its relative phase is different. Further evidence presented in Chapter 7 for the pure wave motion suggests that this mean bed variation is similar to bars that form under a standing wave. However, the shifting phase suggests some effect from net sediment drift, especially in the wave-current case. These bars are probably a result of the combination of these two effects. Unfortunately, insufficient evidence has been found to quantitatively explain their characteristics and behavior.

Table 5.5: Wave-current predicted and measured ripple parameters.

Expt ID	predicted from $a^{(1)}$ u_{bm} [cm/s]	measured @ $z=\delta_w$ u_{bm} [cm/s]	measured (z=5cm) u_c [cm/s]	from predicted u_{bm}, $u_c=0$ η [cm]	λ [cm]	from measured u_{bm}, $u_c=0$ η [cm]	λ [cm]	from predicted u_{bm}, $u_c\neq0$ η [cm]	λ [cm]	from measured u_{bm}, $u_c\neq0$ η [cm]	λ [cm]
A	16.58	13.27	6.92	1.41	8.81	1.19	7.48	2.29	14.35	2.14	13.40
B	18.35	15.18	6.39	1.51	9.45	1.32	8.27	2.22	13.99	2.10	13.18
C	20.19	17.80	6.62	1.60	10.05	1.48	9.26	2.25	14.24	2.18	13.74
D	22.04	20.89	7.49	1.68	10.60	1.63	10.27	2.39	15.19	2.37	15.00
E	23.99	24.06	8.48	1.76	11.13	1.76	11.14	2.46	15.79	2.46	15.79
F	21.53	20.25	6.45	1.66	10.46	1.60	10.07	2.34	14.78	2.30	14.53
G	19.6	18.00	4.04	1.57	9.87	1.49	9.33	2.04	12.86	1.98	12.43
H	17.76	15.63	4.43	1.47	9.24	1.35	8.45	2.03	12.72	1.93	12.09
I	16.21	13.18	7.15	1.38	8.67	1.19	7.44	2.27	14.24	2.14	13.38
J	18.03	14.61	8.76	1.49	9.34	1.28	8.04	2.45	15.42	2.34	14.67
K	19.88	16.40	10.16	1.58	9.95	1.40	8.75	2.59	16.39	2.51	15.82
L	21.98	18.79	11.29	1.68	10.59	1.53	9.60	2.71	17.29	2.67	16.93
M	23.89	22.56	10.30	1.75	11.10	1.70	10.75	2.63	16.85	2.62	16.73
N	21.37	22.51	9.90	1.65	10.41	1.70	10.74	2.58	16.43	2.60	16.56
O	19.4	18.13	5.87	1.56	9.80	1.49	9.37	2.23	14.05	2.19	13.75
P	17.6	15.90	4.35	1.46	9.19	1.37	8.55	2.01	12.64	1.94	12.13
Q	16.08	13.01	6.31	1.38	8.62	1.18	7.36	2.20	13.78	2.05	12.84
		mean	7.41	1.58	9.92	1.47	9.22	2.34	14.83	2.28	14.38
		cycle mean	7.35	1.56	9.84	1.45	9.11	2.33	14.76	2.27	14.29

6. BOTTOM ROUGHNESS FROM WAVE ATTENUATION

As waves propagate over a rough bottom, some of the wave energy is used in overcoming the resistance of the bottom. The dissipation of wave energy in the bottom boundary layer results in a decrease of the wave height. This wave height decrease can be measured and related to the bed friction felt by the wave, and the friction can then be related to the hydrodynamic bottom roughness through a wave-current-bottom interaction theory.

To measure the bottom roughness felt by pure waves and waves in the presence of a current, wave attenuation experiments were performed. This section describes the theory of wave attenuation and energy dissipation, the procedure for measuring the wave attenuation, and how the bottom roughness is derived from the wave attenuation measurements. Also, the results from the measurements are presented. Then, the bottom roughness from wave attenuation is compared to the actual measured bedform geometry.

6.1. ATTENUATION MEASUREMENT PROCEDURE

The wave attenuation measurement procedures are described in detail in Rosengaus (1987) and Mathisen (1993). The basic procedure used in these experiments is briefly discussed here.

The procedure for measuring wave attenuation starts by measuring the variation of the first harmonic wave amplitude along the length of the sand test section. Because the actual change in wave height is small (on the order of millimeters), the larger the distance one can measure over the better, as the change in wave height will be larger – it is easier to measure a larger change in wave height. Therefore, the wave height was measured over the entire length of the sand bed at a spacing of 50cm. This resulted in 33 points along the flume for wave height measurements. A typical first harmonic free surface variation can be seen in Figure 6.1 (a).

The measurements can then be used to fit equation (4.14) by using a least squares linear regression algorithm (described in Rosengaus (1987)). As the phase, $\delta\phi = \phi_r - \phi_i$, is unknown and not determined by the least squares algorithm, its value is varied until the standard error of the fit was minimized, where the standard error ε_{fit} is given by

$$\varepsilon_{fit} = \left[\frac{\sum_{i=1}^{n} \left(\eta_{i,measured} - \eta_{i,fit} \right)^2}{n-2} \right]^{\frac{1}{2}} \tag{6.1}$$

where n is the number of points measured. By fitting equation (4.14), values for the wave characteristics a_i, a_r, and m_t are determined. The values a_i and m_t are not sensitive to $\delta\phi$. However, a_r is extremely sensitive to $\delta\phi$, and can vary ±100% as $\delta\phi$ is varied from 0 to 2π.

6.2. ESTIMATING BOTTOM ROUGHNESS FROM ATTENUATION EXPERIMENTS

Following the formulation of Christoffersen and Jonsson (1985), an energy conservation equation for a combined wave-current flow can be developed by using a wave energy conservation equation

$$\frac{\partial}{\partial x}\left[\frac{E}{\omega - kU} \left(\overline{u_c} + C_{gr} \right) \right] + \frac{E_d - \overline{\tau_w(t) u_c}}{\omega_r} = 0 \tag{6.2}$$

where E is the wave energy per unit area, $\omega\text{-}k\overline{u}_c$ is the radian frequency relative to the mean current, $E/(\omega\text{-}k\overline{u}_c)$ is the wave action, $\overline{u}_c$ is the depth-averaged current velocity, τ_w is the bottom shear stress due to the wave motion, E_d is the energy dissipation due to bottom friction, and C_{gr} is the wave group velocity relative to the mean current. C_{gr} is defined as

$$C_{gr} = \frac{1}{2}\left(\frac{\omega - k\overline{u}_c \cos\phi_{wc}}{k}\right)\left[1 + \frac{2kh}{\sinh(2kh)}\right] \tag{6.3}$$

where ϕ_w is the angle between the wave and current directions, and k is from the dispersion relation

$$(\omega - k\overline{u}_c \cos\phi_{wc})^2 = gk\tanh(kh) \tag{6.4}$$

By following the analysis of Kajiura (1968), Christofferson and Jonsson (1985) showed that, after defining the energy in terms of wave energy, equation (6.2) can be modified to a one-dimensional conservation equation of wave energy, and can be written

$$\frac{\partial}{\partial x}\left[\frac{1}{2}\rho g a^2 C_g\right] = \rho g a_m m_b C_g = E_{dis} = -\frac{1}{4}\rho f_e u_{bm}^3 \tag{6.5}$$

where g is the acceleration due to gravity, m_b is the wave attenuation slope, a_m is the mean wave amplitude over the length of the section used to determine m_b, and f_e is the energy friction factor. Note that C_g here is from equation (6.3) with $\overline{u}_c = 0$. f_e can be related to the wave friction factor f_w through a turbulent phase angle where

$$f_e = f_w \cos\phi_\tau \tag{6.6}$$

As discussed in Section 2.2.4, the wave friction factor can then be related to the bottom roughness through a wave-current-bottom interaction theory. Approximations to the relationship are given by equations (2.35) and (2.36).

The following is the procedure used to obtain an estimate of k_w or k_{wc} from wave attenuation measurements.

1) From attenuation experiments and fitting equation (4.14), obtain a_i, and m_t, ω and $\bar{u}_c$ are known from knowledge of the experimental conditions.

2) Since the wave amplitude changes (decreases) along the flume, use the average amplitude at the sediment bed test section midpoint a_m (midpoint of the sand bed, x_m = 11.3m)

$$a_m = a_i + x_m m_{tot} \tag{6.7}$$

3) Not all energy dissipation is due to the bottom. The fluid is also moving along the flume's glass walls. The sidewall dissipation m_{sw} is calculated based on Hunt's (1952) laminar dissipation theory for smooth wave flume sidewalls:

$$m_{sw} = -\sqrt{\frac{\nu}{2\omega}}\frac{a_m\omega}{bC_g} \tag{6.8}$$

where b = 76.5 cm is the width of the flume and ν is the fluid kinematic viscosity. For most of the experiments, this was taken as the value when the fluid temperature = 15°C, or $\nu = 1.156{*}10^{-6}$ m^2/s. Then the attenuation slope due to the bottom only m_b can be found by taking the difference of the total attenuation slope m_t and the sidewall attenuation slope m_{sw},

$$m_{tot} = m_b + m_{sw} \tag{6.9}$$

4) Determine the energy dissipation from equation (6.5), solving for f_e

$$f_e = \frac{4 g a_m m_b C_g}{u_{bm}^3} \tag{6.10}$$

where

$$u_{bm} = \frac{a_m \omega}{\sinh(kh)} \tag{6.11}$$

5) Then calculate the wave friction factor f_w using a first estimate of $\phi_\tau = 25°$.

$$f_e = f_w \cos\phi_\tau \tag{6.12}$$

6) the roughness k_n can then be, for a first approximation, determined from

$$f_w = C_\mu \exp\left[7.02\left(\frac{C_\mu A_{bm}}{k_n}\right)^{-0.078} - 8.82\right] \tag{6.13}$$

or solving for k_n

$$k_n = k_w, k_{wc} = C_\mu A_{bm}\left[\frac{7.02}{8.82 + \ln\left(f_w / C_\mu\right)}\right]^{\frac{-1}{0.078}} \tag{6.14}$$

7) then the turbulent phase angle can be approximated

$$\phi_\tau = 33 - 6.0\log_{10}\left(\frac{C_\mu A_{bm}}{k_n}\right) \tag{6.15}$$

8) Finally, iterate steps 5-7 until ϕ_τ is accurate to within about 3 decimal places.

This procedure applies to both pure wave and wave-current flows. For wave-current flows, the current shear velocity u_{*c} must be know a priori in order to estimate C_μ.

6.3. WAVE ATTENUATION RESULTS

6.3.1. PURE WAVE ROUGHNESS FROM ATTENUATION

Pure wave attenuation results were determined from the measurements shown in Figure 6.1. (a) shows the variation of the 1st harmonic and (b), the 2nd harmonic. Points (·) are the measurements before the pure wave velocity experiments and crosses (x) are points after. The solid lines are the fits of equation (4.14) or (4.20) to the pre-measurements, and the dashed lines are the fits after the pure wave velocity measurements. The attenuation slopes for the pre (dotted) and post (dash-dotted) measurements are also shown in (a).

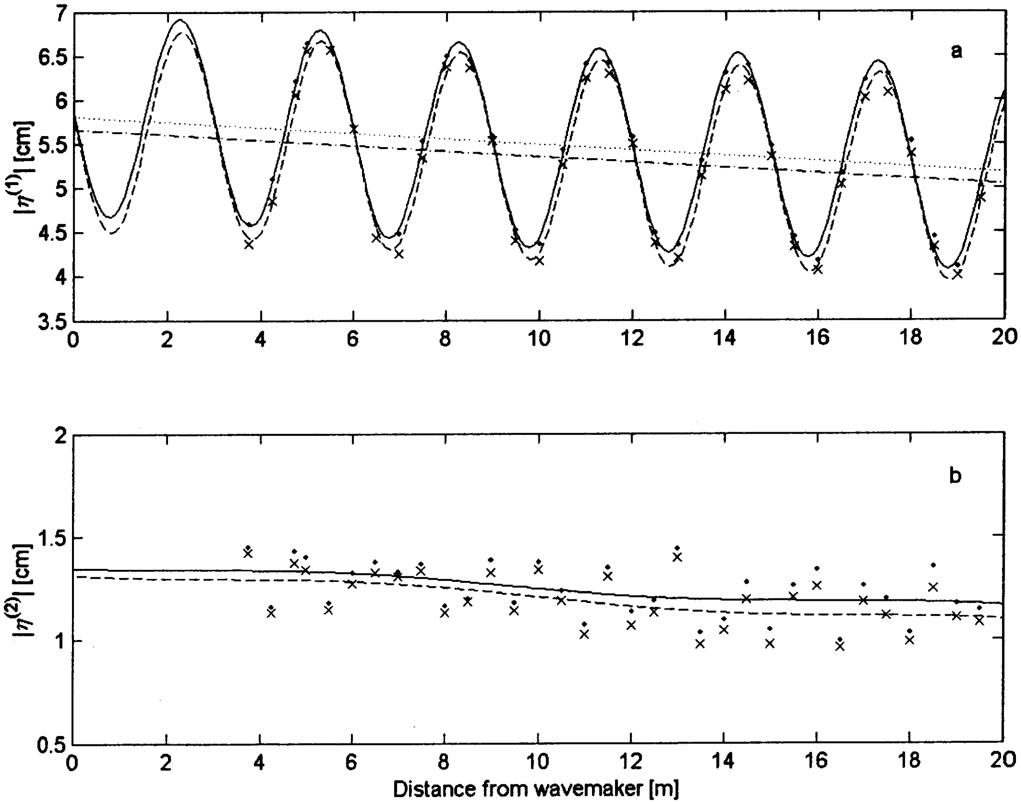

Figure 6.1: Pure wave variation of 1st (a) and 2nd (b) harmonic along the length of the flume as measured for attenuation experiments. Points (·) are the measurements before pure wave velocity measurements, and crosses (x) are measurements after pure wave velocity measurements. The solid line is the fit to the points based on equations (4.14) or (4.20). In (a), the dotted line is the attenuation slope previous to the velocity measurements, and dash-dot line is the attenuation slope after the velocity measurements.

The results of these fits are shown in Table 6.1. The table also shows the values of f_w and k_w determined for the pure wave case. The overall magnitudes of the 1st and 2nd harmonic amplitudes decrease slightly between the pre and post cases. However, the differences are quite small and the wave characteristics are more or less unchanged.

Table 6.1: Attenuation results for pure wave and wave-current experiments.

Parameter		Pure Wave		Wave-Current	
		pre	post	pre	post
T	[s]	2.63	2.63	2.63	2.63
a_{i0}	[cm]	5.81	5.66	5.70	5.83
a_r	[cm]	1.14	1.16	0.92	1.24
m_t	[cm/cm]	-3.1550E-04	-3.1080E-04	-2.6000E-04	-2.6452E-04
m_b	[cm/cm]	-2.7426E-04	-2.7061E-04	-2.1999E-04	-2.2362E-04
u_{bm}	[cm/s]	19.44	18.95	19.6	20.1
A_{bm}	[cm]	7.39	7.21	7.45	7.62
u_{*c}	[cm/s]	--	--	2.45	2.45
u_{*wm}	[cm/s]	7.11	7.10	6.06	6.09
f_e		0.16	0.17	0.13	0.13
f_w		0.27	0.28	0.19	0.18
$\{k_w, k_{cw}\}$	[cm]	10.96	11.51	6.11	5.92

6.3.2. WAVE-CURRENT ROUGHNESS FROM ATTENUATION

Wave-current attenuation results were determined from the measurements shown in Figure 6.2. (a) shows the variation of the 1st harmonic and (b), the 2nd harmonic. Points (·) are the measurements before the wave-current velocity experiments and crosses (x) are points after. The solid lines are the fits of equations (4.14) or (4.20) to the pre-measurements, and the dashed lines are the fits after the velocity measurements. The attenuation slopes for the pre (dotted) and post (dash-dotted) measurements are also shown in (a). The measured free surface for the pre and post cases differs significantly from about $x = 4$m to $x = 9.5$m from the wavemaker. This is from the modification of the mean bed elevation between the pre and post measurements – the mean bed has increased in amplitude from about 5-6cm to about 10cm, as shown in Figure 5.3 (c). These large variation are quite similar to long bars on a beach which reflect some of the wave energy back in the opposite direction of wave propagation. As the waves progress over the bed, waves are reflected back along the entire length of the bed and linearly add to the reflected wave height propagating towards the wavemaker. This increases the reflected wave height linearly in the direction from the beach to the wavemaker. One could reformulate a_r in equation (4.14) to account for this interaction as

$$a_r = a_{r0} - m_r x \tag{6.16}$$

where m_r would be the added wave amplitude resulting from the waves reflected off the bottom bars. However, in this analysis, this enhanced a_r effect is neglected, and the fit of the free surface of the post measurements shown on Figure 6.2 (a) has been fit using only points from 9.5m to 19.5m (neglecting the first 12 points). The resulting free surface matches that of the pre measurements quite well.

The results of these fits are shown in Table 6.1 along with the results from the pure wave attenuation. The table also shows the determination of f_e, f_{wc}, and k_{wc} for the pure wave and wave-current case. While the measurements show a large difference in magnitude between pre and post wave-current cases, the values obtained from the fit of the free surface profile, and therefore the resulting values of f_{wc} and k_{wc} are surprisingly similar.

Table 6.1 shows that there is a large difference between the predicted roughness values for the pure wave and wave-current cases. Table 6.2 compares these values with the measured bedform geometries for the respective cases. The bedform scaling factors α and β for the pure wave case are more than 50% larger than those for the wave-current case. However, Madsen (1993) showed that the values α and β are only accurate to within a factor of two of their suggested values (about 4 for α and about 24 for β). Considering this range of values, the roughness for pure wave is the same as that for waves in the presence of currents.

Table 6.2: Wave and wave-current roughness compared to measured ripple geometry.

		pure wave			wave-current		
		pre	post	mean	pre	post	mean
$\{k_w, k_{wc}\}$	[cm]	10.96	11.51	11.23	6.11	5.92	6.02
				cycle mean			cycle mean
η	[cm]	1.66	1.64	1.65	1.73	1.71	1.73
λ	[cm]	9.66	9.67	9.67	12.23	12.01	12.11
$\alpha=\{k_w, k_{wc}\}/\eta$		6.59	7.03	**6.81**	3.53	3.46	**3.48**
$\beta=\{k_w, k_{wc}\}/[\eta(\eta/\lambda)]$		38.33	41.53	**39.91**	24.95	24.29	**24.44**

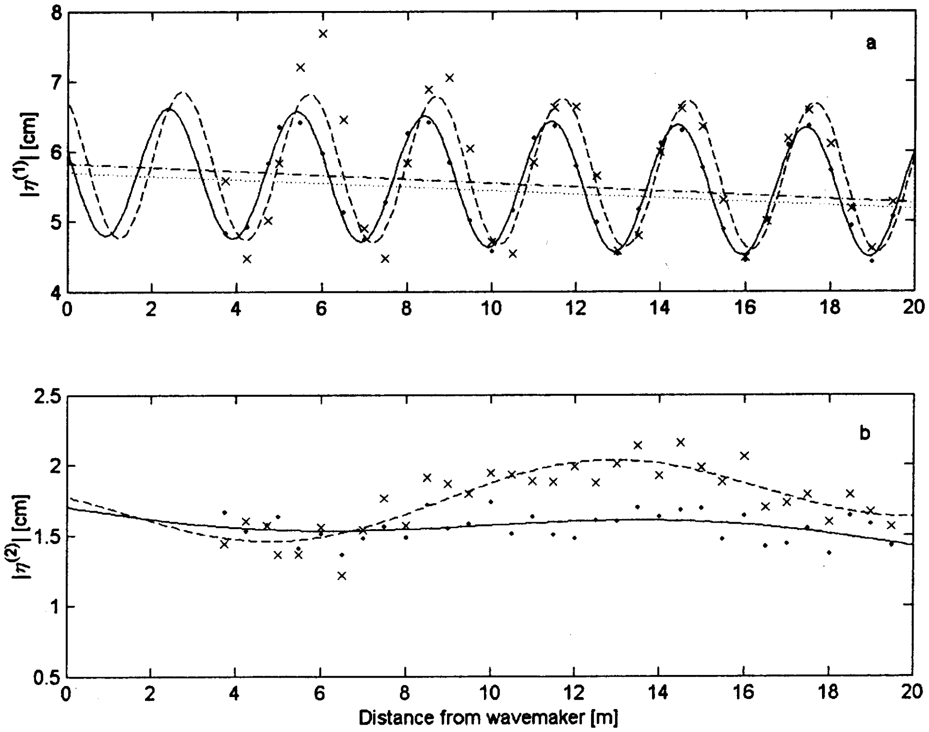

Figure 6.2: Wave-current variation of 1st (a) and 2nd (b) harmonic measured for attenuation experiments. Points (·) are the measurements before WC velocity measurements, and crosses (x) are measurements after WC velocity measurements. The solid line is the fit to the points based on equations (4.14) or (4.20). In (a), the dotted line is the attenuation slope previous to the velocity measurements, and dash-dot line is the attenuation slope after the velocity measurements.

7. PURE WAVE VELOCITY EXPERIMENTS

Mathisen (1993) found that the wave-current flows are modified by the presence of mass transport induced by the waves. Also, as there is a partially standing wave present in both the pure wave and wave-current experiments, effects of the standing wave on the flow field should be examined. With the need to characterize the pure wave flow and any possible influence that the standing wave may have on the bottom bedforms or wave-current flows, velocity profiles were measured for the pure wave experiments at locations along the beat length of the partially standing wave.

This section briefly describes the procedures used to measure the pure wave velocity profiles. Then the results of the profiles are presented. Different methods to characterize the flows are examined - bulk averaging of the flow and separating the flow into its harmonic constituents - and comparisons are made to Stokes solution for a viscous oscillatory flow boundary layer. In addition, some implications of the effects of the net flow on the bedform characteristics and mean bed elevation are discussed.

7.1. PURE WAVE VELOCITY EXPERIMENT PROCEDURE

The wave velocity was measured using a Sontek ADV probe. The basic methodology for making velocity measurements is discussed in Section 3.7, and was applied to the velocity measurements here. 2048 samples were acquired at 24.333Hz, measuring exactly 32 waves. This was repeated 5 times for each point in the profile, so each point represents the characteristics derived from 160 waves. The profile consisted of 14 points measured in the vertical and were logarithmically spaced at $\Delta\ln(z) = 0.25$, covering from $z = 2$cm above the nearest ripple trough to $z = 49$cm. $z = 0$ occurred at the nearest trough to the stated x-location. This was chosen to minimize the influence moving bedforms may have on the velocity profile. This is examined in more detail for pure current flows (Section 8.3) where the bedforms do not move over the measurement time scale, and the effects the ripples have on the near-bottom flow relative to the crest or trough can be obtained by extrapolation here. As it is impossible to eliminate effects of the ripples on the near-field (near-bottom) flow, the points within the wave boundary layer may not be accurate as the ripple may or may no move through the measuring volume over a sampling period. This would variably enhance acceleration of the flow over the ripple crest or enhance deceleration over the ripple trough past the measuring volume during measurements. As moving ripples are unavoidable, they create an inevitable source of variability for all near-bottom velocity measurements.

The velocity profiles were measured at five positions along the flume, and covered one first harmonic free surface beat length 3m in length. Profiles were measured at a node, the upslope between the node and antinode, the antinode, the downslope between the antinode and node, and the next node to act as a measure of repeatability. The exact x-locations and corresponding experiment ID's are detailed in Table 3.3

7.2. PURE WAVE VELOCITY PROFILE RESULTS

7.2.1. MEAN WAVE VELOCITY PROFILES AND WAVE-INDUCED MASS TRANSPORT

The time-averaged pure wave velocity profiles of experiments a, c, e, f, and i are plotted in Figure 7.1 at their relative spatial locations. These averages are simply the average of the velocity time series of 160 waves at each point in x and z. For comparison, the 1st harmonic free surface variation $|\eta^{(1)}|$ is plotted above the velocity profiles. Also, the mean bed elevation measured after the pure wave velocity experiments is shown as the solid line near $z = 0$. The profiles vertical elevation are plotted relative to the mean bed elevation, reflecting more realistically the relative spatial positions of the measured points.

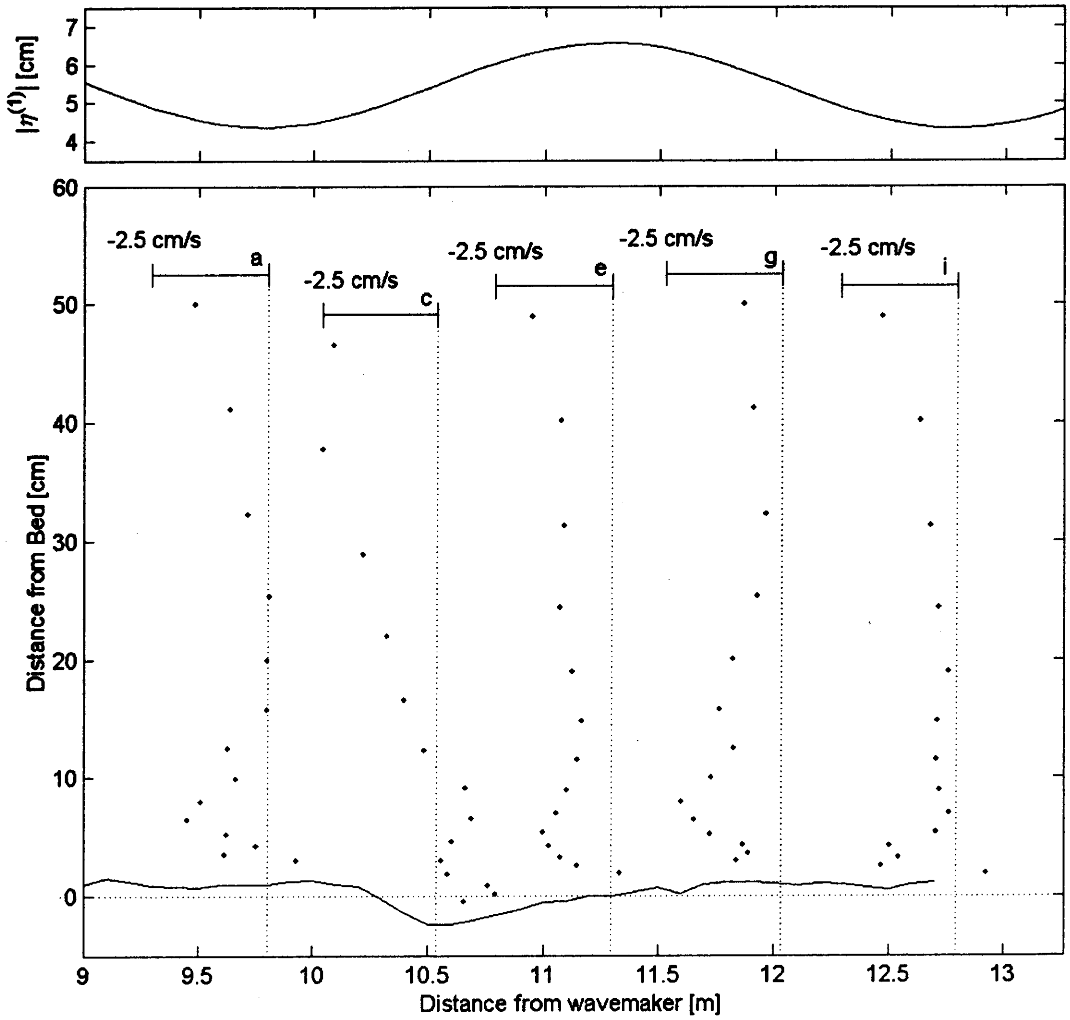

Figure 7.1: Mean pure wave velocity profiles (a – i). Points (·) are the velocity measurements. The dotted vertical lines represent zero velocity for each of the profiles. The solid line near $z = 0$ is the measured post-mean bed elevation. $|\eta^{(1)}|$ is the measured variation of the first harmonic and is plotted on the separate axis above the velocity profiles.

This figure illustrates that there is a significant difference in the mean velocity structure at different points along the beat length, although the underlying patterns are not obvious from this raw representation.

Figure 7.2 shows the same profiles as in Figure 7.1, but here they are superimposed to emphasize their relative variability in structure and magnitude. One would expect the points at the two nodes, experiments a and i (plotted as points (·) and the open squares), to be similar in structure and magnitude. They are similar near the surface and follow the same shape across the mid-depth to the bottom but with different magnitudes. The upslope and downslope, experiments c and g (plusses (+) and open circles), appear as mirror images about the vertical with a negative distortion which shifts the images to more negative velocities.

It was shown by Mathisen (1993) that a net mass transport occurred under pure wave flows in this flume for a similar setup. This structure of the net – negative distortion in the profiles shown in Figure 7.2 suggests a net negative transport. Therefore, a net transport is estimated by averaging the profiles over one cycle of the beat, experiments a, c, e and g. The resulting lumped mean profile is shown in Figure 7.3. For comparison, all measured time-averaged pure wave points are shown as points (·). The averaging over the beat cycle effectively removes the influence of the partially standing wave (assuming that the interaction is completely linear, which is doubtful). A net negative velocity resulting from mass transport by waves is shown to exist in the water column away from the bottom, and near the bottom as predicted by Trowbridge and Madsen (1984a, b). An interesting feature of the net velocity profile is the overshoot velocity between about 3 and 10cm off the bottom. This overshoot may either be an artifact from

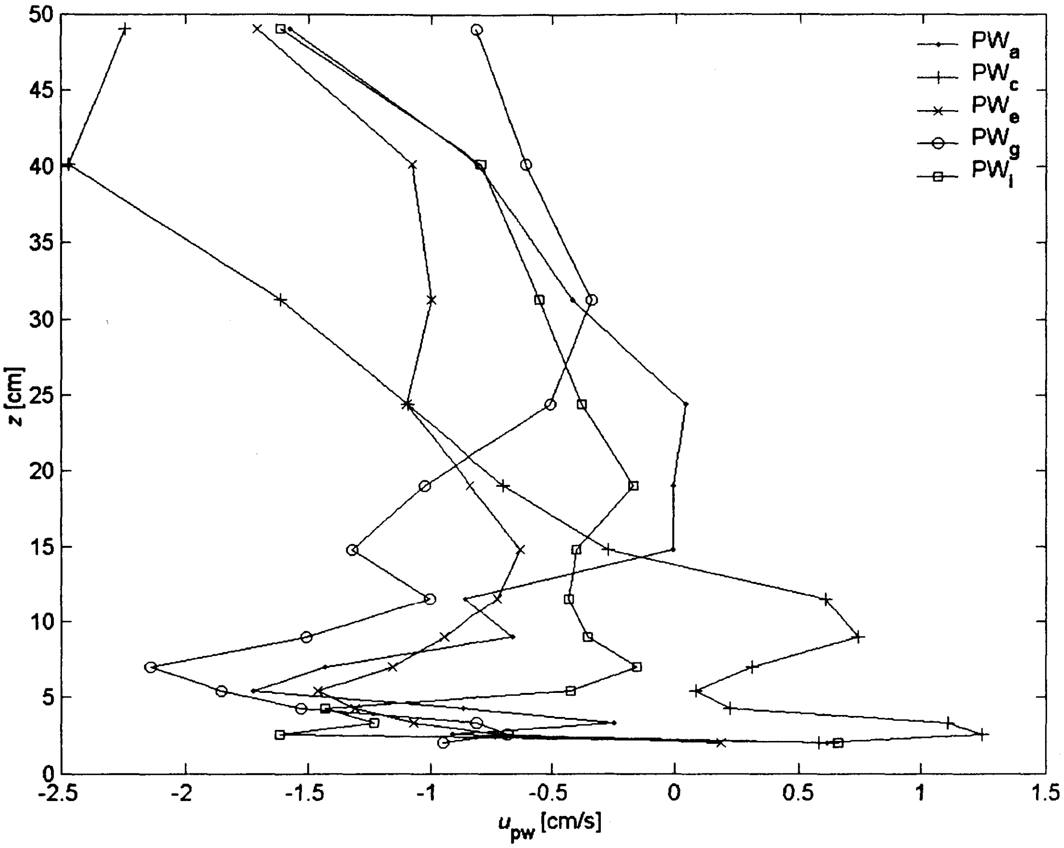

Figure 7.2: Mean pure wave velocity profiles for experiments (a – i).

measuring the velocity over moving ripple crests or a boundary layer developing as a result of flowing over a rough bottom. While it is likely that the moving ripple crests are responsible for some of the variability in the smoothness of the points near the bottom, it is unlikely that they would cause an enhanced velocity as consistently and as large as that seen in the overshoot. Therefore, the overshoot is probably from boundary layer development in the pure wave-induced negative mass transport (Trowbridge and Madsen, 1984a, b).

It is hypothesized by conservation of mass that closer to the surface and above the surface (under the action of the wave crests), there is a net positive velocity that must balance this negative drift, or all the water would pile up at the wavemaker. Unfortunately, the ADV is quite unsuccessful at

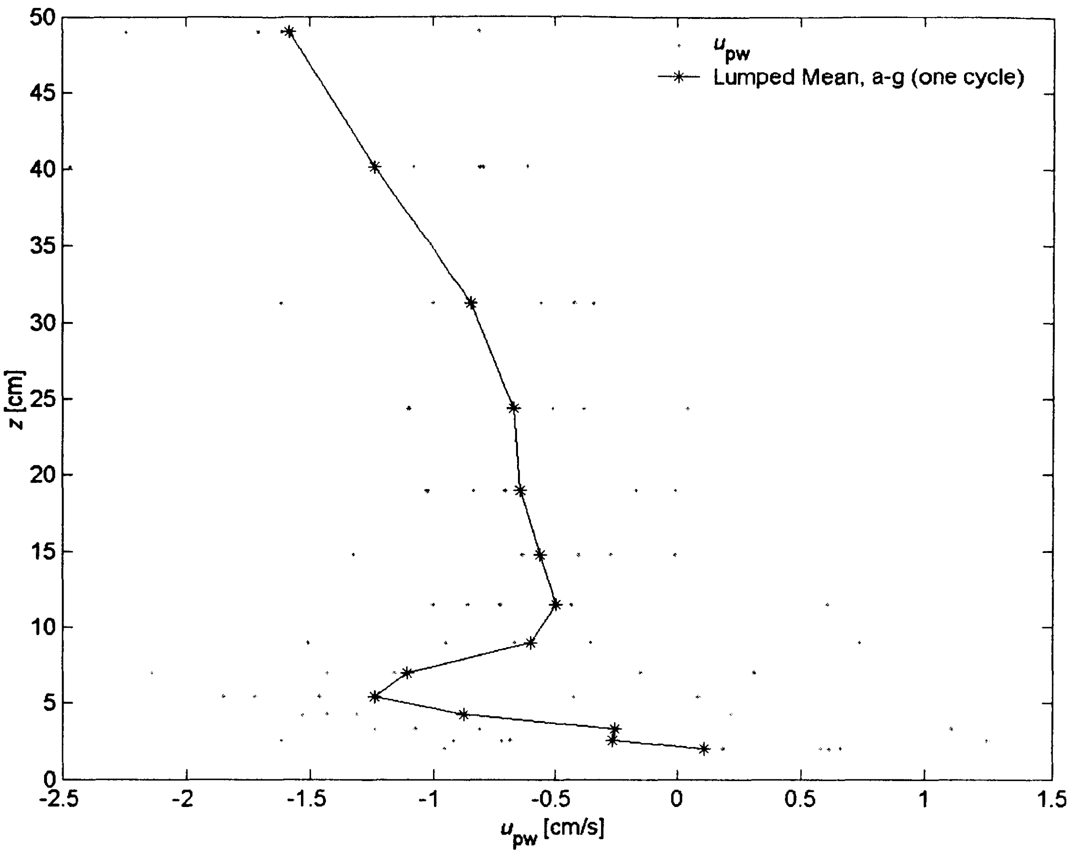

Figure 7.3: Lumped mean pure wave velocity profile and (*) are the averages of one cycle of the beat (a - g).

measuring velocities when the probe head is repeatedly unsubmerged and resubmerged; it must remain below the wave trough at all times. Therefore, this hypothesis cannot be verified quantitatively through measurements, although it is required to be qualitatively true by conservation of mass.

A second structure of mass transport has been shown to occur under a partially standing wave. Mei (1989) suggests that under a beat length, two counter-rotating cells form where a net downward velocity occurs at the node. This forces a flow along the bottom from the node to the antinode, at which point the bottom flows from adjacent nodes converge and cause a net upward flow at the antinodes. Then to finish the circulation, a flow is induced near the surface from the antinode to the node. To extract this type of structure from the measured time-averaged pure wave velocity profiles, each profile is shifted by its respective mass flux, found by integrating the profile over the depth as

$$Q_{pw} = \frac{1}{z} \int_{z_1}^{z_{14}} \overline{u}_{pw}(z) dz \tag{7.1}$$

Where Q_{pw} is the mass flux for each experiment, and for the cycle mean. These values are shown in Table 7.1. For comparison, the net drift can be predicted from by

$$\frac{\overline{u_s \eta}}{h} = -u_r = -(1 - \mathrm{R}^2) \frac{1}{2h} a^2 \omega \coth kh \tag{7.2}$$

where u_s is the surface velocity and u_r is the return current velocity. With a_i = 5.7cm and R = 20%, u_r = -1.16 cm/s which is in agreement with the net velocity associated with the cycle mean profile of –0.88cm/s, shown in Table 7.1. Then to remove the net drift caused by wave-induced mass transport, the cycle mean (shown in Figure 7.3), after being corrected for its mass transport, is subtracted from each profile. The resulting profiles represent the mass flux under a partially standing wave where there is no net drift induced by the progressive waves. These profiles are shown in Figure 7.4

Table 7.1: Net mass flux per unit area for each profile a-i, and the cycle mean.

Expt ID	Q_{pw} [$\mathrm{cm}^3/\mathrm{s}/\mathrm{cm}^2$]
a	-0.58
c	-1.05
e	-1.03
g	-0.86
I	-0.61
Cycle mean	-0.88

The structure suggested in Figure 7.2 can now be seen clearly in Figure 7.4. The antinode and two node profiles, experiments a, e, and i show similar structure – almost zero velocity at the surface and some form near the bottom that may reflect the variation of the flow by the ripples. The profiles at the upslope and downslope, experiments c and g, are now almost mirror images of each other, reflecting the converging flow near the bottom and the diverging flow near the surface, and an inflection point at approximately mid depth.

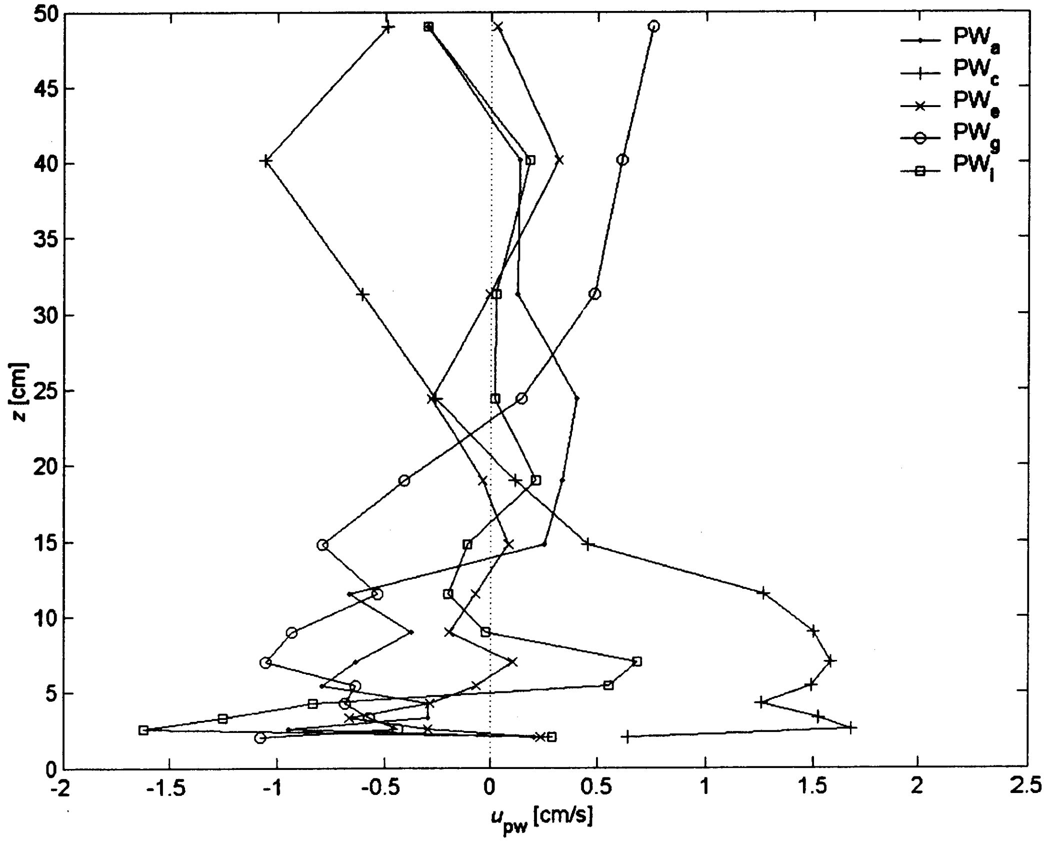

Figure 7.4: Pure wave velocity profiles corrected for mass flux and net mass flux. Vertical dotted line is $u_{pw} = 0$.

When these corrected profiles are plotted in their locations relative to the beat, illustrated in Figure 7.5, their spatial relationship becomes more clear. Here the circulation pattern discussed earlier becomes quite pronounced.

Figure 7.5 gives some hint at the possible genesis or proliferation of the variation of the mean bed. The mean bed variation is seen to somewhat reflect the pattern of the variation of the 1st harmonic free surface. This leads to the thought that the mass transport induced by the partially standing wave plays some role in its shaping. Unfortunately, insufficient evidence is obtained here to ascertain anything further about this phenomenon.

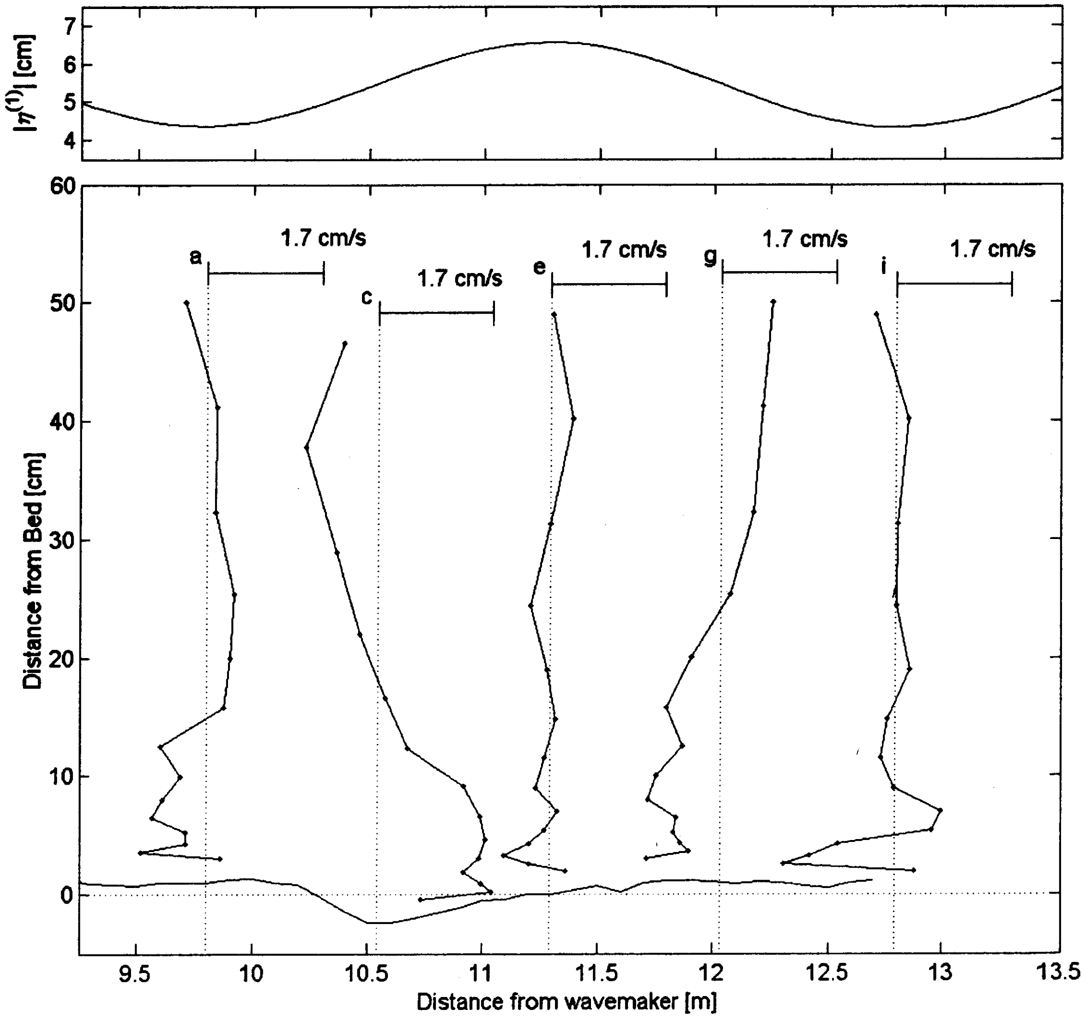

Figure 7.5: Pure wave velocity profiles corrected for mass flux and net mass flux, plotted at their respective spatial locations. Points (·) with solid lines are the corrected velocity measurements. The dotted vertical lines represent zero velocity for each of the profiles. The solid line near $z = 0$ is the measured post-mean bed elevation. $|\eta^{(1)}|$ is the measured variation of the first harmonic and is plotted on the separate axis above the velocity profiles.

7.2.2. 1^{ST} HARMONIC VELOCITY PROFILES

An important aspect of the pure wave velocity field is the flow that occurs at the dominant harmonic component of the oscillatory motion. Figure 7.6 shows the 1^{st} harmonic velocity profiles measured over one beat length in experiments a, c, e, g, and i. This figure shows the profiles' positions relative to the variation of the 1^{st} harmonic free surface elevation, just as Figure 7.1 showed the time-averaged pure wave velocity. Each profile is plotted at its depth relative to the measured mean bed elevation.

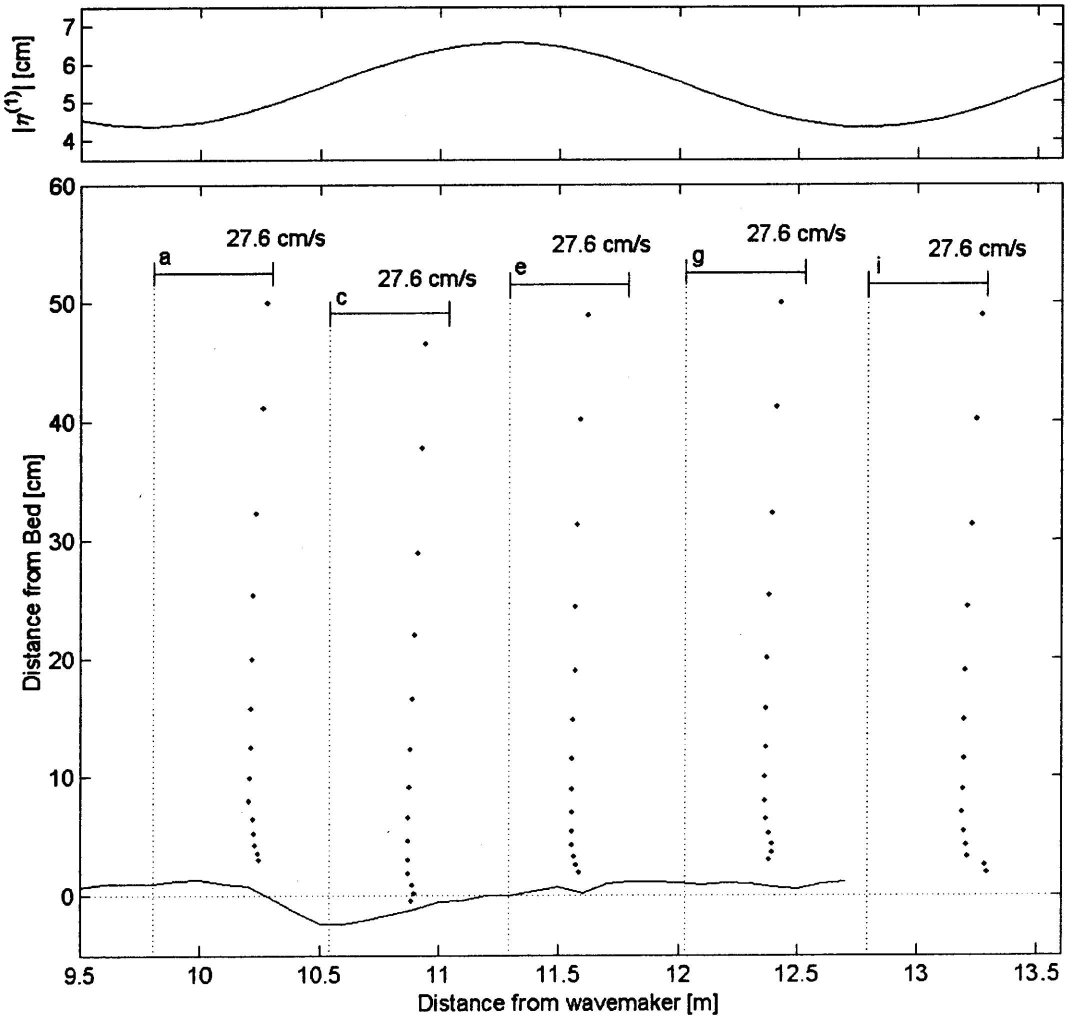

Figure 7.6: 1^{st} harmonic pure wave velocity measurements, $u_{pw}^{(1)}$ for experiments (a - i). Points (·) are the velocity measurements. The dotted vertical lines represent zero velocity for each of the profiles. The solid line near $z = 0$ is the measured post-mean bed elevation. $|\eta^{(1)}|$ is the measured variation of the first harmonic and is plotted on the separate axis above the velocity profiles.

The 1st harmonic pure wave velocities plotted in Figure 7.6 are superimposed in Figure 7.7 to compare their relative magnitudes. Here, the affect of the reflected wave is dramatically demonstrated. As described by linear wave theory, at the nodes (experiments a, points (·), and i, open squares) the velocity of the incident wave and the reflected wave constructively interact and produce a larger velocity profile. At the antinodes (experiment e, crosses), the incident and reflected waves destructively interact and result in a decreased velocity profile. At the mid-points (experiments c, plusses, and g, open circles), the reflected wave does not interact with the incident wave. The bottom-most points in the profile of experiment i demonstrate the effect a ripple crest can have on the measured velocity by enhancing the velocity over the crest.

One interesting implication of the partially standing wave is how it affects the ripple geometry. As shown in Figure 5.1 (a) and (b), the ripple geometry varies in size over the beat length. This can be explained by the variation in bottom velocity shown in Figure 7.7. By using these measured velocities, the ripple geometry can be predicted quite accurately (to within less than 10% of the measured values). The predictions are shown in Figure 5.1 (a) and (b) and were discussed further in Section 5.3.1. Comparisons between the measured and predicted wave orbital velocity over depth are also shown in Figure 7.7. The predictions of the velocity are from using the measured wave amplitude as input to linear wave theory. The values of the measured and predicted bottom velocity u_{bm} are shown in Table 5.2.

Just as was done for the time-averaged velocity profiles, the 1st harmonic velocity profiles can be averaged over the beat to obtain a representative 1st harmonic profile that would occur if the partially standing wave did not exist. To do this, we take the lump average the $u_{pw}^{(1)}$ profiles over

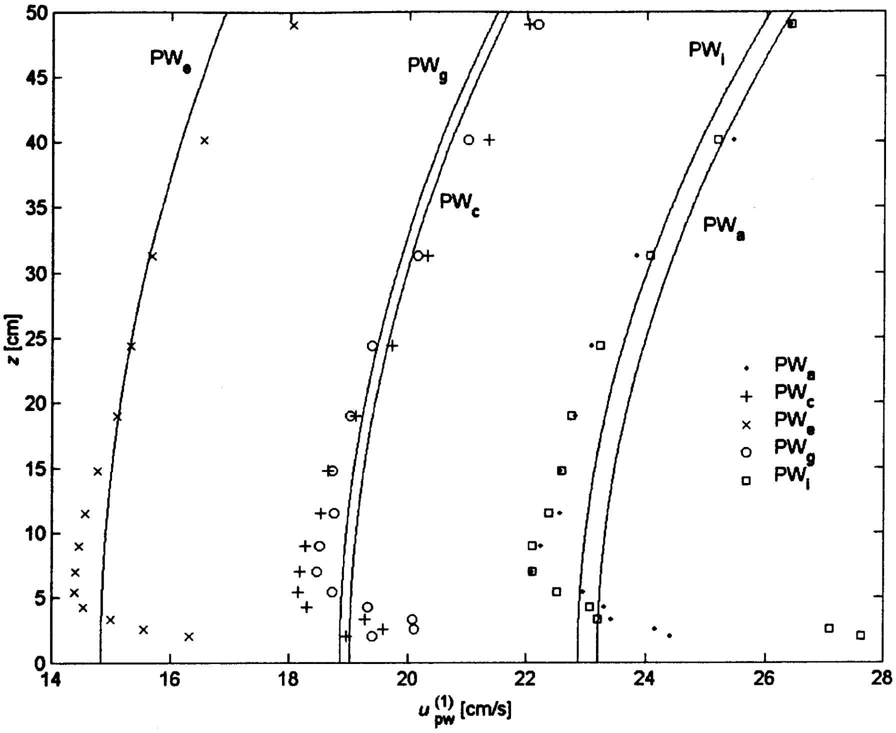

Figure 7.7: 1st harmonic pure wave velocity profiles for experiments (a - i). Points are measurements and solid lines are predictions from measured wave amplitude and linear theory.

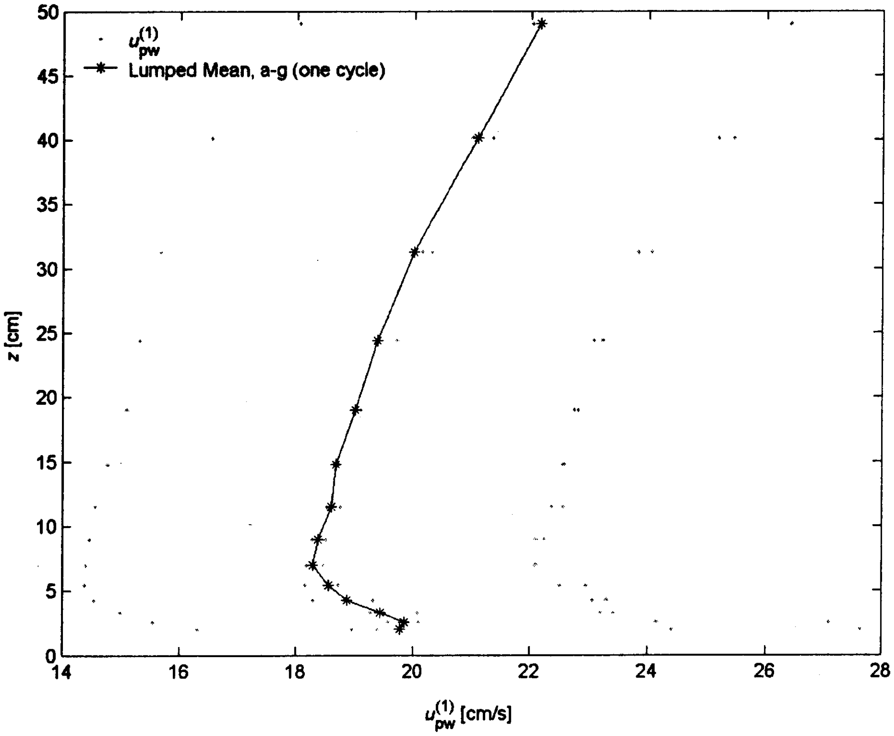

Figure 7.8: Lumped mean pure wave 1st harmonic velocity profile. (*) are the averages of one cycle of the beat (a - g).

the beat cycle, experiments a – g. Figure 7.8 shows the lumped mean for one cycle as (*). As expected, the velocity follows the hyperbolic tangent from the surface down.

In a similar fashion to $u_{pw}^{(1)}$, the phase of $u_{pw}^{(1)}$ can be determined relative to the phase of the wavemaker. Figure 7.9 shows the measured phase for all experiments. The phases here have been shifted so the mean of the upper profile (from $z \cong$ 15cm to 50cm) is equal to zero. The relative shifts are shown in the legend of Figure 7.9. Note that the shifts are spaced regularly and span approximately 180°.

As in Figure 7.8, Figure 7.10 shows the phase profiles after they have been lumped averaged over one beat cycle to obtain a representative phase plot that one might expect if there was no partially standing wave. This figure illustrates how the velocity near the bottom in the boundary layer, on the average, leads the velocity outside the boundary layer.

Figure 7.11 shows the measured cycle-mean 1st harmonic wave orbital velocity and its associated phase compared to the predictions based on Stokes' solution for a viscous oscillatory boundary layer. For Stokes' solution, the predicted boundary layer is pseudo-laminar and is similar to the boundary layer formulation used by Madsen and Salles (1998), found by taking the boundary layer thickness $\delta \sim \sqrt{2\nu/\omega}$. For both Figure 7.11 (a) and (b), Stokes' solution has been scaled vertically by the boundary layer height of the measured velocity by obtaining a value of ν that would give the Stokes' solution the same boundary layer height as the measured wave boundary layer height. Here, $\delta_w = 1.0$cm. Then, we can solve for ν in the pseudo-laminar equation, were $\nu = \delta^2\omega/2$, or $\nu = 1.2$cm^2/s. As illustrated in the figures, the shape of the measured velocity closely

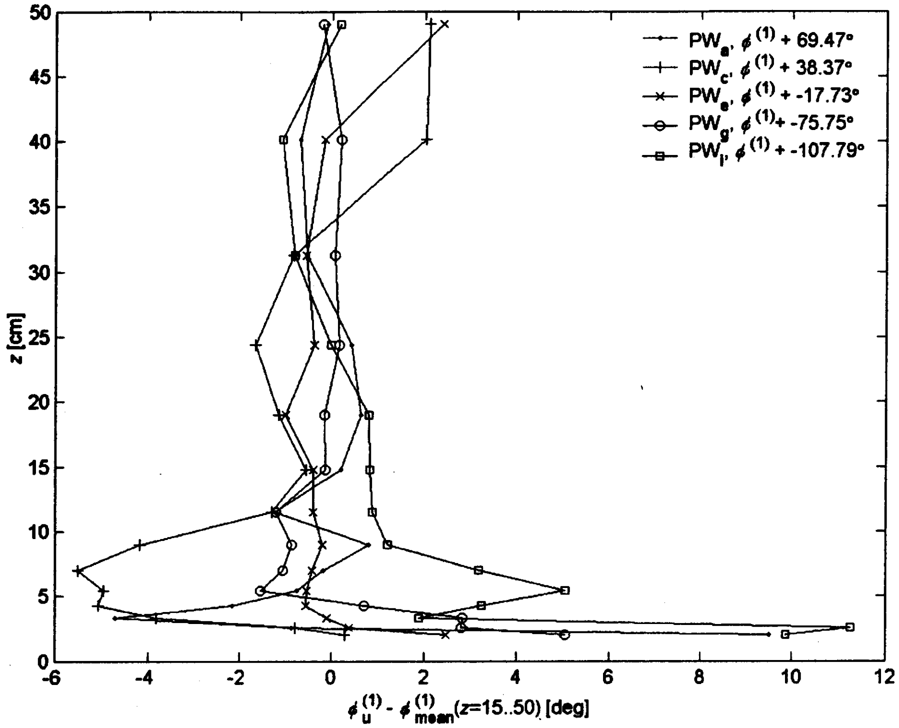

Figure 7.9: Phase profiles of 1st harmonic pure wave experiments (a - i), corrected from their relative phases.

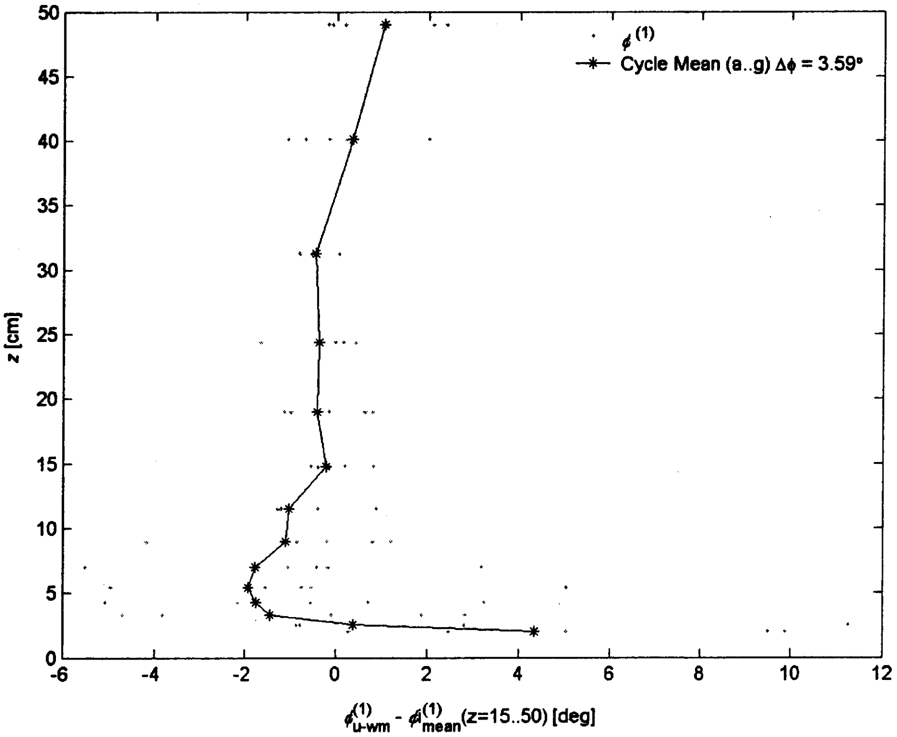

Figure 7.10: Lumped mean pure wave 1st harmonic phase profile. (*) are the averages of one cycle of the beat (a - g).

resembles that from Stokes' solution, especially near the bottom where a velocity overshoot and phase undershoot occurs.

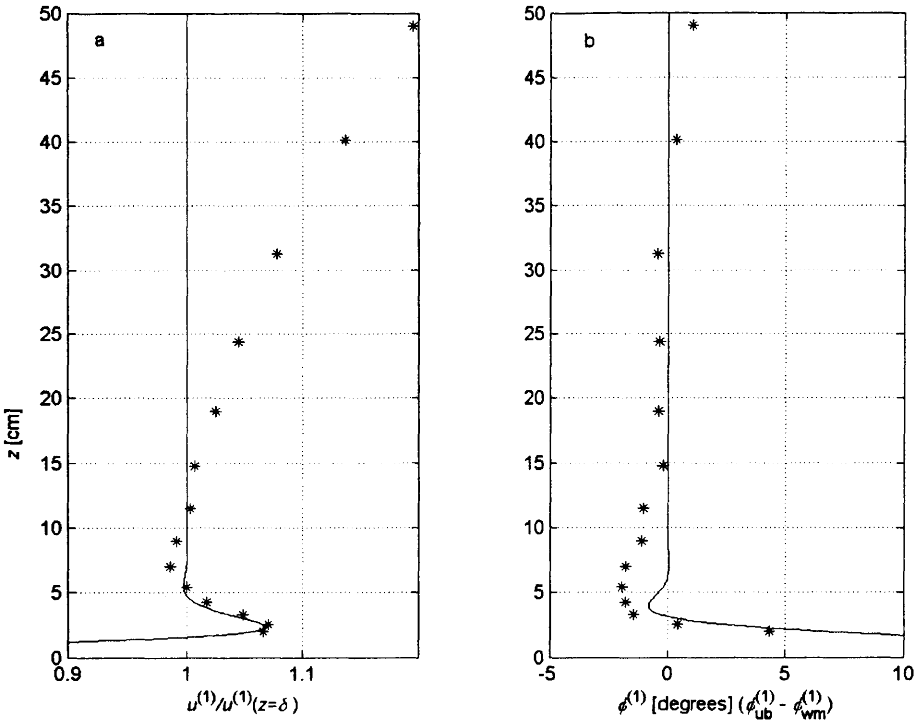

Figure 7.11: Measured cycle-mean $u^{(1)}$ and $\phi^{(1)}$ compared with predictions from Stokes oscillatory boundary layer solution.

8. PURE CURRENT VELOCITY EXPERIMENTS

This section discusses the methods for measuring and analyzing pure current flows. The results of the pure current experiments are presented, and a comparison is made between the roughness derived from the pure current experiments and the actual measured bedform geometry.

8.1. PROCEDURE

The procedure for measuring current velocity and current velocity profiles is discussed in detail in Section 3.7, and is identical to the procedure used in the measuring the wave and wave-current velocity profiles. Measurement of 2048 points at 24.333Hz were taken 5 times at each position in x and z. These measurements were time averaged to give a single point measurement at each of the 14 vertical z positions in a profile. The bottom-most point in the profile was taken at 2cm above the nearest ripple trough. For consistency across experiments and to have equal logarithmic increments off the bottom, the vertical measurements were spaced at $\Delta\ln(z) = 0.25$ increments to a distance of 49cm off the bottom.

Section 5.3.2 discussed how the pure wave ripples adjusted to the pure current flow, and how the initial measurements of the current velocity were made over ripples that were not fully adjusted to the current flow. This progression is useful in understanding how the current modifies the ripples. It is also important to consider when analyzing the data as experiments over ripples that are not fully developed will not be consistent with those that are. Table 3.3 shows the experiments and the corresponding experimental IDs and spatial locations for the pure current experiments, and Table 5.3 details the progression of the pure current measurements.

8.2. ESTIMATING ROUGHNESS FROM PURE CURRENT VELOCITY PROFILES

Determination of the bottom roughness and current shear stress felt by pure current flows follows from an analysis of the time-averaged pure current velocity profiles. As discussed in Section 2.2.3, the current velocity profile is expected to display a logarithmic form following the equation

$$u_c = \frac{u_{*c}}{\kappa} \ln \frac{z}{z_0} = \frac{u_{*c}}{\kappa} \ln \frac{30z}{k_c} \tag{8.1}$$

where the roughness felt by the current $k_c = 30\ z_0$. Then it is convenient to plot ln(z) on the vertical axis and u_c on the horizontal axis. Figure 8.1 shows a typical velocity profile plotted in this semi-logarithmic format. It is assumed in all the current profile analyses that the profile follows a logarithmic shape. Then, where this is valid the data should show a linear region. Data points which are clearly influenced by the individual ripples (near the bottom) or are outside the current boundary layer (near the top) would not follow the same linear shape as the points in the logarithmic boundary layer region. These outlying points are removed from the set, and the remaining points are fit using a least squares regression. The problem is linearized by rearranging equation (8.1) to the form

$$\ln(u_c) = \frac{u_{*c}}{\kappa}(\ln z - \ln z_0) \tag{8.2}$$

The shear stress u_{*c} and the hydraulic roughness z_0 (and thus the equivalent Nikuradse roughness, or current roughness k_c) are determined using a least squares regression.

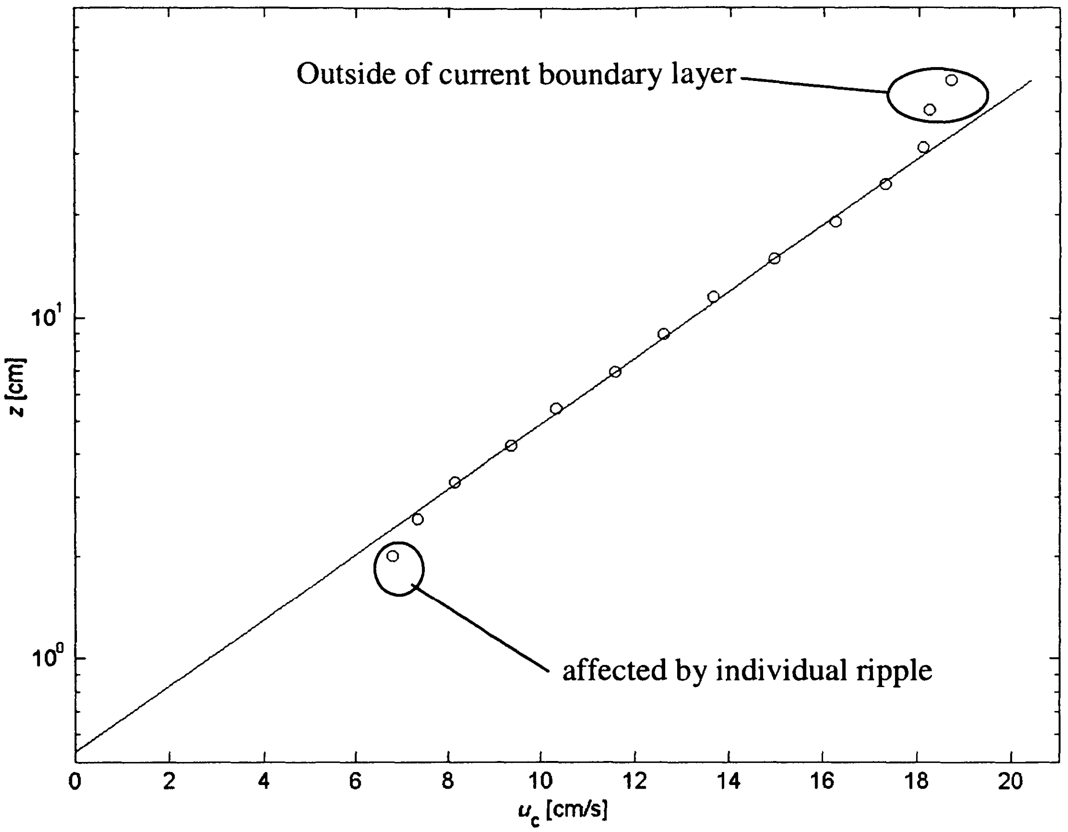

Figure 8.1:Typical pure current velocity profile and current roughness prediction.

The hydraulic roughness length scale depends on the zero-reference elevation from which the elevations are measured. It is common practice when fitting logarithmic profiles to adjust this elevation in order to maximize the goodness of the fit to the data (maximize the regression coefficient r^2). Then when r^2 is a maximum, the fit is said to be a best fit at the new theoretical bed elevation. It was found for all profiles measured in these experiments that the maximum r^2 occurred when the theoretical bed was below the bottom of the flume, and thus not at all realistic. The next best fit that is physically possible occurred when the theoretical bed was set at the level of the local bed, or the actual measured zero elevation. Therefore, all analyses were done with the theoretical bed set at the elevation of the actual measured zero elevation. Then u_{*c} and k_c may be obtained by applying these procedures to each profile. Note that it is necessary to examine each profile individually, as the points to exclude from the fit varies from profile to profile.

Estimates of the accuracy of the fits of u_{*c} and k_c may be determined by analyzing the propagation of errors through the linear regression, and depends on the goodness of fit of each profile. Therefore, the accuracy varies for each profile and fit. For the profile in Figure 8.1, u_{*c} = 1.85cm/s ± 0.03cm/s, k_c = 16.02cm ± 0.61cm, and $r^2 = 0.9983$.

8.3. PROFILE VARIABILITY AND ITS EFFECT ON ROUGHNESS ESTIMATION

The pure current velocity profiles measured in these experiments often showed a significant variability and deviation from the expected logarithmic profile described above. One of the most prominent features was a two-layer region in the profile, where the parameters of the logarithmic fit vary significantly from one another. Figure 8.2 illustrates a profile with the typical two-layer shape. The kink or split between the two regions almost always occurred between z = 7 to 9 cm from the bottom (points 6 and 7, where point 1 is the point closest to the bottom).

To account for this two-layer profile in the analysis of the current profiles in this study, a fit is always made to each of three different combinations of points: the points in the first logarithmic sublayer, called the bottom (bot) points, which includes points 1 to 6 or 7 ($z \cong$ 2cm to $z \cong$ 7 to 9cm, depending on the profile); the second logarithmic sublayer, called the 'top' points and includes points 6 or 7 to about point 11 or 13 ($z \cong$ 7 to 9cm to $z \cong$ 25 to 49cm, depending on the profile); and the combination of the bottom and top points, referred to as 'all', or all the points that display some logarithmic behavior. Figure 8.2 displays these three fits to a typical two-layer profile. The results of the fits are shown in Table 8.1. The different regions yield drastically different results: k_c ranges from about 6cm to 29cm and u_{*c} ranges from about 1.4cm/s to 2.3cm/s.

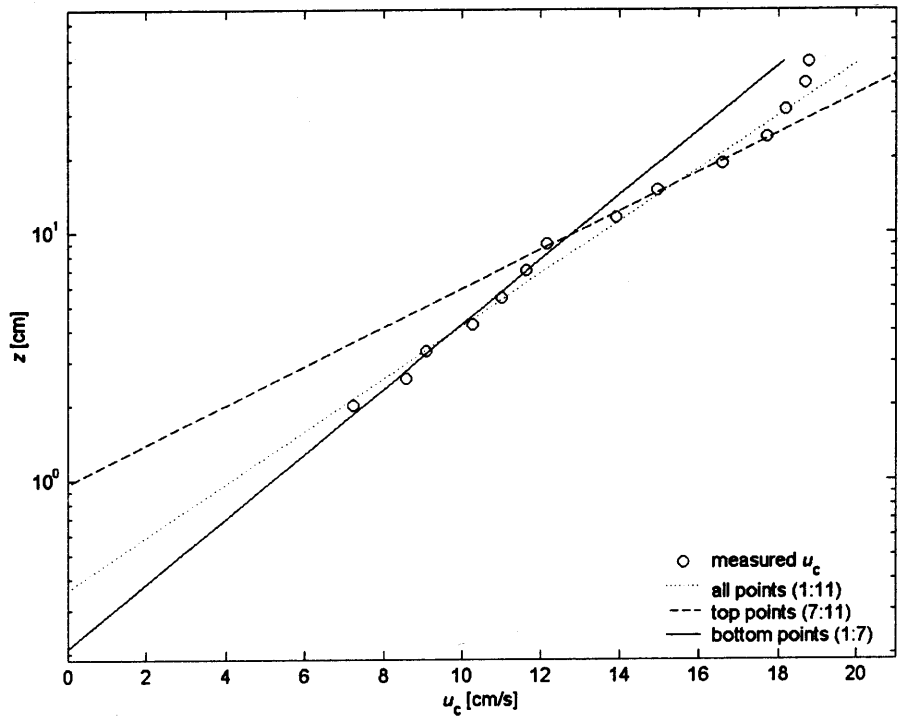

Figure 8.2: Typical two-layer current velocity profile, with fits to the whole logarithmic profile (all, dotted line), top section (top, dashed line), and bottom section (bottom, solid line). Open circles are the measured time-averaged velocity points.

Table 8.1: Regression parameters for the fit of the two layer profile shown in Figure 8.2.

Profile Section (Points)	u_{*c} [cm/s]	k_c [cm]	Regression Coefficient (r^2)
all (1:11)	1.68	10.88	0.9823
top (7:11)	2.27	29.06	0.9939
bottom (1:7)	1.36	6.28	0.9827

In experiments performed by Mathisen (1993) in the same facilities but with fixed roughness elements, it was noticed that when the roughness elements were spaced at 20cm, a profile similar in nature to the two-layer profile occurred. Mathisen explained this phenomenon by hypothesizing that the vortices shed by the ripples at the wide spacing converged at a larger distance off the bottom than the ripples at the standard 10cm spacing. In his experiments, the kink was observed to occur at approximately 6cm off the bottom for the wide ripple spacing, but only about 3cm off the bottom for the standard 10cm spacing. The movable bed ripples measured in this study have a length of about 10cm, corresponding to Mathisen's standard spacing, but the kink occurs near 8cm off the bottom. The mean current velocity in both experiments was about 16cm/s, so the difference is not a result of different flow intensities. For these conditions and the standard spacing, Mathisen attributed the kink to the region where the individual roughness elements can alter the flow field through enhanced acceleration and deceleration. Therefore, the kink observed by Mathisen in either the standard spacing or the wide spacing is probably not caused by the same phenomenon as the kink observed in these experiments.

To propose a hypothesis, consider the bedform geometry in the pure current case. In Section 5.3.2, it was observed that the ripple height, varied with the first harmonic beat for pure current modified wave formed ripples. Then, assuming that the current roughness varies with the ripple height (as proposed as one of the goals of this study to determine), the current roughness will vary with the first harmonic beat. As the current flows over the increased roughness, the water near the bottom is slowed down, and this reduces the water velocity above it and so on upwards. But the increased roughness is not able to penetrate the entire water column instantaneously, so the diffusion of the increased turbulence takes some time to progress upwards in the water column. The near bottom water speeds up as it moves over the smaller roughness while the motion in the upper part of the water column is still feeling the increased roughness from before. Then the water above it slowly recovers until it reaches the next increase in roughness, at which point the whole process is repeated again. Figure 8.3 shows the variation of $u_{*c,top}$ and $u_{*c,bot}$ and the difference between the top and bottom $\Delta u_{*c} = u_{*c,top} - u_{*c,bot}$ along two beat lengths. At the first point on the left, the roughness is a maximum and this slows down the flow near the bottom, reflected as a relatively large $u_{*c,bot}$ for the bottom points. But here, $u_{*c,top}$ is not yet affected by the larger roughness. Then, as the flow progresses to the right towards a smaller roughness, the near bottom $u_{*c,bot}$ decreases. At the same time, the drag from the larger roughness of the bottom flow put on the flow above it begins to take effect, increasing the top $u_{*c,top}$. The difference between the top and bottom Δu_{*c} then increases as the top $u_{*c,top}$ increases and the bottom $u_{*c,bot}$ decreases as the roughness is approaching a minimum. At the minimum roughness, about $x =$ 11.5m, Δu_{*c} is a maximum, and begins to decrease as the bottom $u_{*c,bot}$ begins to feel an increasing roughness and increases while the top $u_{*c,top}$, which has been lagging the bottom $u_{*c,bot}$ finally feels the smaller roughness and begins to decrease. Then at the maximum roughness ($x \cong$ 13m), the process repeats itself.

Regardless of the processes, the top, bottom, and combined top and bottom (all) are all three analyzed for each profile, and their results are presented in the next section. It is thought that the bottom points will reflect the bottom roughness most accurately, since they feel it more directly than the other sections of the flow. Therefore, most of the analysis will concentrate on the bottom points, but will include all for completeness.

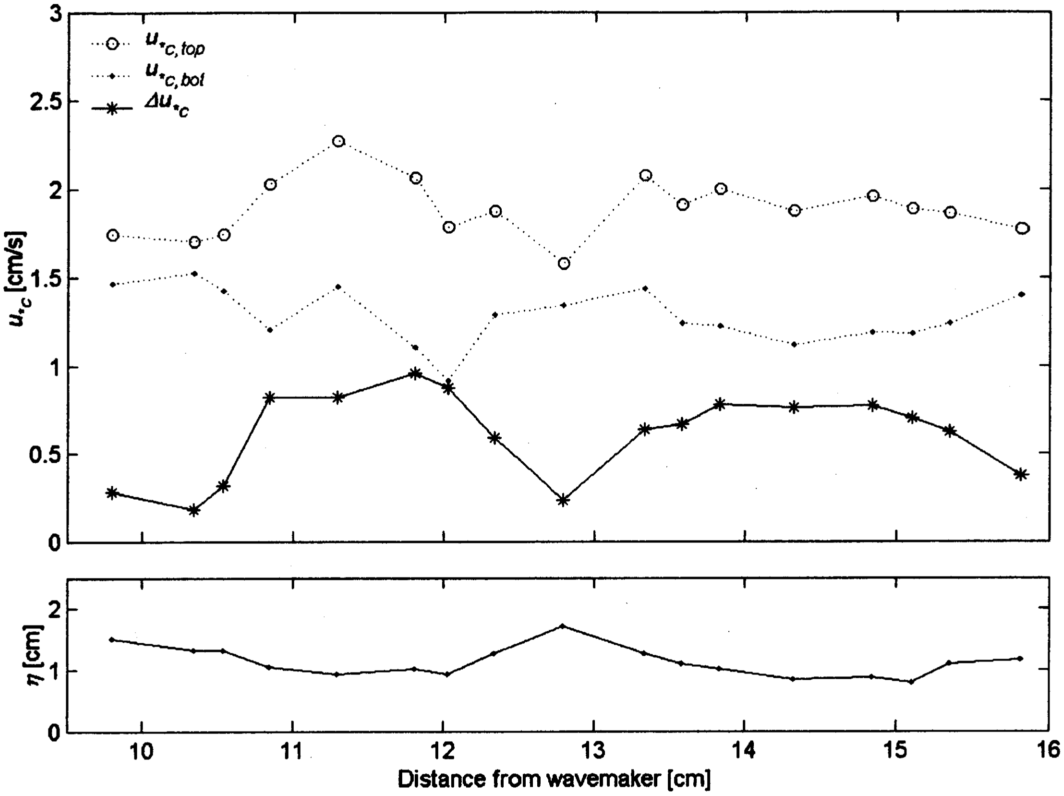

Figure 8.3: Variation of $u_{*c,top}$ top and $u_{*c,bot}$ bottom in x, and Δu_{*c}, the difference between top and bottom. The ripple height η is shown as a scale and spatial reference for the bottom roughness.

Another variability in the current profiles, and thus the current roughness, can come from it's relative position over the ripple. MM showed that flow measured over the crest of a fixed roughness element is different than that over a trough, but the differences only extend to about 2η, in their case 3cm, above the bottom. Similar results can be seen for flow over the movable bed ripples. Figure 8.4 shows the variation of the flow at four different locations over a ripple, the ripple trough (a), lee of the crest (b), directly over the crest (c), and stoss (just in front of, or the up-flow side) of the crest (d). (e) and (f) show these four profiles superimposed. In all of these cases, the fit of the bottom points (1:6 or 1:7) and for different combinations of bottom points are shown on the figures.

When the measuring volume is directly over the crest (c), the bottom 3 to 4cm of flow are faster than for the other profiles. The velocities of the other profiles near the bottom are fairly consistent in magnitude with each other. However, the roughness felt by each section is not. Also, depending on the points selected in each profile, the roughness determined for each profile can vary from 25% to as much as 83%. Obviously, the bottom three points in (c) should not be considered, as they are influenced by the local crest and do not accurately represent the bottom roughness. However, this figure should emphasize the fact that each profile, no matter where it is measured, should be analyzed individually. The bottom points that are influenced by the individual roughness elements will vary from profile to profile. Also, location of the kink at the transition between bottom and top sublayers varies depending on the profile, and the top most points that may be outside the current boundary layer are different for each location as well. Unfortunately, by picking and choosing which points to include introduces some subjectivity into the analysis. Figure 8.4 (d) demonstrates this possibility. Should point 2 be included in the logarithmic fit? Probably not, but then should point 1 be automatically excluded because point 2 was? Generally, yes, because the reasoning is that if point 2 is altered by local near bottom flow, then point 1 must be as well. In this case, it makes no difference. Using the general guidelines as much as possible minimizes the subjectivity of the analysis.

8.4. PURE CURRENT VELOCITY RESULTS

The methods described above were applied to the measured pure current profiles to determine values for u_{*c} and k_c along two beat lengths. Table 8.2 presents the results of the analysis of the pure current experiments. Note that in this table, profiles that were measured over ripples that

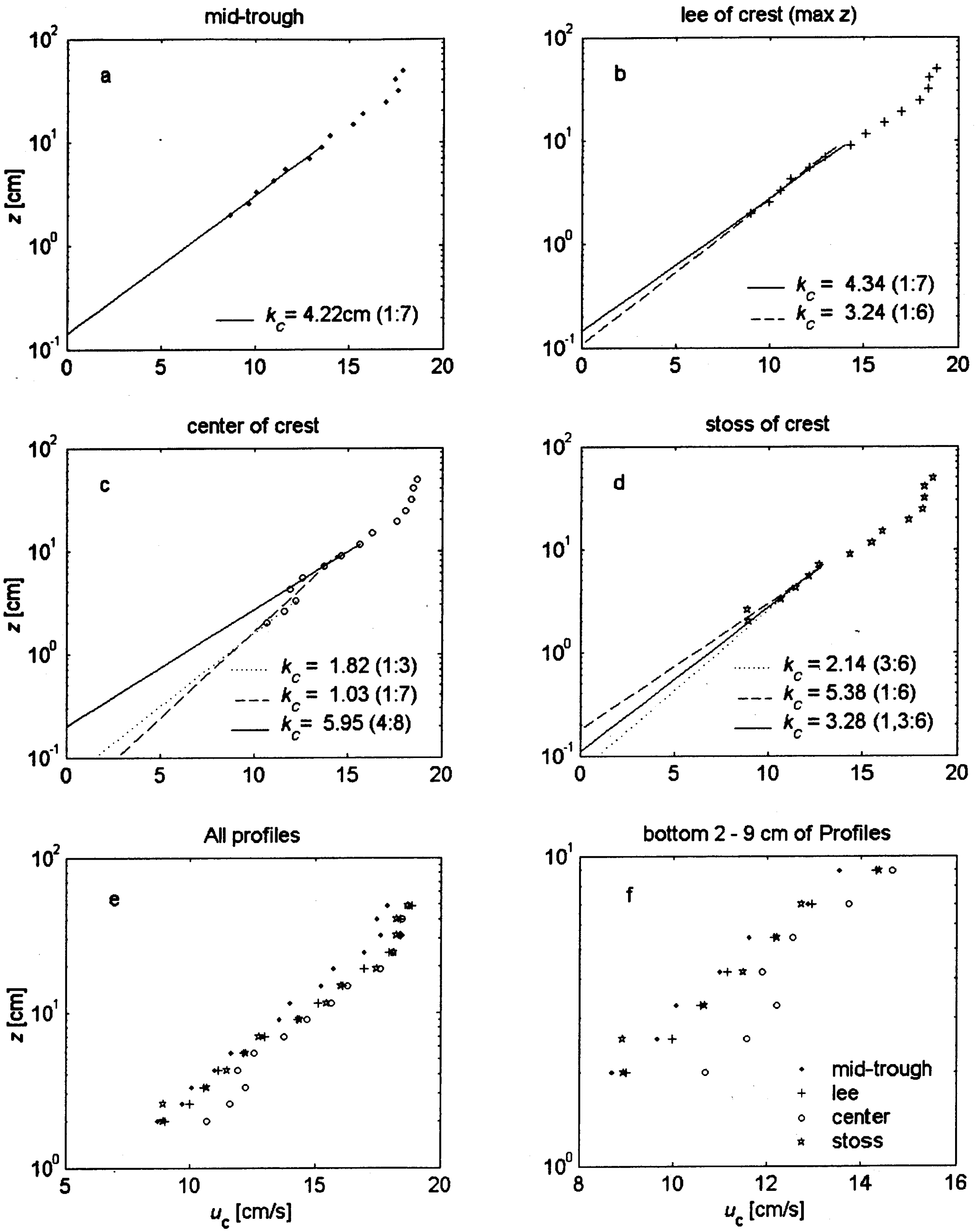

Figure 8.4: Pure current velocity profiles over four quarters of a ripple: (a) mid-trough, (b) lee of crest, (c) directly over the center of the crest, and (d) stoss of crest. (e) shows all profiles ((a) – (d)) overlayed and (f) shows the bottom portion of all profiles ((a) – (d)) overlayed.

were not yet fully developed are not included. Most of the experimental results are averages of at least two separate profiles measured at that point. u_{*c} , k_c, and the regression coefficient r^2 are shown for each point for the three sections of the profile all, top, and bottom (bot). The standard deviation is shown only for the results of the analysis of the bottom sublayer. The rows labeled Mean and Std Dev. show the mean and standard deviation for all values in the column above it. In other words, it is the average of the parameters across two beat lengths. For example, the mean k_c (bot) experienced is 4.53cm, with a standard deviation of the roughness across the two beats $\sigma_{k_c} = 2.05$cm.

Table 8.2: Results of pure current experiments.

Expt ID	x [m]	u_{*c} [cm/s] (all)	u_{*c} [cm/s] (top)	u_{*c} [cm/s] (bot)	k_c [cm] (all)	k_c [cm] (top)	k_c [cm] (bot)	r^2 (all)	r^2 (top)	r^2 (bot)	σ_{u*c} [cm/s] (bot)	σ_{kc} [cm] (bot)
a	9.80	1.56	1.75	1.46	7.36	11.40	6.46	0.9901	0.9930	0.9729	0.10	1.31
b	10.34	1.58	1.70	1.52	8.81	11.73	8.13	0.9890	0.9858	0.9899	0.14	1.57
c	10.54	1.62	1.74	1.43	9.31	12.24	6.72	0.9879	0.9953	0.9485	0.13	1.99
d	10.84	1.57	2.02	1.21	8.14	20.00	3.65	0.9772	0.9870	0.9641	0.09	1.10
e	11.29	1.68	2.27	1.45	10.88	29.06	7.34	0.9823	0.9939	0.9859	0.08	1.17
f	11.81	1.45	2.06	1.10	5.94	22.26	2.24	0.9672	0.9859	0.9823	0.06	0.44
g	12.03	1.40	1.79	0.92	4.73	12.67	0.89	0.9697	0.9848	0.9784	0.09	0.64
h	12.33	1.55	1.87	1.29	7.95	16.15	4.62	0.9803	0.9656	0.9819	0.10	1.17
I	12.79	1.42	1.58	1.34	5.18	8.11	4.33	0.9939	0.9865	0.9792	0.07	0.84
j	13.34	1.66	2.07	1.44	10.68	22.66	7.47	0.9868	0.9935	0.9846	0.06	0.86
k	13.58	1.60	1.91	1.24	9.12	17.35	4.45	0.9827	0.9888	0.9702	0.12	1.59
l	13.83	1.57	2.00	1.22	8.44	20.06	3.93	0.9816	0.9814	0.9898	0.06	0.75
m	14.31	1.55	1.88	1.12	7.47	15.80	2.64	0.9813	0.9928	0.9761	0.08	0.89
n	14.84	1.53	1.96	1.19	7.03	18.68	3.14	0.9750	0.9874	0.9509	0.10	0.91
o	15.10	1.50	1.89	1.18	6.32	16.62	2.76	0.9770	0.9835	0.9738	0.05	0.52
p	15.35	1.53	1.86	1.24	7.66	16.73	3.92	0.9852	0.9819	0.9895	0.06	0.71
q	15.82	1.44	1.77	1.40	4.92	12.35	4.32	0.9811	0.9699	0.9518	0.12	1.13
Mean		1.54	1.89	1.28	7.64	16.70	4.53	0.9817	0.9857	0.9747	0.09	1.03
Std Dev.		0.08	0.17	0.16	1.90	5.16	2.05	--	--	--	--	--
Lumped Mean		1.51	1.84	1.30	7.02	14.80	4.38	0.9898	0.9966	0.9956	0.04	0.45

A different approach to obtaining the average of the current profile is the lumped mean profile. The lumped mean is the result of taking an ensemble average of the velocity measurements of all profiles a-q across their respective z locations. The resulting profile is shown in Figure 8.5. The values in the row in Table 8.2 labeled Lumped Mean are the results of analyzing the lumped mean profile of Figure 8.5. These fitted profiles are also illustrated in the figure. The results of the lumped mean approach are nearly identical to the straight averaged approach, while the goodness of fit (and thus the accuracy) of the lumped mean approach is much better than for the straight averaging; the $\sigma_{k_c} \cong 1\,\text{cm}$ for the straight averaging, while $\sigma_{k_c} \cong 0.5\,\text{cm}$ for the lumped mean.

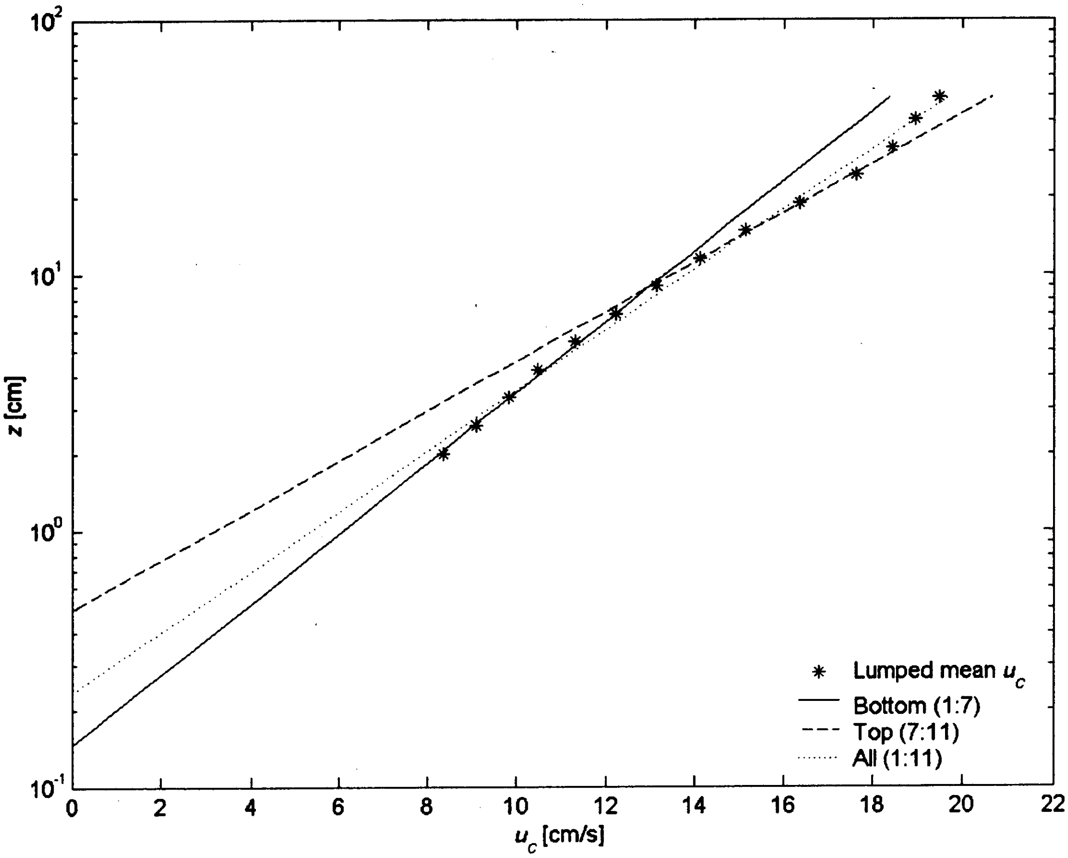

Figure 8.5: Lumped mean pure current velocity profile, averaged over 2 beat cycles.

Figure 8.6 shows the variation of u_{*c} and k_c over the two beat lengths, for all measured profiles over fully developed ripples. This figure illustrates the variation between the different sublayers of the profiles: the top sublayer is shown with open circles, and the average at each x location is shown with the dashed line; the combination of top and bottom, all, is shown with points (·), and

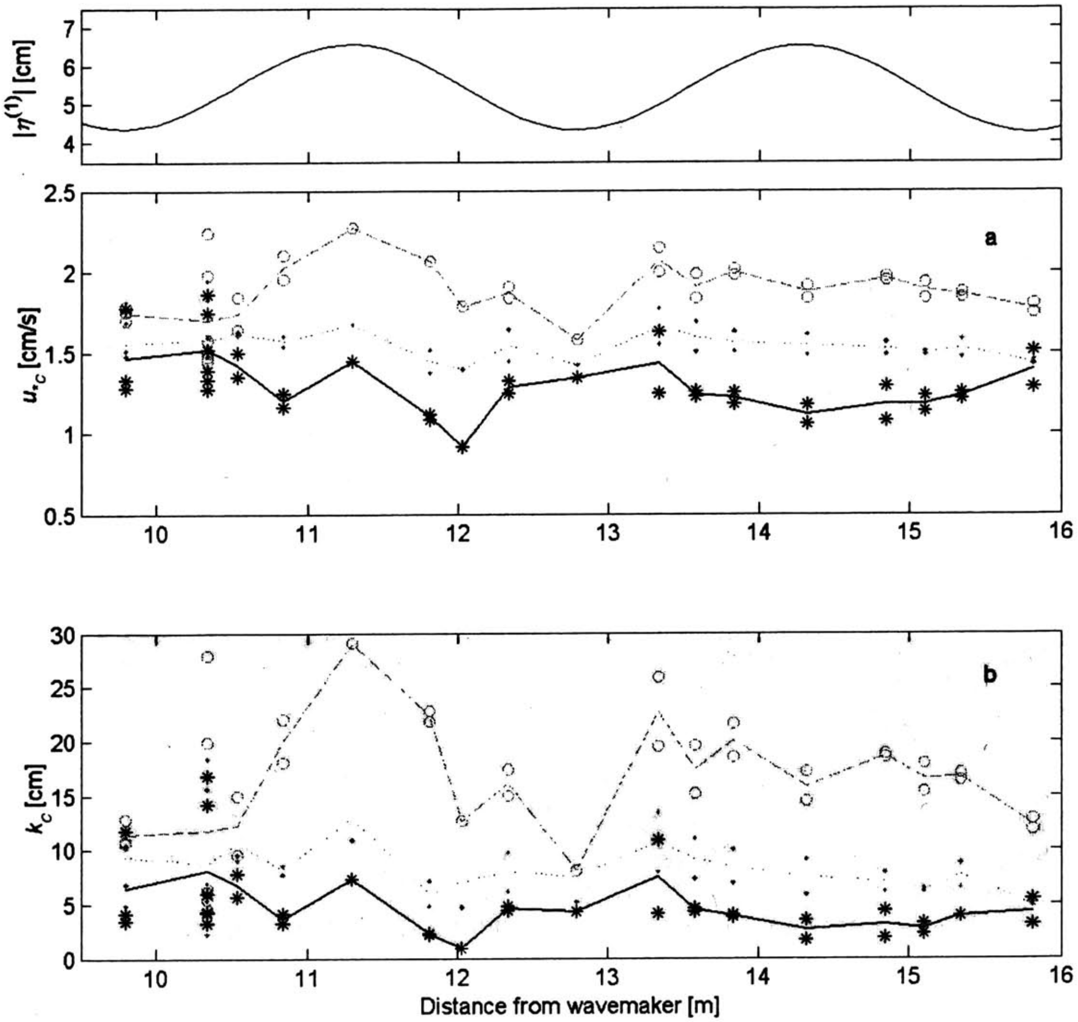

Figure 8.6: (a) u_{*c} and (b) k_c estimates from the measured pure current velocity profiles over only fully developed ripples. (o) with the dashed line are the top sublayer, (·) with the dotted line are the combined (all) points, and (*) with the solid line are the bottom points. The markers are the individual measurements at each x, while the lines are the averages at each x-location. The pure wave 1st harmonic free surface variation is shown above (a) on separate axes.

a dotted line is the average at each x location; the bottom sublayer is shown with (*) and the solid line as the average at each point. An interesting feature is the difference in relative variability between the values measured over the first beat length (9.8 to 12.79m) and the second beat length(12.79 to 15.82m). Both u_{*c} and k_c vary much more over the first beat than the second. One may suggest that this is a result of a larger variability in the ripples over the first beat.

However, the next section shows that the measured ripple geometry is nearly identical between the first and second beat. The source of this variability has not been reconciled, and increases the inaccuracy of the roughness measurements derived from measured velocity profiles.

8.5. COMPARISON OF PURE CURRENT ROUGHNESS TO RIPPLE GEOMETRY

To determine if and how the current roughness scales with the ripple geometry, comparisons are made between the measured ripple height and the calculated current roughness at each point and on the average. As hypothesized in this study, roughness felt by wave, currents, and combined waves and currents should scale with the ripple geometry as

$$k_c = \alpha\eta \quad \text{or} \quad k_c = \beta\eta\frac{\eta}{\lambda} \tag{8.3}$$

Further, we wish to examine if the parameters α and β are constant for all flows and flow types. To address these issues, Table 8.3 compares k_c obtained from the mean velocity profiles to the measured ripple height η and length λ at each x location. The columns for $\alpha = k_c/\eta$ and $\beta = k_c/[\eta(\eta/\lambda)]$ are values of the parameter α and β. The variability α is quite large, and approaches 50% of the mean value. The coefficient of variation (the standard deviation normalized by the mean) for all = 0.3, top = 0.4, and bot = 0.4. Again, it is encouraging that the lumped mean k_c compared to the mean η are nearly the same as for the straight mean values.

For the bottom sublayer, the value of $\alpha \cong 4 \pm 40\%$ and $\beta \cong 35 \pm 45\%$. While the accuracy of these estimation are quite low, the value of 4 for α has been suggested before by Madsen (1993). With this in mind, Figure 8.7 shows the measured ripple height η, u_{*c}, and k_c. In Figure 8.7 (a), u_{*c} is plotted with its error estimates of ± one standard deviation. Figure 8.7 (b) compares 4η to k_c as suggested by the above results. The correlation is quite good – 12 points out of the 17 fall within one standard deviation of the other when comparing k_c to 4η. Thus, for pure current flows, the current roughness is scaled by the actual ripple height.

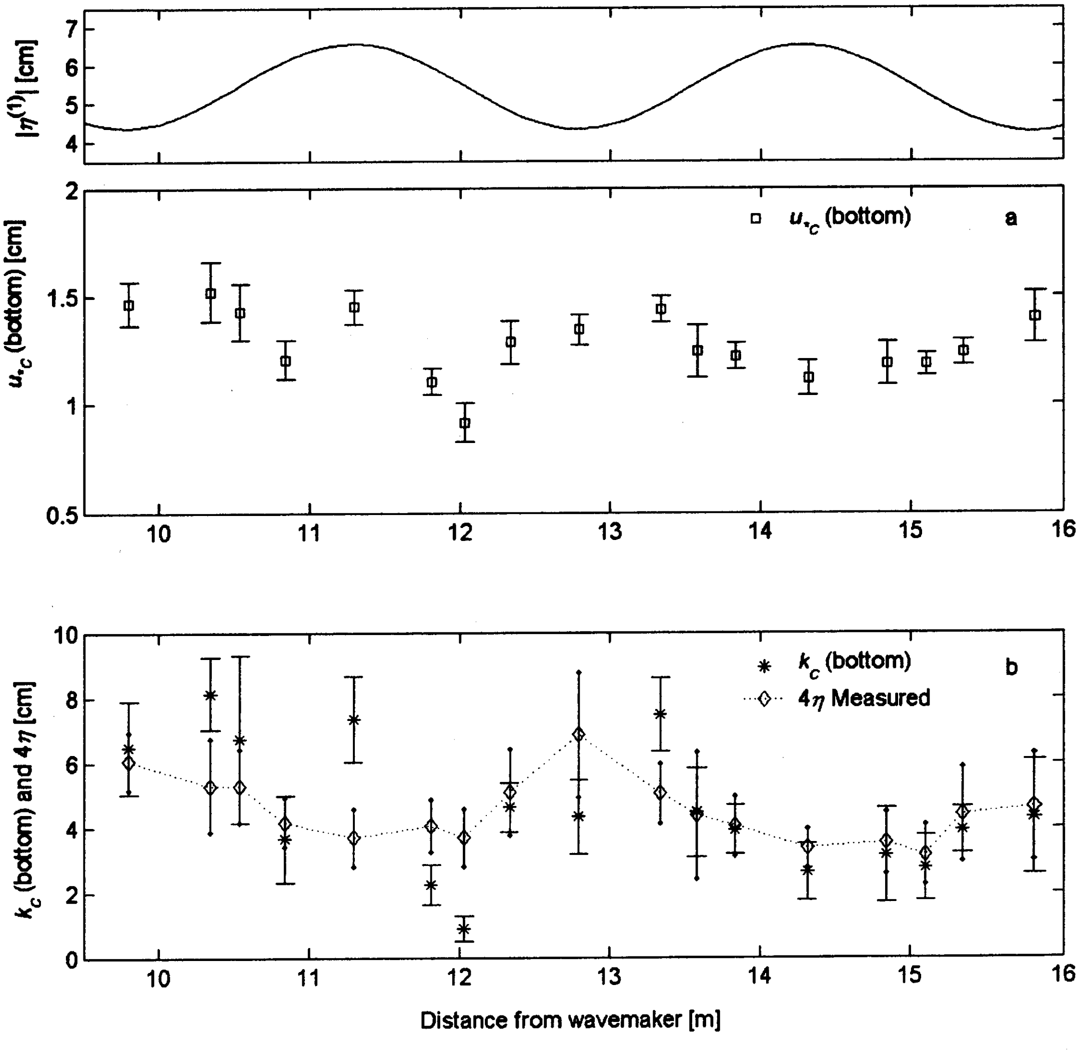

Figure 8.7: Measured ripple geometry compared with (a) pure current u_{*c} and (b) pure current k_c for the bottom sublayer of points. Error bars around the ripple height is ± one standard deviation, and denoted with solid lines ended with points; error bars around u_{*c} and k_c are ± one standard deviation from the fit, and are denoted with solid lines ended with tees. The pure wave 1st harmonic free surface variation is shown above (a) on separate axes.

Table 8.3: Comparison of pure current results to measured bedform geometry.

Expt	x	k_c [cm]			σ_{kc}	η	λ	k_c/η			$k_c/[\eta(\eta/\lambda)]$		
ID	[m]	(all)	(top)	(bot)	(bot)	[cm]	[cm]	(all)	(top)	(bot)	(all)	(top)	(bot)
a	9.80	7.36	11.40	6.46	1.31	1.51	11.28	4.86	7.53	4.26	36.17	56.07	31.76
b	10.34	8.81	11.73	8.13	1.57	1.32	9.91	6.65	8.86	6.14	49.77	66.30	45.94
c	10.54	9.31	12.24	6.72	1.99	1.32	11.07	7.02	9.24	5.07	58.68	77.19	42.35
d	10.84	8.14	20.00	3.65	1.10	1.04	9.88	7.83	19.23	3.51	74.30	182.57	33.29
e	11.29	10.88	29.06	7.34	1.17	0.92	9.36	11.78	31.48	7.95	119.49	319.24	80.67
f	11.81	5.94	22.26	2.24	0.44	1.01	9.23	5.86	21.98	2.21	53.41	200.25	20.15
g	12.03	4.73	12.67	0.89	0.64	0.92	9.48	5.13	13.73	0.97	52.74	141.11	9.94
h	12.33	7.95	16.15	4.62	1.17	1.27	10.50	6.24	12.68	3.62	51.42	104.51	29.87
I	12.79	5.18	8.11	4.33	0.84	1.71	11.97	3.03	4.74	2.53	21.19	33.20	17.71
j	13.34	10.68	22.66	7.47	0.86	1.26	10.28	8.50	18.03	5.95	69.50	147.49	48.63
k	13.58	9.12	17.35	4.45	1.59	1.09	8.29	8.34	15.86	4.07	63.19	120.25	30.86
l	13.83	8.44	20.06	3.93	0.75	1.01	8.63	8.35	19.85	3.89	71.28	169.36	33.20
m	14.31	7.47	15.80	2.64	0.89	0.84	8.00	8.89	18.80	3.14	84.65	178.94	29.89
n	14.84	7.03	18.68	3.14	0.91	0.88	9.40	7.97	21.18	3.56	84.94	225.82	37.97
o	15.10	6.32	16.62	2.76	0.52	0.79	8.80	8.00	21.03	3.49	89.00	234.02	38.85
p	15.35	7.66	16.73	3.92	0.71	1.10	9.39	6.99	15.27	3.58	59.91	130.77	30.67
q	15.82	4.92	12.35	4.32	1.13	1.16	10.47	4.24	10.64	3.72	38.27	95.95	33.58
	Mean	7.64	16.70	4.53	1.03	1.13	9.76	7.04	15.89	**3.98**	63.41	146.06	**35.02**
	Std Dev.	1.90	5.16	2.05	--	0.23	1.04	2.05	6.49	1.66	22.92	72.33	15.73
Lumped Mean		7.02	14.80	4.38	0.45	--	--	6.22	13.12	3.89	53.81	113.55	33.62

9. COMBINED WAVE-CURRENT VELOCITY EXPERIMENTS

This section briefly describes the procedures used to measure the combined wave-current velocity profiles and to obtain estimates of the bottom roughness experienced by a current in the presence of waves, k_{cw}, from the wave-current experiments. Then the results of the experiments are presented. Different methods to analyze and fit the flows are examined, including the effects of mass transport from wave streaming and from the partially standing wave. In addition, some implications of the effects of mean bed elevation are discussed, and the resulting k_{cw} values are compared with the measured ripple geometry.

9.1. WAVE-CURRENT VELOCITY PROFILE MEASUREMENT PROCEDURE

The combined wave-current velocity was measured using a Sontek ADV probe. The basic methodology for making velocity measurements is discussed in Section 3.7, and was applied to the velocity measurements here. 2048 samples were acquired at 24.333Hz, measuring exactly 32 waves. This was repeated 5 times for each point in the profile, so each point represents the characteristics derived from 160 waves. The profile consisted of 14 points measured in the vertical and were logarithmically spaced at $\Delta\ln(z) = 0.25$, covering from z = 2cm above the nearest ripple trough to z = 49cm. $z = 0$ occurred at the nearest trough to the stated x-location. This was chosen to minimize the influence that moving bedforms may have on the velocity profile. As it is impossible to eliminate effects of the ripples on the near-field (near-bottom) flow, the points within the wave boundary layer may not be accurate as the ripple may or may not move through the measuring volume over a sampling period.

The velocity profiles were measured at seventeen (17) positions along the flume, and covered two first harmonic free surface beat lengths for a total of 6m in length from x = 8.42m to 14.43m from the wavemaker. Profiles were measured at positions detailed in Table 3.3

Bedforms were measured just before and just after each velocity profile. This methodology gives the most accurate representation of the bedform geometry experienced by the flow over the measurement time period – the average ripple geometry is thought to best represent the geometry experienced by the flow.

9.2. ESTIMATING APPARENT ROUGHNESS FROM WAVE-CURRENT PROFILES

Determination of the roughness from measured wave-current velocity profiles requires a model of the wave-current boundary layer flow. In this analysis, two models were used: (1) the modified Grant and Madsen model, presented in Grant and Madsen (1986) and modified in Madsen and Salles (1998), referred to as GMm, and (2) the Linear-Constant model developed by Barreto-Acobe (2001), referred to as LC. These models were presented in Chapter 2.

As discussed in Chapter 2, the enhanced turbulence due to the wave motion within the wave boundary layer yields an enhanced apparent bottom roughness experienced by the current. This apparent bottom roughness experienced by the current flow in the presence of waves k_{ca} can be experimentally determined using the exact same procedures discussed in Section 8.2 for pure currents. The velocity measurements are plotted on a semilog plot, and a logarithmic least-squares fit made to the points in the current boundary layer. The apparent bottom roughness z_{0a} is determined from the z-intercept of the fit, and the current shear velocity u_{*c} is determined from the slope of the fit. Points near the water surface are sometimes outside of the current boundary layer and are not included in the log fit. Points near the bottom are either within the wave-boundary layer or are affected by the individual roughness elements and are also not included in the log fit.

There are two possible approaches that can be used to model the wave-current flows. The first uses a value of the bottom roughness obtained either by the other measurements (k_w, k_c, or k_{wc}), or the measured value of the bedform geometry from the bottom profiling and some relationship between the bedform geometry and bottom roughness, like equation (1.2) or equation (1.3), to specify a bottom roughness as input to the model. The velocity profile can then be predicted. The goodness of fit can be determined from equation (6.1) by comparing measured and predicted profiles, and the calculated apparent roughness can be compared to that found from the experiments by fitting the current profile in the presence of waves. This method will be referred to as setting $k_{cw} = 4\eta$.

The second approach is to use the wave-current boundary layer model and the measured velocity profile to back calculate the bottom roughness experienced by the flows. This approach gives the value of the bottom roughness required to predict the measured velocity profile, and provides a means for calculating the scaling factor α or β between the measured bottom geometry and the bottom roughness required to successfully predict the flow. The first approach shows how well the model does at predicting the velocity profile (which is of course dependant on the bottom roughness used to specify the bottom), and the second approach is used to scale the bottom geometry to obtain a fit that matches the data.

The first method requires the wave to be specified by the wave period T, horizontal bottom orbital velocity u_{bm}, and the water depth h. The current must be specified by the current shear velocity u_{*c} or shear stress, and the bottom specified by some bottom roughness. Then by following the procedures detailed in Grant and Madsen (1986) and Madsen and Salles (1998), the velocity profile is predicted.

The second method uses the values of u_{*c} and z_{0a} from the measured profile as inputs to the model to specify the current and bottom (as experienced by the current). Again, the wave is specified by the wave period T, horizontal bottom orbital velocity u_{bm}, and the water depth h. The method to calculate the bottom roughness k_{cw} is explained clearly in Mathisen (1993) and uses the z_{0a} from measurements to back calculate k_{cw}. In this study, an alternative way of determining k_{cw} was adopted which does essentially the same thing, but uses a different approach. In this alternative approach, the velocity profile is predicted with the bottom roughness initially specified by the bottom geometry. The profile is compared to the measured points, and the goodness of fit of the profile is calculated through equation (6.1). The roughness is then changed and the profile calculated again, and the goodness of the is calculated again. This procedure is iterated until the fit is maximized and the best fit determined. When the best fit is achieved, the apparent roughness of the current profile fit and that estimated by the wave-current theory are equal, thus making the two approaches essentially the same. The roughness used to calculate this fit then is the bottom roughness, and the scaling factor between the k_{cw} and η is determined as $\alpha = k_{cw}/\eta$ or $\beta = k_{cw}/[\eta(\eta/\lambda)]$. This method is referred to as the Best fit k_{cw}.

This method is more advantageous than starting from the apparent roughness and back calculating the bottom roughness for two reasons. One is that the LC model is quite cumbersome, and this direct application of the LC model is much simpler than stepping through it backwards. The second is that by maximizing the fit, the specific section of the profile that is being fit can be selected. This way, if the user so desires, individual points in the profile can be used to influence the fit or not, depending on whether or not the user deems them appropriate and real. Although this adds subjectivity to the fitting, the resulting fits more closely match the measured points than if Mathisen's (1993) approach was used.

For both methods, the accuracy of the resulting parameters, specifically k_{cw}, can be estimated from the goodness of the fit, much like in the pure current parameter estimation. The accuracy is expressed in terms of a standard deviation.

9.3. WAVE-CURRENT RESULTS FROM RAW VELOCITY PROFILES

The measured, time-averaged velocity profiles for wave-current flows are shown in Figure 9.1. All 17 profiles are displayed at their x-location relative to the free surface variation of the first harmonic and the mean bed elevation. The profiles are labeled with their respective experiment IDs and profile number. Note that for the top-most vertical point on experiment N (profile 14), the probe was out of the water in the wave troughs, resulting in invalid data for that point. This is not important, as the top point is almost always excluded from the analysis because it is usually outside the current boundary layer.

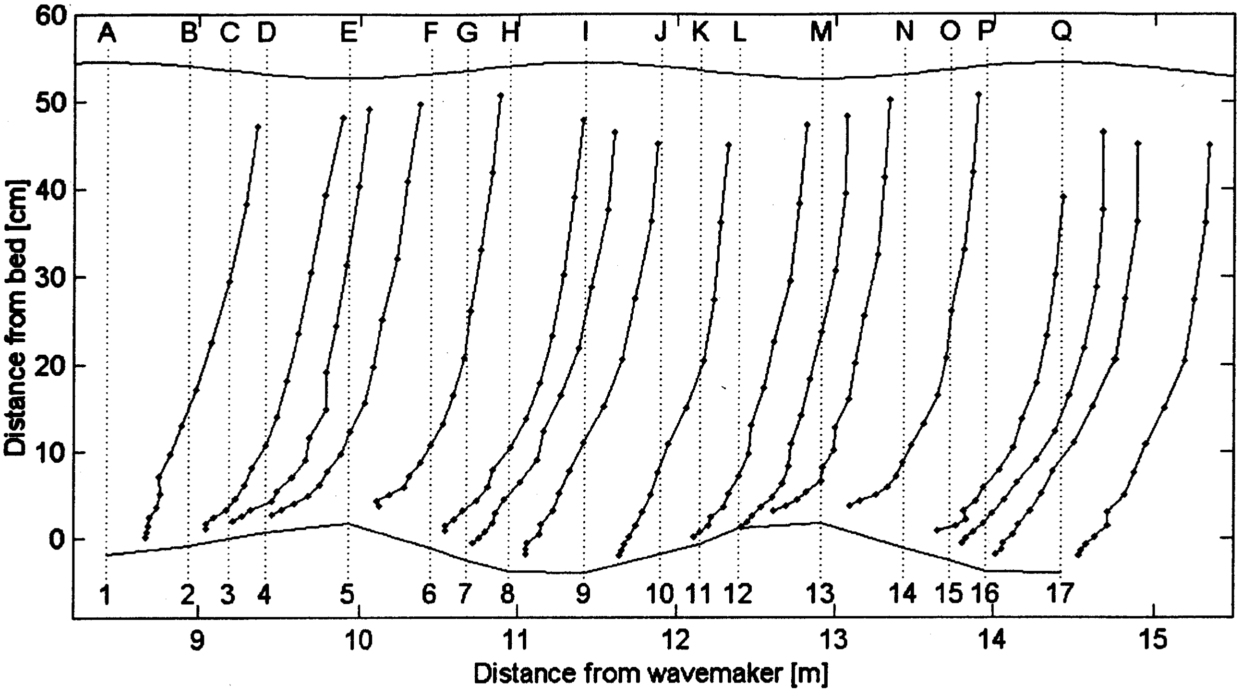

Figure 9.1: Time-averaged wave-current velocity profiles plotted over the mean bed elevation. Each profile is labeled with its experiment IDs and the corresponding profile number. Dotted vertical lines represent zero velocity for each profile.

Table 9.1 shows the experimental parameters for the wave-current flows used in the application of the GMm and the LC models. For each experiment, the water depth h is given based on the local depth, which results from the variation of the mean bed elevation. Two estimates of the depth-averaged velocity are given. The first is $u_{c,mean}$ based on u_{*c} and k_{ca}. Here, $u_{c,mean}$ was found by taking the velocity at the depth were $z = h/\mathrm{e}$, where e is the exponential function (e = 2.718...). The second is from the fact that the volumetric flow rate Q must be constant, where Q = 1200gpm or $7.57*10^{-2}$ m^3/s. Since the water depth changes with x, the velocity $u_{c,mean}$ increases or decreases with decreased or increased depth. The variations in the first method are larger than those for the second method, but the resulting mean value is approximately the same. Values are also given for the lumped mean, where the lumped mean profile is the average of profiles from A-P, and the parameters are then derived from that lumped profile. u_{bm} is the first harmonic orbital velocity near the bottom of the wave-current flows. The column labeled u_{bm} (exps) is from the measured velocity at $z \cong \delta_w \cong 6$ cm, and the column labeled u_{bm} (linear theory) is the bottom velocity calculated from knowledge of the incident and reflected wave amplitude at each point. The GMm and LC models were calculated with u_{bm} measured from experiments. η and λ are the average ripple height and length. They correspond to η_{mean} and λ_{mean} in Table 5.4.

Table 9.1: Base parameters for wave-current experiments.

Expt ID	x [m]	h [cm]	$u_{c,mean}$ from u_{*c}, k_{ca} [cm/s]	$u_{c,mean}$ from Q [cm/s]	u_{bm} (exps) [cm/s]	u_{bm} (linear theory) [cm/s]	η [cm]	λ [cm]
A	8.42	61.82	14.21	16.07	13.27	16.85	1.71	11.66
B	8.93	60.86	14.84	16.32	15.18	18.48	1.78	11.62
C	9.18	59.94	14.95	16.57	17.80	20.17	1.97	12.90
D	9.41	59.31	16.06	16.75	20.89	21.85	2.27	14.19
E	9.93	58.32	17.04	17.03	24.06	23.63	2.67	17.41
F	10.45	61.11	16.84	16.26	20.25	21.36	1.45	12.08
G	10.68	62.55	15.23	15.88	18.00	19.57	1.26	10.14
H	10.95	63.82	15.20	15.57	15.63	17.89	1.20	9.74
I	11.42	64.00	16.14	15.52	13.18	16.52	1.49	9.79
J	11.90	61.80	15.74	16.08	14.61	18.18	1.55	10.80
K	12.15	60.67	16.54	16.37	16.40	19.89	1.85	11.85
L	12.40	58.87	17.14	16.88	18.79	21.81	2.11	15.15
M	12.92	58.32	18.15	17.03	22.56	23.53	2.17	15.43
N	13.43	61.11	19.92	16.26	22.51	21.24	1.84	13.30
O	13.73	62.55	18.77	15.88	18.13	19.45	1.23	9.42
P	13.95	63.82	17.33	15.57	15.90	17.79	1.07	8.28
Q	14.43	64.00	16.33	15.52	13.01	16.40	1.06	7.44
Mean	--	61.345	16.50	16.21	17.66	19.68	1.69	11.83
Std. Dev.	--	1.953	1.49	0.52	3.47	2.30	0.46	2.67
Lumped Mean	--	--	16.39	16.19	--	--	--	--

Now, with the ripple geometry known, the wave-current velocity profiles can be predicted for each position in x, and for the lumped mean profile. By taking the bottom roughness k_{cw} to be 4η at each position, the GMm and LC models were used to estimate the velocity profiles. Figure 9.2 shows the measured and predicted velocity profiles, where (a) is the profile from experiment O

(15), and (b) is the lumped mean profile. The points (·) are the measured velocity profile, and the points with open circles around them are the data points used to obtain k_{ca} and u_{*c}. The solid line is the WC profile based on the GMm model, and the dashed line is from the LC model. Obviously, both models severely over predict the measured velocity.

For the LC model, it is possible that the definition of the scaling parameter of the ripple height α (or β)should be different than 4 (or 24), as was suggested for the GMm model. The values of α and β are model-specific, and depend on the model's definition of the boundary layer height. When better fits to the measured data for the GMm model are available, the appropriate values of α and β will be determined by calculating $k_{cw,LC}/\eta$ and $k_{cw,LC}/\,[\eta(\eta/\lambda)]$, thus determining α and β for the LC model. For now, the LC model fitting will be kept at $k_{cw} = 4\eta$ for comparison and consistency across the different analyses.

By using the best fit k_{cw} method where k_{cw} is varied until the best fit is obtained, profiles are predicted that are required to fit the data well. Figure 9.3 shows these best-fit profiles for (a) experiment O and (b) the lumped mean. The points are the measured velocity profiles, and the points with open circles are the points used in obtaining the best fit k_{cw}. In these plots, especially Figure 9.3 (b), the benefit of the LC model is illustrated, where the model follows the data points well, especially in the wave boundary layer.

Parameters of the fits are shown in Table 9.2 and Table 9.3. The parameters are given for all experiments A-Q, the mean of all the experimental fits (here, A-Q), the standard deviation of the parameters across the 17 profile fits, and the parameters resulting from using the lumped mean profile. Table 9.2 shows the experiments that can be compared with the resulting parameters of the modified analyses that are performed in Sections 9.4 and 9.5. Not all experiments could be analyzed in these sections, as will be explained later. Table 9.3 shows the other experiment that were left out of Table 9.2. The top half of the tables, labeled $k_{cw} = 4\eta$, shows the fit of the current profile in the presence of waves, where u_{*c} and k_{ca} are determined from the measured points (6:10), where (6:10) reflects that points 6 through 10 were used in determining the fit. The points selected to be used to determine the fit were selected because they were the only points in the current boundary layer. Just as in Section 8.2, some points are either in the wave boundary layer or above the current boundary layer, and should be excluded from the fit. Note that not every profile was fit from points 6 to 10. This is because some points, especially near the top of the profile as x increases, are within the boundary layer because it has had more time to develop, and should be included. (6:10) should be regarded as the average points used to make the fit, and not exclusively used for each profile. The standard deviations of the fit, σ_{u*c} and σ_{kca}, are presented, along with the value used for the bottom roughness, 4η. The top half also shows the parameters that result from the fit of the GMm and LC modeled profiles, where the bottom roughness was input as 4η: k_{ca} GMm, k_{ca} LC, and their respective goodness of fit, labeled error GMm and error LC, based on equation (6.1). The error is really as standard deviation between the measured and predicted profiles, and is in units of cm/s. Comparing k_{ca} from the model predictions to the experimental values shows quantitatively what was shown in Figure 9.2 – the fit is bad. The experimental values of z_{0a} are 30% to 70% larger than the fit values for GMm, and 75% to 90% larger for the LC model.

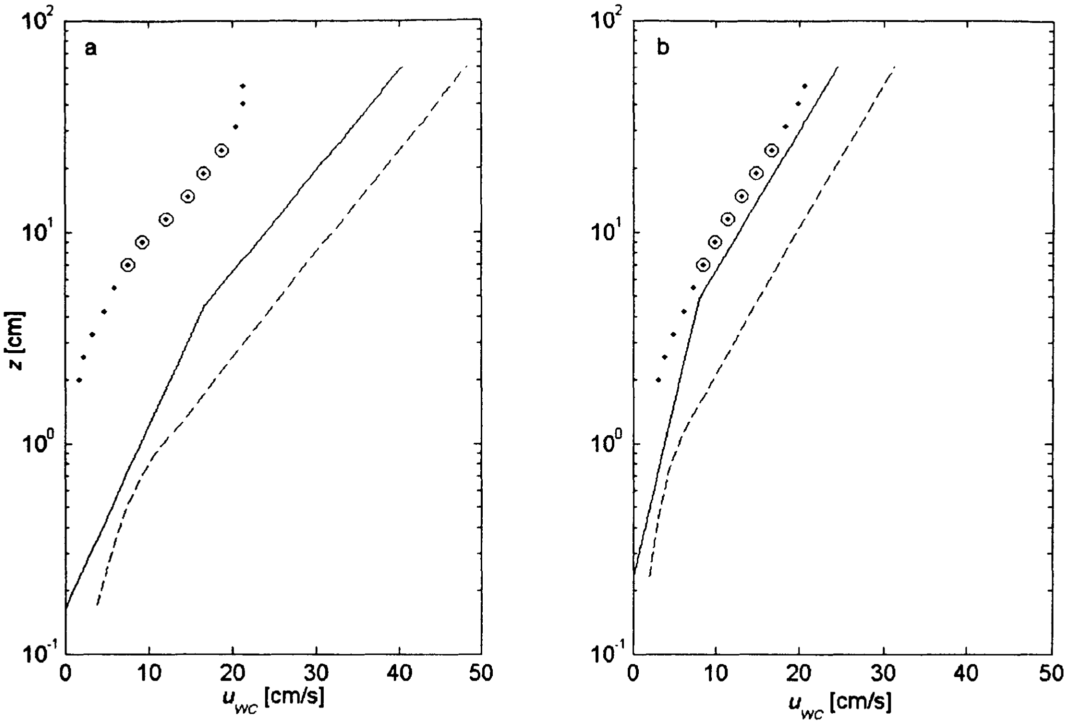

Figure 9.2: Wave-current velocity profiles for (a) experiment O and (b) lumped mean. Solid line is GMm and dashed line is LC predictions using $k_{cw} = 4\eta$.

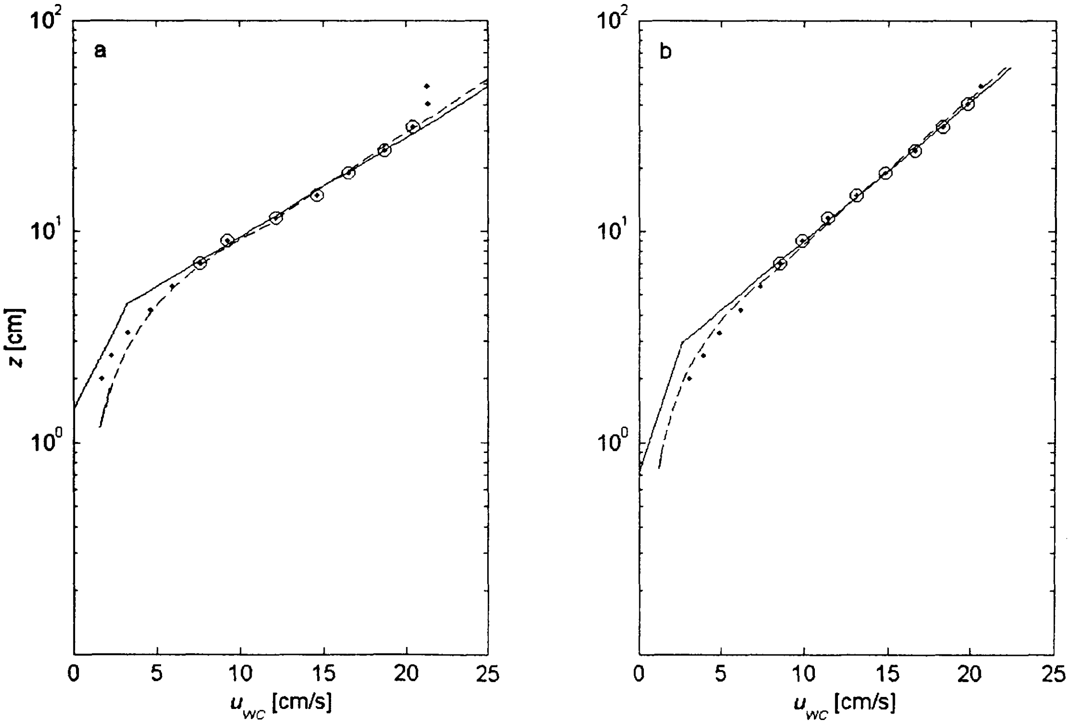

Figure 9.3: Wave-current velocity profiles for (a) experiment O and (b) lumped mean. Fit is the best fit k_{cw}. Solid line is GMm model, dashed is LC model.

The bottom half of Table 9.2 and Table 9.3, labeled Best fit k_{cw}, shows the roughness k_{cw} required to obtain the best fit to the experimental data for both models, and their respective standard deviations. The best fit is generally evaluated over the points that are in the current boundary layer. This is typically points 6 through 10, but can vary from point 4 to point 14. k_{ca} resulting from these predictions are shown. These k_{ca} values should be the same as those from the experimental determination shown in the row k_{ca} (6:10). While these values are not exactly the same, they are well within our ability to predict them.

The best fit k_{cw} values in Table 9.2 are quite high – much higher than the values expected if the bottom roughness is to scale the same for all flow types (at least for the individual profiles; the lumped mean is fairly well predicted by the GMm model). The row $\alpha = k_{cw}/\eta$ is the value of α in equation (1.2) , and the row $\beta = k_{cw}/[\eta(\eta/\lambda)]$ is the value of β in equation (1.3). These values α and β are used to scale the bedform height to the necessary bottom roughness. The value of 8.2 for the GMm model is about two times larger than the expected value of 4, commonly used to scale the bedform height. Mathisen and Madsen (1996b) had a similar problem in predicting the velocity profiles accurately. They found that is was necessary to account for wave-induced mass transport to obtain reasonable results. This is discussed and applied in the next section.

Table 9.2: Results for wave-current experiments on the raw velocity profiles (part 1 of 2) - for comparison with Table 9.6.

		Expt A	Expt C	Expt E	Expt G	Expt I	Expt K	Expt M	Expt O	Expt Q	Mean	Standard Deviation	Lumped Mean
$k_{cw} = 4\eta$													
u_{*c} (6:10)	[cm/s]	3.03	2.04	2.37	3.28	2.89	1.77	2.37	3.76	3.35	2.76	0.65	2.69
σ_{u*c}	[cm/s]	0.17	0.26	0.11	0.19	0.33	0.15	0.17	0.14	0.24	0.19	0.08	0.07
k_{ca} (6:10)	[cm]	104.50	35.19	36.19	107.56	75.73	16.08	29.99	93.77	100.44	65.37	35.89	59.29
σ_{kca}	[cm]	8.72	11.14	3.94	8.27	14.15	4.57	5.62	5.13	10.04	7.58	3.62	3.06
4η	[cm]	6.83	7.88	10.69	5.05	5.96	7.39	8.69	4.91	4.24	6.75	1.84	6.75
k_{ca} GMm	[cm]	38.06	64.08	87.16	26.52	29.86	65.88	72.12	22.19	17.87	46.07	22.55	43.14
k_{ca} LC	[cm]	168.77	183.82	224.49	186.40	167.42	175.85	213.44	9.41	167.84	16.47	7.00	15.32
error GMm	[cm/s]	4.04	2.91	4.64	11.44	6.40	6.41	4.81	14.30	14.31	7.30	5.28	2.28
error LC	[cm/s]	10.55	3.47	1.54	19.05	13.26	1.75	1.58	22.30	21.27	10.76	8.55	9.14
Best fit k_{cw}													
k_{cw} GMm	[cm]	20.04	4.16	4.17	20.34	14.70	1.53	3.42	19.93	22.16	11.97	8.83	9.29
k_{cw} LC	[cm]	54.81	13.22	13.51	56.70	41.58	5.08	11.13	56.25	60.83	33.84	23.27	27.61
σ_{kcw} GMm	[cm]	7.71	5.67	1.89	7.44	11.61	1.69	2.57	4.62	9.60	5.72	4.03	2.04
σ_{kcw} LC	[cm]	17.44	13.63	4.46	16.90	24.80	3.66	5.76	9.28	19.81	12.46	8.45	4.66
k_{ca} GMm	[cm]	101.03	35.46	36.68	109.27	75.48	15.53	30.22	96.33	102.11	66.02	36.91	59.06
k_{ca} LC	[cm]	110.82	36.51	37.79	120.58	82.51	15.69	30.94	106.50	113.44	63.35	41.23	62.94
error GMm	[cm/s]	0.68	0.53	0.32	0.66	0.66	0.54	0.38	0.56	0.55	0.49	0.15	0.17
error LC	[cm/s]	0.88	0.52	0.30	0.52	0.70	0.55	0.36	0.39	0.63	0.48	0.21	0.29
$\alpha = k_{cw,\mathrm{GMm}} / \eta$		11.73	2.11	1.56	16.10	9.87	0.83	1.57	16.23	20.90	**8.88**	8.21	**5.50**
$\alpha = k_{cw,\mathrm{LC}} / \eta$		32.09	6.71	5.06	44.88	27.92	2.75	5.12	45.79	57.38	24.85	21.84	16.37
$\beta = k_{cw,\mathrm{GMm}} / [\eta(\eta/\lambda)]$		80.12	13.80	10.17	129.17	64.91	5.33	11.16	124.40	146.64	**66.16**	63.69	**38.61**
$\beta = k_{cw,\mathrm{LC}} / [\eta(\eta/\lambda)]$		219.13	43.90	32.93	360.11	183.54	17.64	36.36	351.00	402.52	184.88	169.83	114.80

Table 9.3: Results for wave-current experiments on the raw velocity profiles, (part 2 of 2).

		Expt B	Expt D	Expt F	Expt H	Expt J	Expt L	Expt N	Expt P
k_{cw} = 4η									
u_{*c} (6:10)	[cm/s]	2.50	2.51	3.18	3.28	2.03	1.86	2.84	3.92
σ_{u*c}	[cm/s]	0.09	0.12	0.20	0.34	0.14	0.16	0.11	0.29
k_{ca} (6:10)	[cm]	62.32	50.40	80.88	110.15	30.66	16.43	40.68	120.31
σ_{kca}	[cm]	4.18	5.15	8.38	14.96	5.48	4.46	3.67	10.94
4η	[cm]	7.10	9.09	5.78	4.81	6.21	8.45	7.34	4.29
k_{ca} GMm	[cm]	45.56	67.32	34.38	22.97	46.84	77.55	48.17	16.75
k_{ca} LC	[cm]	176.69	207.21	197.70	176.76	162.58	194.78	199.72	187.69
error GMm	[cm/s]	2.13	2.00	7.27	12.46	2.52	7.19	1.71	19.59
error LC	[cm/s]	8.43	5.33	15.01	19.79	3.06	2.36	7.00	27.19
Best fit k_{cw}									
k_{cw} GMm	[cm]	9.74	6.65	13.84	22.39	3.86	1.49	6.27	28.73
k_{cw} LC	[cm]	28.61	20.57	40.18	61.56	12.07	5.03	19.08	75.00
σ_{kcw} GMm	[cm]	2.86	2.96	6.40	14.24	2.77	1.58	2.16	11.55
σ_{kcw} LC	[cm]	6.80	7.07	14.43	31.00	6.23	3.47	4.50	22.53
k_{ca} GMm	[cm]	62.04	50.13	82.33	112.11	29.75	16.03	41.20	126.66
k_{ca} LC	[cm]	66.27	52.59	88.98	124.51	30.52	16.23	43.09	0.00
error GMm	[cm/s]	0.20	0.28	0.40	0.54	0.53	0.43	0.35	0.74
error LC	[cm/s]	0.32	0.34	0.53	0.78	0.55	0.44	0.33	0.00
$\alpha = k_{cw,\,GMm} / \eta$		5.49	2.93	9.58	18.60	2.49	0.71	3.42	26.82
$\alpha = k_{cw,\,LC} / \eta$		16.12	9.05	27.80	51.15	7.78	2.38	10.40	70.01
$\beta = k_{cw,\,GMm} / [\eta(\eta/\lambda)]$		35.92	18.28	80.04	150.46	17.30	5.06	24.74	207.30
$\beta = k_{cw,\,LC} / [\eta(\eta/\lambda)]$		105.49	56.52	232.32	413.78	54.10	17.07	75.32	541.18

9.4. WAVE-CURRENT RESULTS INCLUDING WAVE-INDUCED MASS TRANSORT

9.4.1. MASS TRANSPORT FROM WAVE STREAMING AT THE BOUNDARY LAYER

Mathisen and Madsen (1996b) (MM) found that the mass transport resulting from a time-varying eddy viscosity predicted by Trowbridge and Madsen (1984a, b) (TM) interacts with the wave-current velocity. They further suggested that the resulting mass transport (wave streaming) at the edge of the wave or wave-current boundary layer effectively shifts the wave-current velocity profile by the same order of magnitude as the wave streaming. So to remove this effect, the value of the wave streaming at the edge of the wave or wave-current boundary layer should be subtracted from the entire profile. Since the model derived for the wave streaming by TM cannot predict the wave streaming for large values of the relative roughness, the wave streaming must be determined experimentally. This was verified to be correct in MM (and with more detail in Mathisen, 1993). Therefore, the value of the time-averaged pure wave velocity profiles (shown in Section 7.2.1) at $z = \delta_{wc} \cong$ 6cm were used. Unfortunately, the pure wave velocity profiles were only measured at 5 locations: a node, upslope, antinode, downslope, and node, shown in Table 3.3, while the wave-current velocity profiles were measured at 17 locations, only 9 of which occurred at the same locations relative to the location on the beat. To extend the data set, we assumed that the pure wave-induced velocity over one beat was the same for each separate beat. Therefore, we applied the values for the position of the pure wave velocity profile to all positions, relative to the partially standing wave beat. For example, the pure wave velocity profile measured at the upslope at position C for the pure wave was applied to the wave-current profiles at the upslopes at positions G and O. This resulted in 9 wave-current profiles available for further analysis.

Figure 9.4 shows the velocity profiles corrected for mass transport by subtracting the values of the wave streaming at the wave boundary layer height from the corresponding PW velocity profile. Figure 9.4 (a) is for experiment O, and (b) is the lumped mean. To obtain the lumped mean, the individual profiles were corrected for the mass transport, then averaged.

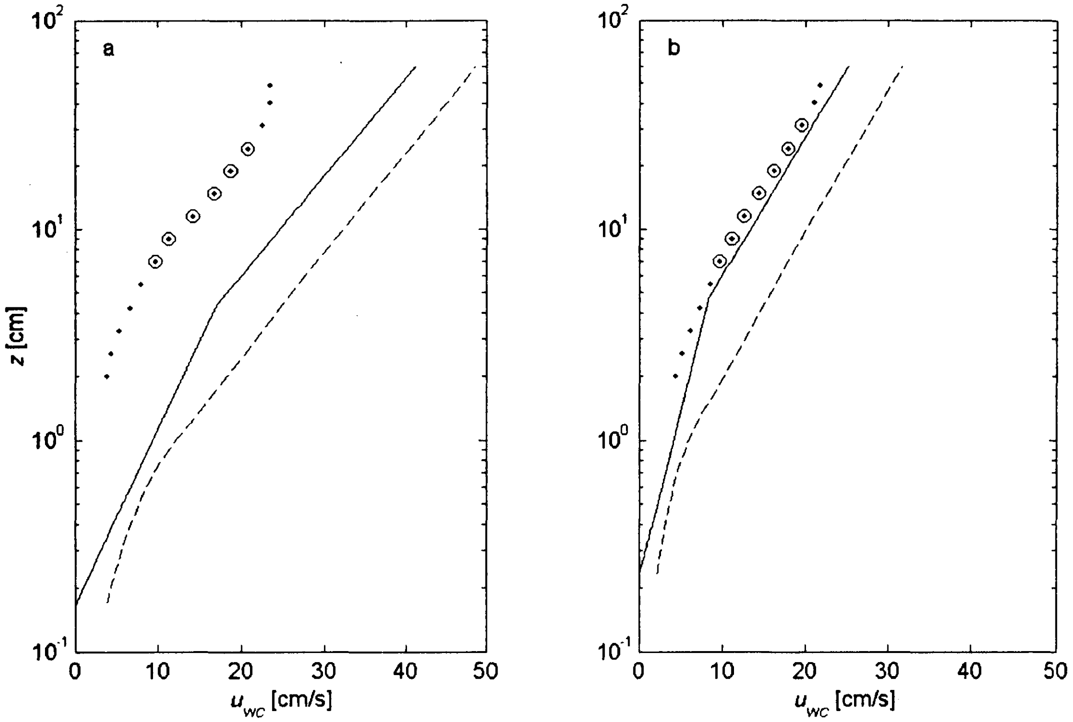

Figure 9.4: Wave-current velocity profiles for (a) experiment O and (b) lumped mean with mass transport as a constant at pure wave velocity at $z = \delta_w$. Solid line is GMm and dashed line is LC predictions with $k_{cw} = 4\eta$.

The predictions with the GMm and LC models here are only slightly better than with no correction at all. Table 9.4 shows the results of the predictions and fits for this case. The table is set up the same as Table 9.2, except that only the results for experiment O, the straight mean, and the lumped mean are shown. The k_{cw} necessary to fit the data to the GMm model was reduced from 19cm to 15cm for experiment O, but did not decrease on the average. The variability also did not decrease. The value of α on the mean did not decrease, but for the lumped average was reduced from 5.5 to about 4.6 – very close to the value of 4 as suggested earlier and by the CEM (2001, Part III Chapter 6) and Madsen (1993).

Table 9.4: Results for wave-current experiments, mass transport from pure wave velocity at $z = \delta_w$.

		Expt 0	Mean	Standard Deviation	Lumped Mean
k_{cw} = 4η					
u_{*c} (6:10)	[cm/s]	3.76	2.80	0.69	2.69
σ_{u*c}	[cm/s]	0.14	0.20	0.07	0.07
k_{ca} (6:10)	[cm]	74.29	59.86	32.69	50.12
σ_{kca}	[cm]	4.68	7.68	3.59	2.80
4η	[cm]	4.91	6.85	2.06	6.75
k_{ca} GMm	[cm]	20.44	45.36	21.92	39.90
k_{ca} LC	[cm]	8.94	16.32	6.76	14.45
error GMm	[cm/s]	12.77	7.39	3.97	1.59
error LC	[cm/s]	20.51	10.37	8.42	8.36
Best fit k_{cw}					
k_{cw} GMm	[cm]	15.76	11.19	8.13	7.82
k_{cw} LC	[cm]	45.09	31.95	21.91	23.48
σ_{kcw} GMm	[cm]	3.89	5.51	3.49	1.77
σ_{kcw} LC	[cm]	7.48	11.34	7.71	3.90
k_{ca} GMm	[cm]	75.75	60.12	32.84	49.92
k_{ca} LC	[cm]	82.91	65.15	37.16	52.72
error GMm	[cm/s]	0.41	0.52	0.16	0.17
error LC	[cm/s]	0.48	0.56	0.22	0.26
$\alpha = k_{cw,\,\mathrm{GMm}} / \eta$		12.83	**8.14**	7.01	**4.64**
$\alpha = k_{cw,\,\mathrm{LC}} / \eta$		36.71	23.10	19.21	13.92
$\beta = k_{cw,\,\mathrm{GMm}} / [\eta(\eta/\lambda)]$		98.32	**58.43**	50.98	**32.52**
$\beta = k_{cw,\,\mathrm{LC}} / [\eta(\eta/\lambda)]$		281.39	165.79	140.40	97.64

This curious result – that the individual profiles are far from being predicted correctly, but that the lumped mean case is predicted quite well – leads to the observation that the lumped mean case effectively removes the influence of the partially standing wave. If the mass transport from wave streaming can influence the wave-current velocity so much, it is quite possible that the mass transport associated with the standing wave also influences the wave-current velocity profile.

9.4.2. MASS TRANSPORT FROM WAVE STREAMING AND THE PARTIALLY STANDING WAVE

In light of this observation, the wave-current velocity profiles can be corrected for the mass transport associated with the wave streaming and with the partially standing wave by subtracting the entire PW velocity profiles shown in Figure 7.2 from the corresponding WC velocity profile. This is done just as in Section 9.4.1 for 9 profiles where the pure wave profiles correspond to the same relative location in the beat as the wave-current profiles. Then the GMm and LC models can be once again used to predict the resulting velocity profiles, as illustrated in Figure 9.5.

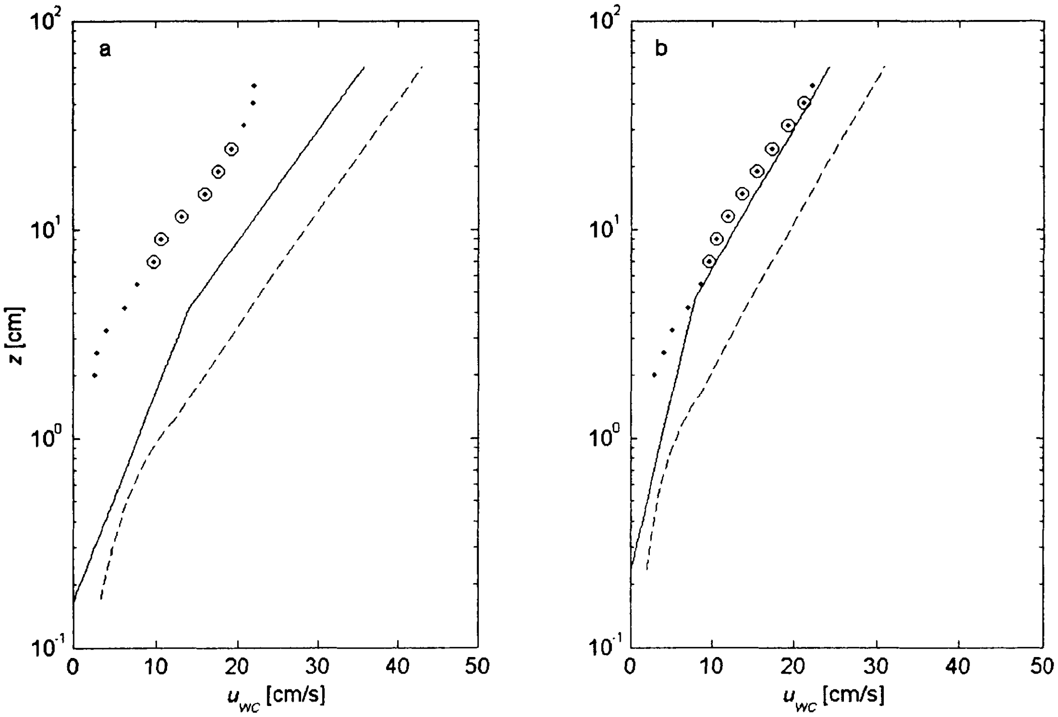

Figure 9.5: Wave-current velocity profiles for (a) experiment O and (b) lumped mean with mass transport from entire pure wave velocity profile. Solid line is GMm and dashed line is LC predictions with $k_{cw} = 4\eta$.

Table 9.5: Results for wave-current experiments, mass transport from pure wave velocity profiles.

		Expt O	Mean	Standard Deviation	Lumped Mean
$k_{cw} = 4\eta$					
u_{*c} (6:10)	[cm/s]	3.35	2.86	0.48	2.63
σ_{u*c}	[cm/s]	0.22	0.22	0.10	0.16
k_{ca} (6:10)	[cm]	67.69	65.04	32.45	50.89
σ_{kca}	[cm]	7.78	9.05	4.77	6.55
4η	[cm]	4.91	6.85	2.06	6.75
k_{ca} GMm	[cm]	22.91	43.38	19.46	40.79
k_{na} GMm	[cm]	13.63	22.15	8.00	21.30
k_{ca} LC	[cm]	9.45	15.65	6.05	14.66
error GMm	[cm/s]	9.91	6.67	4.05	1.61
error LC	[cm/s]	17.29	10.57	7.56	8.10
Best fit k_{cw}					
k_{cw} GMm	[cm]	13.07	12.04	8.41	7.72
k_{cw} LC	[cm]	38.07	34.12	21.77	23.22
σ_{kcw} GMm	[cm]	6.01	6.88	4.64	4.12
σ_{kcw} LC	[cm]	12.17	15.34	4.48	9.18
k_{ca} GMm	[cm]	68.62	65.20	32.85	50.35
k_{ca} LC	[cm]	74.86	77.07	52.34	53.11
error GMm	[cm/s]	0.55	0.57	0.34	0.39
error LC	[cm/s]	0.54	0.85	1.06	0.44
$\alpha = k_{cw,\,\mathrm{GMm}} / \eta$		10.64	**8.43**	6.72	**4.58**
$\alpha = k_{cw,\,\mathrm{LC}} / \eta$		30.99	23.81	18.00	13.76
$\beta = k_{cw,\,\mathrm{GMm}} / [\eta(\eta/\lambda)]$		81.55	**59.68**	47.69	**32.11**
$\beta = k_{cw,\,\mathrm{LC}} / [\eta(\eta/\lambda)]$		237.59	168.69	128.69	96.55

Figure 9.5 shows the measured WC profiles corrected by subtracting the PW velocity profiles for (a) experiment O and for (b) the lumped mean. The points are the measured profiles and the points with open circles are the data points used to obtain k_{ca} and u_{*c}. The GMm and LC models are used to predict the velocity profiles, shown by the solid and dashed lines, respectively. Table 9.5 displays the results of the predictions and fits just as Table 9.4 did for the WC profiles corrected for pure wave velocity at $z = \delta_w$. Here, the fit to the experiment O is not significantly improved. The results are similar to the case shown in Section 9.4.1: these profiles show a large

mean, and a standard deviation that is the same order of magnitude as the value itself. α and β remain unchanged. The lumped mean case has also not shown any real improvement.

9.5. WAVE-CURRENT RESULTS INCLUDING WAVE-INDUCED MASS TRANSPORT AND LOCAL BED ELEVATION

The mean bed elevation for the combined wave-current case varies about 10cm vertically along the two measured beat lengths. Velocity profiles at different locations in x will experience a different water depth, and the velocity measurements are made at different vertical locations in the water column relative to one another. This is illustrated in Figure 9.1. If the profiles are measured in an absolute coordinate system where the vertical positions of profile points are referenced to the same elevation, the change in vertical position relative to the water column is accounted for. So by using the mean bed elevation at each measurement location, the profiles are vertically adjusted to have the same absolute zero, where absolute zero is chosen as the initial elevation of the plane bed.

By using the profiles adjusted for the variation in the mean bed and correcting for the total mass transport by subtracting the PW velocity profile (also adjusted to the absolute coordinate system) from the WC velocity profile at their respective x-locations, we can obtain a better representation of the WC velocity profiles. Note that with this correction, some of the points will now have a negative z-elevation. These points are excluded from the plots and fitting routines. The results of these corrections are plotted on Figure 9.6 (a) along with the predictions of the GMm and LC models. The points ($\cdot$) are the corrected measured data points, and the points with open circles are the data points used to determine k_{ca} and u_{*c}. The comparison between the measured and predicted here are quite good for the GMm model. These results are with the roughness k_{cw} defined as 4η for each location.

Figure 9.6 (b) shows the fit of the models when the roughness k_{cw} is varied to the best fit k_{cw}, as was done for Figure 9.3. Again, the points (·) are the corrected measured data points and the points with open circles are the points used in determining the best fit k_{cw}. Comparing the GMm model in Figure 9.6 (a) and (b) shows almost no difference in the profiles. Of course, the LC model shows a large variation, but this is because the value of $\alpha = 4$ used in Figure 9.6 is not correct for this model, and should be somewhat larger due to the definition of its wave-current boundary layer thickness.

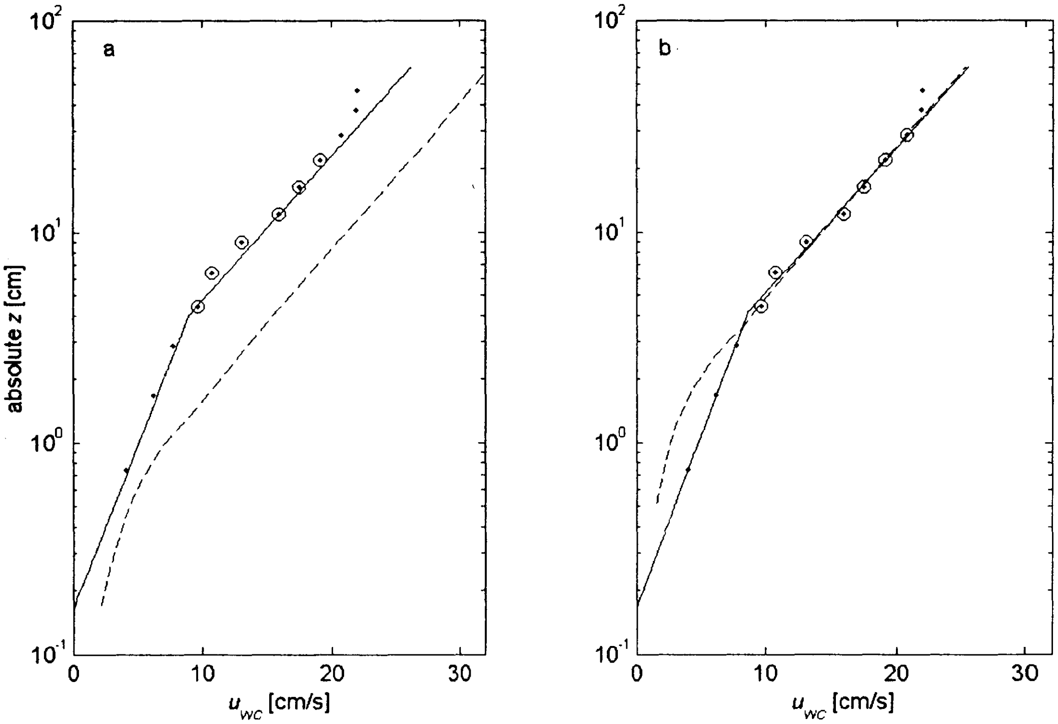

Figure 9.6: Wave-current velocity profiles for experiment O with mass transport from the entire pure wave velocity profile, and $z = 0$ at absolute mean bed elevation. (a) is shows the predictions of GMm and LC predictions with $k_{cw} = 4\eta$ as the solid line and dashed line, respectively, and (b) is the best fit k_{cw} for both the GMm and the LC models.

For this correction in vertical elevation for each profile, combining the data through a lumped mean is not as practical as before when the elevations were from the local depths. Figure 9.7 shows all the profiles corrected to the absolute mean elevation, plotted as points (·). The velocities near the bottom vary widely, and the variation in velocity decreases somewhat as the distance from the mean bed is increased. The illustrates the benefit of choosing the absolute mean elevation to evaluate the profiles. The points near the bottom show more of the effect of the variation of the mean bed elevation. At about 10cm off the absolute zero elevation ($z = 10$cm), the influence of the bottom variation decreases. This is quite similar the results shown in MM, where the effects of the individual ripple were felt to about 2 ripple heights above the bottom. Here, the mean bed variation extends about 5cm above absolute zero, and its effects are felt to about 10cm, or two times this height.The solid line on Figure 9.7 is the prediction of the current velocity profile based on the GMm model, with all parameters taken from the straight mean of all profiles. The straight mean is shown in Table 9.6.

Table 9.6 shows the results for all the corrected profiles. The table is set up just as the other tables in this chapter have been, except that the results for all the profiles are shown. The mean values for k_{cw} GMm and LC are still quite variable across the two beats; the standard deviations are more than half the magnitude of the mean. However, the mean values are on the order of magnitude that we would expect, as shown in the rows $\alpha = k_{cw} / \eta$. For the GMm model, $\alpha = 4 \pm 50\%$ and $\beta = 30 \pm 65\%$, and for the LC model, $\alpha = 12 \pm 50\%$ and $\beta = 90 \pm 60\%$.

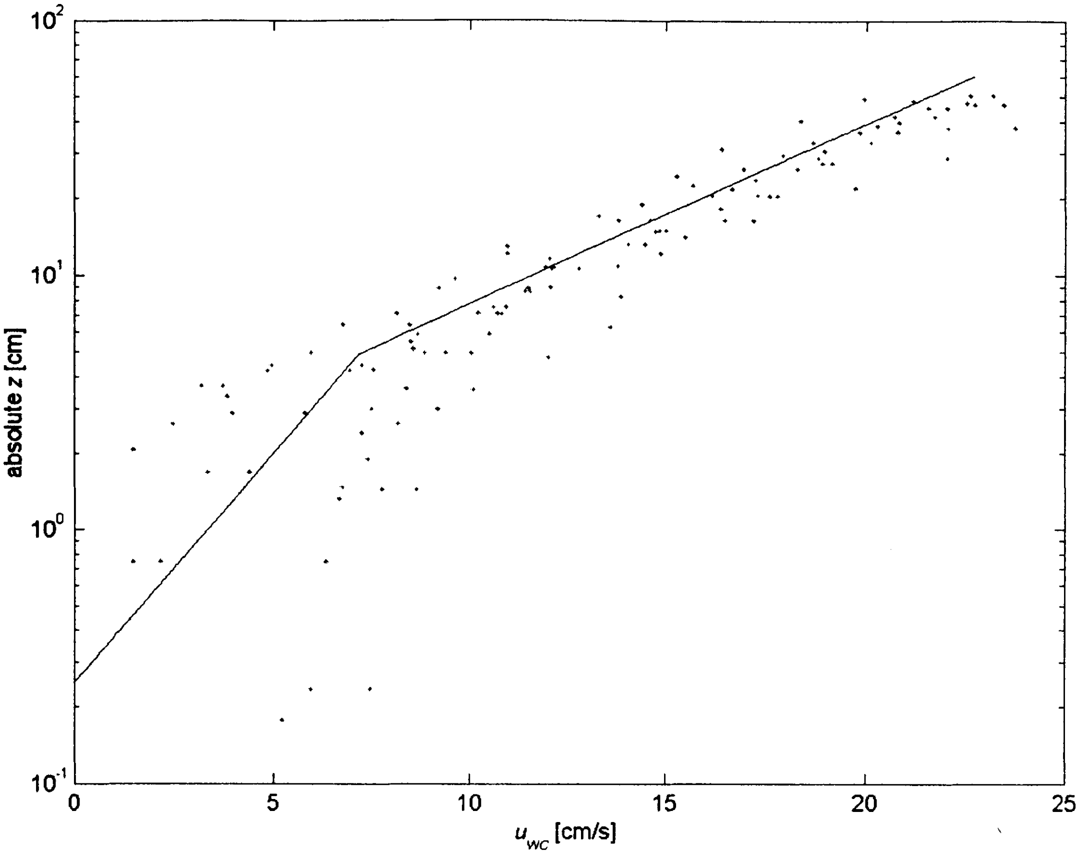

Figure 9.7: Wave-current velocity profiles plotted at the absolute z elevations. Points (·) are the individual measured data points, and the solid line is the prediction of the velocity based on the GMm model calculated with the parameters from the straight mean, shown in Table 9.6.

9.6. COMPARISON OF WAVE-CURRENT ROUGHNESS AND RIPPLE GEOMETRY

Now with velocity profiles where the effects of the mass transport and the variation in the mean bed have more or less been removed, the variation in ripple height can be compared to the bottom roughness experienced by the wave-current flows.

Figure 9.8 compares the measured ripple height with k_{cw} determined from fitting the experimental results with the (a) GMm model and (b) the LC model. For both of the bottom roughness values shown, the mass transport is accounted for by the entire PW velocity profile.

Table 9.6: Results for wave-current experiments, mass transport from pure wave velocity profiles, $z = 0$ at absolute mean bed elevation.

		Expt A	Expt C	Expt E	Expt G	Expt I	Expt K	Expt M	Expt O	Expt Q	Mean	Standard Deviation
k_{cw} = 4η												
u_{*c} (6:10)	[cm/s]	3.25	2.63	2.54	2.27	2.07	2.55	2.57	2.60	2.35	2.54	0.32
σ_{u*c}	[cm/s]	0.30	0.19	0.08	0.09	0.23	0.27	0.09	0.13	0.19	0.18	0.08
k_{ca} (6:10)	[cm]	94.47	60.18	42.34	37.67	23.72	39.03	36.54	31.97	34.11	44.45	21.17
σ_{kca}	[cm]	14.74	8.89	3.20	3.61	7.10	9.89	3.49	4.02	6.25	6.80	3.86
4η	[cm]	6.83	7.88	10.69	5.05	5.96	7.39	8.69	4.91	4.24	6.85	2.06
k_{ca} GMm	[cm]	31.54	48.29	72.23	42.01	56.94	53.47	57.23	29.42	25.63	46.31	15.45
k_{ca} LC	[cm]	12.51	17.16	25.09	14.21	18.86	18.39	19.96	10.87	9.49	16.28	4.96
error GMm	[cm/s]	7.64	2.79	3.25	1.05	5.29	2.40	2.92	1.06	2.33	3.19	2.09
error LC	[cm/s]	14.66	8.91	4.14	5.16	2.68	4.33	4.72	7.17	7.32	6.57	3.59
Best fit k_{cw}												
k_{cw} GMm	[cm]	19.85	9.08	5.20	5.06	3.54	5.75	4.53	4.91	5.82	7.08	5.02
k_{cw} LC	[cm]	53.70	27.12	16.46	15.87	10.74	17.61	14.43	14.87	17.00	20.87	13.07
σ_{kcw} GMm	[cm]	12.77	5.71	1.60	1.97	3.84	5.65	1.69	2.27	3.95	4.38	3.52
σ_{kcw} LC	[cm]	26.33	13.54	3.81	4.48	7.55	12.05	3.85	4.54	7.81	9.33	7.30
k_{ca} GMm	[cm]	95.29	60.16	42.33	37.66	24.10	39.03	36.54	31.97	35.06	44.68	21.31
k_{ca} LC	[cm]	102.44	64.03	43.78	39.51	24.82	40.74	37.65	33.30	36.12	46.93	23.33
error GMm	[cm/s]	1.50	0.59	0.22	0.37	0.95	0.84	0.26	0.52	0.71	0.66	0.40
error LC	[cm/s]	1.89	0.58	0.24	0.36	0.96	0.79	0.28	0.52	0.80	0.71	0.51
$\alpha = k_{cw,\,GMm} / \eta$		11.62	4.61	1.94	4.00	2.38	3.11	2.08	4.00	5.49	**4.36**	2.98
$\alpha = k_{cw,\,LC} / \eta$		31.45	13.76	6.16	12.56	7.21	9.53	6.64	12.11	16.04	**12.83**	7.78
$\beta = k_{cw,\,GMm}$ /	$[\eta(\eta/\lambda)]$	79.36	30.15	12.67	32.11	15.62	19.96	14.80	30.63	38.50	**30.42**	20.47
$\beta = k_{cw,\,LC}$ /	$[\eta(\eta/\lambda)]$	214.72	90.05	40.13	100.78	47.40	61.10	47.15	92.81	112.51	**89.63**	53.80

The case with the open circles (o) is for where the $z = 0$ at the local bottom (as in Section 9.4.2), and for (*), z is defined $z = 0$ in the absolute coordinates at the initial mean bed bottom (as in Section 9.5). In (a) for the GMm model, η is multiplied by 4 ($\alpha = 4$), and in (b) for the LC model, η is multiplied by 12 ($\alpha = 12$). In all cases, the error bars shows ± one standard deviation of the results. The case described by Section 9.5 (*) for both the GMm and the LC models much more closely represent the k_{cw} predicted by $k_{cw} = \alpha\eta$. For this case, only 1 point out of the 10 for the GMm model and 2 out of 10 for the LC model fall outside of the error bars of the estimates of the parameters.

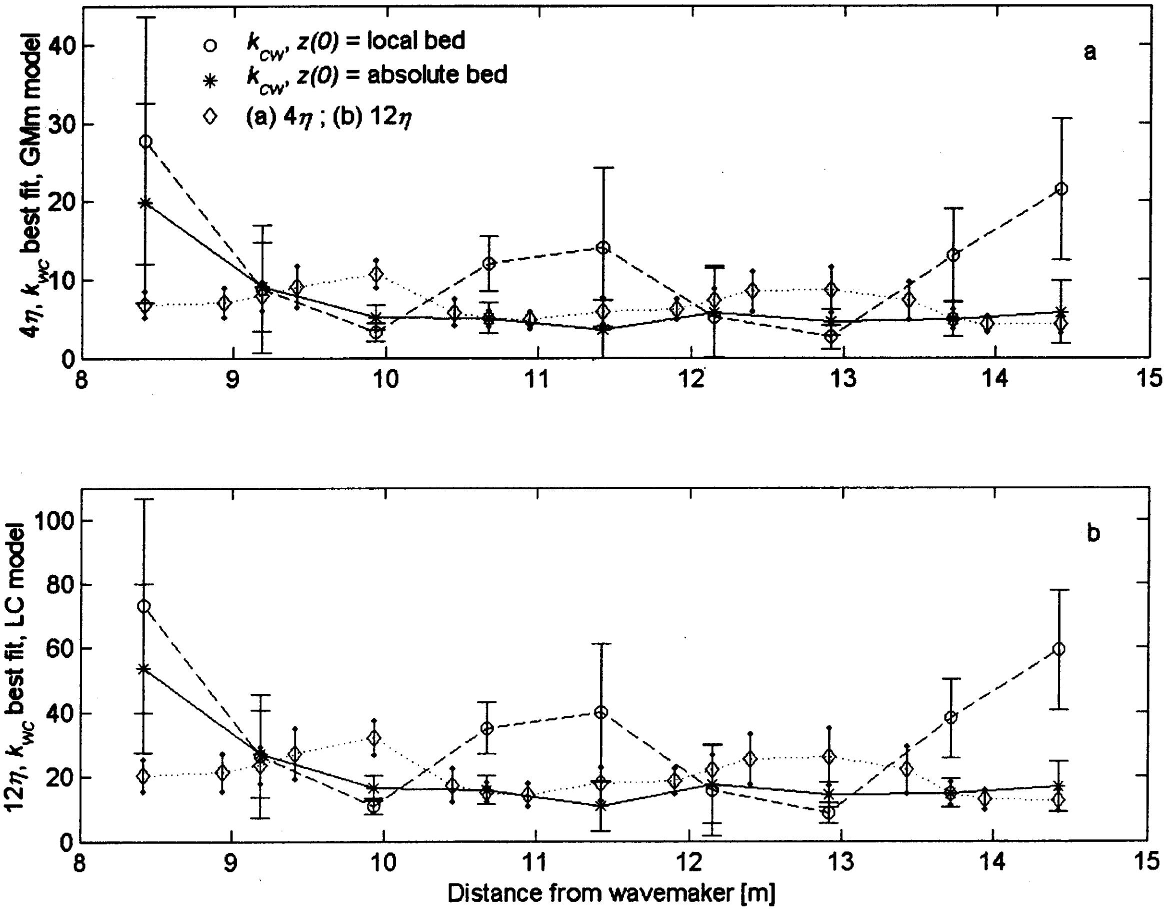

Figure 9.8: Measured ripple height compared with wave-current k_{cw}, open circles (o) are from $z(0)$ = local bed elevation and (*) from $z(0)$ = absolute bed elevation for the (a) GMm and (b) LC models. Error bars around the ripple height is ± one standard deviation, and denoted with solid lines ended with points; error bars around k_{cw} are ± one standard deviation from the fit, and are denoted with solid lines ended with tees.

10. SUMMARY AND CONCLUSIONS

10.1. SUMMARY OF RESULTS

All models for wave-current turbulent boundary layer flows characterize the interaction between the flow and the bottom by a single roughness length scale k_n. The single bottom roughness scale is typically taken to be the same for pure wave, pure current, and wave-current flows. The assumption that the bottom roughness is scaled the same for all flow conditions was explored and verified by Mathisen and Madsen (1996a, b), but only for flows over fixed artificial ripples and co-directional wave-current flows. It has never been verified for flows over a movable rippled bed.

This investigation was undertaken to verify the validity of this basic assumption for flows over a movable rippled bed. An experimental study was performed where pure wave, pure current, and combined wave-current flows were generated over a movable bed with sediment of grain size d_{50} = 0.2mm. Roughness values were experimentally determined for pure waves k_w, pure currents k_c, waves in the presence of a current k_{wc}, and a current in the presence of waves k_{cw}. The roughness determinations were obtained using the Grant and Madsen (1986) model with modifications from Madsen and Salles (1998). Also, for the estimation of k_{cw}, the Linear Constant model developed by Barreto-Acobe (2001) was used to explore the variability of the roughness scale for different models.

Table 10.1 and Table 10.2 summarize the estimates of k_{cw} found by applying the GMm model and LC model, respectively. The tables list both the straight mean and lumped mean results for k_{cw} and $\sigma_{k_{cw}}$, as well as the corresponding roughness scaling factors α and β, defined as

$$k_n = \alpha\eta \tag{10.1}$$

and

$$k_n = \beta\eta\frac{\eta}{\lambda} \tag{10.2}$$

where η is the bedform height and λ is the bedform length.

The turbulent wave-current bottom boundary layer models used in this thesis are all based on 1st order theory (as are all other eddy viscosity models, to the authors knowledge). The flow conditions in the flume exhibited some behaviors that can only be described by higher order theories, such as the wave-induced mass transport inside the wave boundary layer. To account for these higher order effects, the measured velocity profiles had to be adjusted for the GMm and LC models to effectively model the experimental conditions.

One way the measured profiles were adjusted was to average across an integer number of cycles of the 1st harmonic beat length. This method, called the lumped mean, removed most of the effects of the mass transport resulting from the partially standing wave beat. Another method, suggested by MM, is to remove the wave-induced mass transport from the measured wave-current velocity profiles. Two methods can be used to do this. One, labeled 'mass transport from $z = \delta_w$' in Table 10.1 and Table 10.2, takes the measured pure wave time-averaged velocity at the wave boundary layer height and subtracts that value from the entire wave-current profile. The other, labeled 'mass transport from PW profile' in Table 10.1 and Table 10.2 takes the entire

Table 10.1: Summary of results for currents in the presence of waves, GMm model.

GMm model	k_{cw} [cm]		σ_{kcw} [cm]		α		β	
	straight mean	lumped mean	straight mean	lumped mean	straight mean	lumped mean	straight mean	lumped mean
No Mass Transport	11.97	9.29	5.72	2.04	8.88	5.50	66.16	38.61
Mass Transport from $z=\delta_w$	11.19	7.82	5.51	1.77	8.14	4.64	58.43	32.52
Mass Transort from PW profile	12.04	7.72	6.88	4.12	8.43	4.58	59.68	32.11
Mass Transort from PW profile, absolute z	7.08	5.52	4.38	2.88	4.36	3.27	30.42	22.97
Mean	10.57	7.59	5.62	2.70	7.45	4.50	53.67	31.55
Std. Dev.	2.36	1.55	1.02	1.06	2.08	0.92	15.87	6.45

Table 10.2: Summary of results for currents in the presence of waves, LC model.

LC model	k_{cw} [cm]		σ_{kcw} [cm]		α		β	
	straight mean	lumped mean	straight mean	lumped mean	straight mean	lumped mean	straight mean	lumped mean
No Mass Transport	33.84	27.61	12.46	4.66	24.85	16.37	184.88	114.80
Mass Transport from $z=\delta_w$	31.95	23.48	11.34	3.90	23.10	13.92	165.79	97.64
Mass Transort from PW profile	34.12	23.22	15.34	9.18	23.81	13.76	168.69	96.55
Mass Transort from PW profile, absolute z	20.87	17.03	9.33	6.31	12.83	10.09	89.63	70.80
Mean	30.19	22.84	12.12	6.01	21.14	13.54	152.25	94.95
Std. Dev.	6.29	4.36	2.51	2.34	5.59	2.59	42.58	18.14

measured pure wave time-averaged velocity profiles at different locations along the beat and subtracts the pure wave profile from the corresponding wave-current profile. This method was thought to be more effective, as it should also account for the mass transport from the partially standing wave. However, both methods for removing the mass transport work about equally well. That is, for the individual profiles (represented by the straight mean values in Table 10.1

and Table 10.2), the average α was about 8.5 for the GMm model, whereas for the lumped mean, α was about 4.7 for the GMm model. So for this particular experimental setup, the higher order effects (specifically the wave-induced mass transport) act to increase the scaling factors for the bottom roughness of the individual profiles for both the models.

To obtain roughness scaling factors that are closer in magnitude to the other flow conditions, the influence of the variation of the mean bed elevation had to be removed from the measured wave-current velocities. This is shown in the row labeled 'mass transport from PW profile, absolute z' in Table 10.1 and Table 10.2. When the effects of these bar-like variations are removed, the roughness scaling factors are more similar to those obtained for the other flow conditions. This is illustrated in Table 10.3.

The straight mean and lumped mean estimates (where appropriate – see footnotes) of k_w, k_{wc}, k_c, and k_{cw} from the experiments are shown in Table 10.3, along with their respective standard deviations and roughness scaling factors α and β. The bottom roughness results vary for the different flow conditions – from 11cm for the pure wave flow to 4.5cm for the pure current flow. It is interesting to note that the bottom roughness for the wave-current flows, k_{wc} and k_{cw}, are nearly the same – 6cm, 7cm, and 5.5cm (or, if both the k_{cw} results are averaged, 6cm and 6.3cm). For the same flow conditions, different estimates of the bottom roughness yield almost the same value of bottom roughness. This may seem like an obvious result; it should be. But it illustrates the contrast between the different flow conditions. The different flow conditions produce ripples of different sizes, which leads to the idea that different flow conditions will experience different roughnesses because of the different bedform geometries.

If the bottom roughness is scaled by α or β (from equations (1.2) and (1.3)) and α or β are the same across the different flow conditions, then the roughness can be scaled by the same length scale for any of the flow conditions. This is equivalent to saying that if α or β are the same for the different flow conditions, then a single roughness scaling factor can be used for all the different flow conditions, and the major aim of this thesis has been met.

Table 10.3: Summary of measured bottom roughness and bottom roughness scaling factors.

	roughness [cm]	Std. Dev. of roughness [cm]	α	β
k_w	11.23	--	6.8	39.9
k_{wc}	6.02	--	3.5	24.4
k_c^{1}	4.53	1.03	4.0	35.0
k_c^{2}	4.38	0.45	3.9	33.6
$k_{cw}^{1,3}$ (GMm)	7.08	4.38	4.4	30.4
$k_{cw}^{2,3}$ (GMm)	5.52	2.88	3.3	23.0
mean	6.46	2.18	**4.3**	**31.1**
std. dev.	2.54	--	1.3	6.5
$k_{cw}^{1,3}$ (LC)	20.87	9.33	12.83	89.63
$k_{cw}^{2,3}$ (LC)	17.03	6.31	10.09	70.80
Mean	18.95	7.82	11.46	80.22
Std. Dev.	2.71	--	1.93	13.31

[1]: straight mean value

[2]: lumped mean value

3: $z(0)$ = absolute z

Table 10.3 shows the values of α and β for the different flow conditions. These values are obtained by measuring the bedform geometry in each experiment and comparing the geometry with the estimates of the bottom roughness. The values shown in Table 10.3 are the straight mean and the lumped mean values from each experiment, as noted by the footnotes. The values of α and β for pure waves k_w, waves in the presence of a current k_{wc}, and pure currents k_c are virtually the same – the roughness for these flows can be scaled by the same factor. The roughnesses obtained for these flow types are independent of the turbulent wave-current boundary layer models. In fact, in the determination of k_c no wave-current models is applied. While the relationship between the wave attenuation and the friction factor used to determine k_w and k_{wc} requires a wave boundary layer model for its application, the wave friction factor that relates the roughness to the near bottom flow is virtually the same for all wave-current models, and therefore, the roughnesses k_w and k_{wc} do not depend on a specific model. It was found that the bottom roughness determined from the current profile in the presence of waves k_{cw} gave, specifically for the GMm model, $\alpha = 3.9$ and $\beta = 26.7$ (the averages of α and β for GMm shown in Table 10.3). These scaling factors are the same as the scaling factors for k_w, k_c, and k_{wc}. From these results, we can say that a single roughness length scale can be used to represent the bottom interaction for all the different flow conditions considered, as long as the GMm model is used to model the current flow in the presence of waves. The single roughness scaling factors are $\alpha = 4.3 \pm 30\%$, and $\beta = 32 \pm 30\%$. However, these parameters are model dependant. If the LC model is used to determine k_{cw}, α and β increase by about a factor of 3 ($\alpha_{LC} = 11.5$, $\beta_{LC} = 80$). Therefore, the statement that a single roughness scaling factor can be used to characterize the roughness k_w, k_c, k_{wc}, and k_{cw} is only valid if the GMm model is used and only if the wave-current flow is co-directional.

10.2. CONCLUSIONS

The experimental results discussed in this thesis show that a single roughness length scale can be used to characterize pure current, pure wave, and wave-current flows over a movable sediment bed. However, the single roughness scale depends on the model selected to analyze the turbulent wave-current boundary layer, and varies from model to model. The application of the wave-current theory, either the Grant and Madsen model (1986) modified by Madsen and Salles (1998) or the Linear-Constant model by Barreto-Acobe (2001), when applied to the raw measured wave-current velocity data, on average over-predicts the velocity for all experiments and for both models, and underestimate the apparent roughness experienced by the current when the bottom roughness was specified as four times the ripple height (the popularly accepted scale between bedform geometry and bottom roughness). This is due to the fact that the models are valid only to 1st order, and the conditions in the flume often exhibited higher order behavior such as wave-induced mass transport within the wave boundary layer.

This discrepancy was also experienced by Mathisen and Madsen (1996a, b). They showed that the wave-induced mass transport is theoretically equivalent to the wave-induced streaming as predicted by Trowbridge and Madsen (1984a, b). Unfortunately, the model developed by Trowbridge and Madsen is not applicable to the present conditions, as the relative roughness, A_b/k_n, is of order 1 or less, while the model is valid only to values as low as order 10. Therefore, measurements of the time-averaged wave velocity from the pure wave experiments were used to estimate the wave streaming, and were shown to be in qualitative agreement with Trowbridge and Madsen's model – the mass transport at the outer edge of the wave boundary layer is in the opposite direction of that of wave propagation. After adjusting the measured wave-current profiles by removing the measured wave streaming, the models were better able to predict the measured velocity profiles. However, there was still a large variability in the profiles and the predictions.

This variability was attributed to the variation of the mean bed elevation. Bars formed on the bed with a length of oscillation on the order of half the incident wave length and a height of between 3cm for the pure wave case and up to 10cm for the wave-current case. While the processes that led to the formation of these bars were not uncovered, it is thought that they are a result of a secondary mass transport induced by the partially standing wave and an interaction with the current variability over the bars. The origin of the bars is left for further research to explore.

To reduce the effect of the bars on the estimation of the bottom roughness for currents in the presence of waves, an absolute coordinate systems was adopted that treated each profile at different locations along the bed at the same relative vertical locations. Then, by neglecting the measurements of velocity within about 10cm of the absolute bottom (where the bottom was defined as the mean elevation of the bed), the GMm model was able to predict the current profile in the presence of waves quite accurately (with the bottom roughness specified as 4η).

Therefore, by adjusting the measured conditions to better reflect 1^{st} order conditions, a single bottom roughness length scale was shown to characterize the effects of the bottom for pure currents, pure waves, waves in the presence of a current, and a current in the presence of waves over a movable bed, but only when the GMm model is used to model the current flow in the presence of waves, and only then the waves and currents are co-directional.

The fact that the LC model results in a different roughness scaling factor casts some doubt on the generality of this conclusion. While k_w, k_c and k_{cw} may be scaled by the same factor, the scaling of k_{cw} requires more investigation for models other than the GMm, e.g. numerical models employing sophisticated turbulence closure schemes, before a single roughness value for all flow types can be accepted.

10.3. FUTURE RESEARCH

These experiments have shown that a single roughness scale can be used to characterize wave and current boundary layer flows over a movable bed. However, a number of questions about its applicability still exist.

These experiments were only performed for a single set of experimental conditions. More experiments should be performed which test the use of a single roughness scale over the full range of applicability of the GMm model. The relative roughness in these experiments is near the lower bound of applicability of the GMm model. Further, the wave streaming for the large roughness values present here, which has some influence on the applicability of the GMm model, is not adequately predictable with any model known to the author. Theoretical development of a higher-order boundary layer model that includes wave streaming would greatly improve the ability to predict the velocity profiles in flow over large roughness elements.

Another extension to this research would be to use conditions more typically found in the field. Only monochromatic waves were used in this study. If the roughness scale is assumed to be valid for use in the field, it should be verified for a range of spectral wave conditions. Also, in field conditions, waves and currents are rarely co-directional. A more typical situation is to have waves and currents at some angle, often close to 90°. There is no clear evidence that suggests the roughness scale is independent of the angle of interaction. Experimental work should be performed to explore this dependency. Further, bedforms in the field are not simply uniform, two-dimensional ripples. There is a large range of possible cases, varying from the uniform two-dimensional ripples in the equilibrium range used in this study to more three-dimensional and diamond shaped ripples that form at higher bottom velocity intensities and even up to sheet flow conditions of ripples where bedload may dominate the roughness, rather than the bedforms. At present, the bottom roughness values felt by waves and currents from any bedforms beyond the equilibrium, two-dimensional case studied here are completely unknown.

To apply the results presented in this thesis, one is required to know *a priori* the bedform geometry. That is a basic premise of the work – the roughness felt by the flows can be predicted from the bedform geometry. To apply this model elsewhere, it would be necessary to predict the bedform geometry before the actual flows can be modeled. For waves alone, the prediction of ripple geometry has been established. However, much scatter is present in the data used to obtain the empirical predictive formulas, and there is considerable room for improvement. To predict bedforms for combined wave-current flows, no previous work (to the knowledge of the author) has been done. A method to predict the bedform geometry for wave-current flows was developed in Chapter 5. This method is simply a modification to the empirical equations for pure wave flows. The method is able to give a higher and lower bound to the bedform geometry, but is far from providing an accurate prediction. This method needs further adjustment and verification.

Specific to these experimental facilities, in any further experiments performed here, the reflection of the incident wave should be reduced from that experienced in these experiments. Verifying the results in these experiments would have been much simpler if the reflected wave was smaller. Further, it is thought that the variation of the mean bed – the formation of long bars in the sediment bed – was primarily a result of the partially standing wave. While it proved an interesting exercise verifying that linear wave theory is in fact quite good at predicting the wave conditions resulting from the partially standing wave, the bars had an unpredictable influence on the different flow conditions. In particular, the pure current and wave-current conditions could possibly violate the assumption of uniform current flow if the bars were large enough to cause a significant spatially periodic change in velocity. These effects could be greatly reduced or eliminated by effectively removing the reflected wave.

REFERENCES

Anderson, S., A. Lohrmann. 1994. Open water test of the SonTek Acoustic Doppler Velocimeter, *5th IEEE Working Conf. on Current Measurements*, St. Petersburg, FL, USA, ASCE, pp. 366-375.

Arnskov, M.M., J. Fredsoe, B.M. Sumer. 1993. Bed shear stress over a smooth bed in three-dimensional wave-current flow. *Coastal Eng.*, 20, pp. 277-316.

Asano, T., Y. Iwagaki. 1984. Bottom turbulent boundary layer in wave-current co-existing systems. *Proc. 19th Int. Conf. on Coastal Eng.*, Chap 161. Houston, TX, USA, pp. 2397-2413.

Asano, T., M. Nakagawa, Y. Iwagaki. 1986. Changes in current properties due to wave superimposing. *Proc. 20th Int. Conf. on Coastal Eng.*, Chap 70. Taipei, Taiwan, pp. 925-939.

Bakker, W.T., T. van Doorn. 1978. Near-Bottom velocities in waves with a current. *Proc. 16th Int. Conf. on Coastal Eng.*, pp.1394-1413.

Barreto-Acobe, C.D. 2001. Turbulent wave-current boundary layers revisited. M.S. thesis, MIT.

Barrantes, A.I. 1996. Turbulent boundary layer flow over two-dimensional bottom roughness elements. Sc.D. thesis, MIT.

Barrantes, A.I., and O.S. Madsen. 2000. Near-bottom flow and flow resistance for currents obliquely incident to two-dimensional roughness elements. *J. Geophysical Res.*, Vol. 105(C11) 26253-26264.

Biesel, F., and F. Suquet. 1951. Les appareils generateurs de houle en laboratoire. *La Houille Blanche* 6(2):147-165.

Brevik, I. and B. Aas. 1980a. Flume experiment on waves and currents, I, Rippled bed. *Coastal Eng.*, 3:149-177.

Brevik, I. and B. Aas. 1980b. Flume experiment on waves and currents, II, Smooth bed. *Coastal Eng.*, 3:89-110.

Carstens, M.R., F.M. Nielson, and H.D. Altinbek. 1969. Bed forms generated in the laboratory under oscillatory flow: Analytical and experimental study. U.S. Army Corps of Engineers, CERC Technical Memorandum No. 28.

Chan, E. 1986. Deepwater breaking waves forces on structures. Sc.D. thesis, MIT

Christoffersen, J.B., and I.G. Jonsson. 1985. Bed friction and dissipation in a combined current and wave motion. *Ocean Eng.,* 12(5):387-423.

Coastal Engineering Manual. 2001. U.S. Army Corps of Engineers, CERC

Fredsoe, J., K.H. Andersen, and B.M. Sumer. 1999. Wave plus current over a ripple covered bed. *Coastal Eng,* 38:177-221.

Grant, W.D., and O.S. Madsen. 1979. Combined wave and current interaction with a rough bottom. *Journal of Geophysical Research.* 79(C4):1797-1807.

Grant, W.D., and O.S. Madsen. 1982. Movable bed roughness in unsteady oscillatory flow. *Journal of Geophysical Research* 87(C1):469-481.

Grant, W.D., and O.S. Madsen. 1986. The continental shelf bottom boundary layer. *Annual Review of J. Fluid Mech.* 18:265-305.

Gray, C.J., J. Fredsoe, and R. Deigaard. 1991. Flume experiments on bed wave shape and sand transport by currents and waves. Inst. of Hydrodynamics and Hydraulic Engineering, Tech. Univ. of Denmark, Lyngby. Prog. Report 73, pp.7-20.

Hunt, J.N. 1952. Viscous damping of waves. *Le Houille Blanche* 7:836-842.

Jonsson, I.G. 1966. Wave boundary layers and friction factors. *Proc. 10th Conf. on Coastal Eng.*, ASCE, 1:127-148.

Kajiura, K. 1968. A model of bottom boundary layer in water waves. *Bulletin of the Earthquake Research Institute* (University of Tokyo) 46:75-123.

Kemp, P.H., and R.R. Simons. 1982. The interaction of waves and a turbulent current: waves propagating with the current. *J. Fluid Mech.* 116:227-250.

Kemp, P.H., and R.R. Simons. 1983. The interaction of waves and a turbulent current: waves propagating against the current. *J. Fluid Mech.* 130:73-89.

Kularatne, K.A.S.R. 2001. An experimental study of orthogonal wave-current flows over a movable bed. M.Eng. thesis, National University of Singapore.

Kraus, N.C., A. Lohrmann, R. Cabrera. 1994. New acoustic meter for measuring 3D laboratory flows. *J. Hydraulic Eng.* 120(3):406-412.

Lodahl, C.R., B.M. Sumer, J. Fredsoe. 1998. Turbulent combined oscillatory flow and current in a pipe. *J. Fluid Mech.* 373, 313-348.

Lofquits, K.E.B. 1986. Drag on naturally rippled beds under oscillatory flows. U.S. Army Corps of Engineers, CERC, Misc. Paper CERC-86-13.

Lohrmann, A., R. Cabrera. 1994. Direct measurements of Reynolds stress with an acoustic Doppler velocimeter. *5th IEEE Working Conf. on Current Measurements*, St. Petersburg, FL, USA, ASCE, pp. 351-365.

Lundgren, H. 1972. Turbulent currents in the presence of waves. *Proc. 13th Int. Conf. Coastal Eng.*, 33:623-634.

Madsen, O.S. 1970. Waves generated by a piston-type wavemaker. *Proc. 12th Conf. on Coastal Eng.*, 589-607.

Madsen, O.S. 1971. On the generation of long waves. *Journal of Geophysical Research* 76(36):8672-8683.

Madsen, O.S. 1993. Sediment transport outside the surf zone. Unpublished Tech. Report, U.S. Army Engineer Waterways Experiment Station, Vicksburg, MS.

Madsen, O.S. 1994. Spectral wave-current bottom boundary layer flows. *Proc. 24th Int. Conf. Coastal Eng.,* Kobe, Japan. pp384-398.

Madsen, O.S., and W.D. Grant. 1976. Quantitative description of sediment transport by waves. *Proc. 15th Conf. on Coastal Eng.*, ASCE 2:1093-1112.

Madsen, O.S., P.N. Wikramanayake. 1991. Simple models for turbulent wave-current bottom boundary layer flow. U.S. Army Corps of Engineers, WES Report No. DRP-91-1.

Madsen, O.S., and P. Salles. 1998. Eddy viscosity models for wave boundary layers. *Proc. Intl. Conf. Coastal Eng.*, Copenhagen, 2615-2627.

Mathisen, P.P. 1989. Experimental Study on the response of fine sediments to wave agitation and associated wave attenuation. M.S. thesis, MIT.

Mathisen, P.P. 1993. Bottom roughness for wave and current boundary layers over a rippled bed. Ph.D. thesis, MIT.

Mathisen, P.P., and O.S. Madsen. 1996a. Waves and currents over a fixed rippled bed 1: Bottom roughness experienced by waves in the presence and absence of currents. *J. Geophysical Research* 101(C7):16522-16542.

Mathisen, P.P., and O.S. Madsen. 1996b. Waves and currents over a fixed rippled bed 2: Bottom roughness experienced by currents in the presence and absence of waves. *J. Geophysical Research* 101(C7):16543-16550.

Mei, C.C. 1989. *The applied dynamics of ocean surface waves*. Advanced Series on Ocean Engineering, World Scientific Publishing Co., Singapore.

Myrhaug, D., K. Reed, A.J. Fyfe. 1987. Seabed boundary layer studies for pipelines: large scale laboratory experiments. *Proc. Int. Symp. on Offshore Eng.* Rio de Janeiro, pp. 345-359.

Ranasoma, K.I.M., and J.F.A. Sleath. 1994. Combinded oscillatory and steady flows over ripples. *J. Waterway, Port, Coastal, and Ocean Eng.,* 120(4):331-346.

Rapp, R.J., 1986. Laboratory measurements of deep water breaking waves. Ph.D. thesis, MIT.

Rosengaus, M.M. 1987. Experimental study on wave generated bedforms and resulting wave attenuation. Sc.D. thesis, MIT.

Shore Protection Manual. 1984. U.S. Army Corps of Engineers, CERC

Simons, R.R., A. Kyriacou, R.L. Soulsby, A.G. Davies. 1988. Predicting the near bed turbulent flow in waves and currents. *Proc. IAHR Symposium on Mathematical Modelling of Sediment Transport in the Coastal Zone.* Copenhagen, pp. 33-47

Simons, R.R., T.J. Grass, M. Mansour-Tehrani. 1992. Bottom shear stresses in the boundary layers under waves and currents crossing at right angles. *Proc. 23rd Conf. on Coastal Eng.*, Chap 45, Vol 1. Venice, Italy, pp. 604-617.

Simons, R.R., A.J. Grass, W.M. Saleh, and M.M. Tehrani. 1994. Bottom shear stresses under wave with a current superimposed. *Proc. 24th Int. Conf. on Coastal Eng.*, Chap. 42, Vol 1. Kobe, Japan, pp. 604-617.

Sleath, J.F.A. 1990. Velocities and bed friction in combined flow. *22nd Int. Conf. on Coastal Eng.*, Vol 1. Delft, ASCE, pp. 450-463.

Sleath, J.F.A. 1991. Velocities and shear stresses in wave-current flows. *J. Geophysical Res.* 96(C8):15237-15244.

Smith, J.D. 1977. Modeling of sediment transport on continental shelves. *In the Sea*, Vol 6, Marine Modeling, ed. E.D. Goldberg et al. John Wiley, N.Y., pp. 538-577.

Sontek. 2002. http://www.sontek.com. Last updated August 13, 2002.

Tanaka, H., N. Shuto. 1981. Friction coefficient for a wave-current coexisting system. *Coastal Eng. in Japan* 24:105-128.

Titus, J.G., R.A. Park, S.P. Leatherman, J.R. Weggel, M.S. Greene, P.W. Mausel, S. Brown, C. Gaunt, M. Trehan, and G. Yohe. 1991. Greenhouse effect and sea level rise: The cost of holding back the sea. *Coastal Management* 19:171-210.

Trowbridge, J.H., and O.S. Madsen. 1984a. Turbulent wave boundary layers 1: Model formulation and first-order solution. *J. Geophysical Res.* 89(C5):7989-7997.

Trowbridge, J.H., and O.S. Madsen. 1984b. Turbulent wave boundary layers 2: Second order theory and mass transport. *J. Geophysical Res.* 89(C5):7999-8007.

US Environmental Protection Agency. 2002. http://www.epa.gov. Last updated August 14, 2002.

APPENDIX A.

ACCURACY OF BOTTOM ROUGHNESS ESTIMATION

The bottom roughness for currents and currents in the presence of waves is determined from measured current and wave-current velocity profiles. Each individual point measured in the velocity profile is subject to instrument variabilities as well as the variabilities of the flow resulting from turbulence and the proximity to the individual bottom roughness elements. When all the measured velocity points are combined into a profile, each of the points individual variabilities can influence the overall accuracy of the determination of the bottom roughness.

This appendix explains the procedure used to determine the variability of the measured velocities, and from there determine the accuracy of the estimation of the bottom roughness. The variability of the flow can only be reduced by increasing the sampling time, allowing for more points to be averaged. The accuracy of the ADV instrument is fixed, and therefore the flow measurements are, at best, limited to the accuracy of the instrument. Therefore, there is a sampling time at which the accuracy of the measured bottom roughness cannot be improved by increasing the sampling time of the velocity measurements. Further, the variability of the bottom roughness estimation due to the regression approximation limits the accuracy of the bottom roughness estimates. Knowledge of these uncertainties will lead to the optimum time for sampling and the resulting best possible accuracy available in determining the bottom roughness for currents and currents in the presence of waves.

A.1. FLOW VARIABILITY AND SAMPLING TIME

This method applies to both currents and currents in the presence of waves. Because the sampling conditions for both measurements are to be the same, and because of the fact that the variability of the flow for combined waves and currents is larger due to the increased turbulence in the flow, the flow variability resulting from the sampling time will be determined using wave-current flows.

The instrument variability follows a normal distribution, while that from the flow is of an unknown distribution, but here is assumed to be normal. Therefore, the uncertainties of the velocity measurements can be lumped into one measurement of the overall variability of the flow. This will be expressed as a standard deviation of the velocity, σ_u.

This standard deviation σ_u will decrease with increasing sampling time as it approaches some long-term quasi-minimum standard deviation. To determine this value and the decrease in σ_u with sampling time, the velocity is recorded at a specific z-elevation for a long time. Here, we chose to sample for one hour. Also, two measurement elevations were selected, z = 1cm above a crest (which would approximately correspond to z = 2cm above the nearest trough; the crest was chosen at the starting point to insure that the measurements would include the time of maximum variability of the flow), and z = 5cm above a crest.

The average velocity is the average of the hour-long sample, and the quasi-minimum standard deviation of the velocity, $\sigma_{u,min}$, is the standard deviation of the hour-long sample. Then to explore how the variability of the measurements changed with sampling time, the long-tem sample is split into smaller sub-samples, and the sub-samples are averaged. The standard deviation of the averages of the sub-samples gives the standard deviation as a function of sampling time. For example, to obtain the standard deviation of the velocity for a sampling length of 5 minutes, the long term sample is broken into 12 samples of 5 minutes each. The average of each of these 5 minute samples is obtained. Then, the standard deviation is found from the 12 averages. This procedure is repeated for sampling times of 1, 2, 3, 4, 5, 6, 7, 8, 9, 10, 15, 20, and 30 minutes. Figure A.1 shows the variability of (a) the mean and (b) the standard deviation with sampling time. Because the total sampling time was only 1 hour, the number of samples that the long-term sample can be broken into for averaging decreases with increasing sampling time – for sampling times of 30 minutes, only 2 estimates of the mean can be made. To circumvent this, starting at a sampling time of 7 minutes, the long-term average was broken into sub samples by overlapping the actual times used to obtain the averages so at least 10 averages could be used to obtain the standard deviation for every sampling length. For example, to obtain σ_u for the 15 minute sampling time, the first estimate of the mean was obtained by averaging from $t = 0$ to 15 minutes. The second from $t = 5$ to 20, the third from $t = 10$ to 25, and so on to $t = 45$ to 60 minutes. This gives a total of 10 averages of 15 minute samples.

Overlapping the samples causes a small deviation in the estimates of the means, since parts of the velocity will be averaged multiple times due to the overlapping. This can be seen in Figure A.1 (a) where the mean normalized by the long-term mean begins to deviate from 1 at 7 minutes of sampling time, where the overlapping was first implemented. The influence of the overlapping is quite small, causing an error of less than 1% of the long-term mean velocity, and therefore is considered insignificant.

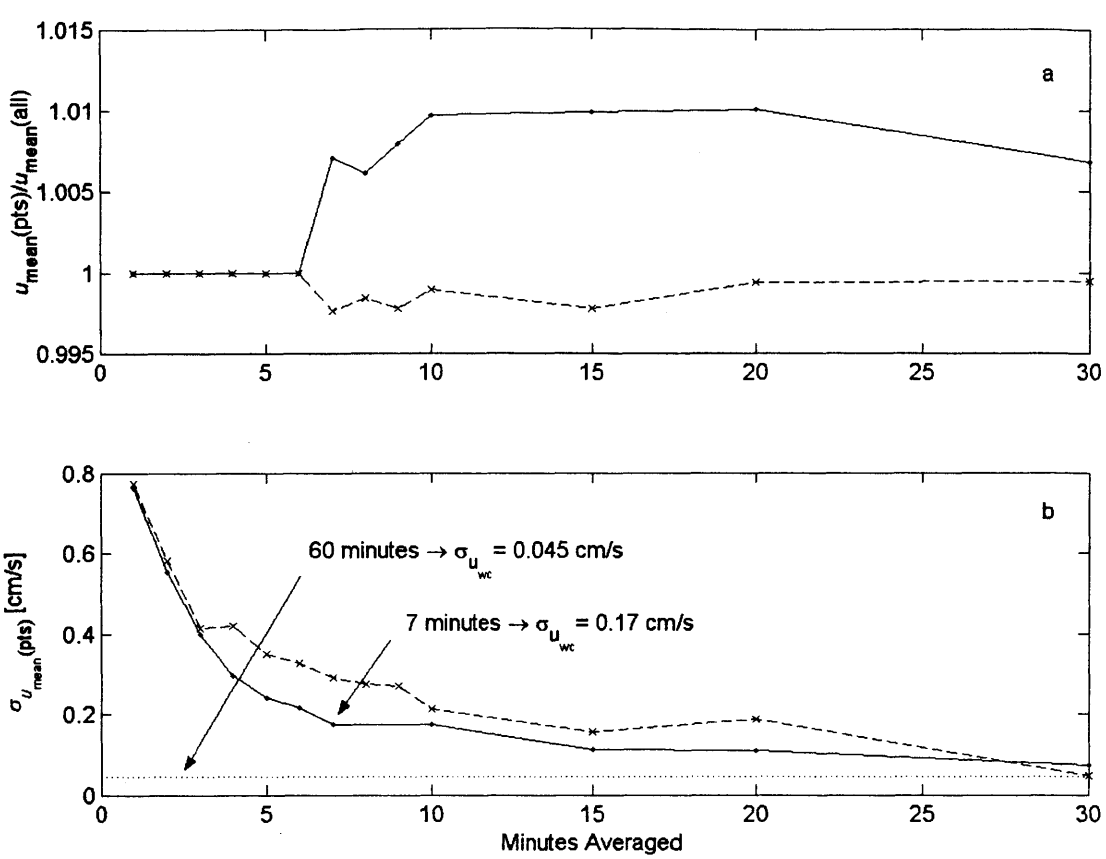

Figure A.1: Variability of (a) mean and (b) standard deviation of measured velocity with sampling time. Solid line with points (·) from measurements at z = 1cm above crest, dashed line with crosses (x) from measurements at z = 5cm above crest.

The trend in the standard deviation is shown in Figure A.1 (b). As the sampling time increases, σ_u decreases. It is interesting to note that the measurements taken at z = 5cm show more variability than that shown by the measurements taken at z = 1cm from a sampling time of 4 minutes to 30 minutes. This is thought to be a result of the fact that while the velocity a z = 1cm should have more variability due to greater turbulent fluctuation, the magnitude of the velocity at z = 5cm is greater, which would lead to a larger magnitude of variability.

In the best-case scenario, the variation of the velocity will only be the uncertainties that results from instrument error with no variation contributed from the flow itself. In this case, we know the uncertainty – it is defined by Sontek (2002) as ±1% of the velocity range of the instrument. The velocity range used during these measurements is ± 30cm/s, yielding an accuracy of ±0.3cm/s. Since the noise from the ADV is normally distributed, the accuracy given here can be assumed to cover almost all possible variations of the velocity, making the ±0.3cm/s the 95% confidence interval, or about 2 standard deviations around the mean. Then the best-case standard deviation of the velocity measurements is $\sigma_{u,best} = 0.15$cm/s. At a sampling time of 7 minutes, the curve for σ_u for the sample at $z = 1$cm has a $\sigma_u = 0.17$cm/s, about the same as can be expected from the instrument.

A.2. BOTTOM ROUGHNESS VARIABILITY

A.2.1. BOTTOM ROUGHNESS VARIABILITY FROM SAMPLING TIME THROUGH STATISTICAL SIMULATION

Next, we simulate velocity profiles with a velocity that can vary with a standard deviation of $\sigma_{u,best} = 0.15$cm/s at each point. This is accomplished by using known u_{*c} and k_c (here, from the pure current velocity profiles, not wave-current), and then predicting the velocity profile as $u = u_{*c}/\kappa \ln(30z / k_c)$ for each of the 14 z-locations used in the original sampling scheme. Each point in this velocity profile is introduced to a variability based on a normal distribution with zero mean and a standard deviation of $\sigma_{u,best}$, typically written as $N(0, \sigma_{u,best})$, by multiplying each point by a randomly generated number based on the distribution. The simulated profile is fit with the typical log-fitting procedures described in Section 8.2 to obtain new values of u_{*c} and k_c that result from the simulated profile. Then by repeating this simulation many times (here, 1000) and choosing a different set of random numbers each time, the possible variability of u_{*c} and k_c is obtained by taking the standard deviation of the 1000 estimates made from the simulated profiles. This gives estimates of $\sigma_{u*c,sim}$ and $\sigma_{kc,sim}$ for a σ_u = 0.15cm/s.

By repeating this procedure with increasing σ_u values, $\sigma_{kc,sim}$ can be plotted as a function of σ_u, as shown in Figure A.2. A linear regression shows the relationship to be

$$\sigma_{kc,sim} = 9.45\ \sigma_u + 0.059. \tag{A.1}$$

Now we can estimate the approximate standard deviation we would expect from the variability of the flow. If a sampling time of 7 minutes is used, we can expect σ_u = 0.17cm/s. Combining this with the known instrument variability of 0.15cm/s, the total best-case σ_u expected is the square root of the sum of the squares of 0.17cm/s and 0.15cm/s, yielding $\sigma_{u,tot}$ = 0.23cm/s. Introducing this $\sigma_{u,tot}$ into equation (A.1) for σ_u, the best-case estimate of σ_k = 2.2cm.

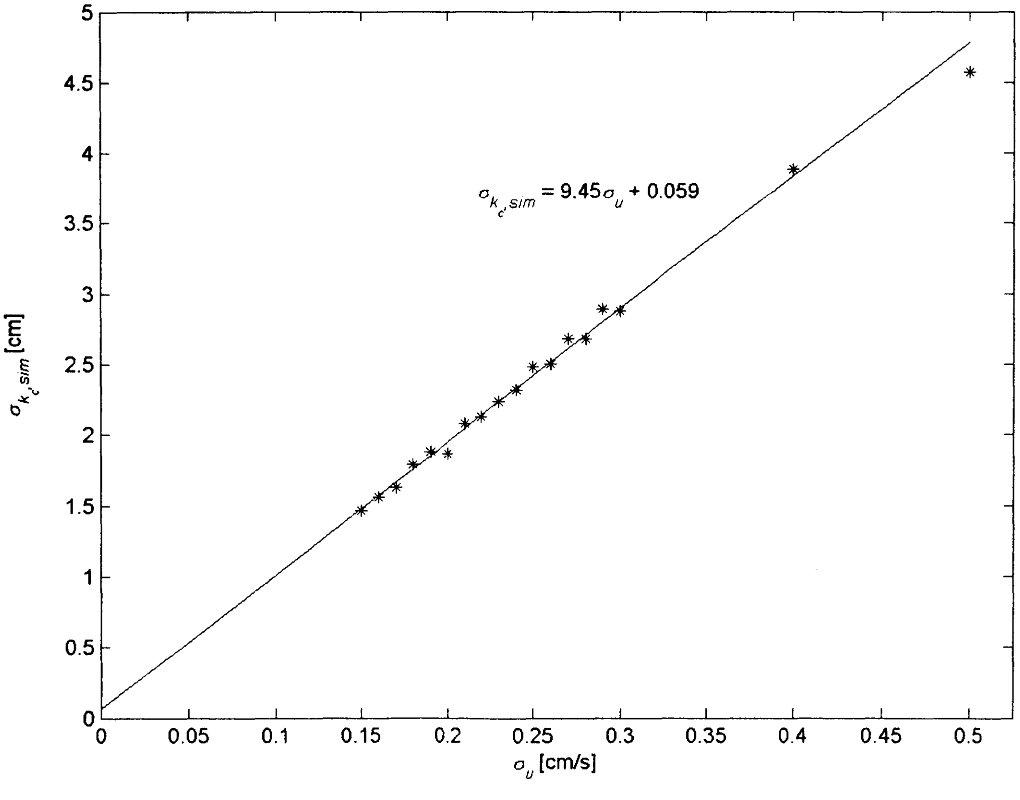

Figure A.2: Variation of $\sigma_{kc,sim}$ with σ_u resulting from the simulated profiles.

A.2.2. BOTTOM ROUGHNESS VARIABILITY FROM REGRESSION ROUTINE

To find the error in the estimates of the bottom roughness due to the linear regression, we take all measured velocity profiles and fit the best-fit velocity profile to the data based on the methods described in Section 8.2 for pure currents and Section 9.2 for combined waves and currents. The uncertainty due to the linear regression can be found based on the confidence intervals of the fit extended to $z = 0$. Then by averaging this uncertainty for all measurements, we obtain an estimate of the uncertainty based on the linear regression, $\sigma_{k,fit}$. This value will vary between the pure current and wave-current flows, as the magnitudes of the roughness fits vary. However, for the wave-current experiments, the average $\sigma_{k,fit} = 3.8$cm, larger than the predicted best-fit $\sigma_k =$ 2.2cm obtained in the previous section. The actual measured profiles show more variability than that predicted by the simulation.

A.3. RELATING BOTTOM ROUGHNESS VARIABILITY TO THE SAMPLING TIME

We now have the ability to relate the sampling time and the roughness variability based purely on the variability of the velocity measurements. For a given standard deviation of roughness, we can step through the above process in reverse and find the corresponding standard deviation of measured velocity through equation (A.1). Then we take the value of σ_u obtained from equation (A.1), and using Figure A.1 (b), the sampling time required to get the roughness variability selected can be determined.

Using the $\sigma_{k,fit} = 3.8$cm found in Section A.2.2 obtained from the actual measured profiles, substitution into equation (A.1) gives $\sigma_u = 0.40$cm/s. This is significantly larger than the 0.23cm/s expected in the best-case scenario; the actual variability of the velocity measurements in the profiles used to obtain the roughnesses is more than expected. Using this model, the sampling time necessary to obtain $\sigma_u = 0.40$cm/s and thus a $\sigma_{k,fit} = 3.8$cm is about 4 minutes, 3 minutes less than that actually used. However, as suggested in Section A.1, the variability in the velocity is probably better modeled as a coefficient of variation, where the standard deviation is proportional to the magnitude of the velocity. This is a physically reasonable assumption, since the magnitude of the velocity as well as the turbulent fluctuations in the velocity will grow as a function of the distance from the bottom. If this is the case, the above model is expected to under-predict the total variability of the profile. Finally, the model used to obtain our estimate of uncertainty assumed the validity of the log-fit to the data. Many of the profiles in these experiments exhibited regions in the profile that certainly were logarithmic, but the entire profiles were not completely logarithmic. In fact, the analysis performed for the pure current experiments in Chapter 8 assumes that there are 2 distinct log regions, and they cannot be reasonably treated as one. Furthermore, there are individual points in the profile that lie outside of the log region that are included here. These effects certainly increases the uncertainty in the roughness estimates, and are the likely culprit for the increased $\sigma_{k,fit}$ seen here.

APPENDIX B.

BEAD EXPERIMENTS, 60 CM WATER DEPTH

A preliminary set of experiments were completed using a single layer of 0.64cm (1/4in) glass spheres (beads) for the bottom roughness with a water depth of h = 60cm. These roughness elements were selected based on the friction factor diagram developed by Jonsson (1966) to give a fully rough turbulent bottom boundary layer with a relative roughness $A_b/k_n > 10$. For the experiments in the main text, $A_b/k_n < 1$ which is near the model's theoretical range of validity. Experiments in this appendix are performed just as in the main text for pure waves, pure currents, and combined wave-current flows. Analysis of these experiments show the bottom roughness values for k_w, k_c, k_{wc}, and k_{cw} for the flows over the beads.

These experiments were performed with the exact same equipment and facilities as explained in Chapter 3. The water depth was h = 60cm, the wave has a period T = 2.63s and an amplitude of about a = 5cm. The depth averaged current velocity was about $\bar{u}_c$ = 16.5cms/.

A summary of all the experiments performed for these conditions is shown in Table B.1. The x-locations of the pure wave and wave-current experiments were selected to measure one full cycle of the partially standing wave at the node, upslope, antinode, and downslope. The pure wave and wave-current measurements were made at the same 4 locations in the tank relative to the 1st harmonic free surface, but the actual distance from the wavemaker varied slightly, as the free surface is slightly changed by the presence of the current. The pure current measurements were made at different locations along the flume to get profiles of different levels of boundary layer development. The approximate boundary layer thickness is shown under the heading δ_c. At experiment e (x = 5m), the boundary layer thickness was about 9cm, while at the last location, experiment h, x = 15m, the boundary layer thickness was about 30cm, or half the water depth.

Table B.1: Summary of experiments over beads, h = 60cm.

Experiment ID	x [m]	Location Description
pure wave		
a	10.23	node
b	10.99	upslope
c	11.74	antinode
d	12.50	downslope
pure current		δ_c [cm]
e	5.00	7
f	5.85	12
g	11.00	20
h	15.00	30
wave-current		
A	10.32	node
B	11.06	upslope
C	11.79	antinode
D	12.53	downslope

B.1. BOTTOM ROUGHNESS FROM WAVE ATTENUATION

Attenuation measurements were performed for both the pure wave and wave-current flows to obtain a measurement of the bottom roughness felt by the waves k_w and the bottom roughness felt by the wave in the presence of a current k_{wc}. The procedures followed here are exactly the same as those described in Chapter 6. The pure wave attenuation measurements were performed just prior to the pure wave velocity measurements. The free surface profiles observed for pure waves are shown in Figure B.1. (a) is the 1st harmonic with the fit (solid line) prescribed by equation (4.14). The dotted line on (a) is the attenuation slope of the first harmonic amplitude,

$a_{i0} - m_t x$. (b) shows the second harmonic, and the fit prescribed by equation (4.18). The values obtained from the fit of the first harmonic fit are listed in Table B.2.

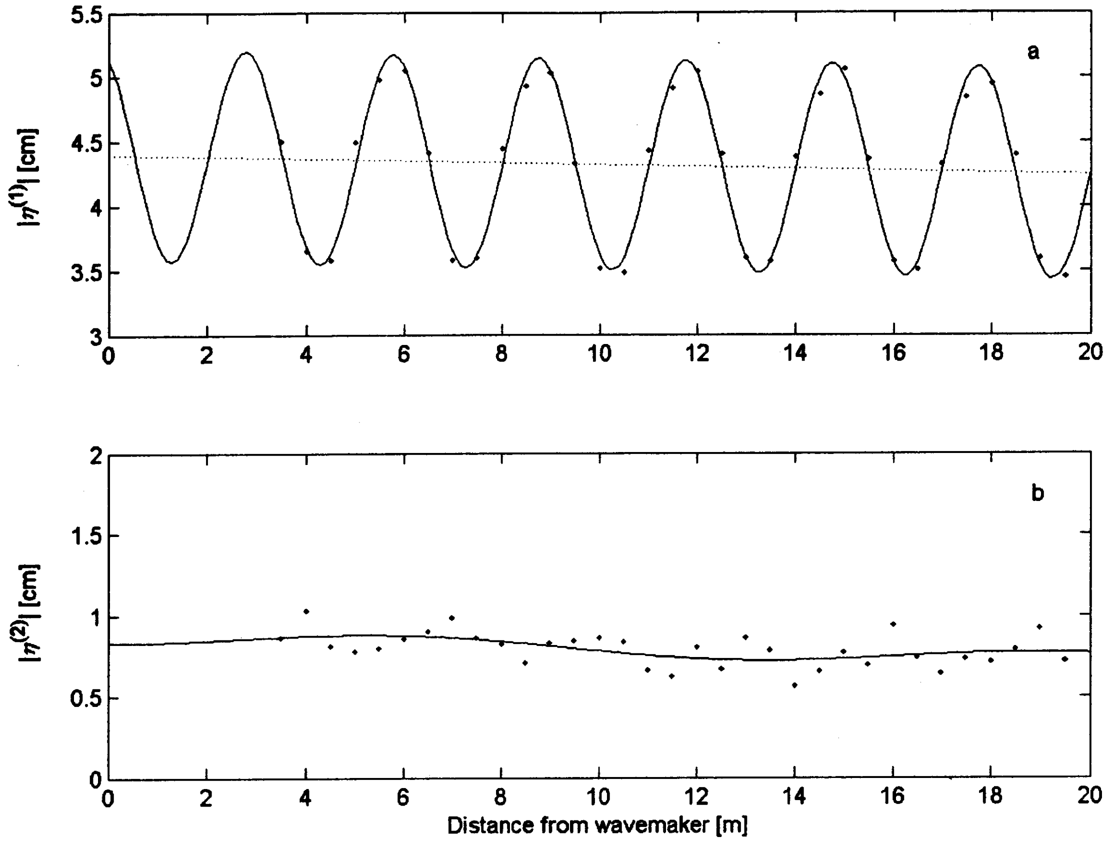

Figure B.1: Attenuation measurements for pure waves over beads, h = 60cm. (a) is the 1st harmonic and (b) is the 2nd harmonic. Dotted line on (a) shows the attenuation slope of the 1st harmonic amplitude.

Figure B.2 shows the measured and fit (a) 1st and (b) 2nd harmonic free surface profiles for combined waves and currents, just as in Figure B.1 for pure waves. The fit to the 1st harmonic is from equation (4.14), and for the 2nd harmonic, equation (4.18). The wavelengths were modified by the current as described in Section 4.4.2. Table B.2 shows the values obtained from the fit of the 1st harmonic for both the pure waves and the combined waves and currents. Notice that the reflection for these cases are R = 19% and 13% for the pure wave and wave-current cases, respectively.

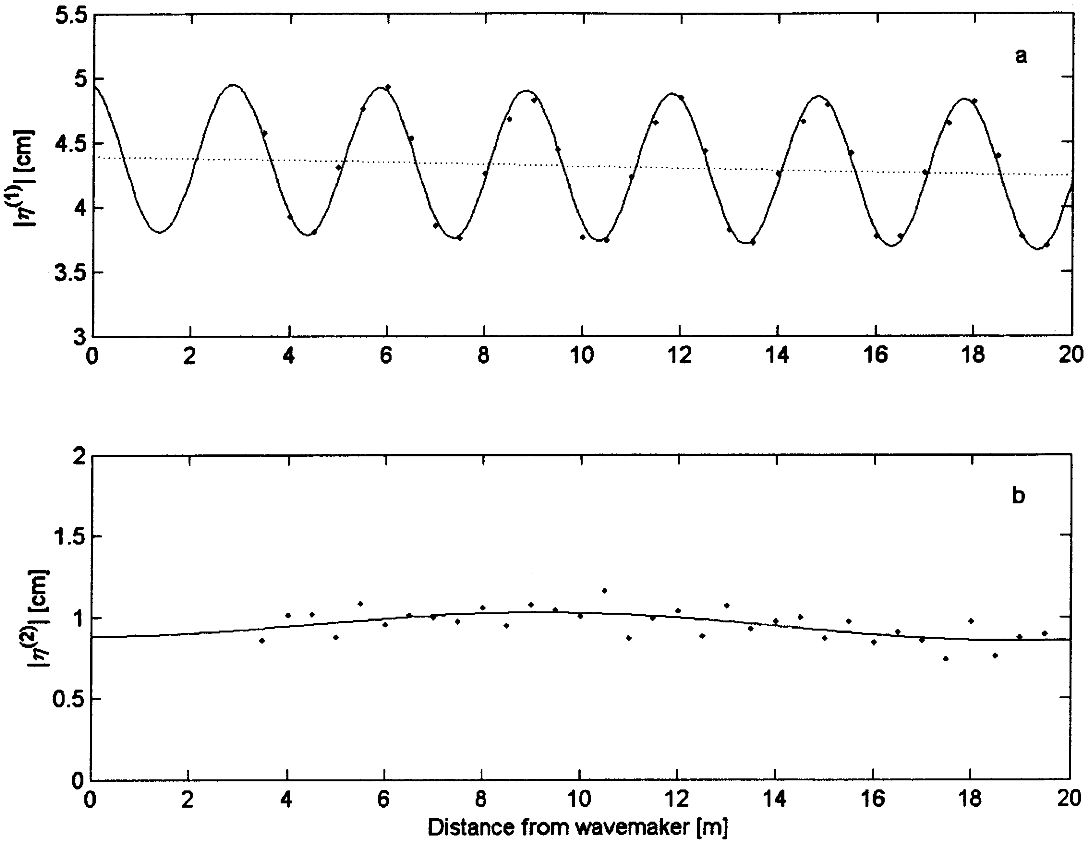

Figure B.2: Attenuation measurements for combined waves currents over beads, h = 60cm. (a) is the 1st harmonic and (b) is the 2nd harmonic. Dotted line on (a) shows the attenuation slope of the 1st harmonic amplitude.

Table B.2 also shows the friction factors and the bottom roughnesses for the pure wave and wave-current flows. The wave roughness from pure waves and waves in the presence of a current are approximately the same, and are 75% and 63% of the diameter of the beads, respectively. Estimating the roughness from the attenuation experiments is cumbersome, as the attenuation from the beads themselves is on the same order of magnitude as the attenuation from the sidewalls. Also, the change in wave amplitude over the test section is about 1.3mm, which approaches the accuracy of the wave gages and makes the measurement of such a small quantity quite difficult.

Table B.2: Attenuation results for pure wave and wave-current experiments over beads, h = 60cm.

Parameter		Pure Wave	Wave-Current
T	[s]	2.63	2.63
a_{i0}	[cm]	4.40	4.39
a_r	[cm]	0.82	0.58
m_t	[cm/cm]	-7.5930E-05	-7.6800E-05
m_b	[cm/cm]	-4.3310E-05	-4.4495E-05
u_{bm}	[cm/s]	15.37	15.6
A_{bm}	[cm]	6.43	6.54
u_{*c}	[cm/s]	--	1.08
u_{*wm}	[cm/s]	2.44	2.46
f_e		0.04	0.04
f_w		0.05	0.05
$\{k_w, k_{cw}\}$	[cm]	0.48	0.39

B.2. PURE WAVE VELOCITY EXPERIMENTS

Pure wave velocity profiles were measured at the 4 locations listed in Table B.1. For these experiments 27 vertical points were possible for each profile. More detail was added near the bed, as the first 10 points are taken below 2cm from the top of the beads. The first point was measured 3mm above the top of the beads so that the sampling volume of the ADV was just above the highest point on the bead layer. The vertical spacing of the points was $\Delta\ln(z) = 0.2$, and measurements were made up to 49.7cm above the beads. The sampling rate was 24.333Hz and 2048 points were sampled 5 times at each point in x and z. This yielded a total 160 waves measured for each point in the profile.

The time-averaged wave velocity profiles for experiments a, b, c, and d are plotted in Figure B.3 at their relative spatial locations. The 1st harmonic free surface variation $|\eta^{(1)}|$ is plotted above the velocity profiles on a separate axis. The velocity structure near the bed is significantly different at the different locations along the beat, suggesting some mass transport from both wave streaming and the partially standing wave, as suggested in Section 7.2.1.

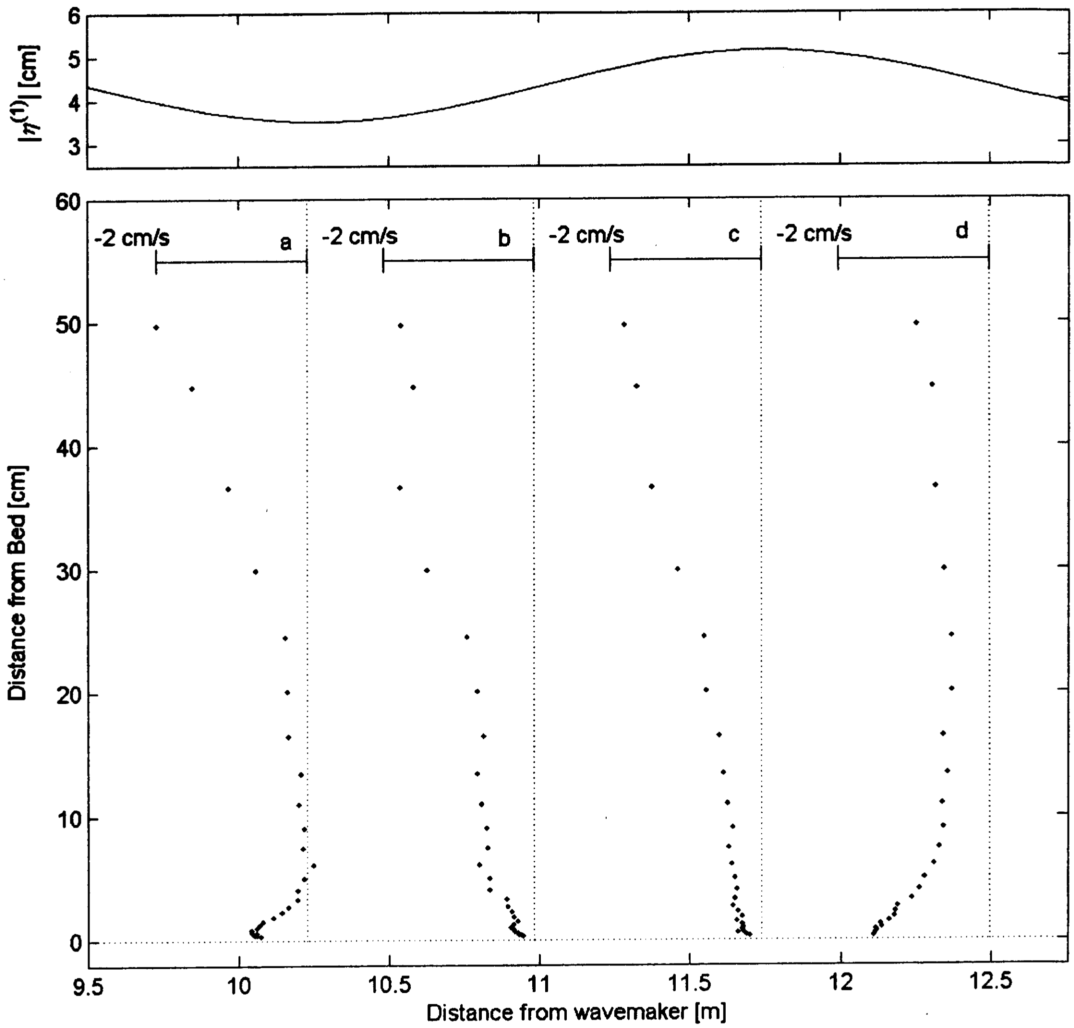

Figure B.3: Time-averaged pure wave velocity profiles (a-d) over beads, h = 60cm. Points (·) are the velocity measurements. The dotted vertical lines represent zero velocity for each of the profiles. $|\eta^{(1)}|$ is the fit of the variation of the 1st harmonic and is plotted on a separate axis above the profiles.

Figure B.4 shows the same profiles as in Figure B.3, but here are superimposed and plotted on a natural log *z* axis to emphasize the variability and detail near the bed. A similar structure to that seen in Figure 7.2 is shown here, where there is some net negative drift superimposed on a circulation cell induced by the partially standing wave. To extract the net drift from these measurements, a lumped mean profile was obtained. Figure B.5 shows the lumped mean pure wave velocity profile. The lumped mean is the ensemble average across depth, resulting in a profile that removes the variability due to the beat by averaging out any circulation induced by the beat.

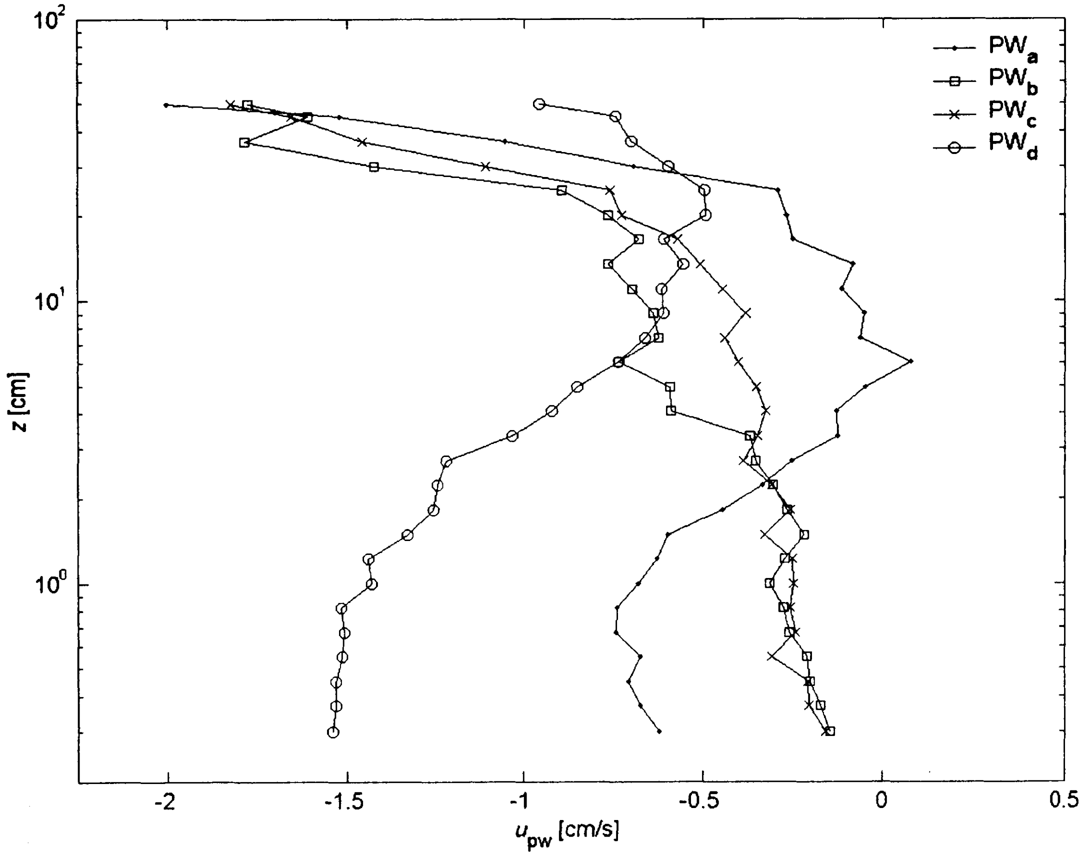

Figure B.4: Time-averaged pure wave velocity profiles for experiments (a-d) over beads, *h* = 60cm. Note that *z*-elevation is plotted on a log scale.

The lumped mean results shows a net negative velocity over the entire measured depth. These results are similar to those shown in Figure 7.3. Very near the bottom in the wave boundary layer, as proposed by Trowbridge and Madsen (1984a, b), the net mass transport occurs with a velocity of about 0.5cm/s. There is a noticeable velocity overshoot present here as there was in Figure7.3 for the pure wave *h*=60cm case. Here it occurs closer to the bed, as δ_w ~ 1cm, a result of the smaller roughness.

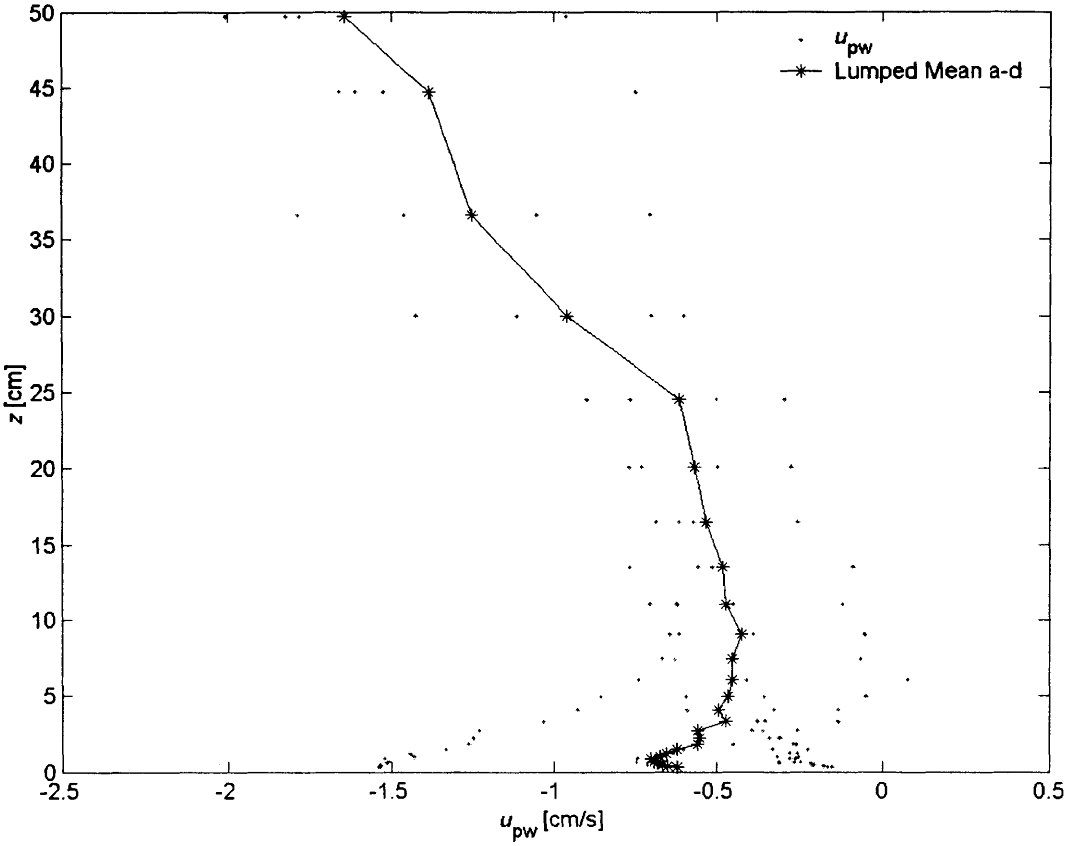

Figure B.5: Lumped mean pure wave velocity profile over beads, h = 60cm. (*) are the lumped mean, and the points (·) are the measured time-averaged individual velocity profile points.

To resolve the circulation that results from the partially standing wave, we follow the same procedures as in Section 7.3. The net transport of each profile is shown in Table B.3. The return current predicted from linear theory (equation (7.2)) here for a_i = 4.4cm and R = 20% gives a return current of u_r= -0.64cm/s, on the same order of magnitude as the lumped cycle mean, – 0.86cm/s. Then, by removing the lumped cycle mean from each profile, a picture of the circulation induced by the partially standing wave can be made, and is shown in Figure B.6.

In Figure B.6, the circulation pattern described in Section 7.3 can be seen. There is a drift from the node to the antinode along the bottom, resulting in a positive velocity near the bottom for

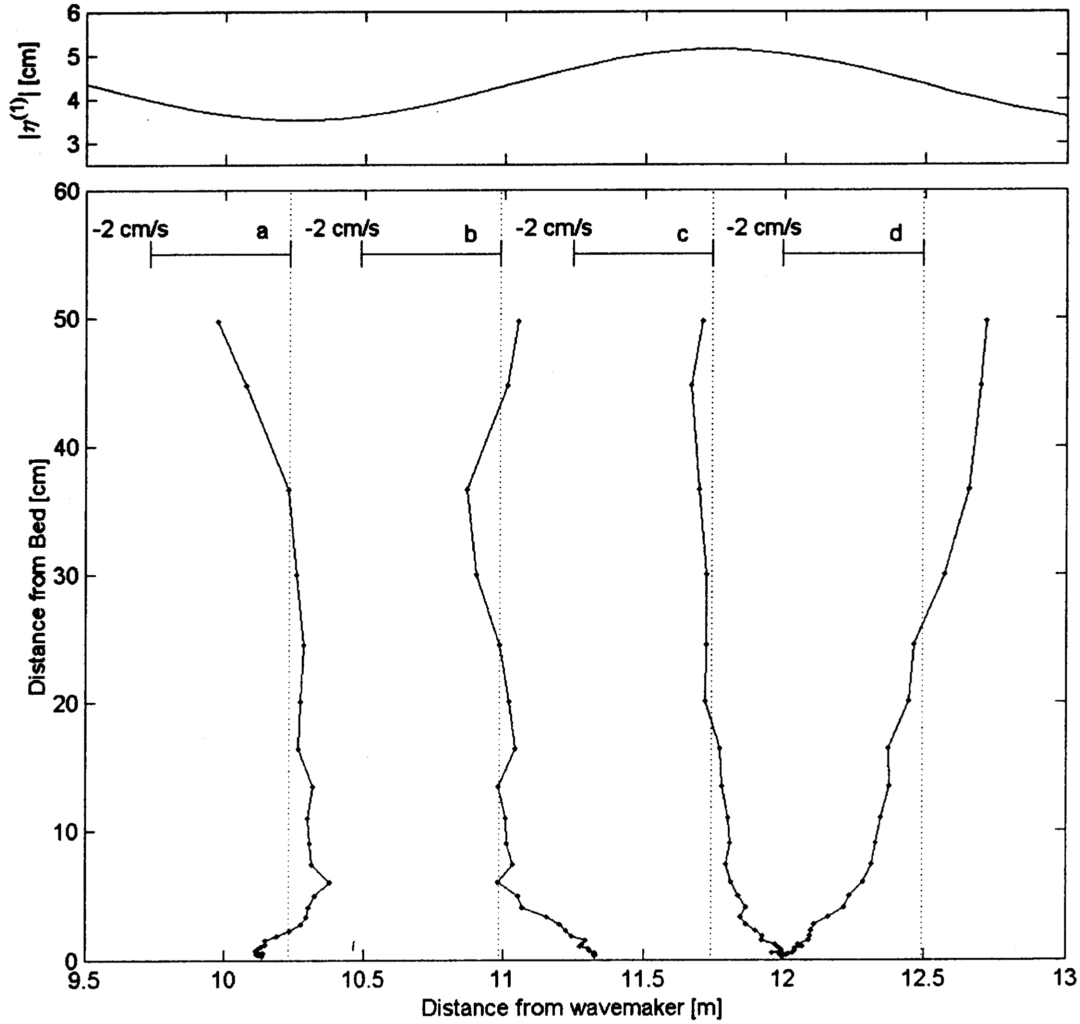

Figure B.6: Pure wave velocity profiles over beads, h = 60cm, corrected for mass flux and net mass flux, plotted at their respective spatial locations. Points (·) with solid lines are the corrected velocity measurements. The dotted vertical lines represent zero velocity for each of the profiles. $|\eta^{(1)}|$ is the measured variation of the first harmonic and is plotted on the separate axis above the velocity profiles.

Table B.3: Net mass flux for each profile a-d and the cycle mean.

Expt ID	Q_{pw} [$cm^3/s/cm^2$]
a	-0.65
b	-1.14
c	-0.97
d	-0.68
Cycle mean	-0.86

profile b and a negative velocity at the bottom of profile d. These two drifts meet at the antinode (profile c), pushing the flow up. This results in a return circulation near the surface from the antinodes to the nodes, as can be seen by the slightly negative velocity at profile b, and the positive velocity at the downslope profile d. These return velocities are not as large as the bottom velocities as they occur over a greater portion of the water column.

B.3. PURE CURRENT VELOCITY EXPERIMENTS

The pure current velocity profiles were measured at the 4 locations e, f, g, and h listed in Table B.1. The same methods for analyzing the current profiles in Chapter 8 are employed here. Typically, the pure current profile did not exhibit a bend in the profile between the bottom and top points as was seen in the h = 60cm experiments over sand, described in Chapter 8. Thus, the roughness for the pure current should be found by analyzing the entire current profile in the logarithmic boundary layer. However, the analysis performed here considers the different sections (all, top and bottom points) to allow for comparison between these measurements and those of the other experiments performed in this thesis. In these profiles, the first 4 or 5 points near the bottom were excluded as they were influenced by the individual beads. The upper portion of the profile is not within the current boundary layer, so all points out of the boundary layer are excluded (the thickness is shown in Table B.1). The thickness varies from profile to profile, from points 17 (z = 7cm) to 24 (z = 30cm). These points were selected from observation, where the points are obviously no longer in the current boundary layer. Figure B.7 shows this for the pure current experiments h and e, along with the log fit of the profile from about point 4 to the edge of the boundary layer. Note that the line showing the log fit stops at the last point in the boundary layer.

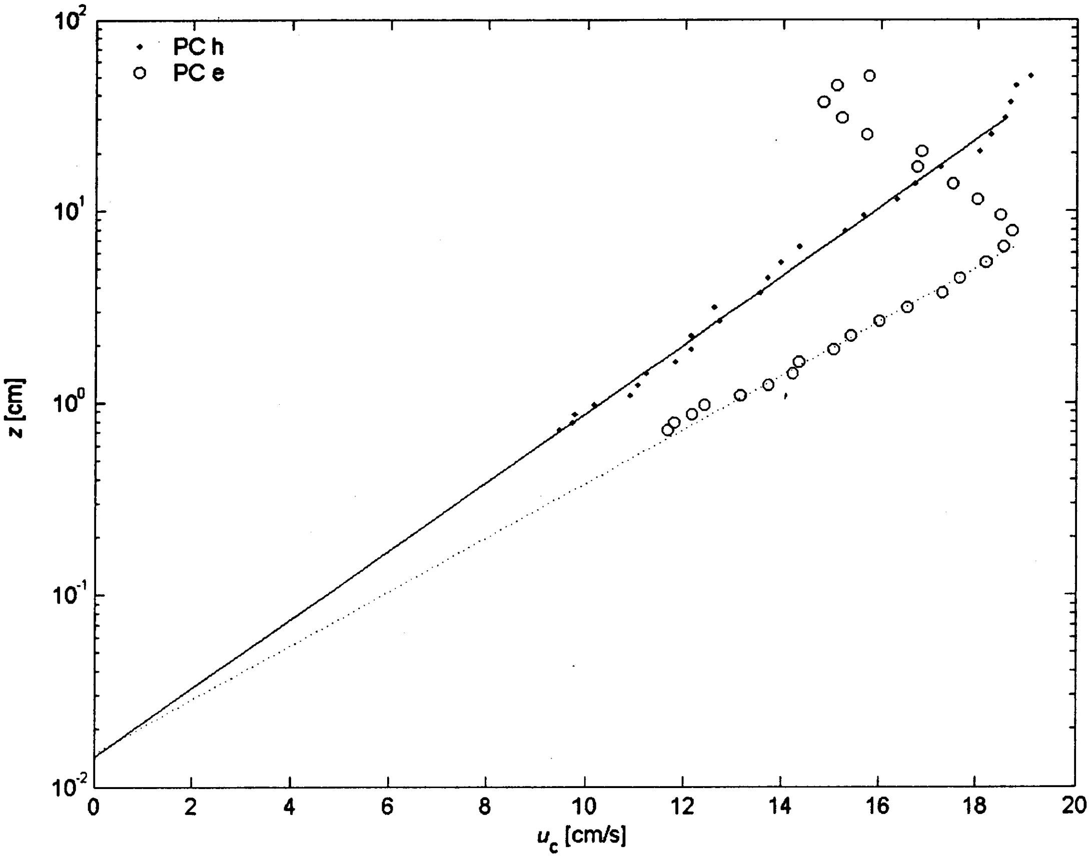

Figure B.7: Pure current velocity profiles with corresponding log fits. Open circles with the dotted line is experiment e, points (·) with the solid line is experiment h. Lines stop at last point used in log fit.

Table B.4 shows the results of the pure current experiments. The current shear velocity u_{*c}, the bottom roughness k_c, and their respective standard deviations are shown for all points, the top points, and the bottom points. The break between the top and bottom points here was taken at the midpoint of the points used in the fit, as no noticeable bends in the profiles were apparent. Also, the lumped mean results are given for all three combinations.

As discussed in Section 8.2, it is common practice to adjust the theoretical bed elevation of pure current profiles maximize the log fit to the data. Here, we consider the fits with and without adjustment of the theoretical bed. The top portion of Table B.4 labeled 'theoretical bed $\Delta z = 0$ (no adjustment)' shows the results of the analysis with no adjustment of the theoretical bed elevation, so that $z = 0$ occurs at the top of the spheres. The resulting roughness values are quite small; $k_c = 0.11$cm for the straight mean and 0.06cm for the lumped mean. The bottom portion of the table, labeled 'theoretical bed Δz at bottom of roughness elements' shows the results for the profiles after they have been adjusted so that $z = 0$ occurs at the bottom of the roughness elements. The current roughness values obtained now are neary the same as for the waves and waves in the presence of a current: $k_c = 0.36$cm for the straight mean and 0.21cm for the lumped mean. These roughness values are on the order of half the diameter of the glass spheres.

B.4. WAVE-CURRENT VELOCITY EXPERIMENTS

The combined wave-current velocity profiles were measured at the 4 location A, B, C, and D shown in Table B.1. The velocity profiles were measured in the same manner as the pure wave profiles: 2048points sampled at 24.333Hz and repeated 5 times at 27 vertical locations spaced at $\Delta\ln(z) = 0.2$.

Table B.4: Results of the pure current experiments over beads, h = 60cm.

Expt ID	x [m]	u_{*c} [cm/s]			k_c [cm]			σ_{u*c} [cm/s]			σ_{kc} [cm]		
		(all)	(top)	(bot)	(all)	(top)	(bot)	(all)	(top)	(bot)	(all)	(top)	(bot)
theoretical bed Δz = *0* (no adjustment)													
a	5.00	1.03	1.10	1.03	0.11	0.17	0.11	0.02	0.03	0.02	0.01	0.03	0.01
b	5.85	0.91	1.14	0.91	0.08	0.32	0.08	0.03	0.04	0.03	0.02	0.06	0.02
c	11.00	0.85	1.13	0.85	0.09	0.71	0.09	0.03	0.10	0.03	0.02	0.44	0.02
d	15.00	0.87	1.19	0.87	0.16	1.25	0.16	0.03	0.06	0.03	0.04	0.35	0.04
Mean		0.92	1.14	0.92	0.11	0.61	0.11	0.03	0.06	0.03	0.02	0.22	0.02
Std Dev.		0.08	0.04	0.08	0.04	0.48	0.04	--	--	--	--	--	--
Lumped Mean		0.83	0.91	0.83	0.06	0.11	0.06	0.02	0.04	0.02	0.01	0.03	0.01
theoretical bed Δz at bottom of roughness elements													
a	5.00	1.26	1.28	1.32	0.44	0.47	0.54	0.04	0.04	0.02	0.04	0.08	0.08
b	5.85	1.11	1.27	1.04	0.32	0.67	0.22	0.04	0.04	0.03	0.05	0.11	0.05
c	11.00	0.96	1.17	0.83	0.26	0.94	0.11	0.03	0.11	0.02	0.04	0.57	0.03
d	15.00	0.99	1.24	0.82	0.42	1.61	0.15	0.03	0.06	0.03	0.07	0.44	0.04
Mean		1.08	1.24	1.00	0.36	0.92	0.26	0.04	0.06	0.03	0.05	0.30	0.05
Std Dev.		0.14	0.05	0.23	0.09	0.50	0.20	--	--	--	--	--	--
Lumped Mean		0.98	1.03	0.95	0.21	0.28	0.18	0.02	0.05	0.02	0.02	0.08	0.02

The experimental parameters for the wave-current flows used in the application of the GMm and the LC models are given in Table B.5. Two estimates of the depth averaged velocities are found by the same methods as described in Section 9.3. The flow rate Q for these experiments is 1200gpm (0.076m^3/s). This gives the straight mean depth-averaged current velocity as about 16.6cm/s. If the depth-averaged velocities are obtained from the measured wave-current velocity profiles, the velocity is 17.3cm/s.

Table B.5: Base parameters for the wave-current experiments over beads, h = 60cm.

		Expt A	Expt B	Expt C	Expt D	Mean	Standard Deviation
x	[m]	10.32	11.06	11.79	12.53	11.42	0.95
h	[cm]	60.00	60.00	60.00	60.00	60.00	0.00
$z(u=u_m)$	[cm]	22.07	22.07	22.07	22.07	22.07	0.00
$u_{c,\mathrm{mean}}$ from u_{*c}, k_c	[cm/s]	17.16	17.40	17.14	17.45	17.29	0.16
$u_{c,\mathrm{mean}}$ from Q	[cm/s]	16.56	16.56	16.56	16.56	16.56	0.00
measured u_{bm}	[cm/s]	16.53	14.36	12.08	14.53	14.37	1.82
predicted u_{bm}	[cm/s]	17.73	15.76	13.51	15.34	15.59	1.73

The same methods for analyzing the wave-current profiles described in Chapter 9 were employed here. First, the apparent roughness felt by the current and the current shear velocities are obtained from the measured velocity profiles. Then, the velocity profile is predicted with the GMm and LC models based on the roughness values obtained from any of the other experiments, k_w, k_c, or k_{wc}. For this analysis, the value of k_c = 0.36cm was used. Then, the roughness is varied until a best fit profile is achieved, giving the value of the bottom roughness required to fit the predicted profile to the measured conditions.

Figure B.8 shows the lumped mean wave-current velocity measurements with (a) velocity profile predictions with the GMm and LC models based on $k_{cw} = 0.36$cm, and (b) the fit using the predictions based on the best fit k_{cw} for the GMm and LC models. The points ($\cdot$) are the measured data, the points with circles in (a) are used to obtain k_{ca} and u_{*c}, and the points with circles in (b) are used to obtain the best fit k_{cw}. Notice that here, the current boundary layer thickness extends nearly to the top points, and is about 30cm thick. This is because the apparent roughness for the wave-current flows are greater than those for the pure current flows, allowing the boundary layer to grow more over about the same distances. The model predictions based on the a roughness of 0.36cm (approximately half the bead diameter) are poor – they under-predict the current velocity by about 4cm/s with the the LC model, and about 6cm/s with the GMm model.

The results of the wave-current analysis on the raw wave-current velocity profiles are shown in Table B.6. This table is set up the same as the tables presenting the analysis in Chapter 9, such as Table 9.2. Results are given for all 4 experiments. The predictions of the wave-current velocity profiles are poor, with the errors of the predictions about half that of the depth averaged velocity. The roughnesses determined from the best fit k_{cw} are low by a factor of about 30 for the GMm model (factor of 10 for the LC model) compared to the bead diameter. This is shown by the ratio of the best fit bottom roughness to the actual bead diameter in Table B.6 as k_{cw}/d, where d is the diameter of the beads (0.64cm).

The fact that the profiles are already under-predicted suggests that adjusting the profiles for the wave-induced mass transport will not help the models better predict the flows, as the net wave-induced transport is negative. Adjusting for the transport would shift the profiles in the positive direction, causing the models to under-predict them even more. However, for comparison with the other experiments, the wave-current velocity profiles were adjusted for the pure wave-induced mass transport by subtracting the pure wave velocity profiles at the same locations from the wave-current profiles, just as was done in Section 9.4.2. Then the wave-current velocity profiles were predicted and Table B.7 shows the results. The analysis of the profiles adjusted for mass transport show nearly the same results as for the raw data.

As was done for the pure current experiments over beads, next we adjust the theoretical bed to the bottom of the flume just at the bottom of the beads. The results are shown in Table B.8, and

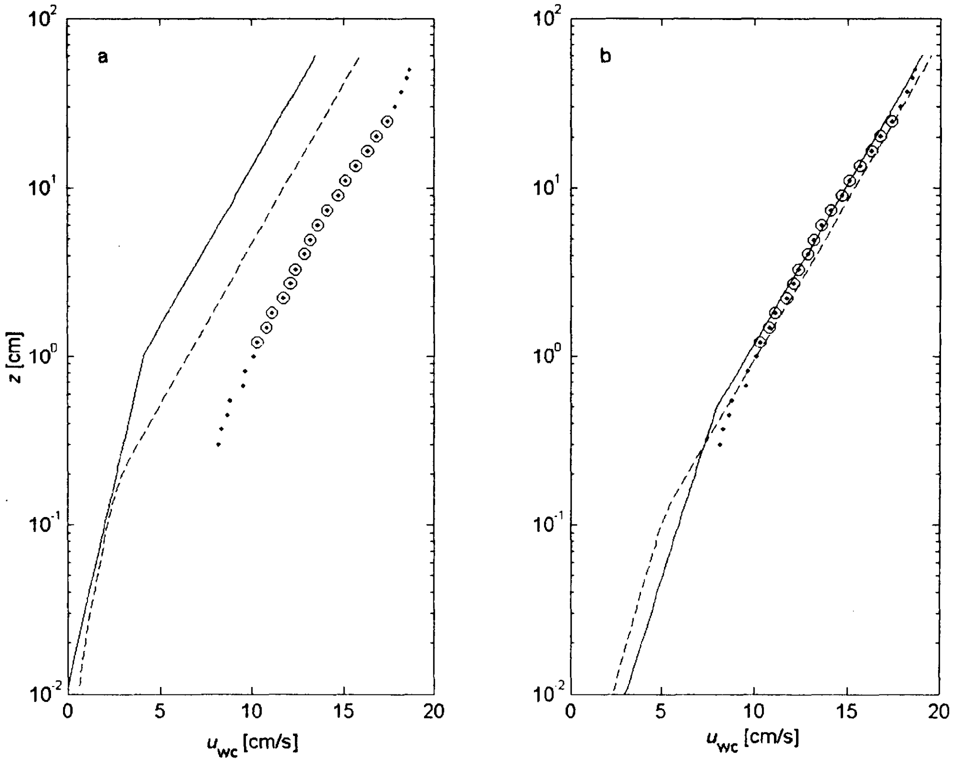

Figure B.8: Wave-current velocity profile of the lumped mean for beads, h = 60cm. (a) Solid line is GMm and dashed line is LC predictions using k_{cw} = 0.36. Points (·) are the measured velocity data, and points with open circles are used to determine u_{*c} and k_{ca}. (b) Predictions based on the best fit k_{cw}. Solid line is GMm and dashed is LC models. Points (·) are the measured velocity data, and points with open circles are used to determine best fit k_{cw}.

Table B.6: Results of wave-current experiments over beads, h = 60cm, raw velocity profiles.

		Expt A	Expt B	Expt C	Expt D	Mean	Standard Deviation	Lumped Mean
k_{cw} = 0.36cm								
u_{*c} (8:23)	[cm/s]	0.978	0.995	0.895	0.919	0.947	0.047	0.943
σ_{u*c}	[cm/s]	0.019	0.023	0.023	0.023	0.022	0.002	0.017
k_{ca} (8:23)	[cm]	0.593	0.608	0.313	0.334	0.462	0.160	0.436
σ_{kca}	[cm]	0.066	0.082	0.051	0.052	0.063	0.015	0.046
k_{ca} GMm	[cm]	5.920	4.764	4.326	5.368	5.094	0.697	5.120
k_{ca} LC	[cm]	2.035	1.714	1.569	1.866	1.796	0.200	1.802
error GMm	[cm/s]	5.709	5.180	6.028	6.342	5.815	0.496	5.867
error LC	[cm/s]	3.730	3.342	4.377	4.484	3.983	0.542	4.022
Best fit k_{cw}								
k_{cw} GMm	[cm]	0.028	0.038	0.023	0.018	**0.027**	0.008	**0.026**
k_{cw} LC	[cm]	0.062	0.079	0.041	0.035	**0.054**	0.020	**0.048**
σ_{kcw} GMm	[cm]	0.009	0.015	0.010	0.008	0.011	0.003	0.008
σ_{kcw} LC	[cm]	0.021	0.031	0.018	0.015	0.021	0.007	0.014
k_{ca} GMm	[cm]	0.588	0.590	0.320	0.337	0.459	0.150	0.459
k_{ca} LC	[cm]	0.534	0.531	0.273	0.297	0.409	0.143	0.370
error GMm	[cm/s]	0.198	0.252	0.246	0.234	0.233	0.024	0.223
error LC	[cm/s]	0.763	0.816	0.815	0.776	0.793	0.027	0.772
$k_{cw,\mathrm{GMm}}/d$		0.044	0.059	0.036	0.028	**0.042**	0.013	**0.041**
$k_{cw,\mathrm{LC}}/d$		0.097	0.123	0.064	0.055	**0.085**	0.031	**0.075**

Table B.7: Results of wave-current experiments over beads, h = 60cm, mass transport from pure wave velocity profiles.

		Expt A	Expt B	Expt C	Expt D	Mean	Standard Deviation	Lumped Mean
k_{cw} = 0.36cm								
u_{*c} (8:23)	[cm/s]	0.948	1.080	0.956	0.792	0.944	0.118	0.938
σ_{u*c}	[cm/s]	0.035	0.021	0.027	0.030	0.028	0.006	0.023
k_{ca} (8:23)	[cm]	0.449	0.768	0.388	0.078	0.421	0.283	0.337
σ_{kn}	[cm]	0.102	0.081	0.069	0.024	0.069	0.033	0.052
k_{ca} GMm	[cm]	6.163	4.267	3.967	6.468	5.216	1.281	5.154
k_{ca} LC	[cm]	2.096	1.592	1.481	2.140	1.827	0.339	1.811
error GMm	[cm/s]	6.603	4.819	5.863	8.819	6.526	1.695	6.634
error LC	[cm/s]	4.660	2.940	4.178	7.096	4.718	1.743	4.781
Best fit k_{cw}								
k_{cw} GMm	[cm]	0.018	0.056	0.031	0.015	**0.030**	0.018	**0.018**
k_{cw} LC	[cm]	0.041	0.095	0.055	0.015	**0.052**	0.034	**0.035**
σ_{kcw} GMm	[cm]	0.013	0.017	0.015	0.006	0.013	0.005	0.008
σ_{kcw} LC	[cm]	0.030	0.029	0.026	0.006	0.023	0.012	0.016
k_{ca} GMm	[cm]	0.410	0.753	0.386	0.371	0.480	0.183	0.318
k_{ca} LC	[cm]	0.395	0.565	0.327	0.175	0.365	0.161	0.282
error GMm	[cm/s]	0.419	0.220	0.283	3.247	1.042	1.472	0.273
error LC	[cm/s]	0.919	0.946	0.867	2.190	1.230	0.640	0.842
$k_{cw,\mathrm{GMm}}/d$		0.028	0.087	0.049	0.023	**0.047**	0.029	**0.028**
$k_{cw,\mathrm{LC}}/d$		0.064	0.149	0.086	0.023	**0.081**	0.052	**0.054**

are only a slight improvement over the raw data, with the roughness about 9% of the bead diameter for the GMm model, and about 20% for the LC model.

After further inspection of the velocity profile in Figure B.8, it appears that the points below about 5cm fall off the line for those points closer to the surface. If we exclude these points from the fit of the wave-current profile, using only the points 15 to 23 (z = 5cm to 25cm), and adjust the z elevation so $z = 0$ is at the bottom of the beads ($z = z+\Delta z$), we obtain another set of results, shown in Table B.9. The predictions of the wave-current profiles for this adjustment are shown in Figure B.9 (a) by taking k_{cw} = 0.36cm. Predictions using the best fit k_{cw} are shown in Figure B.9 (b). The measurements shown in both (a) and (b) are the lumped mean of the measurements.

Here, the predictions using the LC model are good, and under-predict the measured velocity by only about 0.7cm/s (0.5cm/s for the lumped mean). The GMm model still under-predicts the velocity significantly by about 3.3cm/s, resulting in about a 30% difference in the average velocities. The k_{cw} predicted using the LC model is now about 45% of the bead diameter, significantly closer to the estimates of the roughness found using pure waves, pure currents, and waves in the presence of a current. However, the roughness found using the GMm model is only about 17% of the bead diameter.

The fact that the models under-predict the velocity so substantially suggests that either the flow was not fully rough turbulent or that this type of uniform roughness is scaled differently than the uniform ripple crests or sand grains. Mathisen (1993) performed the same experiments over beads with waves and currents of about the same magnitude. The values of roughness he obtained for a current in the presence of wave (k_{cw}) varied, but was 0.09cm for the case when T = 2.63s. This is on the same order of magnitude as the results seen here where k_{cw} = 0.02 to 0.11cm with the GMm model.

The comparison between the LC and GMm models is interesting. In the experiments containing ripples, the GMm model needed about the same roughness as the pure wave, pure currents, and waves in the presence of a current, while the LC model needed a roughness about 3 times as large. Here, for the case of the beads, the LC model is about the same as the other estimates, while the GMm model needs a roughness of about 3 times smaller.

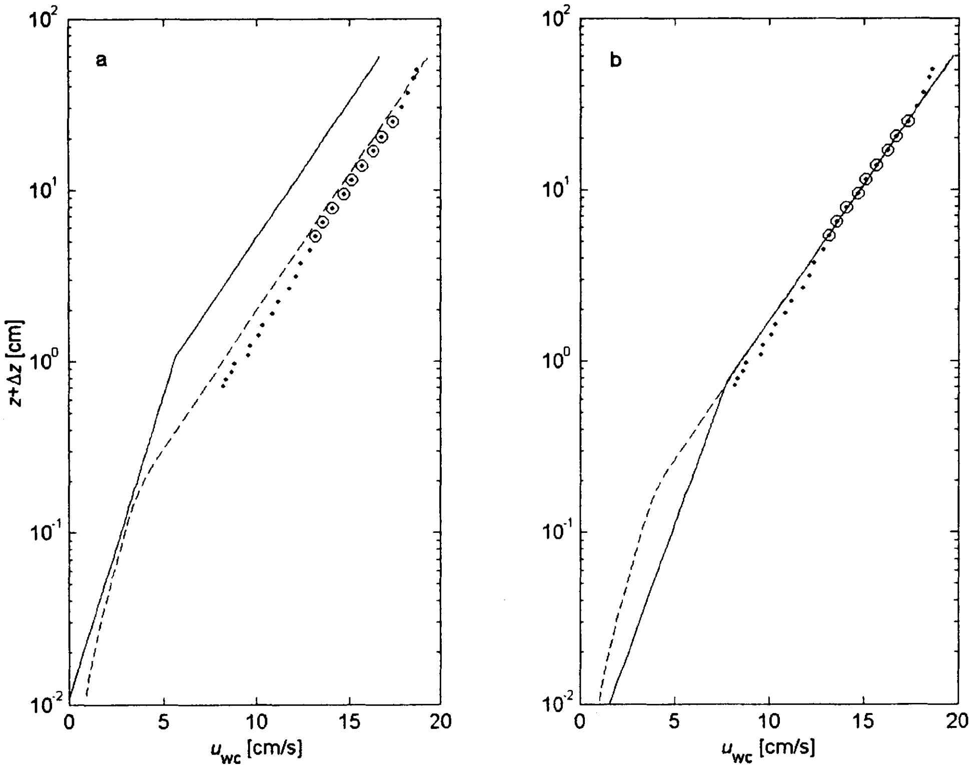

Figure B.9: Wave-current velocity profile of the lumped mean, z=z+Δz, for beads, h = 60cm. (a) Solid line is GMm and dashed line is LC predictions using k_{cw} = 0.36. Points (·) are the measured velocity data, and points with open circles are used to determine u_{*c} and k_{ca}. (b) Predictions based on the best fit k_{cw}. Points (·) are the measured velocity data, and points with open circles are used to determine best fit k_{cw}.

Table B.8: Results of wave-current experiments, $z = z + \Delta z$, over beads, h = 60cm.

		Expt A	Expt B	Expt C	Expt D	Mean	Standard Deviation	Lumped Mean
k_{cw} = 0.36cm								
u_{*c} (8:23)	[cm/s]	1.068	1.086	0.977	1.004	1.034	0.052	1.030
σ_{u*c}	[cm/s]	0.016	0.021	0.021	0.023	0.020	0.003	0.013
k_{ca} (8:23)	[cm]	1.056	1.079	0.587	0.626	0.837	0.267	0.796
σ_{kn}	[cm]	0.082	0.109	0.074	0.082	0.087	0.016	0.055
k_{ca} GMm	[cm]	5.276	4.236	3.853	4.783	4.537	0.623	4.560
k_{ca} LC	[cm]	1.875	1.584	1.454	1.721	1.658	0.181	1.664
error GMm	[cm/s]	4.338	3.715	4.677	5.017	4.437	0.555	4.496
error LC	[cm/s]	2.162	1.767	2.883	2.967	2.445	0.578	2.480
Best fit k_{cw}								
k_{cw} GMm	[cm]	0.059	0.079	0.051	0.041	**0.057**	0.016	**0.055**
k_{cw} LC	[cm]	0.143	0.185	0.102	0.087	**0.129**	0.044	**0.121**
σ_{kcw} GMm	[cm]	0.014	0.024	0.017	0.015	0.018	0.004	0.011
σ_{kcw} LC	[cm]	0.035	0.056	0.035	0.032	0.039	0.011	0.024
k_{ca} GMm	[cm]	1.036	1.061	0.608	0.645	0.837	0.244	0.810
k_{ca} LC	[cm]	0.960	0.995	0.544	0.573	0.768	0.243	0.732
error GMm	[cm/s]	0.158	0.203	0.219	0.228	0.202	0.031	0.135
error LC	[cm/s]	0.507	0.540	0.565	0.508	0.530	0.028	0.504
$k_{cw, GMm}/d$		0.092	0.123	0.079	0.064	**0.089**	0.025	**0.086**
$k_{cw, LC}/d$		0.223	0.289	0.160	0.135	**0.202**	0.069	**0.189**

Table B.9: Results of wave-current experiments, $z = z + \Delta z$, fitting using top points, over beads, h = 60cm.

		Expt A	Expt B	Expt C	Expt D	Mean	Standard Deviation	Lumped Mean
k_{cw} = 0.36cm								
u_{*c} (15:23)	[cm/s]	1.147	1.195	1.063	1.112	1.129	0.056	1.121
σ_{u*c}	[cm/s]	0.037	0.025	0.047	0.037	0.036	0.009	0.010
k_{ca} (15:23)	[cm]	1.595	1.861	0.993	1.183	1.408	0.393	1.322
σ_{kn}	[cm]	0.280	0.209	0.264	0.228	0.245	0.032	0.067
k_{ca} GMm	[cm]	4.791	3.715	3.441	4.173	4.030	0.591	4.067
k_{ca} LC	[cm]	1.754	1.454	1.352	1.571	1.533	0.172	1.542
error GMm	[cm/s]	3.494	2.288	3.658	3.879	3.330	0.713	3.483
error LC	[cm/s]	0.343	0.809	0.936	0.895	0.746	0.274	0.491
Best fit k_{cw}								
k_{cw} GMm	[cm]	0.103	0.159	0.093	0.090	**0.111**	0.032	**0.103**
k_{cw} LC	[cm]	0.286	0.426	0.223	0.229	**0.291**	0.094	**0.266**
σ_{kcw} GMm	[cm]	0.055	0.052	0.067	0.049	0.056	0.008	0.015
σ_{kcw} LC	[cm]	0.152	0.140	0.161	0.126	0.145	0.015	0.039
k_{ca} GMm	[cm]	1.592	1.843	0.981	1.185	1.400	0.390	1.318
k_{ca} LC	[cm]	1.596	1.855	0.989	1.183	1.406	0.392	1.317
error GMm	[cm/s]	0.140	0.102	0.179	0.141	0.140	0.032	0.040
error LC	[cm/s]	0.139	0.101	0.177	0.143	0.140	0.031	0.040
$k_{cw, GMm}/d$		0.160	0.248	0.145	0.140	**0.173**	0.051	**0.160**
$k_{cw, LC}/d$		0.446	0.665	0.348	0.358	**0.454**	0.147	**0.415**

B.5. SUMMARY

Table B.10 summarizes the values of the roughness experienced by a current in the presence of waves, k_{cw} for both the GMm and LC models for the different adjustments made to the measurements in an attempt the obtain a better fit with the other bottom roughness values. No significant improvement was made by adjusting the profiles for wave-induced transport. The roughness values approximately doubled when $z = 0$ was set at the bottom of the roughness elements instead of the top, similar to what was seen for the pure current flows. By only considering the points above 5cm yielded another doubling of the roughness. Even after these adjustments, the roughness values are about 40% of the bead diameter for the LC model and about 17% of the bead diameter for the GMm model

Table B.10: Summary of lumped mean wave-current bottom roughness values for GMm and LC models.

	k_{cw} (GMm) [cm]	k_{cw} (LC) [cm]
No mass transport	0.026	0.048
Mass transport from Pure Wave	0.018	0.035
No Mass transport $z = z + \Delta z$	0.055	0.121
No Mass transport $z = z + \Delta z$, top points	0.103	0.266

Table B.11 summarizes the bottom roughness values obtained from the pure waves, waves in the presence of a current, pure currents, and currents in the presence of waves for beads with h = 60cm. The different methods of averaging (both straight and lumped mean) are shown (note the footnotes in the table). The values of k_{cw} are from the adjustments made to the theoretical bed and only considering the points above 5cm.

Table B.11: Summary of mean bottom roughness values.

	roughness [cm]	Std. Dev. of roughenss
k_w	0.480	--
k_{wc}	0.393	--
k_c^1	0.416	0.066
k_c^2	0.205	0.023
$k_{cw}^{1,3}$ (GMm)	0.111	0.056
$k_{cw}^{2,3}$ (GMm)	0.103	0.015
mean	0.285	--
std. dev.	0.165	--
$k_{cw}^{1,3}$ (LC)	0.291	0.145
$k_{cw}^{2,3}$ (LC)	0.266	0.039
mean	0.278	--
std. dev.	0.018	--

[1]: straight mean value.

[2]: lumped mean value.

[3]: no mass transport.

For k_w and k_{wc}, the dissipation due to the bottom, m_b, is only about half of the total dissipation, m_t, leaving the other half to be the dissipation for the sidewalls, m_{sw}. When m_{sw} is such a large contributor to the total dissipation, its estimation is critical for an accurate estimation of the bottom roughness. Here, the sidewall dissipation estimation is based only on laminar dissipation, which may not be the case. Further, there could easily have been dissipation due to a surface film that was unaccounted for. In the experiments over a rippled bed, the sidewall and surface dissipation play a minor role – they account for about 10% of the total dissipation and only an order of magnitude estimate is needed. But here, not accounting for the surface film or correctly accounting for the sidewall dissipation could incorrectly increase the estimates of k_w and k_{wc}. Furthermore, the roughness experienced by the current shows a wide range of bottom roughness estimates. If the theoretical bed is not adjusted, k_c estimates are somewhere between 0.06cm and 0.11cm – much closer to the estimates of k_{cw}. This fact combined with possibility that k_w and k_{wc} values may be over-estimated brings the estimates of the k_{cw} into the range that would allow one to state that the estimates of all the roughnesses could be represented by a single value of the roughness, although no definite conclusion can be made either way on this fact.

To address the k_{cw} values, Mathisen argued that for these wave conditions over the beads, the boundary layer flow would not be fully rough turbulent, and therefore the model would be out of its range of validity. This certainly may be the case. For these conditions, Jonsson's (1966) friction factor diagram puts us right on the edge of the fully rough turbulent region. From knowledge of fluid mechanics, we know that the transition to turbulent flows is not a specific number. There is certainly a transition region that occurs, and where we are within that region could be influenced by any number of things such as how closely the beads are packed at the specific region of interest and along the entire bottom leading up to that point, if the water temperature is 10°C or 20°C, if there is construction outside that could induce perturbations in the flow – any number of variabilities can influence the flow in this delicate transition region.

While acknowledging that the flow may be in the transitional region rather than being fully rough turbulent might well be causing the model's poor wave-current prediction, the fact that the roughness is so low may possibly be explained by the geometry of the beads. The beads impart less drag on the flow than their equivalent sand grains since the beads have smooth, rounded surfaces and are made of polished glass while sand is angular with more irregular edges.

If this was exclusively the case, we would expect that all the values estimated for the roughness would be smaller. While this may explain why the k_w, k_c, and k_{wc} values are smaller than the diameter of the beads –about ¾ to ¼ the diameter, the k_{cw} values remain the outliers. However, there is reason to believe that the other values are in fact too high. In any case, the small values of k_{cw} remain unexplained and the experiments presented in this appendix remain as a whole inconclusive.

APPENDIX C.

40CM WATER DEPTH MOVABLE BED EXPERIMENTS

An additional set of experiments were run over the sediment bed with a water depth of $h = 40$cm. These experiments served two purposes. One was to provide an extra data set to allow for a comparison with the results of the main study. The second was to match conditions of an experiment performed at the National University of Singapore by Kularatne (2001) who studied the roughness experienced by waves and currents at a 90° angle. The experiments performed in the appendix provide a data set for co-directional waves and currents and allow for a comparison between the two cases.

These experiments were performed with the exact same equipment and facilities as explained in Chapter 3. The water depth was changed to $h = 40$cm, the wave conditions were changed to a have a period $T = 1.5$s and an amplitude of about $a = 5$cm. The desired current velocity was a depth averaged mean of about $\bar{u}_c = 10$cms/. Unfortunately, the current could not be reduced to that low a value without fear of burning out the pump. Therefore, a current velocity of $\bar{u}_c \cong$ 11.5cm/s – the lowest that could be achieved – was used throughout these experiments.

The free surface for $T = 1.5$s waves proved to be quite irregular and did not display the typical beat pattern shown for the T=2.63s, h=60cm experiments. This is explained more in Section C.1. The resulting pattern showed some node-antinode patterns, but not in a regular way. Therefore, the profile measurement locations were positioned at 5 locations along what was thought to be one "beat" pattern. The locations were selected at the local maximum and minimum points until the pattern seemed to repeat itself.

A summary of all the experiments performed for these conditions is shown in Table C.1. The *x*-location occurs at local maxima of minima of the wave segment measured. In the table, H (H anti or H node) refers to the higher segment maximum or minimum, and L (L anti or L node) refers to the lower maximum or minimum.

The pure wave measurements and wave-current measurements were made at the same 5 locations in the tank relative to the 1st harmonic free surface. The first 5 pure current measurements were made at the same locations as the pure wave and wave-current. These are denoted pure current experiments a, b, c, d, and e. A second set of pure current measurements were made at 15 locations over a bed free of any mean bed elevation, but still covered with pure wave ripples modified by the current. These are denoted with experiment IDs af – tf. The first 5 of these experiments were done at the same locations as the original PC experiments, and the other 10 were done at other locations along the flume without specifically noting the position relative to the pure wave free surface.

During these experiments, the ADV bottom profiler had not yet been developed. Therefore, the majority of the bedform measurements were made by tracing the ripple geometry by hand on the side of the tank. The locations where this was performed is denoted "side" in the Bedform geometry column of Table C.1. The ADV profiling was undergoing testing during these experiments, so some profiles were made with the ADV. These data are available for experiments denoted "ADV" in the Bedform geometry column. At some locations, both side and ADV measurements were made. This is also noted in the table.

Table C.1: Summary of experiments over sand, h = 40cm.

Experiment ID	x [m]	Wave Segment	Bedform geometry
pure wave			
a	9.45	H anti	side
b	10.20	H node	side, ADV
c	10.79	L anti	side
d	11.35	L node	side
e	12.10	H anti	side, ADV
pure current, mean bed variation present			
a	9.45	H anti	side
b	10.20	H node	side
c	10.79	L anti	side
d	11.35	L node	side
e	12.10	H anti	side
pure current, no mean bed variation			
af	9.45	H Anti	no
bf	10.20	H node	no
cf	10.79	L Anti	ADV
df	12.10	L node	ADV
ef	12.50	H anti	no
gf	8.00	--	no
hf	8.50	--	no
if	9.00	--	ADV
jf	11.00	--	no
kf	11.35	--	no
lf	13.00	--	no
mf	13.50	--	no
nf	14.00	--	no
of	14.50	--	no
pf	15.00	--	ADV
wave-current			
A	9.45	anti	side
B	10.20	node	side, ADV
C	10.79	anti	side
D	11.35	node	side
E	12.10	anti	side, ADV

C.1. FREE SURFACE RESOLUTION

As noted above, the free surface for the T = 1.5s waves does not follow the same simple beat pattern discussed in Section 4.2 of the text for the h = 60cm case. Figure C.1 illustrates the measured 1st and 2nd harmonic free surface elevation for these conditions. As explained in Chapter 4, the beat length is $L_b^{(1)} = L_i/2$ (or equation (4.12)). For T = 1.5s and h = 0.4m, the incident wave length is L_i = 2.61m, and the expected beat length is $L_b^{(1)}$ = 1.307m. For the second harmonic, by applying equation (4.19), we obtain the 2nd harmonic beat length as $L_b^{(2)}$ = 2.62m. Figure C.1 (a) and (b) shows the fit of the free surface using equations (4.14) and (4.18), respectively for the 1st and 2nd harmonics. The second harmonic seems to fit well, but the first harmonic fit is poor. It seems there is some variation at this beat length (1.31m), but the measured free surface varies widely from the prediction.

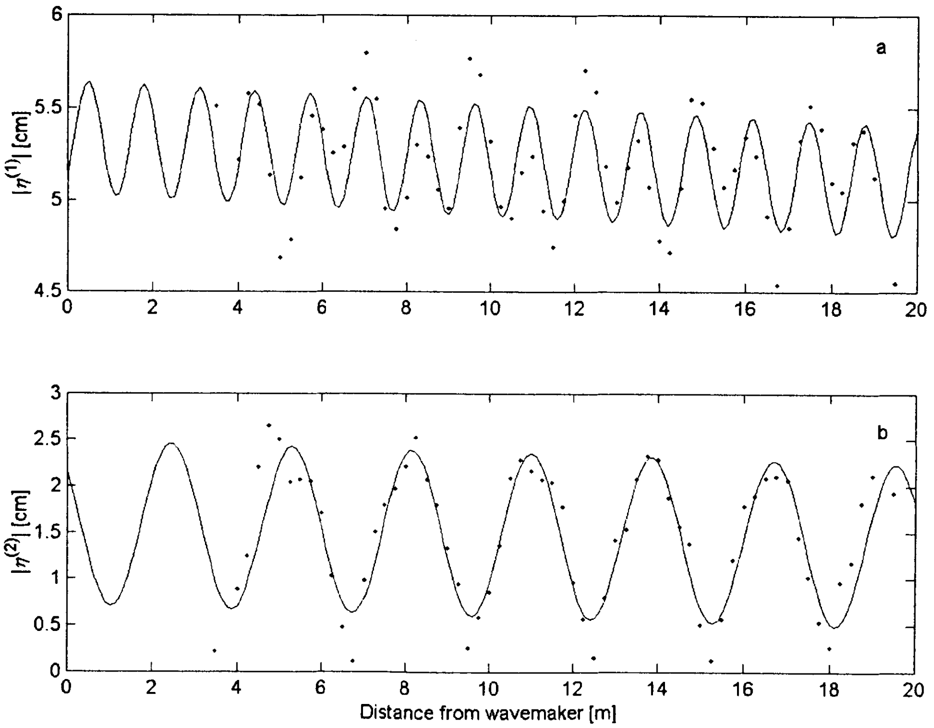

Figure C.1: (a) 1st and (b) 2nd free surface measurements over sand, h = 40cm with 3-term fits of free surface profiles. Points (·) are the measurements and the solid lines are the fits from equations (4.14) in (a) and (4.18) in (b).

To better resolve the wave conditions present, consider the following. The current filter is in place for these experiments. As described in Section 4.3, the filter acts as an semi-impermeable barrier to waves with periods less than about 1s. Because we are generating waves with a period of 1.5s, the second harmonic is $T/2 = 0.75$s, less than what can pass through the filter. Therefore, the harmonic control we were able to impose on the waves in Chapter 4 is not possible here. We cannot use the method of Madsen (1971) to correct for the free second harmonic in the flume, as any 2nd harmonic generated will not pass through the filter with any regularity. The free second harmonic present is quite large, and as shown in Figure C.1, is on the same order of magnitude as the bound second harmonic; $a_F / a_b \cong 1$.

In Chapter 4, when the free second harmonic was not corrected for, interaction occurred between the first and second harmonic as shown in Figure 4.2. When the second harmonic is low, the first harmonic is high, and when the second harmonic is high, the first harmonic is low. But the interaction for those cases was small, as the amplitude of the free 2nd harmonic was only about 10% to 20% of the bound 2nd harmonic. For the present conditions, however, the free 2nd harmonic is the same size as the bound. Therefore, we expect the interaction to be greatly exaggerated.

To model this interaction, an additional term is proposed for the shape of the free surface in equation (4.14) that relates the interaction between the first and second harmonic by a sinusoidally varying term of some amplitude β_{12} that linearly relates the interaction between the

1st and 2nd harmonics. The term should vary at a length of that of the 2nd harmonic beat, $L_b^{(2)}$. The proposed term is formulated as

$$\beta_{12}\cos\left(k_b^{(2)}x+\phi_{12}\right) \tag{C.1}$$

where $k_b^{(2)} = 2\pi/L_b^{(2)}$ and ϕ_{12} is the relative phase of this interaction term. Then adding (C.1) to equation (4.14), the free surface can be described as

$$\left|\eta^{(1)}\right| = a_{io} - m_t x + a_r \cos\left[(k_i + k_r)x + (\phi_r - \phi_i)\right] + \beta_{12}\cos\left(k_b^{(2)}x+\phi_{12}\right) \tag{C.2}$$

To fit this equation to the free surface, a simple least-squares method is applied. First, we express equation (C.2) as

$$\left|\eta_{fit}^{(1)}\right|_j = y_j = A - Bx_j + CF_j + DG_j \tag{C.3}$$

Where $A = a_{io}$, $B = m_t$, $C = a_r$, $D = \beta_{12}$, $F_j = \cos\left[(k_i + k_r)x_j + (\phi_r - \phi_i)\right]$, and

$G_j = \beta_{12}\cos\left(k_b^{(2)}x_j + \phi_{12}\right)$. Then, the usual least squares error term is written as

$$error = \varepsilon = \left[\sum_{j=1}^{n}\left\{\frac{\left(\left|\eta_{meas}^{(1)}\right|_j - \left|\eta_{fit}^{(1)}\right|_j\right)^2}{n-2}\right\}\right]^{\frac{1}{2}} \tag{C.4}$$

To perform the least squares fit, ε is minimized with respect to each variable A, B, C, and D, yielding 4 equations

$$\frac{\partial \varepsilon}{\partial A} = 0 \Rightarrow \overline{y} = A + B\overline{x} + C\overline{F} + D\overline{G} \tag{C.5}$$

$$\frac{\partial \varepsilon}{\partial B} = 0 \Rightarrow \overline{yx} = A\overline{x} + B\overline{x^2} + C\overline{Fx} + D\overline{Gx} \tag{C.6}$$

$$\frac{\partial \varepsilon}{\partial C} = 0 \Rightarrow \overline{yF} = A\overline{F} + B\overline{xF} + C\overline{F^2} + D\overline{GF} \tag{C.7}$$

$$\frac{\partial \varepsilon}{\partial D} = 0 \Rightarrow \overline{yG} = A\overline{G} + B\overline{xG} + C\overline{FG} + D\overline{G^2} \tag{C.8}$$

These equations can be solved in the least squares sense, obtaining values for A, B, C, and D that give the best fit to the measured points. This method is referred to as the 4-term fit, while the method that neglects the 1st –2nd harmonic interaction developed by Rosengaus (1987) and used extensively in the thesis text is referred to as the 3-term fit.

Applying the 4-term fit to the 1st harmonic data shown in Figure C.1, a fit is obtained and shown in Figure C.2. Here, the parameters $k_b^{(1)}$, $k_b^{(2)}$, $\Delta\phi$ and ϕ_{12} have been left as free parameters to be adjusted to obtain the best fit.

The fit to the 1st harmonic is quite good. Table C.2 shows the values of the fit that characterize the free surface for these conditions for both the 3-term fit (displayed in Figure C.1(a)) and the 4-term fit (as shown in Figure C.2(a)). Surprisingly, the values of a_i, a_r, and m_t are not dramatically different. However, the error (the measure of the goodness of the fit) has improved significantly from 0.27545m for the 3-term to 0.0508m for the 4-term fit. The error can be interpreted as a standard deviation of the fit, and is expressed in units of meters. R, the reflection coefficient, is quite low here at only 6%. This may be real, or may be an artifact of the 4-term fit where β_{12} unrealistically accounts for too much of the variation, artificially reducing a_r. Nevertheless, we can now resolve the variation of the 1st harmonic free surface, and therefore can better interpret the results of the experiments.

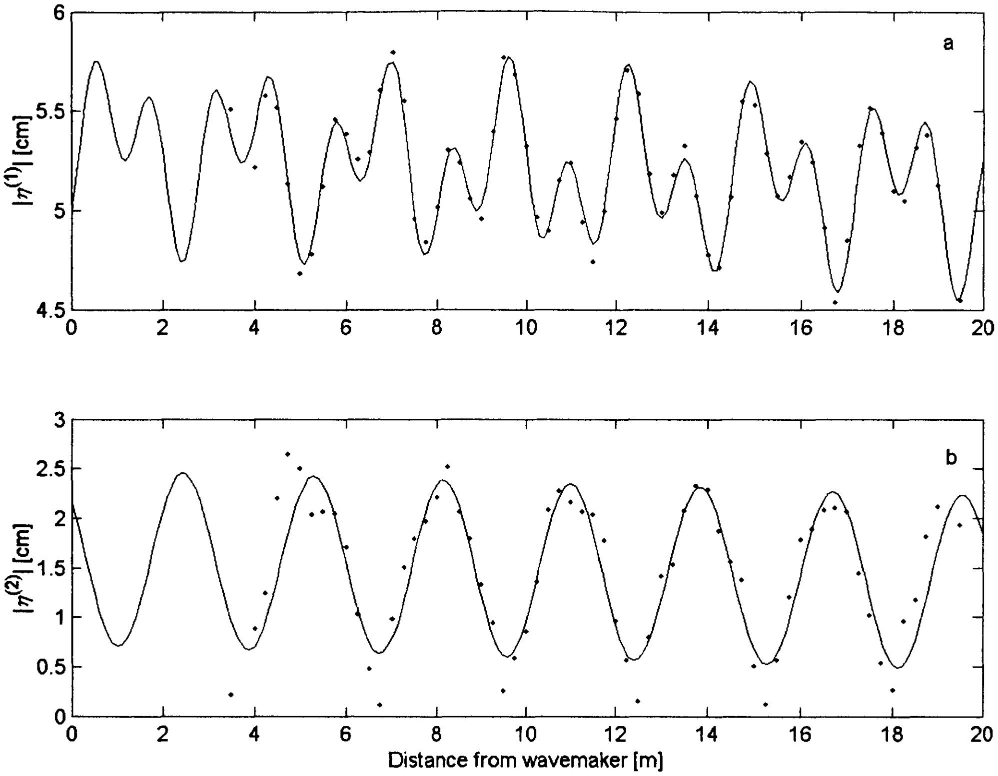

Figure C.2: (a) 1st and (b) 2nd free surface measurements over sand, h = 40cm, with 4-term fit of 1st harmonic, 3-term fit of 2nd harmonic.

Table C.2: Comparison of 3-term and 4-term 1st harmonic fit of the free surface over sand, for h = 40cm pure waves.

	$L_b^{(1)}$ [m]	$L_b^{(2)}$ [m]	a_i [cm]	a_r [cm]	R	m_{tot} [cm/cm]	β_{12} [cm]	error [m]
3 term fit	1.307	--	5.34	0.31	0.06	-1.21E-04	--	**0.2745**
4 term fit	1.310	2.850	5.32	0.30	0.06	-1.13E-04	0.26	**0.0508**

C.2. BEDFORM GEOMETRY OBSERVATION AND PREDICTION

The bedform geometry measurements for this set of experiments were primarily performed by tracing the ripple geometry on the side of the tank. Traces were made before and after each velocity profile measurement. The traces were typically 22cm long (2 transparency sheets), and the geometry was measured by hand. The error in these measurements can be from either human error, giving a possible error of about one fourth the ripple height (about 0.2cm on average), or from the fact that the ripples on the side of the tank are different from those felt by the flow. Little can be done to account for the second kind of error.

The results of the bedform measurements from the side-tracing method are shown in Table C.3. The row labeled mean is the average of the values for that parameter for all experiments listed. The side-tracing bedform measurements were only done at the locations for PW and PC experiments a-e, and for WC experiments A-E, all of which occurred at the same *x*-locations. 'pre' refers to measurements before the velocity profile, and 'post' refers to measurement after the velocity profile. For the PC case, measurements were only performed before, as the flow was too weak to change the geometry.

Table C.3: Bedform geometry measured with the side-tracing method for sand, h = 40cm.

	Pure wave				Pure current		Wave-current			
	pre		post		pre		pre		post	
x [m]	η [cm]	λ [cm]	η [cm]	λ [cm]	η [cm]	λ [cm]	η [cm]	λ [cm]	η [cm]	λ [cm]
9.45	0.83	6.00	1.00	6.18	0.73	5.31	0.78	5.44	0.68	4.16
10.20	1.00	5.85	0.70	5.00	1.00	6.72	0.90	5.08	0.80	4.65
10.79	0.83	5.48	0.68	4.70	0.74	5.08	0.82	4.70	0.67	4.38
11.35	0.78	4.58	0.83	5.09	0.70	4.48	0.95	5.74	0.74	5.13
12.10	0.70	4.76	1.00	5.38	0.95	5.50	--	--	0.88	5.45
mean	0.83	5.33	0.84	5.27	0.82	5.42	0.86	5.24	0.75	4.75
Std. Dev.	0.19	0.94	0.18	0.74	0.19	1.07	0.13	0.85	0.16	0.68

The ADV bed profiler was in development during the time of these tests, and thus, few profiles were measured with the ADV. Table C.4 shows those measurement made by the ADV. Note that all these measurements, except for the PC measurements, were taken after all velocity profile experiments had been performed. On the average, the ADV and side-tracing results are quite similar. Only the pure current ripple geometries vary significantly: η = 0.82cm (side) to 0.76cm (ADV), and λ = 5.42cm (side) to 6.13cm (ADV). Statistically, these measurements are not significantly different as the values fall within one standard deviation of each other.

Table C.4: Ripple geometry measured with the ADV profiler sand, h = 40cm.

	Pure wave		Pure current		Wave-current	
x [m]	η [cm]	λ [cm]	η [cm]	λ [cm]	η [cm]	λ [cm]
9.00	--	--	0.78	6.26	--	--
10.20	0.91	6.14	--	--	0.70	4.80
10.79	--	--	0.90	6.96		
12.10	0.74	5.81	0.60	4.88	0.79	5.83
15.00	--	--	0.77	6.40	--	--
mean	0.83	5.98	0.76	6.13	0.75	5.32
Std. Dev.	0.12	0.23	0.12	0.88	0.06	0.73

The ripple geometry can be predicted just as was done in Section 5.3.1 for pure wave ripples and Section 5.3.3 for the wave-current ripples. Table C.5 shows the predicted pure wave ripples. Predictions were only made with the measured orbital bottom velocity $u_{bm}^{(1)}$, as the highly variable free surface and interactions between 1st and 2nd harmonics made predicting the bottom velocities difficult. Overall, the predictions are quite good, but tend to be smaller than the observed values. The percent difference in ripple height and length are shown in the columns $\%\Delta\eta$ and $\%\Delta\lambda$. On average, the predicted height is 9% smaller and the predicted length is 10% shorter than the observed values.

Table C.6 shows the predicted and measured wave-current ripples. As in Section 5.3.3, two methods were used to bracket the ripple geometry. Again, only the measured bottom velocity was used to predict the geometry; no predictions were made of the bottom velocity based on the free surface. The first method of ripple prediction neglects the current and calculates the ripples based only on the wave action. This is labeled in Table C.6 as 'from measured u_{bm}, u_c=0'. These predictions are low on average by about 10%. The second method accounts for the current, as explained in Section 5.3.3. These predictions on average are high by some 40%.

Table C.5: Measured and predicted pure wave ripple geometry for sand, h = 40cm.

Expt ID	x [m]	$u_{bm}^{(1)}$ [cm/s]	η [cm]	λ [cm]	η_{measured} [cm]	$\lambda_{\text{measured}}$ [cm]	$\%\Delta\,\eta$	$\%\Delta\,\lambda$
a	9.45	16.95	0.78	4.88	0.92	6.09	-18.06	-24.76
b	10.20	19.17	0.84	5.27	0.85	5.43	-1.68	-2.94
c	10.79	15.53	0.73	4.60	0.75	5.09	-2.59	-10.55
d	11.35	16.27	0.76	4.75	0.80	4.83	-6.07	-1.75
e	12.10	15.59	0.74	4.61	0.85	5.07	-15.57	-9.81
	mean	16.70	0.77	4.82	0.83	5.30	-8.80	-9.96
	Std. Dev.	1.50	0.04	0.27	0.06	0.49	7.55	9.17

Table C.6: Measured and predicted wave-current ripple geometry for sand, h = 40cm.

	measured @ $z=\delta_w$	measured (z=2cm)	from measured u_{bm}, u_c=0		from measured u_{bm}, $u_c\neq0$		measured ripple geometry	
Expt ID	u_{bm} [cm/s]	u_c [cm/s]	η [cm]	λ [cm]	η [cm]	λ [cm]	η [cm]	λ [cm]
A	12.80	4.38	0.64	4.04	0.96	6.03	0.73	4.80
B	16.04	3.33	0.76	4.75	1.14	7.19	0.85	4.87
C	15.44	3.77	0.74	4.62	1.19	7.45	0.74	4.54
D	16.80	3.11	0.78	4.90	1.14	7.17	0.85	5.43
E	14.19	3.40	0.69	4.35	1.12	7.05	0.88	5.45
	mean	3.60	0.72	4.53	1.11	6.98	0.81	5.02
	Std. Dev.	0.50	0.05	0.34	0.09	0.55	0.07	0.41

Measurement of the mean bed variations were made using the same method as described in Section 3.8.2 – traces were made on the side of the tank. The mean bed elevation was measured before the pure wave velocity measurements (called pre PW; the bed had been exposed to a total of 15hrs of pure wave action) and after the pure wave velocity measurements (called post PW; a cumulative total of 25hrs of wave action). Then the wave-current flow was allowed to act on the bed for 3 hours. No observable changes occurred (as the current is weak compared to the waves), and the wave-current velocity measurements were performed for a total of 10 hours. The mean bed was measured after the wave-current experiments (called post WC; a cumulative total of 38 hours, 13 from the wave-current flow). These measurements are shown in Figure C.3 (b). The lines through the points are 3-point moving averages of the measured data. Figure C.3 (a) shows the fits to the PW (solid line) and WC (dotted line) free surface elevations. At its largest, the mean bed has a total height of almost 8cm. It's length is on the order of the 2nd harmonic beat length, about 3m.

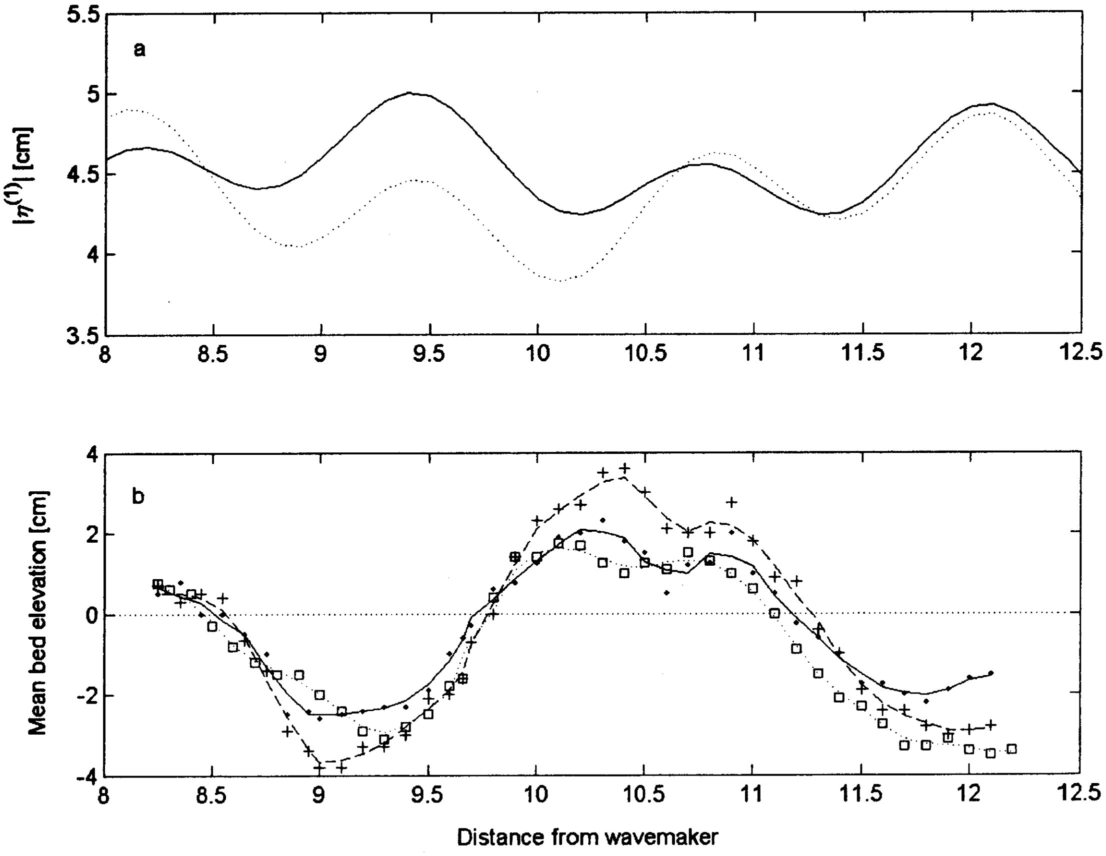

Figure C.3: (a) 1st harmonic free surface elevation for the pure wave and wave-current experiments over sand, h = 40cm; (b) mean bed elevation for pre pure wave, post pure wave, and post wave-current experiments. Lines in (b) are the 3-point moving averages of the measurements. Solid line is for pre PW, dashed line is post PW, and dotted line is post WC. The horizontal dotted line is $z = 0$.

C.3. BOTTOM ROUGHNESS FROM WAVE ATTENUATION

Attenuation measurements were performed for both the pure wave and wave-current flows to obtain a measurement of the bottom roughness felt by the waves k_w and the bottom roughness felt by the wave in the presence of a current k_{wc}. The procedures followed here are exactly the same as those followed in Chapter 6. The pure wave attenuation measurements were performed just prior to the pure wave velocity measurements. The free surface profiles observed for pure waves are shown in Figure C.4. (a) is the 1st harmonic with the fit (solid line) prescribed by equation (C.2). The dotted line on (a) is the attenuation slope of the first harmonic amplitude, $a_{i0} - m_t x$. (b) shows the second harmonic, and the fit prescribed by equation (4.18). The values obtained from the fit of the first harmonic fit are listed in Table C.7.

Figure C.5 shows the measured and fit (a) 1st and (b) 2nd harmonic free surface profiles for combined waves and currents, just as in Figure C.4 for pure waves. The fit to the 1st harmonic is from equation (C.2), and for the 2nd harmonic, equation (4.18). The wavelengths were modified by the current as described in Section 4.4.2. Table C.7 shows the values obtained from the fit of the 1st harmonic for combined waves and currents. Notice that the reflection for these cases R = 5% and 7%, significantly less than for the h=60cm waves described in Chapter 4 which was about 20%. This is thought to be from the geometry of the dissipating beach, but could also be an artifact of the updated fitting algorithm of Section C.1, where the interaction between the 1st and 2nd harmonic (the term β_{12}) incorrectly accounts for too much of the reflected wave that acts at twice the length of the β_{12} term.

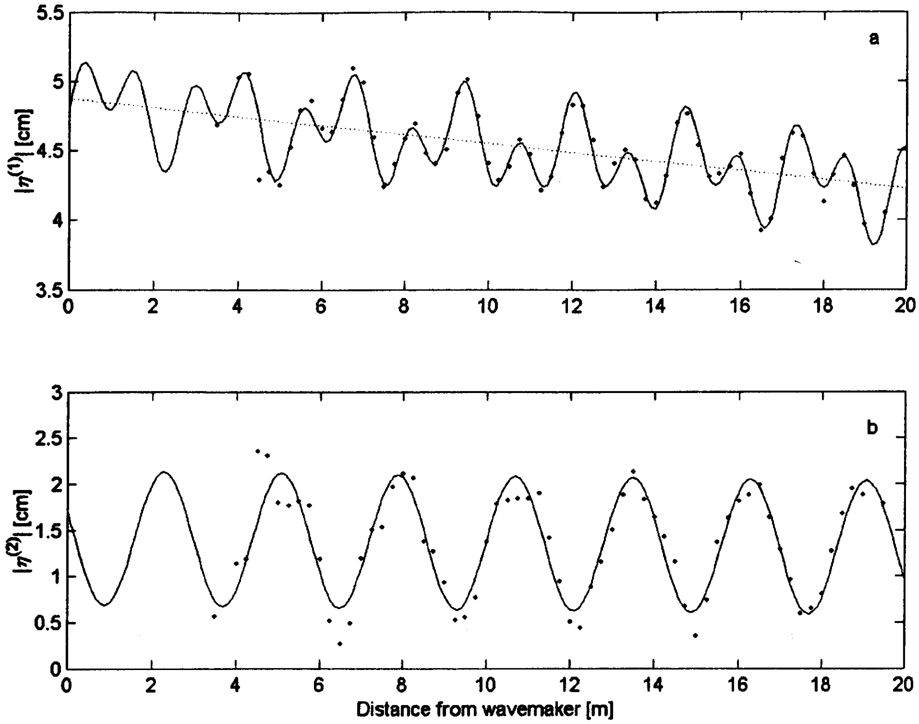

Figure C.4: Attenuation measurements for pure waves o over sand, $h = 40$cm. (a) is the 1st harmonic and (b) is the 2nd harmonic. Dotted line on (a) shows the attenuation slope of the 1st harmonic amplitude.

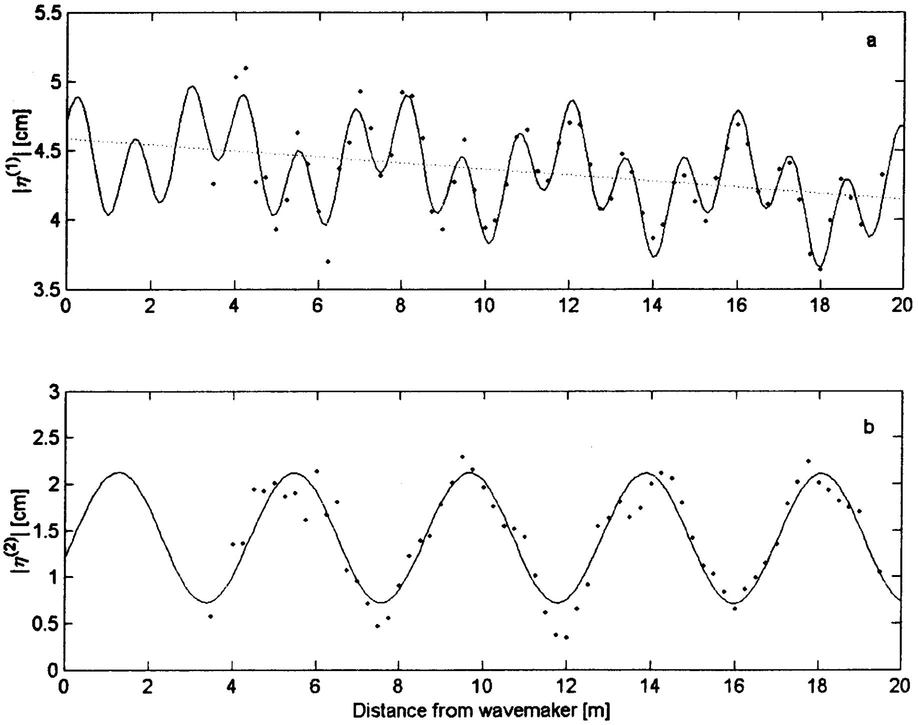

Figure C.5: Attenuation measurements for wave-current flow over sand, $h = 40$cm. (a) is the 1st harmonic and (b) is the 2nd harmonic. Dotted line on (a) shows the attenuation slope of the 1st harmonic amplitude.

Table C.7 also shows the friction factors and the bottom roughnesses for the pure wave and wave-current flows. Table C.8 compares k_w and k_{wc} to the measured ripple geometry as well as the bottom roughness scaling factors α and β. The ripple geometries are the averages of all the measurements available (from both side and ADV). The wave roughness from pure waves is significantly larger than that for waves in the presence of a current.

Table C.7: Attenuation results for pure wave and wave-current experiments over sand, h = 40cm.

Parameter		Pure Wave	Wave-Current
T	[s]	1.5	1.5
a_{i0}	[cm]	4.87	4.59
a_r	[cm]	0.25	0.31
m_t	[cm/cm]	-3.2540E-04	-2.1980E-04
m_b	[cm/cm]	-2.5858E-04	-1.6991E-04
u_{bm}	[cm/s]	16.77	16.9
A_{bm}	[cm]	4.00	4.03
u_{*c}	[cm/s]	--	1.77
u_{*wm}	[cm/s]	5.38	3.89
f_e		0.13	0.08
f_w		0.21	0.11
$\{k_w,\ k_{cw}\}$	[cm]	3.64	1.08

Table C.8: Wave and wave-current roughness compared to measured ripple geometry for sand, h = 40cm.

Parameter		Pure Wave	Wave-Current
$\{k_w, k_{wc}\}$	[cm]	3.64	1.08
η	[cm]	0.83	0.81
λ	[cm]	5.30	5.00
$\alpha = \{k_w, k_{wc}\}/\eta$		4.36	1.33
$\beta = \{k_w, k_{wc}\}/[\eta(\eta/\lambda)]$		27.72	8.26

C.4. PURE WAVE VELOCITY EXPERIMENTS

Pure wave velocity profiles were measured at the 5 locations listed in Table C.1. For this water depth, only 12 vertical points were possible for each profile. The sampling rate was 21Hz, and

2048 points were sampled 5 times at each point in x and z. This yields a total 325 waves measured for each point in the profile. The vertical spacing of the points was $\Delta \ln(z) = 0.25$, starting at 2cm from the local trough up to 27cm.

The time-averaged wave velocity profiles for experiments a, b, c, d, and e are plotted in Figure C.6 at their relative spatial locations. The 1st harmonic free surface variation $|\eta^{(1)}|$ is plotted above the velocity profiles on a separate axis. Also, the mean bed elevation measured after the PW velocity profiles is shown as the solid line near $z = 0$. The vertical profiles plotted are relative to their mean bed elevation in z, to more realistically reflect the spatial variations in the points in the vertical. The velocity structure near the bed is significantly different at the different locations along the 'beat'. Near the surface, however, the velocities are quite similar: all are increasingly negative as they approach the surface.

Figure C.7 shows the same profiles as in Figure C.6, but here they are superimposed. As noted above, from the bottom to about 15cm off the bottom, the velocity varies from profile to profile. Above 15cm, the variability decreases and all profiles become increasingly negative. No clear pattern of circulation due to the reflected wave is present here. This could be from the fact that the reflection R = 6% is significantly less than for the h = 60cm waves, where R = 20%, which would result in a much weaker secondary circulation. However, it is also possible that the interaction between the 1st and 2nd harmonic free surface has confused the velocity structures and made it quite difficult to extract any information about secondary circulations.

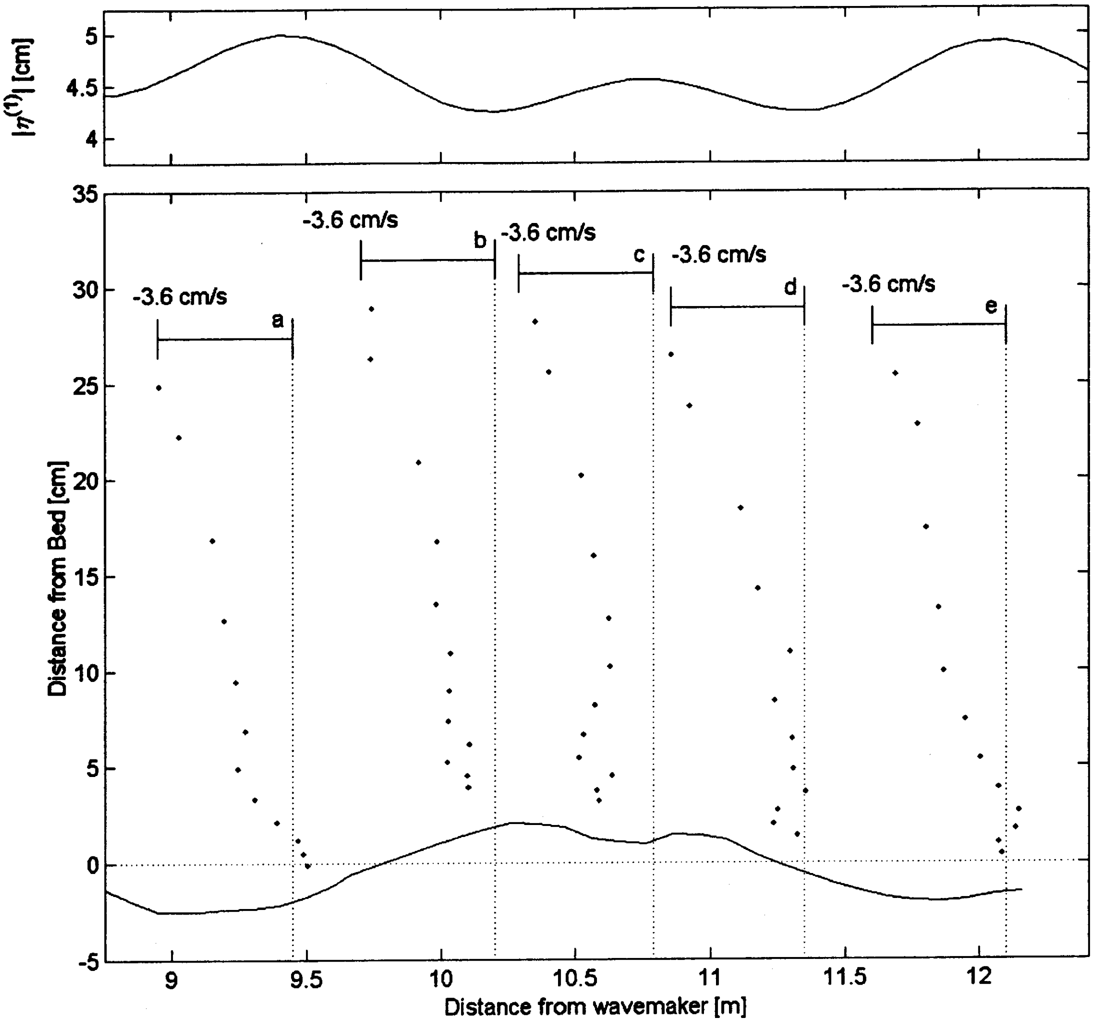

Figure C.6: Time-averaged pure wave velocity profiles (a-e) over sand, h = 40cm. Points (·) are the velocity measurements. The dotted vertical lines represent zero velocity for each of the profiles. The solid line near z=0 is the measured post-PW mean bed elevation. $|\eta^{(1)}|$ is the fit of the variation of the first harmonic and is plotted on a separate axis above the profiles.

Figure C.8 shows the lumped mean pure wave velocity profile, and shows a negative velocity even near the bed in the wave boundary layer, as proposed by TM. However, there is no noticeable velocity overshoot present here as there was in Figure 7.3 for the pure wave h=60cm case. The return current predicted from linear theory here for an amplitude a_i = 4.9cm and reflection of R = 6% gives a u_r = -1.67cm/s. The lumped cycle mean yields a return current of approximately u_r = -1.71cm/s, in excellent agreement with the theoretical prediction.

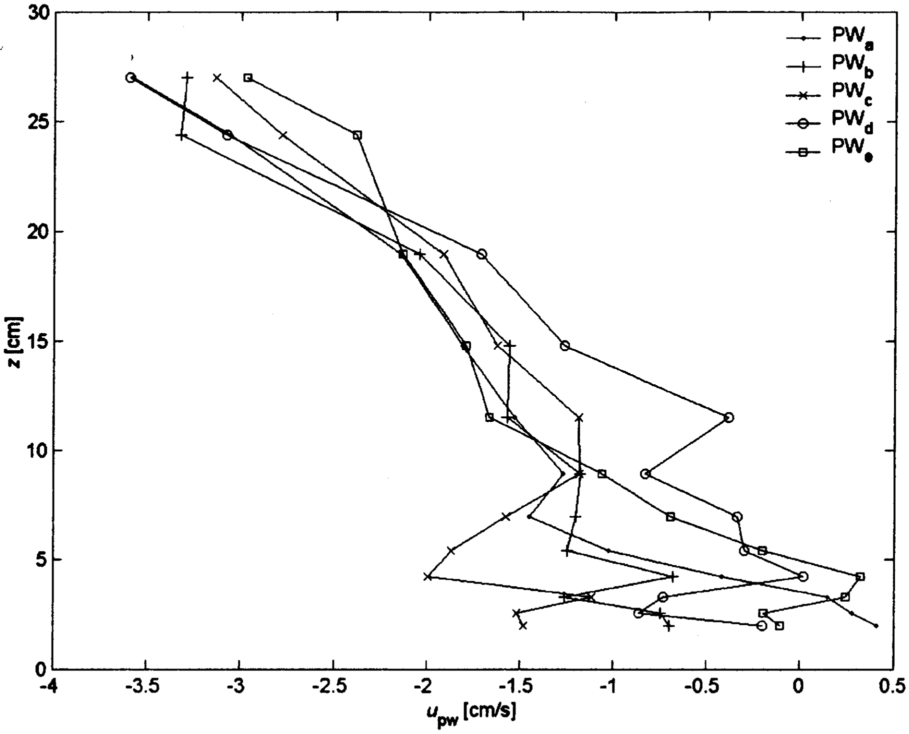

Figure C.7: Time-averaged pure wave velocity profiles for experiments (a-e) over sand, h = 40cm.

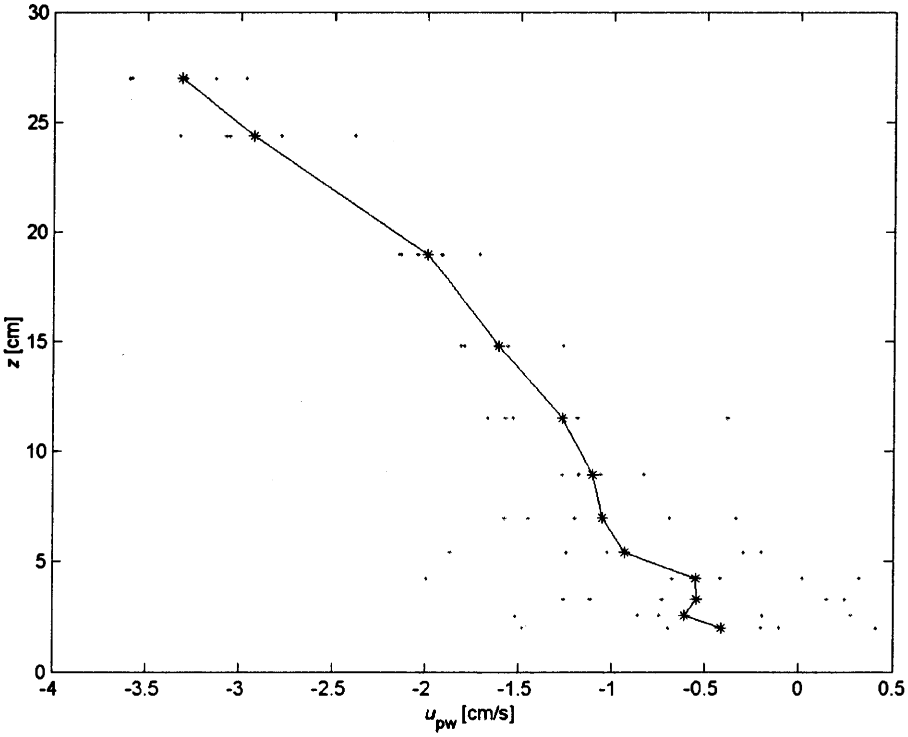

Figure C.8: Lumped mean pure wave velocity profile over sand, h = 40cm. (*) are the lumped mean, and the points (·) are the measured time-averaged individual velocity profile points.

C.5. PURE CURRENT VELOCITY EXPERIMENTS

The pure current velocity profiles were initially measured at the 5 locations a, b, c, d, and e shown in Table C.1. However, these measurements were made over the bottom that was left from the pure wave experiments with a mean bed variation present, as shown in Figure C.3(b), the post PW bottom. This variation will cause the current flow to be non-uniform. Therefore, after the initial pure current and wave-current experiments were complete, the bed was smoothed and pure waves were allowed to develop new ripples for 1hr. This was enough time to give fully developed pure wave ripples, but short enough so that any variation of the mean bed was not yet observable. Then 15 pure current profiles were measured from x = 8m to x = 15m along the flume, including the x-locations of the original 5 points at a, b, c, d, and e. Few bedform geometry measurements were performed for these second 15 current profiles.

The same methods for analyzing the current profiles in Chapter 8 are employed here. Typically, the pure current profile exhibited a difference between the top and bottom portions of the profile, much like was shown for the h = 60cm experiments. The bend in the profile usually occurred around z = 6cm from the bottom so the log fits were made for the three sections all, top and bottom. The first 1 or 2 points near the bottom and the top 1 or 2 points near the surface are often excluded from the log fit as explained in Chapter 8. An example of a measured pure current velocity profile is shown in Figure C.9. Also, the log fits using top, bottom, and all points are shown with dashed, solid, and dotted lines, respectively. The resulting u_{*c} , k_c, and standard deviations of this velocity profile can be seen in Table C.9.

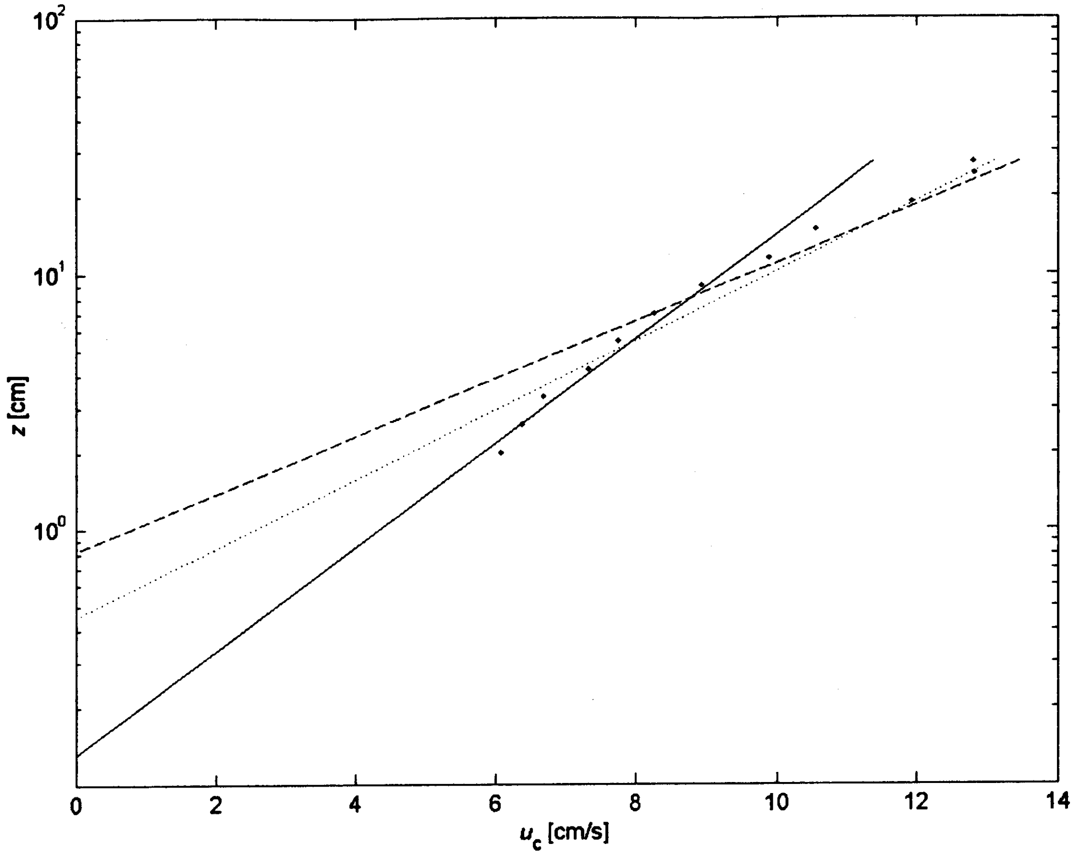

Figure C.9: Pure current velocity profile for experiment kf. Points (·) are measured velocity, solid line is log fit using points 3 to 6 (bottom points), dashed line is log fit using points 6 to 11 (top points), and dotted line is log fit using points 3 to 11 (all points).

Table C.9 shows the results of the pure current experiments. The current shear velocity u_{*c}, the bottom roughness k_c, and their respective standard deviations are shown for all points (excluding those outside the log layer), the top points, and the bottom points. Averages are given for the first 5 experiments a-e, the last 15 experiments af-pf, and the combination of all 20 measurements. Also, the lumped mean results are given for those three combinations.

The variability of the roughness for the first 5 experiments a-e is quite high, as expected since the flow is over the variable mean bed elevation. However, the roughnesses for the experiments af-pf over the zero-mean bed are quite variable as well. It is possible that this variability is due to a variable ripple geometry that may form because of the free surface. This may cause a pattern of changing roughness that influences the current velocity as explained in Section 8.3 and shown in Figure 8.3. If a result such as this occurred, it would appear quite random and induce significant variability in the profiles. Nevertheless, the results of the lumped mean are nearly equal for the first 5 and last 15, both falling within one standard deviation of the other.

Table C.10 shows the comparison of the roughness experienced by the current to the measured ripple geometry. For experiments af-pf, the ripple geometry was only measured at 4 locations. For the locations where the geometry was not measured, the total mean of all the measured geometries, η = 0.8cm and λ = 5.75cm was used. These are denoted by smaller italic text in the table. The bottom roughness scaling factors α ($\alpha = k_c/\eta$) and β ($\beta = k_c/[\eta(\eta/\lambda)]$) are shown in the table and calculated for the all, top and bottom points of the profile. For the straight mean of these experiments, α = 5.2 ± 40%, and β = 37 ± 40%. These values are somewhat higher than those shown in Section 8.5 for the h=60cm flow. However, the variability is nearly the same. If this variability is considered, all the estimates of α or β are statistically the same for the pure current case here, and when compared to the pure current case in Section 8.5.

C.6. WAVE-CURRENT VELOCITY EXPERIMENTS

The combined wave-current velocity profiles were measured at the 5 location A, B, C, D, and E shown in Table C.1. These measurements were made over the bottom that was left from the pure wave and initial 5 pure current experiments with a variable mean bed elevation present, as shown in Figure C.3(b) as the post PW bottom. The bed after the wave-current experiments is also shown and labeled as post WC bottom. The velocity profiles were measured in the same manner

9: Results of the pure current experiments over sand, $h = 40$cm.

Expt ID	x [m]	u_{*c} [cm/s] (all)	(top)	(bot)	k_c [cm] (all)	(top)	(bot)	σ_{u*c} [cm/s] (all)	(top)	(bot)	σ_{kc} [cm] (all)	(top)	(bot)
a	9.45	1.34	1.81	0.81	12.76	30.70	3.22	0.09	0.14	0.04	2.37	5.71	0.53
b	10.20	0.98	1.26	0.85	1.76	5.64	2.55	0.04	0.17	0.06	0.34	3.24	0.31
c	10.79	1.23	1.06	1.39	5.12	2.62	4.57	0.04	0.04	0.09	0.60	0.47	1.25
d	11.35	1.58	1.56	1.52	16.49	15.91	7.93	0.02	0.05	0.09	0.66	1.71	1.87
e	12.10	1.57	1.77	1.20	25.37	35.07	3.16	0.08	0.12	0.61	3.33	6.00	1.02
Mean		1.34	1.49	1.15	12.30	17.99	4.29	0.06	0.10	0.17	1.46	3.43	0.99
Std Dev.		0.25	0.33	0.32	9.37	14.55	2.17	--	--	--	--	--	--
Lumped Mean		1.23	1.31	1.06	7.75	9.60	5.03	0.03	0.11	0.04	0.70	3.01	0.65
gf	8.00	1.10	1.33	0.91	7.24	14.32	3.91	0.04	0.05	0.07	1.00	1.71	1.03
hf	8.50	1.07	1.29	0.93	6.77	13.50	4.21	0.04	0.07	0.08	0.96	2.42	1.17
if	9.00	1.31	1.52	0.96	14.41	22.84	6.10	0.07	0.19	0.14	2.34	8.03	2.84
af	9.45	1.14	1.50	0.96	9.55	22.81	5.06	0.09	0.35	0.18	2.39	14.70	3.41
bf	10.20	1.22	1.80	1.06	10.95	35.46	6.40	0.08	0.65	0.06	2.19	28.95	1.33
cf	10.79	1.18	1.52	0.97	10.35	23.74	3.36	0.09	3.13	0.10	2.47	71.37	2.00
jf	11.00	1.12	1.48	0.80	7.95	21.66	2.04	0.07	0.24	0.05	1.69	11.27	0.65
kf	11.35	1.28	1.54	0.80	13.55	24.61	2.30	0.08	0.09	0.05	2.47	4.02	0.77
df	12.10	1.28	1.46	1.08	14.23	22.57	4.73	0.05	0.13	0.11	1.78	6.10	2.63
ef	12.50	1.17	1.79	0.84	9.70	35.97	3.07	0.09	0.04	0.09	2.40	1.87	1.46
lf	13.00	1.16	1.44	0.84	8.35	18.76	2.21	0.06	0.05	0.20	1.62	1.98	3.03
mf	13.50	1.15	1.58	0.86	8.78	26.58	3.97	0.06	0.13	0.14	1.60	6.30	2.35
nf	14.00	1.32	1.55	0.81	15.38	25.72	3.50	0.07	0.09	0.04	2.50	4.50	0.68
of	14.50	1.16	1.80	0.79	9.46	40.29	2.48	0.07	0.10	0.04	1.97	6.15	0.60
pf	15.00	1.22	1.54	1.07	12.94	28.69	5.79	0.06	0.14	0.13	2.00	7.70	3.19
Mean		1.19	1.54	0.91	10.64	25.17	3.94	0.07	0.36	0.10	1.96	11.80	1.81
Std Dev.		0.08	0.15	0.10	2.80	7.53	1.43	--	--	--	--	--	--
Lumped Mean		1.10	1.46	0.86	7.88	21.34	3.67	0.05	0.07	0.03	1.23	3.27	0.53
ats of all measurements													
Mean		1.23	1.53	0.97	11.06	23.37	4.03	0.07	0.30	0.12	1.83	9.71	1.60
Std Dev.		0.15	0.20	0.20	4.98	9.82	1.59	--	--	--	--	--	--
Lumped Mean		1.16	1.33	0.94	7.69	12.84	4.07	0.04	0.05	0.04	0.80	1.65	0.58

Table C.10: Comparison of the pure current results to the measured bedform geometry over sand, $h = 40$cm.

Expt	x	k_c [cm]			η	λ	k_c/η			$k_c/[\eta(\eta/\lambda)]$		
ID	[m]	(all)	(top)	(bot)	[cm]	[cm]	(all)	(top)	(bot)	(all)	(top)	(bot)
a	9.45	12.76	30.70	3.22	0.73	5.31	17.60	42.35	4.44	128.99	310.33	32.54
b	10.20	1.76	5.64	2.55	1.00	6.72	1.76	5.64	2.55	11.85	37.91	17.13
c	10.79	5.12	2.62	4.57	0.74	5.08	6.91	3.54	6.18	47.47	24.27	42.40
d	11.35	16.49	15.91	7.93	0.70	4.48	23.56	22.73	11.33	150.75	145.48	72.50
e	12.10	25.37	35.07	3.16	0.95	5.50	26.71	36.92	3.33	154.61	213.72	19.26
	Mean	12.30	17.99	4.29	0.82	5.42	15.31	22.24	**5.56**	98.73	146.34	**36.77**
	Std Dev.	9.37	14.55	2.17	0.14	0.82	10.69	17.64	3.50	65.04	120.51	22.47
Lumped Mean		7.75	9.60	5.03	--	--	9.41	11.66	**6.12**	61.97	76.79	**40.27**
gf	8.00	7.24	14.32	3.91	*0.80*	*5.75*	9.05	17.90	4.89	65.05	128.63	35.17
hf	8.50	6.77	13.50	4.21	*0.80*	*5.75*	8.46	16.87	5.26	60.80	121.28	37.79
if	9.00	14.41	22.84	6.10	0.78	6.26	18.47	29.28	7.82	148.25	234.99	62.77
af	9.45	9.55	22.81	5.06	*0.80*	*5.75*	11.94	28.52	6.33	85.81	204.95	45.46
bf	10.20	10.95	35.46	6.40	*0.80*	*5.75*	13.68	44.32	8.00	98.35	318.57	57.50
cf	10.79	10.35	23.74	3.36	0.90	6.96	11.50	26.38	3.73	88.91	203.99	28.87
jf	11.00	7.95	21.66	2.04	*0.80*	*5.75*	9.94	27.07	2.55	71.42	194.58	18.33
kf	11.35	13.55	24.61	2.30	*0.80*	*5.75*	16.93	30.76	2.88	121.70	221.11	20.66
df	12.10	14.23	22.57	4.73	0.60	4.88	23.71	37.62	7.88	192.84	305.97	64.12
ef	12.50	9.70	35.97	3.07	*0.80*	*5.75*	12.12	44.96	3.84	87.15	323.18	27.58
lf	13.00	8.35	18.76	2.21	*0.80*	*5.75*	10.44	23.45	2.76	75.04	168.54	19.86
mf	13.50	8.78	26.58	3.97	*0.80*	*5.75*	10.98	33.23	4.96	78.92	238.83	35.67
nf	14.00	15.38	25.72	3.50	*0.80*	*5.75*	19.23	32.15	4.37	138.22	231.06	31.41
of	14.50	9.46	40.29	2.48	*0.80*	*5.75*	11.83	50.36	3.10	85.04	361.99	22.28
pf	15.00	12.94	28.69	5.79	0.77	6.40	16.80	37.26	7.52	139.66	309.72	62.50
	Mean	10.64	25.17	3.94	0.79	5.85	13.67	32.01	**5.06**	102.48	237.83	**38.00**
	Std Dev.	2.80	7.53	1.43	0.06	0.44	4.38	9.62	2.00	37.53	72.59	16.57
Lumped Mean		7.88	21.34	3.67	--	--	9.98	27.02	**4.64**	73.90	200.06	**34.38**
Stats of all measurements												
	Mean	11.06	23.37	4.03	0.80	5.74	14.08	29.57	**5.19**	101.54	214.96	**37.69**
	Std Dev.	4.98	9.82	1.59	0.08	0.57	6.22	12.35	2.36	43.94	92.69	17.58
Lumped Mean		7.69	12.84	4.07	--	--	9.64	16.08	**5.10**	69.34	115.66	**36.71**

as the pure wave profiles: 2048points sampled at 21Hz repeated 5 times at 12 vertical locations spaced at $\Delta\ln(z) = 0.25$. Ripple geometry was primarily measured with the side-tracing method, and was performed just before and just after each velocity profile measurement.

The same methods for analyzing the wave-current profiles described in Chapter 9 were employed here. First, the apparent roughness felt by the current and the current shear velocities are obtained from the measured velocity profiles. Then, the velocity profile is predicted with the GMm and LC models based on the local observed bottom roughness. The bottom roughness input to the models is scaled by the ripple geometry using $\alpha = 4\eta$. This shows how well the models can predict the velocity, and the goodness of the fit is measured. Then, the roughness is varied until a best fit profile is achieved, giving the actual value of the bottom roughness felt by the particular profile. By comparing this roughness with the observed bedform geometry, estimates of the required scaling factors α and β can be obtained.

The experimental parameters for the wave-current flows used in the application of the GMm and the LC models are given in Table C.11. The two estimates of the depth-averaged velocities are found by the same methods as described in Section 9.3. The flow rate Q for these experiments is about 570gpm (0.036m^3/s). This gives the straight mean depth-averaged current velocity as about 11.5cm/s.

Figure C.10 shows the velocity profile predictions of the GMm and LC models for (a) experiment D and (b) the lumped mean velocity profile. The GMm model predictions are quite good, and match the WC data almost perfectly for the lumped mean case. The top-most points

Table C.11: Base parameters for wave-current experiments over sand, h = 40cm.

		Expt A	Expt B	Expt C	Expt D	Expt E	Mean	Standard Deviation
x	[m]	9.45	10.20	10.79	11.35	12.10	10.78	--
h	[cm]	42.58	38.43	38.73	41.73	43.43	40.98	2.28
$z(u=u_m)$	[cm]	15.67	14.14	14.25	15.35	15.98	15.08	0.84
$u_{c,mean}$ from u_{*c}, k_c	[cm/s]	10.24	12.28	12.38	11.62	11.18	11.54	0.88
$u_{c,mean}$ from Q	[cm/s]	11.05	12.24	12.15	11.28	10.83	11.51	0.65
measured u_{bm}	[cm/s]	12.80	16.04	15.44	16.80	14.19	15.05	1.58
measured η	[cm]	0.73	0.85	0.74	0.85	0.88	0.81	0.07
measured λ	[cm]	4.80	4.87	4.54	5.43	5.45	5.02	0.41

fall off of the predicted profile. This is thought to be from the interaction with the wave-induced mass transport, which is quite large at these top-most points (about –3.5cm/s). The points (·) are the measured data and the points used to obtain k_{ca} and u_{*c} are shown with points inside open circles. As discussed in Section 9.3 and shown by the data in Chapter 9, the LC model requires a bottom roughness scaling factor about 3 times larger than that required for the GMm model. This is related to the definition of the boundary layer thickness of the LC model. In Figure C.10, the predictions were made with $k_{cw} = 4\eta$. To get a better prediction with LC, it should be made with $k_{cw} = 12\eta$. This shown by the data in Table C.12.

The results of the wave-current analysis on the raw wave-current velocity profiles are shown in Table C.12. This table is set up the same as the tables presenting the analysis of the profiles in Chapter 9, such as Table 9.2. Results are given for all 5 experiments. The predictions of the wave-current velocity profiles are good, and the errors of the predictions are on the same order as the errors from the fits, about 1.4cm/s for the GMm model (the LC cannot be compared, as the

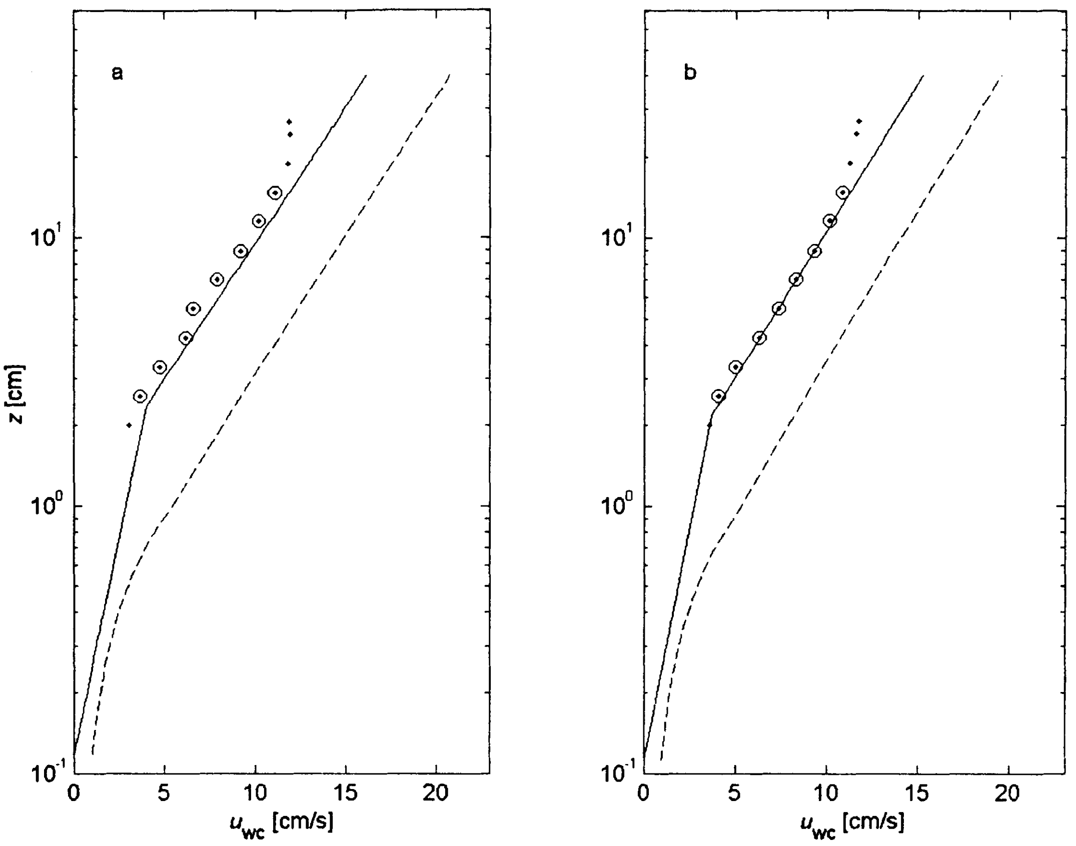

Figure C.10: Wave-current velocity profiles over sand, h = 40cm for (a) experiment D and (b) lumped mean. Solid line is GMm and dashed line is LC predictions using $k_{cw} = 4\eta$. Points (·) are the measured velocity data, and points with open circles are used to determine u_{*c} and k_{ca}.

predictions were made with an incorrect value of the roughness). The bottom roughness scaling factors closely match the results of the h=60cm experiment of Chapter 9. For the GMm model, α = 4.5 ± 20% and β = 27.7 ± 20% and for the LC model, α = 13.3 ± 15% and β = 82 ± 15%.

The fact that these predictions are so close to the measured profiles are initially quite surprising, as these predictions are without any adjustments to the measured velocity profiles. But consider the adjustments that were made in Chapter 9. The main premise of the adjustments were that the wave-induced mass transport near the edge of the wave boundary layer effectively shifts the measured velocity profile by the wave-induced streaming, as suggested by Mathisen and Madsen

Table C.12: Results of wave-current experiments over sand, h = 40cm, raw velocity profiles.

		Expt A	Expt B	Expt C	Expt D	Expt E	Mean	Standard Deviation	Lumped Mean
k_{cw} = 4η									
u_{*c} (2:9)		1.30	1.82	1.74	1.75	1.68	1.66	0.21	1.62
σ_{u*c}		0.12	0.18	0.11	0.05	0.08	0.11	0.05	0.05
k_{ca} (2:9)		19.88	28.51	24.78	32.40	33.34	27.78	5.57	26.60
σ_{kca}		4.25	5.35	3.34	1.63	2.70	3.45	1.43	1.73
4η		2.91	3.40	2.97	3.38	3.50	3.23	0.27	3.23
k_{ca} GMm		23.98	25.75	22.69	27.60	25.58	25.12	1.87	25.54
k_{ca} LC		8.14	8.78	7.73	9.33	8.78	8.55	0.63	8.67
error GMm		0.81	1.59	1.54	1.31	1.57	1.37	0.33	0.90
error LC		3.33	6.45	6.15	6.22	6.27	5.68	1.32	5.28
Best fit k_{cw}									
k_{cw} GMm	[cm]	2.40	3.79	3.26	4.04	4.72	3.64	0.87	3.38
k_{cw} LC	[cm]	7.28	11.39	9.87	12.06	13.52	10.82	2.38	10.15
σ_{kcw} GMm	[cm]	2.38	3.36	1.99	1.02	1.86	2.12	0.85	1.04
σ_{kcw} LC	[cm]	7.21	10.09	6.02	3.04	5.33	6.34	2.59	3.12
k_{ca} GMm	[cm]	20.08	28.49	24.81	32.32	33.59	27.86	5.55	26.58
k_{ca} LC	[cm]	20.91	30.31	26.16	34.52	35.92	29.57	6.16	28.11
error GMm	[cm/s]	0.72	1.74	1.81	1.11	0.90	1.26	0.49	1.14
error LC	[cm/s]	0.65	1.58	1.68	0.97	0.77	1.13	0.47	1.01
$\alpha = k_{cw,\,GMm} / \eta$		3.30	4.46	4.38	4.78	5.39	**4.46**	0.76	**4.19**
$\alpha = k_{cw,\,LC} / \eta$		10.00	13.40	13.28	14.27	15.45	**13.28**	2.03	**12.56**
$\beta = k_{cw,\,GMm} / [\eta(\eta/\lambda)]$		21.78	25.51	26.72	30.76	33.59	**27.67**	4.61	**25.99**
$\beta = k_{cw,\,LC} / [\eta(\eta/\lambda)]$		65.98	76.71	81.01	91.75	96.24	**82.34**	12.07	**77.98**

(1996a, b). The pure wave time-averaged lumped mean velocity profile shown in Figure 7.3 exhibits the large wave streaming and velocity overshoot at the edge of the wave boundary layer. The velocities at that location are as high as about –1.25cm/s. However, the velocities at the wave boundary layer for the h=40cm experiments ($z = \delta_w \cong$ 2-3cm) are only about 0.5cm/s. This wave-streaming is much less than that found for the h=60cm experiments. Consequently, the profiles do not feel the same effects from the wave-streaming here as they did in Chapter 9, and no adjustment for mass transport is required to obtain a good fit.

However, for comparison, the wave-current velocity profiles were adjusted for the pure wave-induced mass transport by subtracting the pure wave velocity profiles at the same locations, just as was done in Section 9.4.2. Figure C.11 shows the predictions of the GMm and LC models to

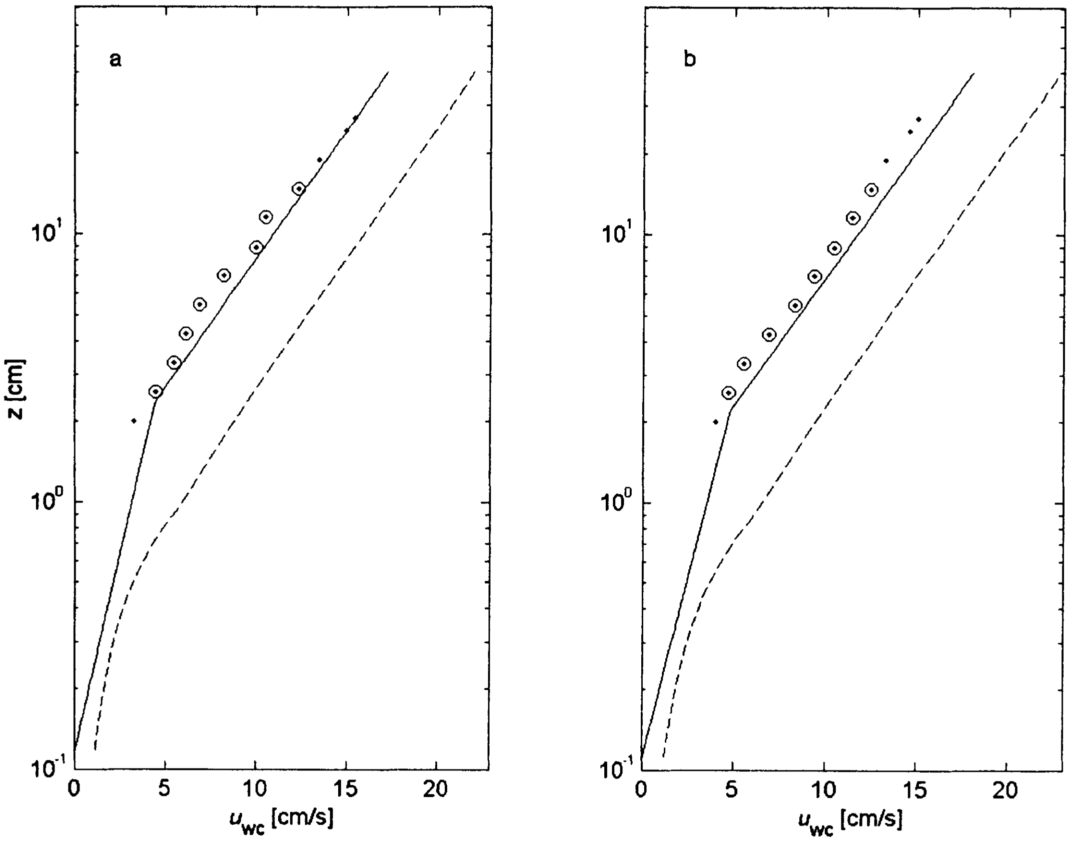

Figure C.11: Wave-current velocity profiles over sand, h = 40cm for (a) experiment D and (b) lumped mean adjusted for the mass transport from the entire pure wave velocity profiles. Solid lines are GMm and dashed lines are LC predictions using $k_{cw} = 4\eta$. Points ($\cdot$) are measured velocity, and points with open circles are used to determine u_{*c} and k_{ca}.

the wave-current velocity profiles adjusted for pure wave mass transport for experiment D and the lumped mean profile.

Table C.13 shows the results of this analysis. Here, the results are quite similar to those from the raw data. In this case, the predictions fit the data slightly worse than the predictions based on the raw data. Also, the variability of the results has increased. For the straight mean of the GMm model, $\alpha = 5.8 \pm 40\%$ and $\beta = 36.2 \pm 40\%$ and for the LC model, $\alpha = 16.8 \pm 40\%$ and $\beta = 105 \pm 40\%$.

Table C.13: Results of wave-current experiments over sand, h = 40cm, mass transport from pure wave velocity profiles.

		Expt A	Expt B	Expt C	Expt D	Expt E	Mean	Standard Deviation	Lumped Mean
k_{cw} = 4η									
u_{*c} (2:9)		1.84	1.99	1.77	1.85	2.22	1.93	0.18	1.86
σ_{u*c}		0.18	0.18	0.19	0.10	0.15	0.16	0.03	0.05
k_{ca} (2:9)		31.70	26.22	18.10	31.27	44.99	30.45	9.80	27.66
σ_{kca}		5.77	4.83	4.51	3.29	4.65	4.61	0.89	1.34
4η		2.91	3.40	2.97	3.38	3.50	3.23	0.27	3.23
k_{ca} GMm		18.11	23.96	22.37	26.44	20.35	22.25	3.21	22.89
k_{ca} LC		6.44	8.28	7.64	8.98	7.36	7.74	0.96	7.90
error GMm		2.91	1.08	1.03	0.81	4.89	2.15	1.75	1.06
error LC		7.97	6.48	4.50	6.03	10.89	7.17	2.42	6.33
Best fit k_{cw}									
k_{cw} GMm	[cm]	5.21	3.73	2.37	4.10	8.16	4.71	2.18	3.95
k_{cw} LC	[cm]	14.96	11.35	7.37	12.20	22.41	13.66	5.60	11.76
σ_{kcw} GMm	[cm]	4.24	3.02	2.45	2.08	3.96	3.15	0.94	0.85
σ_{kcw} LC	[cm]	12.19	9.20	7.63	6.19	10.87	9.22	2.41	2.54
k_{ca} GMm	[cm]	31.85	26.20	18.10	31.43	46.58	30.83	10.40	27.63
k_{ca} LC	[cm]	34.61	28.02	18.81	33.35	50.65	33.09	11.62	29.42
error GMm	[cm/s]	0.70	0.70	0.70	0.41	0.41	0.58	0.16	0.18
error LC	[cm/s]	0.72	0.72	0.70	0.40	0.56	0.62	0.14	0.25
$\alpha = k_{cw,\,GMm} / \eta$		7.16	4.39	3.19	4.85	9.33	**5.78**	2.45	**4.88**
$\alpha = k_{cw,\,LC} / \eta$		20.56	13.35	9.91	14.43	25.61	**16.77**	6.26	**14.55**
$\beta = k_{cw,\,GMm} / [\eta(\eta/\lambda)]$		47.20	25.13	19.44	31.18	58.11	**36.21**	16.04	**30.31**
$\beta = k_{cw,\,LC} / [\eta(\eta/\lambda)]$		135.63	76.41	60.46	92.82	159.52	**104.97**	41.41	**90.31**

C.7. SUMMARY

The results of the application of the GMm model to the wave-current velocity data are shown in Table C.14. These results emphasize the fact that the mass transport in these experiments plays a minor role in the wave-current velocity profile prediction.

Table C.15 summarizes the bottom roughness values obtained from the pure waves, waves in the presence of a current, pure currents, and currents in the presence of waves. The different methods of averaging (both straight and lumped mean) as well as the wave-current results from both neglecting and including mass transport are shown (note the footnotes in the table). For the

Table C.14: Summary of the bottom roughness and the bottom roughness scaling factors for a current in the presence of waves over sand, h = 40cm for the GMm model.

	No mass transport			Mass transport from Pure Wave		
	k_{cw} [cm]	α	β	k_{cw} [cm]	α	β
	2.40	3.30	21.78	5.21	7.16	47.20
	3.79	4.46	25.51	3.73	4.39	25.13
	3.26	4.38	26.72	2.37	3.19	19.44
	4.04	4.78	30.76	4.10	4.85	31.18
	4.72	5.39	33.59	8.16	9.33	58.11
mean	3.64	4.46	27.67	4.71	5.78	36.21
Std. Dev.	0.87	0.76	4.61	2.18	2.45	16.04
Lumped Mean	3.38	4.19	25.99	3.95	4.88	30.31

Table C.15: Summary of mean measured bottom roughness and bottom roughness scaling factor values for sand, h = 40cm.

	roughness [cm]	Std. Dev. of roughenss	α	β
k_w	3.64	--	4.36	27.72
k_{wc}	1.08	--	1.21	7.48
k_c^1	4.03	1.59	5.19	37.69
k_c^2	4.07	0.58	5.10	36.71
$k_{cw}^{1,3}$ (GMm)	3.64	2.12	4.46	27.67
$k_{cw}^{1,4}$ (GMm)	4.71	3.15	4.95	30.74
$k_{cw}^{2,3}$ (GMm)	3.38	1.04	4.19	25.99
$k_{cw}^{2,4}$ (GMm)	3.95	0.85	4.88	30.31
mean	3.53	--	**4.2**	**28.0**
std. dev.	1.26	--	1.5	10.9
$k_{cw}^{1,3}$ (LC)	10.82	6.34	13.28	82.34
$k_{cw}^{1,4}$ (LC)	11.38	3.23	15.09	93.39
$k_{cw}^{2,3}$ (LC)	10.15	3.12	12.56	77.98
$k_{cw}^{2,4}$ (LC)	11.76	2.54	14.55	90.31
mean	11.03	--	**13.9**	**86.0**
std. dev.	0.70	--	1.2	7.1

[1]: straight mean value.

[2]: lumped mean value.

[3]: no mass transport.

[4]: mass transport from pure waves.

GMm model, α and β were about the same for all cases except for k_{wc}. This discrepancy is thought to be related to the highly variable free surface, but could also be from the uncertainty in the sidewall correction, as discussed in Section B.5. Nevertheless, it was found that $\alpha = 4.2 \pm 35\%$ and $\beta = 28 \pm 40\%$. Also, when using the LC model, it was shown that the scaling factors α and β should be multiplied by a factor of 3.